2005

A tracer monitored titration for seawater total alkalinity

Todd R. Martz
The University of Montana

Maureen and Mike
MANSFIELD LIBRARY

The University of

Montana

Permission is granted by the author to reproduce this material in its entirety, provided that this material is used for scholarly purposes and is properly cited in published works and reports.

Please check "Yes" or "No" and provide signature

Yes, I grant permission _____

No, I do not grant permission _____

Author's Signature: _____

Date: _____

Any copying for commercial purposes or financial gain may be undertaken only with the author's explicit consent.

8/98

A Tracer Monitored Titration for Seawater Total Alkalinity

By

Todd R. Martz

B.S. Chemistry, Newman University, 2000

B.A. Mathematics, Newman University, 2000

Presented in partial fulfillment of the requirements
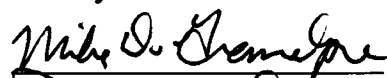
for the degree of

Doctor of Philosophy

The University of Montana

December 2005

Approved by:

Chairperson

Dean, Graduate School

12/19/05

Date

UMI Number: 3205444

INFORMATION TO USERS

The quality of this reproduction is dependent upon the quality of the copy submitted. Broken or indistinct print, colored or poor quality illustrations and photographs, print bleed-through, substandard margins, and improper alignment can adversely affect reproduction.

In the unlikely event that the author did not send a complete manuscript and there are missing pages, these will be noted. Also, if unauthorized copyright material had to be removed, a note will indicate the deletion.

UMI®

A Tracer Monitored Titration for Seawater Total Alkalinity

Chairperson: Michael D. DeGrandpre *MᵢƟ*

We introduce a new titration method *MᵢƟ* named Tracer Monitored Titration (TMT), in which analyses are free of volumetric and gravimetric measurements, and insensitive to pump precision and reproducibility. Conventional seawater total alkalinity (TA) measurements require calibrated volumetric flasks, pipets and titration cells to quantify sample and calibrated burets or piston pumps to dispense titrant. Consequently, of the very few fully automated systems that exist, none are sufficiently simple to be readily adapted to an autonomous sensor. Spectrophotometric monitoring of titrant dilution factor rather than volume increment lays the burden of performance solely on the spectrophotometer. Titrant is prepared by quantitative addition of a sulfonephthalein indicator to a standardized solution of HCl. Dilution of a pulse of titrant in a titration vessel is tracked using the total indicator concentration, measured spectrophotometrically. The concentrations of protonated and unprotonated indicator species, derived from Beer's Law, are used to calculate titrant and sample dilution factors in addition to the equilibrium position of the titration mixture. We present data from 286 titrations on three types of total alkalinity standards: Na_2CO_3 in 0.7 mol kg-soln^{-1} NaCl, NaOH in 0.7 mol kg-soln^{-1} NaCl and a seawater certified reference material (CRM). The accuracy and precision are $\pm 0.2\%$ and $\pm 0.1\%$ (4 and 2 μmol kg-soln^{-1} for TA ~2100-2500 μmol kg-soln^{-1}, n = 242), using low precision solenoid pumps (reproducible to no better than 10%). Excellent accuracy and stability are achieved without the need for standard calibrations as a result of optimizing the performance of the spectrophotometric detection system and relying upon basic chemical thermodynamics for calculating the equivalence point. The TMT system built for this study is fully automated, with maximum sample throughput of 90 day^{-1} (~16 minutes per titration). We observed no drift over a 40-day period without calibration. The system is currently capable of ~3000 continuous titrations without an operator (e.g. hourly samples for 4.5 months). Although applied to acid-base titrations in this project, the approach should be generally applicable to other types of titrations.

Acknowledgements

This research was supported by grants funded through the National Science Foundation and Department of Defense.

I wish to thank the Department of Chemistry at the University of Montana for providing a relaxed yet challenging learning environment. I also thank the Chemistry faculty for selecting me as the Stanley Ames scholar and the Bertha Morton Foundation for their scholarship.

Research Specialist Cory Beatty facilitated my introduction to the DeGrandpre laboratory. Over the past five years Cory provided continuous technical advice, saving me countless hours of confusion.

Research Technician David Kemple at Sunburst Sensors helped fabricate some of the analog circuitry used in my research. I also subjected him to a number of discussions regarding my lacking knowledge of electronics.

Graduate Students Shigui Yuan and Matthew Seidel aided me in numerous experiments and provided many welcomed hours of distraction from this work.

Administrative Assistant Becky Gray facilitated a great deal of clerical work, rescuing me from the toils of purchasing and university bureaucracy.

Reuben Darlington and Mark O'Day (Big Sky Machining) were helpful in machining the flow cell.

Professor Andrew Dickson was kind enough to accept me as a visiting researcher in his laboratory at Scripps Institution of Oceanography. During this time, George Anderson taught me several essential laboratory techniques. Andrew personally educated me on several subjects that were critical in the research presented here. I consider my time at SIO as a major enlightenment in my understanding of chemistry. Andrew is a truly brilliant scientist.

Professor Michael DeGrandpre recruited me during my graduate school search and has been my research advisor for the past five years. I cannot imagine a better mentor. Over the years Mike has always provided excellent professional guidance. After working with him during the most influential time of my career, I feel qualified in stating that Mike has a gift for conducting quality research and a vision for attacking important scientific problems. I will always treasure the discussions we shared while hiking in the Montana mountains.

Table of Contents

v

vi

List of Tables

List of Figures

ix

Terminology

chemical terms

TA	total alkalinity
A_C	carbonate alkalinity
C_T	total dissolved inorganic carbon
B_T	total boron
F_T	total fluoride
S_T	total sulfate
$[I]_{a/i}$	total indicator concentration in titrant mixture
$[I]_{stock}$	total indicator concentration in a stock solution
$[I]_T$	total indicator concentration during a titration
Acy	total acidity of titrant mixture
K_{1C}	first dissociation constant of carbonic acid
K_{2C}	second dissociation constant of carbonic acid
K_B	dissociation constant of boric acid
K_F	dissociation constant of hydrogen fluoride
K_S	second dissociation constant of sulfuric acid
K_I	dissociation constant of acid-base indicator (BCG)
K_W	ion product of water
BCG	Bromocresol green
m	mols solute per kilogram solution (mol kg-soln^{-1})
m	mols solute per kilogram solvent (molality)
M	mols solute per liter solvent (molarity)
N	normality, equivalents per liter solvent
a/i	pertaining to the acid/indicator titrant mixture
D	dilution factor
ep	equivalence point
I	ionic strength
M_x	mass of solution x
ΔH	enthalpy of reaction
ρ	density

optical terms

au	absorbance unit
b	optical pathlength
bp	spectral bandpass
CWL	center wavelength
FWHM	full width at half maximum
PWL	peak wavelength
εb	effective molar absorbtivity
$_\lambda A$	optical absorbance at wavelength λ
$_\lambda \varepsilon_x$	molar absorptivity of species x at wavelength λ

miscellaneous terms

CRM	certified reference material
NLLS	non-linear least squares
r	residual

x

RSD   relative standard deviation
S   salinity
SAMI   submersible autonomous moored instrument
TMT   tracer monitored titration
σ   1 standard deviation

Chapter 1   Total Alkalinity: Background, Definition and Importance

Contemporary oceanographic studies that utilize total alkalinity (TA) require

precision and accuracy of ~0.1% or <3 μmol kg-soln^{-1} (μm) (Dickson and Riley, 1978).

Although a number of well-refined methods are already in place and functioning with

excellent accuracy and precision, very few fully automated titration systems exist. Of the

automated systems developed thus far, none are sufficiently simple to be readily

adaptable to an autonomous instrument. Below, we present a new titration methodology

named tracer monitored titration (TMT) engineered for simplicity, with the ultimate goal

of autonomous operation. This type of titration has not been reported by others. The

research described here is therefore at the proof-of-concept stage of development.

Accordingly, our primary goal was an extensive laboratory-based testing of TMT. The

results verify that TMT is capable of achieving the precision and accuracy required by

oceanographers. The system built for this study successfully titrated samples in fully

automated mode over long periods (days-weeks) achieving high accuracy and precision,

without any noticeable drift. In many ways, this system is simpler than its counterparts,

and holds potential for adaptation to an autonomous instrument.

The main body of this document is the first ~100 pages; the ~125 pages thereafter

are supplementary appendices. The vital details of the research conducted for this project

are contained in the ~65 pages from Chapter 2 to 4. Chapter 1 (Introduction) reviews the

concept of TA, addresses the need for a simplified TA method and explains the basic

theory behind TA measurement. Chapter 2 (Theoretical) further develops the specific

theory of TA measurement by TMT and discusses measurement errors based on a

theoretical model and uncertainty calculations. Chapter 3 (Experimental) gives the

1

details of the laboratory design and procedures involved in TMT. Chapter 4 (Results and Discussion) presents the results of measurements using the TMT system and summarizes these findings. In-depth information and complementary experiments regarding various components of the instrument are found in Appendix A. Appendices B-E describe programs, calculations and procedures pertinent to this research, but too detailed for inclusion in the main body.

1.1 Historical overview[1]

Around 1770, Lavoisier realized that carbonate salts are present in seawater (Riley and Skirrow, 1965), but the mental picture of acids and bases was still too primitive at that time to put forth a meaningful explanation of alkalinity or acidity. Tørnoe and Dittmar, in the mid 1880's, developed the first systematic alkalinity determinations, involving addition of a strong acid to seawater and quantifying the neutralizing effect of seawater on the acid (Dickson, 1992). At about the same time several pivotal figures in chemistry, including Arrhenius[2], van't Hoff, and Ostwald, realized the laws of mass action, chemical equilibrium and electrolytic dissociation (Arrhenius, 1912). In the second decade of the 20th century, Sørenson's pioneering work on the measurement of pH further connected Arrhenius' solution theory to the fast-evolving field of acid-base chemistry. In the 1920's, insights by Debye, Hückel, Brønsted and Lowry filled in most of the gaps in acid-base theory, providing the widely accepted aqueous models of ion activity and proton transfer. Between 1920 and 1950, several researchers (most notably Buch) diligently investigated the dissociation of

---

[1] Riley and Skirrow (1965) and Dickson (1992) provide fascinating accounts of the historical development of our present-day understanding of seawater alkalinity.

[2] Incidentally, it was Arrhenius who first recognized the greenhouse effect and the human potential for its alteration; one of primary motivations behind modern measurements of seawater TA.

2

carbonic acid in seawater, tying together the earlier chemical dissociation and equilibrium theories with the newer concept of ionic strength (Mehrbach et al., 1973). It seems that Tørnoe and Dittmar understood that carbonate salts were the source of seawater's ability to neutralize strong acid (Riley and Skirrow, 1965) although as late as 1920, prominent oceanographers confused the alkalinity supply with alkali-earth (i.e. Ca and Mg) hydroxides (Herdman, 1923). From the 1930's to present day, scores of researchers have introduced widely differing and increasingly sophisticated methods for the determination of seawater's capacity to neutralize a strong acid, a parameter now referred to as the *Total Alkalinity*.

1.2 Rationale

There is great demand for simplified titrations that can be automated for operator-free applications in industrial, medical and environmental monitoring and research. Conventional titration methods use calibrated volumetric flasks and titration cells or gravimetry to quantify sample and calibrated burets or pipets to dispense titrant. Automated systems typically use volumetric analysis because gravimetric measurements of sample and titrant are very difficult to automate (Yao and Byrne, 1998). These techniques have been automated using in-line pipets and sample loops for sample quantification along with motorized burets and coulometry for titrant quantification (Liang, 1990; Roche and Millero, 1998). Fully automated robotic systems have also been developed (Metrohm Inc.). These methods achieve excellent accuracy and precision, but require careful empirical calibration specific to each vessel in addition to several sophisticated motorized components (pumps, valves, piston burets). Some automated methods, for example, flow injection analysis (Ruzicka, 1988), sequential injection

3

analysis (Fletcher and van Staden, 2003; Mesquita and Rangel, 2004), continuous on-line endpoint monitoring (Tanaka et al., 2000; Watanabe et al., 2004) and a variety of unsegmented batch titrations (Almeida et al., 2000; Korn et al., 1995), do not require volumetric or gravimetric measurements. These titrations use peak width measurements with a time abscissa or directly incorporate flow rate into the endpoint calculation. These so-called 'volumetric-gravimetric-free' techniques are therefore dependent upon flow rate and, to obtain the best data, require use of high precision pumps and the repeated introduction of standards to compensate for pump fluctuations. The development of an automated method, free of volumetric and gravimetric measurements in addition to pump precision, would simplify titrimetric analysis making it more amenable to unattended operation. Here, I present a new method named Tracer Monitored Titration (TMT), which quantifies dilution factors of titrant and sample through a chemical tracer (colorimetric indicator) in the titrant. Relative proportions of sample and titrant (dilution factors) are used in the equivalence point calculation, in place of physically metered volumes, masses, flow rates or peak width (time). In the method described here, the titrant is a standardized mixture of an acid-base indicator and HCl. The mass ratio of titrant in the sample is then tracked by spectrophotometric measurement of the total indicator concentration. Measuring the individual concentration of each indicator species allows calculation of titrant and sample dilution factors (from total indicator concentration) in addition to the pH of the titration mixture (from the ratio of indicator species).

Our primary motivation in developing a simplified titration system is driven by our research on the marine inorganic carbon cycle. It is very challenging to obtain the

4

0.1% TA precision and accuracy desired for oceanographic studies. In addition, titrations must be performed continuously at sea on a medium to high frequency (~15 minutes or less). All data collected during the major oceanographic surveys (GEOSECS, JGOFS, WOCE and OACES) were obtained from batch titrations that require a full time operator.

A few researchers have successfully built fully automated seawater TA systems. Although flow injection analysis is probably the most convenient approach to automated titration, it has not met the accuracy and precision required for geochemical calculations of the seawater carbon dioxide system (Turner et al., 1987). Similarly, sequential injection analysis methods for TA reported inadequate precision (Fletcher and van Staden, 2003). Graneli and Anfalt (1977) ingeniously built an internally stirred syringe with a custom photometer (Anfalt and Graneli, 1976) attached to the glass barrel. They reported a TA RSD of 0.1% on ten seawater samples. Due to the sheer complexity of their approach, it is not surprising that oceanographers never adopted this method. Roche and Millero (1998) developed a fully automated spectrophotometric system that achieved accuracy and precision ~0.1%. Most recently, Watanabe et al., (2004) developed a potentiometric method based on daily calibrations of an electrode's response to standards under highly precise mixing conditions. All of these systems, however, rely on accurate and precise volumetric delivery. The oceanographic community would greatly benefit from a simplified titration system for shipboard studies that could be more easily adapted for in situ measurements. An autonomous instrument for TA, similar to those already developed by us for pCO$_2$ (DeGrandpre et al., 1995) and pH (Martz et al., 2003) would allow continuous TA monitoring from moorings or autonomous floats, in place of the current shipboard methods. Here, TMT is proposed for these purposes.

5

Some methods, even further removed from the definition of a titration (IUPAC, 1997) have also been suggested for measurement of seawater TA. One such method involves equilibrating a seawater sample with CO_2 gas of known pCO_2 and measuring the pH (Keir et al., 1977). Using spectrophotometric pH measurements, the CO_2 equilibration method achieves precision of ±1 μm (Breland and Byrne, 1992). This method has the advantage of volumetric-gravimetric free measurements and should be free of drift if spectrophotometric pH is utilized. However, a long equilibration time (~40 min) and requirement of CO_2 gas standards limits this technique to the laboratory. TA has also been successfully measured by ion chromatography (IC) (Hu et al., 2001). This method involves conditioning a reversed phase column with a strong acid, and eluting alkaline samples with acidified lithium dodecyl sulfate. The IC technique features low sample consumption (~10-100 μL), very low detection limit (~10 μm) and simultaneous identification of the major monovalent cations, but the precision of this method (±15 μm) is currently too poor and the divalent cations in seawater (Ca^{2+}, Mg^{2+}) may irreversibly bind to the column over time. No TA method is fully divorced from the concept of a titration. Closer inspection reveals that the equilibration method is indeed a titration, but with a gas titrant. Similarly, the ion-chromatographic titrant is immobilized in the solid phase.

1.3 Definition of TA and aqueous carbon dioxide parameters

The four parameters total alkalinity (TA), total dissolved inorganic carbon (C_T), hydrogen ion concentration ($[H^+]$; pH), and partial pressure (or fugacity) of CO_2 (pCO_2), define the aqueous carbonate equilibria. As discussed in Section 1.3.1, these four terms are the primary marine buffer system and are related in such a way that measurement of

6

any two allows calculation of the other two. Before defining TA, it is useful to briefly review the terms C_T and [H^+]. The sum of all aqueous-phase inorganic carbon, C_T, is defined as

$$C_T = [CO_2(aq)] + [H_2CO_3] + [HCO_3^-] + [CO_3^{2-}] \qquad \textbf{1.1}$$

where $CO_2(aq)$ is solvated carbon dioxide[3], H_2CO_3 is carbonic acid (hydrated carbon dioxide), HCO_3^- is bicarbonate ion, CO_3^{2-} is carbonate ion, and brackets denote concentration in m = mol kg-soln^{-1}. The hydrogen ion concentration[4] of a solution is the number of moles of solvated protons, symbolized by H^+, per unit of volume or mass. Unless otherwise stated, [H^+] is taken as mols H^+ per kilogram of solution, m.

Conceptually, seawater TA can be thought of as the negative charge required to balance the small excess of positive charge found when the sum of charge from the major anions (Cl^-, SO_4^{2-}, Br^-) is subtracted from the sum of charge of the major cations (Na^+, Mg^{2+}, Ca^{2+}, K^+) (Broecker and Peng, 1982). This balancing negative charge is supplied by bicarbonate and carbonate ions. Total alkalinity is defined as follows (Dickson, 1981):

> *The total alkalinity of a natural water sample is thus defined as the number of moles of hydrogen ion equivalent to the excess of proton acceptors (bases formed from weak acids with a dissociation constant $K \leq 10^{-4.5}$, at 25^oC and zero ionic strength) over proton donors (acids with $K > 10^{-4.5}$) in one kilogram of sample.*

---

[3] The hydration kinetics of $CO_2(aq)$ are relatively fast (milliseconds), but not well known (Soli and Byrne, 2002), so a common simplification is to group the unionized terms in Equation 1.1 such that [$H_2CO_3^*$] = [$CO_2(aq)$] + [H_2CO_3]. The practical dissociation constant of $H_2CO_3^*$ is actually a combination of constants for the hydration reaction of carbon dioxide and the true dissociation of carbonic acid (Stumm and Morgan, 1996).

[4] In seawater (particularly at low pH) certain ions are found associated with H^+. This fact has given rise to alternative pH scales for seawater, which consider [H^+]$_T$ to be the sum of concentrations for H^+ and those species associated with H^+ (i.e. HSO_4^-, HF) (Dickson, 1993).

7

This formal definition allows unambiguous distinction of all chemical entities as proton donors, proton acceptors or neither. In the case that a species does not fall under the category of donor or acceptor, it is referred to as the "basis species" (Butler, 1998) and said to be in the "zero level" (Dickson, 1981) of protons. For seawater, we find that

$$
\begin{aligned}
TA = [HCO_3^-] + 2[CO_3^-] + [B(OH)_4^-] + [OH^-] + [HPO_4^{2-}] \\
+ 2[PO_4^{3-}] + [SiO(OH)_3^-] + [NH_3] + [HS^-] + [B]... \\
- [H^+] - [HSO_4^-] - [HF] - [H_3PO_4] - [HA]...
\end{aligned}
\qquad \textbf{1.2}
$$

where [HA]... and [B]... represent any minor or unidentified donor or acceptor species, respectively. Total alkalinity is therefore the difference between the sum of proton acceptors and the sum of proton donors. Total acidity, Acy, is simply the negative of total alkalinity. Species that can accept or furnish multiple protons to reach the zero level are multiplied by that number of protons. In general, minor acid-base species in seawater (e.g. boron, sulphate, fluoride) behave conservatively with salinity. Common exceptions include nutrients such as phosphate and ammonium as these components are upwelled from anoxic waters and delivered by rivers. There are also hints of unidentified protolytes in seawater at concentrations of 10-20 μm (Bradshaw and Brewer, 1988; Breland and Byrne, 1993). These unknowns are likely an ensemble of organic acids with pK_a sufficiently high that they remain protonated at low pH, greatly simplifying the alkalinity balance (i.e. this unknown concentration is grouped into a single term and assumed to not contribute protons via dissociation).

During the titration of of an alkaline sample with strong acid, an equivalence point is reached where TA = Acy = 0, this is known as a *proton condition*[5] (Dickson,

---

[5] Butler first introduced the 'proton condition' in 1964 (Butler, 1998).

8

1981). According to Butler (1998), a proton condition is also obtained by combining

mass and charge balances[6] to eliminate the large terms of the basis species and tracer ions

that have no role in the acid-base equilibria, leaving an equation where all proton donors

just equal all proton acceptors. Equation 1.2 can therefore also be derived independent of

the formal definition given above, by combining the mass and charge balances to get the

proton condition, then subtracting the donors from both sides of the equation, and setting

this value equal to the TA. Another approach that should be mentioned is the proton

balance equation (PBE) described by Pankow (1991). This expression is derived by

equating protons, hydroxide ions and their respective sources in such a way as to balance

all of the protons gained or lost by the basis species. Pankow's PBE is exactly equivalent

to Butler's proton condition[7]. Because this equation is a combination of mass and charge

balances, it is not linearly independent of them (Pankow, 1991) and contains no new

information (Butler, 1998). Below, a proton condition is derived using (1) Dickson's

1981 definition and (2) a combination of mass and charge balances as described by Butler

(1998). This example illustrates why Dickson's definition is the more rigorous approach

and demonstrates how an amiguity might arise if TA is defined solely from mass and

charge balances.

The triprotic phosphoric acid equilibria is a good example of these principles

because it contains both proton donors and acceptors

$$H_3PO_4 \xrightleftharpoons{K_{P1}} H_2PO_4^- + H^+ \quad (K_{P1} \sim 1 \times 10^{-2}) \qquad \textbf{1.3a}$$

$$H_2PO_4^- \xrightleftharpoons{K_{P2}} HPO_4^{2-} + H^+ \quad (K_{P2} \sim 1 \times 10^{-7}) \qquad \textbf{1.3b}$$

---
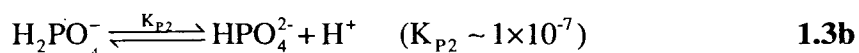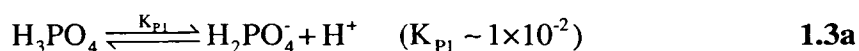
[6] The mass balance equation follows from conservation of mass. The charge balance or 'electroneutrality' equation follows from the condition that all solutions are electrically neutral.

[7] In my opinion, both authors rely too heavily on a conceptual derivation. It is more straightforward and less prone to mistake if the PBE or proton condition is always derived from mass and charge balances.

9

$$HPO_4^{2-} \xrightarrow{K_{P3}} PO_4^{3-} + H^+ \qquad (K_{P3} \sim 1 \times 10^{-2}) \qquad \textbf{1.3c}$$
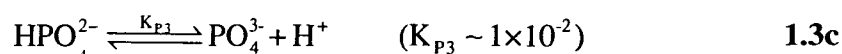
Using the definition of Dickson (1981) (see above), we classfiy each of the four species

as follows: H_3PO_4 is a proton donor because it is an acid with $K > 10^{-4.5}$. $H_2PO_4^-$ is in the

zero level of protons because it fits neither criteria for donor or acceptor. HPO_4^{2-} and

PO_4^{3-} are both proton acceptors because they are conjugate bases of weak acids with $K <$

$10^{-4.5}$. Because PO_4^{3-} requires two protons to reach the zero level ($H_2PO_4^-$), it is

multiplied by 2. Including the dissociation of water, the proton condition for the

phosphoric acid equilibria, based on Dickson's definition, is

$$[H_3PO_4] + [H^+] = [HPO_4^{2-}] + 2[PO_4^{3-}] + [OH^-] \qquad \textbf{1.4}$$

and the total alkalinty is

$$TA = [HPO_4^{2-}] + 2[PO_4^{3-}] + [OH^-] - [H_3PO_4] - [H^+]. \qquad \textbf{1.5}$$

Based on Dickson's definition, Equations 1.4 and 1.5 are equally valid for solutions of

phosphoric acid, the three phosphate salts (e.g. NaH_2PO_4, Na_2HPO_4, Na_3PO_4) or any

mixture of these four compounds. Now, consider two simple aqueous solutions of (a)

NaH_2PO_4 and (b) Na_2HPO_4. The respective mass balance equations for solutions a and b

are

$$[Na^+] = P_T = [H_3PO_4] + [H_2PO_4^-] + [HPO_4^{2-}] + [PO_4^{3-}] \qquad \textbf{1.6a}$$

$$[Na^+] = 2P_T = 2[H_3PO_4] + 2[H_2PO_4^-] + 2[HPO_4^{2-}] + 2[PO_4^{3-}] \qquad \textbf{1.6b}$$

where the letter of each equation also denotes the solution (a and b) and P_T is total

phosphate. The charge balance for both solutions is

$$[Na^+] + [H^+] = [H_2PO_4^-] + 2[HPO_4^{2-}] + 3[PO_4^{3-}] + [OH^-]. \qquad \textbf{1.7}$$

10

Combining Equations 1.6 and 1.7 to eliminate [Na^+] gives the (different) proton conditions

$$[H^+]+[H_3PO_4] = [HPO_4^{2-}]+2[PO_4^{3-}]+[OH^-] \qquad \textbf{1.8a}$$

$$[H^+]+2[H_3PO_4]+[H_2PO_4^-] = [PO_4^{3-}]+[OH^-] \qquad \textbf{1.8b}$$

Notice that the basis species is $H_2PO_4^-$ for Equation 1.8a and HPO_4^{2-} for Equation 1.8b. Different TA expressions are therefore derived for the two solutions, from Equations 1.8a and 1.8b. It is evident that in deriving the same proton condition from the mass and charge balances as would be found using Dickson's definition, one must select the correct zero level of protons. Potential ambuigities of this sort are altogether avoided using Dickson's approach of first selecting a threshold value for the dissociation constant, and letting this limit define the zero level of protons, rather than arbitrarily selecting the zero level of protons for each set of equilibria.

Carbonate alkalinity, A_C, is due only to bicarbonate, carbonate, hydrogen and hydroxide ions

$$A_C=[HCO_3^-]+2[CO_3^{2-}]. \qquad \textbf{1.9}$$

A_C is found by first measuring the TA by titration, then subtracting all the terms in Equation 1.2 except [HCO_3^-], $2[CO_3^{2-}]$. Species that contribute to the TA other than bicarbonate and carbonate are therefore a complication that must not be neglected. In general, the largest contributors to Equation 1.2, other than carbonate species (i.e. $B(OH)_4^-$, HF^-, HSO_4^-), are all easily calculated by their well-established conservative relationship with seawater salinity. Problems arise, however, when other acid-base species are introduced (e.g. river-derived phosphate in an estuary; dissolved organic

11

matter with proton acceptor-donor groups); and, in this case, the additional acid-base

species must be directly measured and accounted for in the TA equation.

1.3.1   Thermodynamic calculations

Around 1900, researchers were beginning to draw a connection between the

various aqueous carbonate parameters and by the 1940's chemical oceanographers had

Table 1.1 Summary of the variables and equations of the aqueous carbon dioxide system. A_c is calculated from TA by subtracting the minor acid-base species measured during a titration.

Equations	Variables
Henry's Law $K_H = [H_2CO_3^*]/pCO_2$ *Carbonic acid dissociation* $K_1 = [H^+][HCO_3^-]/[H_2CO_3^*]$ $K_2 = [H^+][CO_3^{2-}]/[HCO_3^-]$ *Total dissolved inorganic carbon* $C_T = [H_2CO_3^*] + [HCO_3^-] + [CO_3^{2-}]$ *TA (Carbonate Alkalinity)* $TA = A_C + ... = [HCO_3^-] + 2[CO_3^{2-}] + ...$	K_H K_1 K_2 pCO_2 $[H^+]$ $[H_2CO_3^*]$ $[HCO_3^-]$ $[CO_3^{2-}]$ C_T A_C

worked out the basic calculations tying them all together (Sverdrup, Johnson and

Fleming, 1942). As shown in Table 1.1, there are four measurable carbonate parameters:

A_c (as TA), C_T, $[H^+]$, and pCO_2. The combination of any two of the four parameters

allows calculation of the other two[8] through algebraic rearrangement of the five equations

---

[8] At first glance, this (now ubiquitous but over simplified) statement seems counterintuitive because the unique solution to at least one variable in a system of four linearly independent equations with four variables must be a combination of the other three variables. As seen in Table 1.1, the aqueous carbonate system actually has ten linearly independent variables and five equations (DOE, 1994). This means that each variable has a solution in terms of five others. Because three of the ten variables are well-defined constants, measurement of two of the remaining seven is sufficient to calculate the remaining five.

12

shown in the left column and the three constants given in the right column (Park, 1969). Because $H_2CO_3^*$, HCO_3^- and CO_3^{2-}, are not directly measurable, oceanographers speak of the four measurable variables, pCO_2, $[H^+]$, C_T and A_C, with the subsequent calculation of the other quantities implied.

1.4 Processes reflected in TA and the role of autonomous TA measurements

TA is an important parameter in several areas of oceanography. High precision, high accuracy TA measurements play a crucial role in our understanding of, for example, the marine $CaCO_3$ budget and saturation state, anthropogenic CO_2 penetration into the oceans, biological activity (photosynthesis and respiration), calcareous phytoplankton blooms, and coral reef dynamics. For those interested, descriptions of these topics are included in this section. Following this overview, the need for autonomous measurement of TA is addressed in greater detail.

The conservative[9] properties of TA hold true in many ocean locations, where no chemical or biological alterations occur. For this reason, it has been suggested that TA be parameterized with salinity and temperature, saving researchers the trouble of actually measuring it (Millero et al., 1998; Yao and Byrne, 1998). Although salinity-temperature-alkalinity relationships stay relatively constant in many sections of the ocean, a number of biological, chemical and physical processes are responsible for nonconservative behavior at other locations. Sources and sinks of TA include both physicochemical and biochemical processes. The most influential is the precipitation and dissolution of calcium carbonates and river inputs. Less important, but still significant, are the formation and remineralization of organic matter (in both the water column and sediments), ion exchange and redox equilibria on the surface of particles and in

---

[9] Controlled by mixing only

13

sediments, and hydrothermal inputs. Understanding these events and their environmental repercussions requires quantification of their accompanying chemical fluxes. I discuss a few of these processes below.

1.4.1 The calcium problem

First articulated by Brewer et al. (1975), the apparent excess of dissolved Ca over that expected from TA (i.e. $CaCO_3$ dissolution) was termed the "calcium problem". The frequently observed anomaly of $\Delta Ca/\Delta TA > 0.5$ (Brewer et al, 1975) or, rather, variations in the normalized calcium-normalized alkalinity regression slope (Shiller and Gieskes, 1980) results from an alkalinity sink, a calcium source, or a combination.

Brewer et al. (1975) held that the major cause was the release of protons during organic matter oxidation and they introduced the term potential alkalinity[10] (PA) as the TA of a homogenous water mass before neutralization. Changes in PA were first approximated by measuring/estimating changes in TA and the nutrients nitrate and phosphate from their preformed[11] values. Chen (1978) explained the changes in Ca as a function of changes in TA and nitrate. More recently, researchers have opted for an alternative correction to the proton flux, based on the apparent oxygen utilization[12] (AOU) rather than nitrate values (Anderson and Sarmiento, 1994). Other alkalinity

---

[10] Potential alkalinity is calculated from nutrient values by adding the amount of TA equivalents that were theoretically neutralized by redox reactions back to the measured TA, in order to subtract biologically induced changes in TA.
[11] last in contact with the atmosphere
[12] apparent oxygen utilization (AOU) is the deficiency in O_2, relative to atmospheric saturation, that occurs as a result of respiration once a water parcel loses contact with the atmosphere and leaves the euphotic zone.

14

neutralizing proton fluxes may result from reverse weathering[13] or high-temperature

basalt[14]-seawater interactions (Shiller and Gieskes, 1980).

Dismissed by Brewer et al. (1975) on lack of evidence, the possibility of a

secondary source of calcium (other than $CaCO_3$) was later embraced by Wolery and

Sleep (1976), Corliss (1979) and Shiller and Gieskes (1980). Based on the speculation of

Wolery and Sleep (1976) and Shiller and Gieskes (1980), deVilliers (1998) and deVilliers

and Nelson (1999) revisited the problem with better instrumentation and more available

data, concluding that low-temperature hydrothermal flux is a major source of marine

Ca^{2+}. Although the calcium-TA discrepancy now appears to be balanced, questions of,

perhaps, even greater significance were spawned from these early studies of the calcium

problem (see below).

1.4.2 The marine $CaCO_3$ budget and saturation state

The calcium carbonate budget refers to the balance between dissolved $CaCO_3$

injected into the ocean by rivers and solid $CaCO_3$ removed by sedimentation.

Understanding carbonate sinks and sources is important because the marine $CaCO_3$ cycle

is intimately connected with ocean-atmosphere CO_2 fluxes and, hence, climate.

Calculating the budget involves estimating several poorly constrained fluxes, such as

continentally derived carbonate (from weathering), in situ dissolution, planktonic calcite

production (from estimates of primary productivity), and vertical export to the deep

ocean (from sediment traps or mass accumulation rates) (Milliman, 1993). All of these

processes involve an alkalinity flux. Although researchers generally agree that there

---

[13] Carbonate weathering refers to the removal of atmospheric CO_2 by the reaction $CaCO_3(s)+CO_2(g)+H_2O$ $= Ca^{2+}+2HCO_3^-$. Reverse weathering (i.e. calcification) removes alkalinity and restores CO_2 to the atmosphere.
[14] Lava rock

15

exists a considerable alkalinity flux in the upper water column, the source of this flux is still debated. Milliman et al. (1999) attribute it mostly to biologically induced dissolution of calcium carbonate, while Chen (2002) argues that the primary source is a proton sink located in the continental margins. The answer to this problem will surely require a great deal of high quality TA, C_T, Ca and organic carbon measurements.

The saturation state of calcium carbonate plays a central role in studies of the $CaCO_3$ budget. From the surface to mid-depths the ocean is supersaturated with respect to $CaCO_3$. There is, however, considerable independent evidence (based on TA measurements) that $CaCO_3$ dissolution occurs above the lysocline[15] (Milliman et al., 1999; Sabine et al., 2002a; Chung et al., 2003). A flux of CO_2 from the atmosphere into the ocean changes the saturation state. Concurrently, lysocline shoaling (presumably due to oceanic uptake of anthropogenic CO_2) has been directly recorded in the Pacific and Indian Oceans (Sarma et al., 2002) as well as the Atlantic Ocean (Chung et al., 2004). Two major implications of a marine alkalinity flux and/or changing saturation state include controls on short-term buffering of anthropogenic CO_2 (i.e. the Revelle Factor[16], Broecker and Peng, (1982)) and biogenic calcification response (Feely et al., 2004).

1.4.3 Anthropogenic CO_2 penetration into the oceans

In the two decades since Brewer (1978) and Chen and Millero (1979) first proposed methods for estimating the anthropogenic CO_2 (C_T^{ant}) signal in the oceans, a new branch of chemical oceanography has emerged regarding the subject. The first large-scale inventories used GEOSECS data (Chen et al., 1982; Gruber et al., 1996) but

---

[15] The depth where conditions shift from supersaturated to undersaturated. Depending on the ocean basin, the calcite lysocline is ~2000 m deeper than the aragonite (metastable $CaCO_3$, formed by pteropods) lysocline.
[16] aka the buffer factor, is a measure of the time required to achieve air-sea pCO_2 equilibrium. It is inversely correlated with carbonate ion concentration.

16

the reliability of these estimates was questionable due to the quality of the measurements (Wanninkhof et al., 1999). Recently collected data, from the WOCE, OACES, and JGOFS studies are extremely reliable, due to refinements in C_T and TA measurement and the implementation of Certified Reference Materials (CRM). Studies that utilize these later projects are at the cutting edge of modern oceanography and at the center of the recent climate debate. GLODAP scientists recently completed the C_T^{ant} inventories for each major ocean basin (see e.g. *Pacific Ocean*: Feely et al., 2002; Sabine et al., 2002b; Sarma et al., 2002. *Atlantic Ocean*: Lee et al., 2003; Chung et al., 2004. *Indian Ocean*: Sabine et al., 2002a).

In general, the anthropogenic CO_2 signal for a water mass is calculated by measuring C_T, then subtracting the preindustrial[17] CO_2 and all of the changes that occurred in situ that perturb the C_T. In situ changes that must be accounted for are due to biological activity (organic growth or remineralization) and $CaCO_3$ dissolution. If the calculation is performed correctly, the remaining value is C_T^{ant}. The original experimental/computational approach involves measurement of C_T, TA, and AOU and estimation of the preformed TA and C_T. The difference in preformed C_T values between water masses of different ages is assumed to be the anthropogenic signal. Some of the major modifications to the original technique include (1) using a water mass age tracer (e.g. CFCs) to calculate preformed C_T while accounting for the air-sea pCO_2 disequilibrium (Gruber et al., 1996) rather than a conservative mass tracer (salinity) with the assumption of constant air-sea pCO_2 equilibrium (Chen and Millero, 1979); (2) improved approaches to biological correction such as updated elemental ratios for organic matter (Anderson and Sarmiento, 1994) and the inclusion of denitrification

---

[17] The CO_2 in the water mass previous to 1850.

17

reactions (Sabine et al., 1999); (3) more sophisticated mixing models (Sabine et al.,

2002b); and, (4) updated parameterizations of potential alkalinity (Gruber et al., 1996;

Sabine et al., 2002b).

Reports of direct observations on C_T^{ant} are rare because the C_T^{ant} signal is very

small compared to the background C_T pool and its increase (~1.2 μm yr^{-1}) is confounded

by natural seasonal variability (20-40 μm yr^{-1}). The only direct observations come from

the two long standing oceanographic stations HOT (Hawaii Ocean Time-Series) and

BATS (Bermuda Atlantic Time-Series) with 10+ year records of monthly C_T (Karl et al.,

2001). Perhaps, one day, a continuous record of the marine CO_2 rise will become as

highly publicized as the now famous Keeling Curve for atmospheric CO_2. In the interim

TA will play a crucial role in all estimations of C_T^{ant}.

1.4.4 TA and nutrients

Redfield et al. (1963) reported the atomic ratios of carbon, nitrogen and

phosphorous (C:N:P) in plankton as 106:16:1. This nutrient ratio is an approximation to

the ratio of *change*[18] that accompanies photosynthesis by phytoplankton and,

consequently, grazing by zooplankton and aerobic respiration of organic material by

bacteria. In the surface ocean, depending on the type of autotroph, TA may increase or

decrease with photosynthesis[19] (Stumm and Morgan, 1996). Below the euphotic zone,

TA decreases due to the release of protons during oxidative bacterial decomposition of

organic matter (respiration). Using the model of Redfield et al. (1963), respiration of

organic carbon releases 106 equivalents of C and consumes 17 equivalents of TA (16

from HNO_3^- and 1 from H_3PO_4) (Chen, 1978). As described above, these stoichiometric

---

[18] It is not the absolute elemental ratio found in the ocean.
[19] NH_4^+ assimilation releases protons, decreasing TA; NO_3^- assimilation consumes protons, increasing TA.

18

calculations were used in the initial investigations of the calcium problem (Brewer et al., 1975; Chen, 1978) and calculations of anthropogenic CO_2 (Brewer, 1978; Chen and Millero, 1979). Redfield et al. did not establish a unifying theory, but their stoichiometric ratio underscores some fundamental physiological laws of marine life (Hood, 2001).

JGOFS ushered in the first major rift between the classical viewpoint of a relatively constant nutrient ratio throughout the ocean and a dynamically changing element cycle (Anderson and Sarmiento, 1994). It is now commonly accepted that the ratios are location dependent as a result of differing ecosystems (e.g. HOT vs. BATS, Karl et al., 2001). The implications of nutrient ratio variability are substantial. For example, C_T^{ant} is calculated by correcting TA measurements using nutrient data (see above). Furthermore, it is now thought that atmospheric N_2 fixation by marine organisms (diazotrophs), a process which contributes to variations in nutrient ratios, lies at the center of a negative feedback mechanism working against runaway cooling and warming, in effect, maintaining our current climate stability (Michaels et al., 2001).

1.4.5 Calcareous phytoplankton blooms

During photosynthesis, certain types of phytoplankton such as coccolithophorids, foraminifera, and pteropods form $CaCO_3$ shells. These organisms alter TA through removal of CO_3^{2-} by precipitation with Ca^{2+} and the redox-based proton flux associated with nutrient uptake (Section 1.4.4). Photosynthesis and respiration directly influence pCO_2 and C_T, but alter TA only slightly, though nutrient cycling. Calcification (see equation in footnote 13), on the other hand, changes TA at twice the rate of C_T. Interestingly, biologically induced calcification events hold the potential to block CO_2 flux from the atmosphere into the ocean, while simultaneously exporting carbon to the

19

ocean's interior. These counterbalancing effects of coccolithophore blooms are not easily quantified and remain an uncertain aspect of the global carbon cycle. A coccolithophore bloom provides a net carbon sink because some of the $CaCO_3$ formed in the surface ocean is exported and a small fraction is eventually buried in sediment. On a seasonal scale, however, the CO_2 increase that accompanies calcification events has the net effect of increasing pCO_2, thus blocking a portion of the atmospheric CO_2 sink or, perhaps acting as a source.

Early coccolithophore studies utilized remote sensing (i.e. satellite-derived reflectance) for quantitative calculations relating backscattered light to coccolith abundance along with ship-based measurements of simple parameters such as cell count, chlorophyll concentration and light attenuation (Holligan et al., 1983). These studies provided new information on mesoscale[20] albedo effects (Balch et al., 1991), but lacked quantitative information regarding the CO_2 system because calculating C_T and TA drawdown or pCO_2 rise from simple surface measurements of beam attenuation or remotely sensed backscattering is probably unreliable (Holligan et al., 1993). Calcification events are difficult to study because blooms are short-lived. Robertson et al. (1994) and Bates et al. (1996) both reported a similar seasonal reduction in CO_2 uptake (~20%) with potential for CO_2 source behavior during bloom conditions. Murata and Takizawa (2002) directly recorded super-saturated pCO_2 levels (~400 μatm), confirming that such blooms are capable of acting as a source, not just a reduced sink. Robertson et al. (1994) and Bates et al. (1996) attributed the higher pCO_2 levels during the blooms to calcification; noting that the potential alkalinity-C_T relationship indicated some level of calcification and that the pCO_2 rise could not be accounted for by physical

---

[20] Larger than storm-scale, smaller than synoptic-scale; ranging from ~100-500 km across.

forcing or net community respiration. On the contrary, Murata and Takizawa (2002)

concluded that the source suggested by Robertson et al. and Bates et al. was not

responsible for the elevated pCO$_2$ Murata and Takizawa recorded in a coccolithophore

bloom, stating that "None of the previously proposed mechanisms adequately explained

the elevated pCO$_2$ in the eastern Bering Sea shelf". The unraveling of this ambiguity will

likely require a better temporally resolved data set of carbonate parameters (especially

TA) and nutrients in conjunction with the classically measured biological and optical

properties on active coccolithophore blooms.

1.4.6   Coral reef dynamics

TA is an essential parameter in coral reef studies because it helps distinguish the

dominating biogeochemical processes. Whether or not a particular reef behaves as a CO$_2$

sink or source depends on several processes, including photosynthesis, respiration,

calcification, dissolution, pCO$_2$ of the reef and surrounding waters, and physical forcings

that control mixing of reef water with surrounding water (Bates et al., 2001; Suzuki and

Kawahata, 2003).   Photosynthetic pCO$_2$ drawdown is simultaneously met by pCO$_2$

replenishment via calcification and respiration. TA, removed by calcification, is restored

by CaCO$_3$ dissolution. Surrounding waters with a different composition of CO$_2$

parameters impinge on reef waters on short time scales (Bates, 2002). Coexisting

effects[21] obscure the processes at work (Suzuki et al., 1995)

Several studies have focused on decoupling the effects of

photosynthesis/respiration and calcification/dissolution to better understand a particular

reef's potential as a source or sink to atmospheric CO$_2$. The first studies calculated the

---

[21] photosynthesis enhances calcification via CO$_3^{2-}$ saturation; calcification benefits photosynthesis by raising pCO$_2$; respiration induces CaCO$_3$ dissolution by lowering pH.

ratio of released CO_2 to precipitated $CaCO_3$ (see e.g. Frankignoulle et al., 1994). Based on model predictions (Suzuki et al., 1995), the ratio of organic carbon to inorganic carbon production is a direct indicator of sink/source behavior, but this value proves difficult to evaluate in practice (Suzuki, 1998). Most recently, researchers have adopted the Deffeyes diagram (Deffeyes, 1965); a graphical approach where TA and C_T are normalized to a constant salinity and plotted against each other (Bates et al., 2001; Suzuki and Kawahata, 2003). Each biogeochemical process leaves a unique imprint on TA and C_T, allowing graphical identification of processes contributing to a measured set of TA and C_T values.

In addition to the interest in sink/source behavior, there is also a scramble to understand the apparent widespread degradation of modern day reef ecosystems (Aronson et al., 2003; Hallock, 2005). Among other things[22], reefs are highly dependent on coral's ability to form $CaCO_3$ and the anthropogenically induced changes in aragonite saturation (see e.g. Chung et al., 2004) are expected to threaten corals worldwide within the next 50 years (Kleypas et al., 1999; Langdon et al., 2000).

1.4.7   Air-Sea CO_2 fluxes

The most studied short-term process related to the CO_2 cycle is the ocean-atmosphere flux of CO_2. Exchange of CO_2 into or out of a water mass, however, does not change the TA[23]. Because the atmosphere is almost[24] constant in pCO_2, the main driving force of daily, seasonal, and yearly fluxes originates in the ocean. Processes controlling ocean pCO_2 on these time scales affect TA in generally well-understood patterns.

---

[22] Reefs are very sensitive to sea surface temperature, sea level and dominant biota.

[23] This is a result of defining TA (section 1.3) with H_2CO_3 as a basis species. Also, indirect TA changes are possible via $CaCO_3$ dissolution triggered by CO_2 exchange.

[24] Atmospheric CO_2 is rising at ~1.4 μatm yr^{-1} (from anthropogenic inputs) and cycles by ~5 μatm yr^{-1} (due to the seasonal global photosynthetic rate).

22

Difficulties arise, however, in diverse marine ecosystems (e.g. coral reefs, upwelling areas) where these processes occur contemporaneously. Air-sea flux of CO_2 is usually calculated by direct measurement of ΔpCO_2 (surface ocean pCO_2 – atmospheric pCO_2 at the surface) (Takahashi, 2002). As described above, pCO_2 can also be calculated from measurements of other carbonate parameters. This provides an independent constraint of CO_2 flux, without measuring pCO_2. Because C_T and TA were the most commonly measured parameters in past studies (i.e. OACES, JGOFS), ΔpCO_2 calculated from these parameters potentially offers better coverage than past flux estimates based on pCO_2 measurements. The first global scale estimates were calculated from the GLODAP data set and compared to pCO_2-based fluxes (Gloor et al., 2003).

1.4.8 The role of TMT TA measurement: autonomous operation

In the context of the issues described above, the need for autonomous instrumentation becomes clear. Projects designed to study these issues require hundreds to thousands of TA measurements, run continuously throughout a cruise. Despite the immense number of measurements carried out thus far[25], the need for better spatial and temporal resolution is evident. For example, cruises through coccolithophore blooms and around coral reefs have provided snapshots of the effects of calcification on surface water carbonate parameters (i.e. CO_2 flux behavior), but diurnal calcification rates are poorly constrained because few researchers have attempted to conduct 24 hour studies in a single location. Another example is the disagreement between seasonal to yearly pelagic alkalinity fluxes (i.e. carbonate productivity) and benthic carbonate sequestration.

---

[25] Between 1991 and 1998 the Joint Global Ocean Flux Study (JGOFS), World Ocean Circulation Experiment (WOCE) and Ocean Atmosphere Exchange Study (OACES) sampled CO_2 parameters at more than 12,000 depth resolved hydrographic stations, resulting in over 350,000 discrete measurements (CDIAC, 2005).

23

Indeed, the natural variability of each of the processes described above is rarely considered on time scales shorter than yearly because continuous (e.g. hourly for weeks to months) biogeochemical measurements are extremely difficult to achieve. The validity of carbon flux estimates that fail to consider short-term variability is therefore questionable.

At sea, TA methods are limited to volumetric-based measurements, and these have been optimized to an acceptable level of performance (Millero et al., 1993). Almost all TA measurements today are carried out in auto-assist mode, requiring constant attendance by an operator to reload each sample. Considering the price required to fund operators for these measurements, a fully automated instrument is not hard to justify. But, the cost of simply parking a ship in a single spot for the amount of time required to document seasonal or subseasonal dynamics of the carbonate system greatly outweighs the cost saved by automating a titration system (Karl et al., 2001). The primary motivation behind this research is therefore the development of a method that could eventually be adapted to an in situ TA analyzer for extended mooring and buoy deployments.

1.5 TA techniques

The following section briefly describes the well-established TA techniques that laid the foundation for TMT. Reviewing the principles of these techniques provides a good introduction to the problem of total alkalinity and is important for understanding the historical context of contemporary methods. These TA methods might first be divided into spectrophotometric and potentiometric. Other distinctions may include gravimetric

24
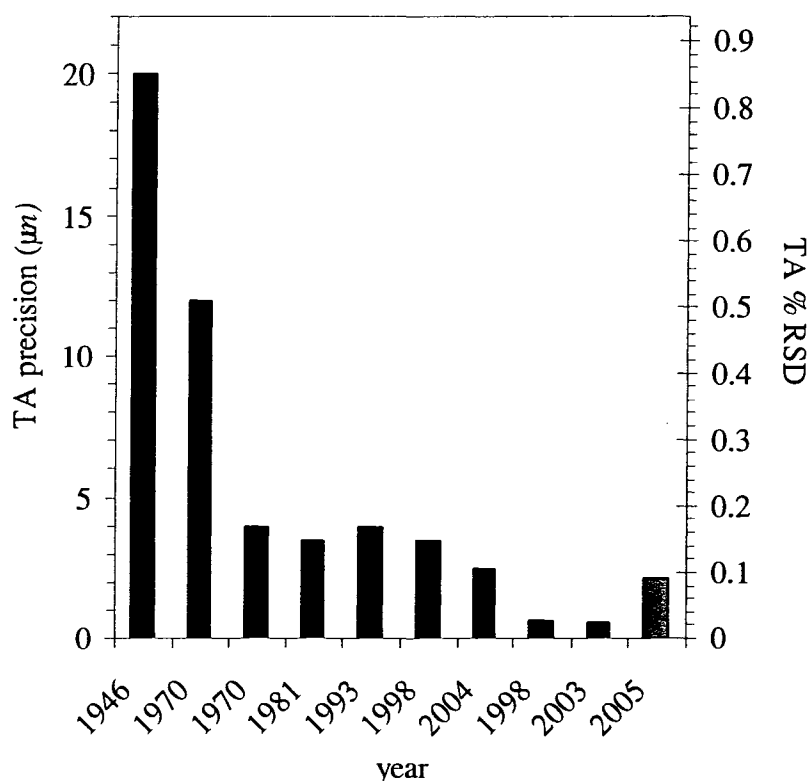
Figure 1.1 Timeline of improvements in seawater TA precision. This study is shown in grey. See Table 1.2 for the corresponding references.

Table 1.2 Summary of the major advances in precision reported by other researchers for seawater-type TA measurements. The TA in every study reported here was between 2300-2400 μm.

Method	sample	1 s.d. (m)	% RSD	reference	year
Pot. (e.a.)	SW	>20	>1	123, 2	1931, 1946
Pot. (e.a.)	SW	4	0.17	33	1970
Pot. (G)	SW	4	0.17	47, 48	1967, 1970
Pot. (MG) at sea	SW	2-5	0.1-0.2	60, 15	1973, 1981
Pot. (NLLS) at sea	SW, CRM	2-6	0.1-0.3	39, 95	1981, 1993
Spec. (e.a.) at sea	SW, CRM	2-5	0.1-0.2	106	1998
Pot. (e.a.)	std, CRM	2-3	0.1-0.2	126	2004
Spec. (e.a.)	CRM	0.4-0.9	~0.03	130	1998
Pot. (NLLS)	SW,CRM	0.4-0.8	~0.03	45	2003
TMT (NLLS)	Std, CRM	2.1	0.1	This study	2005

Pot potentiometric titration with a pH electrode
Spec spectrophotometric titration with acid-base indicator
e.a. excess acid technique
G Gran calculation
MG modified Gran calculation
NLLS non-linear least squares
SW seawater
CRM certified reference material
std independently prepared standard
TMT Spectrophotometric tracer monitored titration (this study)

25

vs. volumetric, single point vs. multipoint and closed cell vs. open cell. As shown in Figure 1.1 and Table 1.2, seawater TA precision has improved considerably over the last 60 years. All of these methods are different forms of the titration of a weak base with a strong acid.

TMT is a spectrophotometric multipoint titration. This approach is rarely used because most multipoint methods require data over a pH range of >1 pH unit and indicators are most reliable over a very narrow pH range (<0.5 pH units). As shown in Chapter 4, in TMT this trade-off is met by limiting the spectrophotometric pH to a very narrow range, as usual, but still collecting a sufficient number of data points within that range, using a reduced titrant increment.

1.5.1 Excess acid

This method involves making a single quantitative addition of HCl to an alkaline sample (of known mass or volume) sufficient to lower the pH past the equivalence point of the titration, followed by a single pH measurement to compute the excess acid. As seen in Table 1.2, the excess acid technique has evolved alongside TA from the onset of TA measurements. It was first proposed by Thompson and Bonnar (1931), who used a crude colorimetric endpoint determination, and later adapted for the electrode by Anderson and Robinson (1946). Culberson et al., (1970) developed a high precision, potentiometric version which involved driving off CO_2 from the acidified sample. The importance of purging CO_2 is now considered a vital step in the excess acid method because H_2CO_3 dissociation affects the endpoint pH measurement. Breland and Byrne (1993) and Yao and Byrne (1998) adapted the method for high precision spectrophotometric pH measurements. Using this spectrophotometric technique, Yao and

26

Byrne (1998) obtained the best precision (±0.3 μm) reported in the literature for seawater TA measurement.

1.5.2 Multipoint titrations: Gran and Modified Gran titrations

The principles of a multipoint TA titration have changed little over the past forty years. The instrumentation has, of course, become more sophisticated (e.g. better electrodes, motorized burets), but the titration procedure remains the same. The major developments are in our approach to analyzing the data obtained during a titration. A brief discussion of Gran titrations will therefore serve to introduce multipoint TA titrations and help us to understand how the equivalence point is calculated in simpler terms before jumping into the (more complicated) description of solving the equivalence point by curve fitting.

Dyrssen and Sillén (1967) first applied Gran's method (Gran, 1952) to seawater alkalinity titrations. The technique was refined by Edmond (1970). Soon after Edmond's 1970 paper, Hansson and Jagner (1973) pointed out that Gran plots for seawater TA titrations are subject to systematic errors due to the competing acid-base equilibria in seawater and proposed an iterative 'modified' Gran calculation (explained below).

TA Gran titrations record a pH electrode's response to sequential volumetric or gravimetric additions of strong acid to a seawater sample. Classically, data are collected between the bicarbonate-carbonic acid equivalence point (ep) and after the carbonic acid equivalence point (the dashed line in Figure 1.2). Additions after the carbonic acid ep are extrapolated to find the titrant volume corresponding to TA. If desired, the TA ep can then be used to calculate the carbonate-bicarbonate ep and thus, C_T. Due to the development of improved methods for C_T measurement, titrations are now rarely used for

27
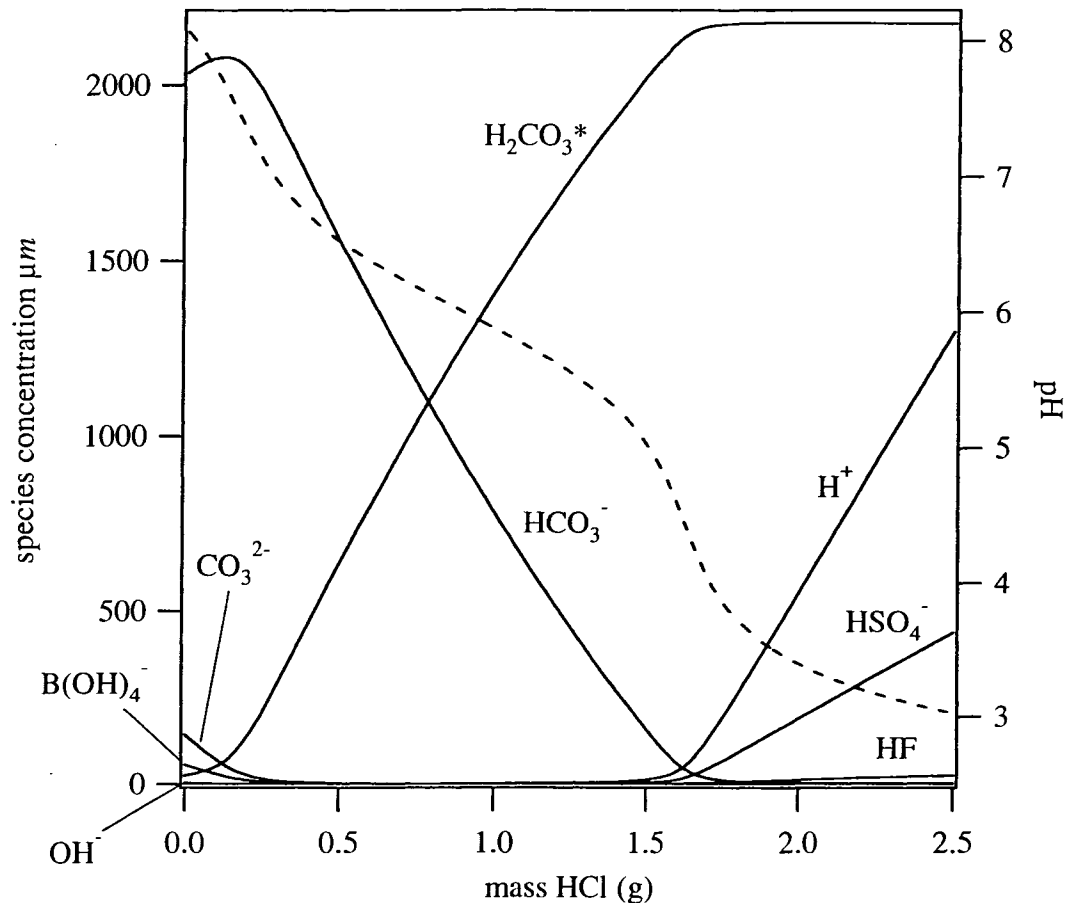
Figure 1.2 Concentration of the major alkalinity components of seawater during a titration (left axis, lines) and pH (right axis, dashed line). H_2CO_3* is not a component of the alkalinity, but it is shown for clarity. Before addition of titrant, CO_3^{2-}, $B(OH)_4^-$, and OH^- contribute ~ 140, 50 and 5 μm, respectively, to the TA. See Table 1.3 for initial concentrations.

C_T determination. Therefore, contemporary Gran or Modified Gran titrations involve measurements exclusively after the carbonic acid ep (dashed line in Figure 1.2, M > 1.75, pH < 4.5), and the following discussion is limited to this. The Gran function is derived by first writing the analytical excess of hydrogen ion

$$(M_o + M_a)[H] = Acy \times M_a - TA \times M_o = (M_a - M_{ep})Acy \qquad \textbf{1.10}$$

where M_o and M_a are mass of sample and titrant, respectively, Acy (acidity) is titrant concentration, and M_{ep} is the mass of acid required to reach the equivalence point. After

28

the equivalence point, [H] ~ [H$^+$], so a graph of (M$_o$+M$_a$)[H$^+$] vs. M$_a$ should be linear

with a slope of Acy, and an x-intercept of M$_a$ = M$_{ep}$.

Using the concentrations shown in Table 1.3 and equilibrium constants of DOE

(1994) in a seawater equilibrium model, the speciation of a seawater titration is calculated

(Figure 1.2). These data are used to test different methods of TA calculation for

Table 1.3 Concentrations used to generate theoretical
titration data (Figure 1.2) for testing different types of
TA calculations. See Terminology for parameter
definitions

Parameter	Conc.(m)
TA	2450×10^{-6}
C$_T$	2200×10^{-6}
B$_T$	420×10^{-6}
S$_T$	28240×10^{-6}
F$_T$	70×10^{-6}
Acy	0.3

correctness (Gran, modified Gran and NLLS, below). The TA input used to model

Figure 1.2 was 2450 μm (Table 1.3). Figure 1.3 shows the Gran plot for Figure 1.2.

Figure 1.3 gives a titrant volume corresponding to 1.626 g HCl and TA = 2440 μm (0.4%

error) for the range pH < 4.0. The distortions in the 'linear' region of the Gran plot are

not visually apparent, but they can be estimated by using the titration model to vary a

constituent and observe the resulting change in calculated TA. Because each species

effect is pH dependent, the distorting effect is also conditional on the section of the Gran

plot used. For example, using data in the region 3.05 < pH < 3.30 gives an answer very

close to the correct TA, but only because the offsetting effects of C$_T$, F$_T$ and S$_T$

approximately cancel each other for a linear extrapolation of this section of the Gran plot.

29
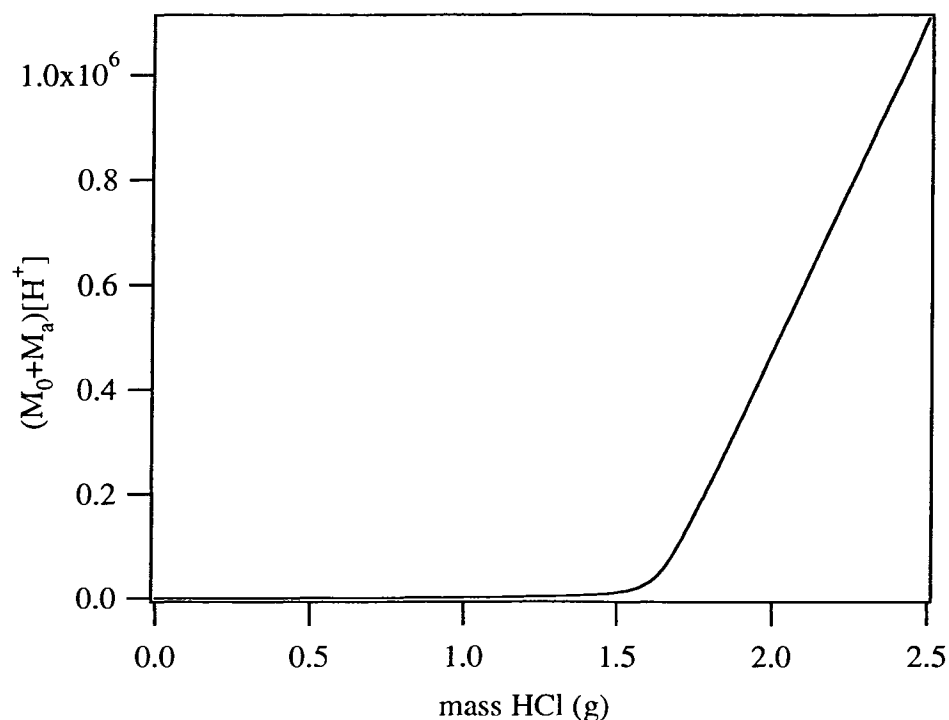
Figure 1.3 Gran plot for the data shown in Figure 1.2.

The modification proposed by Hansson and Jagner[26] (1973) involves (1)

calculating an average E_0 of the electrode using the titration data and the first ep solved

by a regular Gran plot (2) using the new E_0 to re-calculate [H^+] (3) calculating the

speciation using equilibrium constants and total concentrations and replacing [H^+] in the

Gran function with the alkalinity balance [H^+]$_{free}$ + [HSO_4^-] + [HF] - [HCO_3^-] - 2[CO_3^{2-}]

- [$B(OH)_4^-$] - [OH^-]. This first iteration for the previously calculated Gran plot (TA =

2440 μm, pH < 4.0) gives TA = 2442 μm. Second and third iterations give 2449.6 and

2450.0 μm, respectively. Due to this high level of accuracy, modified Gran calculations

gained widespread acceptance by oceanographers during GEOSECS (Bradshaw et al.,

1981) and remain in use today.

---

[26] According to Bradshaw et al., (1981), Arnold Bainbridge (GEOSECS director) actually developed the modified Gran calculations a couple of years before Hansson and Jagner published their 1973 paper.

30

Gran plots were used for their simplicity in the early stages of TMT development. With a spectrophotometric multipoint titration, however, it is very difficult to get a sufficient number of linear titration points due to limits in the indicator's pH range. As described in the next section, curve fitting by a non-linear least squares minimization technique (NLLS) proved to be more robust for pinpointing errors in the titration. We therefore developed an NLLS approach, based on DOE (1994). Gran plots are revisited in Section 3.6 for their application to the titration of a weak acid-strong acid mixture (a/i titrant) by strong base.

1.5.3   Non Linear Least Squares (NLLS)

Solving for TA from a set of titration data by minimizing the sum of a set of squared residuals was first proposed by Dickson (1981). Data are collected as described above for Gran plots. In essence, the NLLS approach performs a calculation related to the modified Gran plot: titrations are compared to a chemical model, and experimental parameters are adjusted to achieve the best agreement between all of the data (or a region that the data are restricted to). A 'residual' is calculated for each titration point using the model and the same adjustable experimental parameters. For example, solving a set of titration data for TA, where all of the parameters are known except TA, involves rearranging Equation 1.2 to equal zero (i.e. the residual), calculating this equation for each titration point using the titrant masses, pH, and a single value for TA, and then adjusting TA until the set of residuals is closest to zero.

There are several advantages to using NLLS to solve for TA. In theory, one is not restricted to a single region of the data (as in the Gran plot), because fewer simplifications are made in the chemical model. The plot of residual values allows visual

31

confirmation that the chemical model is correct and instrumentation is functioning

properly. The residual is calculated by subtracting one side of the analytical

concentration of hydrogen ions

$$\frac{Acy \times M_a - TA \times M_o}{M_a + M_o} = [H^+] + [HSO_4^-] + [HF] -$$
$$[HCO_3^-] - [CO_3^{2-}] - [H(BO)_4^-] - [OH^-] \qquad \textbf{1.11}$$

to give an equation theoretically equal to zero.

$$residual = \frac{Acy \times M_a - TA \times M_o}{M_a + M_o} - [H^+] - [HSO_4^-] - [HF] +$$
$$[HCO_3^-] + 2[CO_3^{2-}] + [H(BO)_4^-] + [OH^-] \approx 0 \qquad \textbf{1.12}$$

Residuals are squared, and the sum of the squares is then minimized using a computer

algorithm such as Gauss-Newton, Levenberg-Marqurdt, or Generalized Reduced

Gradient (e.g. Excel Solver). Applying this method to the same data as shown in Figure

1.2 produces the same answer as the third iteration of the modified Gran plot (2450.0

μm). An added advantage is that the graphical error is visually apparent in a residual plot

(Figure 1.4), but not in a Gran plot (Figure 1.3). As an example of this advantage,

residual trends are shown in Figure 1.4 for some commonly encountered errors in the

titration data shown in Figure 1.2. A similar analysis is presented for the

spectrophotometric TMT method (Section 2.3.1).

32
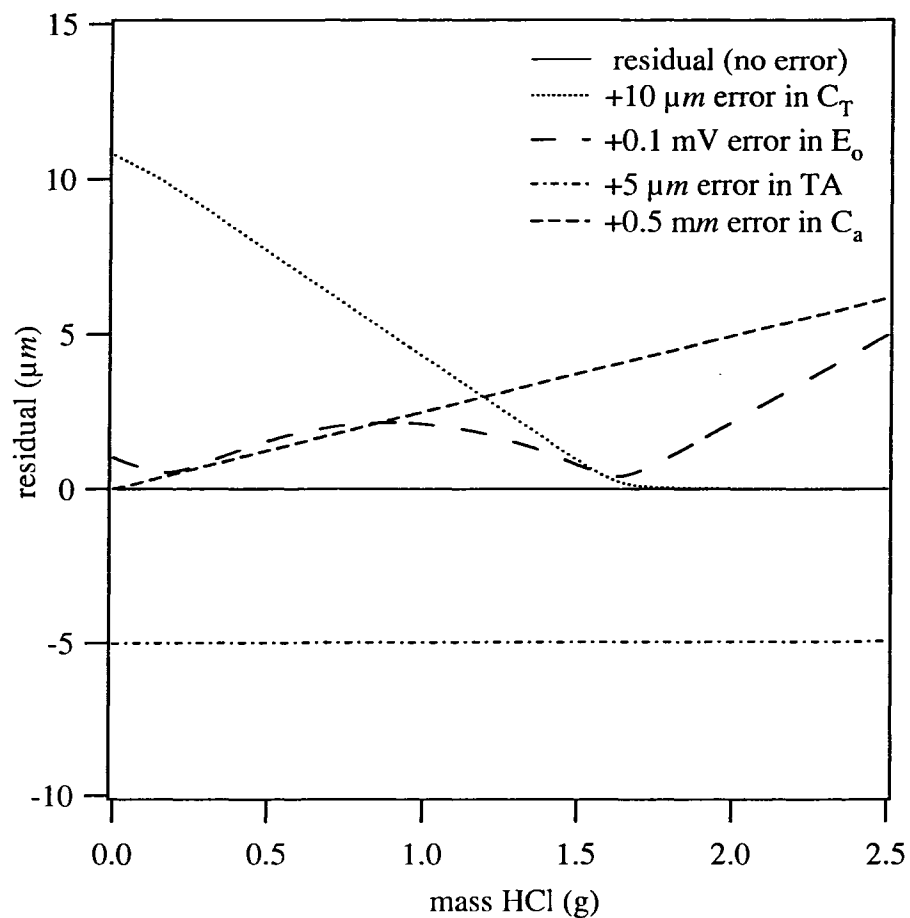
Figure 1.4 Residuals calculated for the titration shown in Figure 1.2. Trends are shown for some common experimental errors. This approach helps identify potential problems in a titration system, whereas the Gran plot does not.

33

Chapter 2   TMT Theory

This chapter continues the discussion of TA from Chapter 1, focusing on the equations developed for the TMT version of TA measurement. A discussion of the potential sources of error is presented here to reflect the order of method development: ideas & theories → theoretical simulations & analysis → laboratory experiment → data analysis.

2.1   Philosophy

TMT is set apart from other types of titrimetry when perceived in terms of its extensive[27] and intensive[28] macroscopic thermodynamic properties. All titrations require measurement of an intensive property (e.g. optical absorbance, chemical potential, ion activity) to signify an equivalence point. To our knowledge, every titration method reported in the literature to date relies on measurement of at least one extensive property (e.g. volume, mass, time) as well. For example, although flow injection analysis titrations avoid volumetric and gravimetric measurements, they are highly dependent upon time (peak width). In contrast, TMT requires measurements of optical absorbance and temperature only. Freedom from physical metering (i.e. extensive property measurements) places TMT apart from classical titrimetry as a fundamentally original titration methodology.

A spectrophotometric titration is typically carried out by adding a small, non-quantitative amount of indicator to the titration solution and monitoring optical absorbance at a single wavelength. The maximum slope or inflection of the absorbance vs. volume of titrant curve gives the endpoint. More sophisticated spectrophotometric

---

[27] Description of a system as the sum of its parts.
[28] Independent of amount of material present; the ratio of two extensive properties.

34

methods use quantitative addition of indicator to the titration solution, accurate absorbance measurements at two or more wavelengths and subsequent calculation of solution pH with correction for perturbations by the acid-base indicator (see e.g. Breland and Byrne, 1993). The equivalence point is found from the volume (or mass) of titrant added and the pH of the titration mixture, as determined by the indicator. To our knowledge, TMT is the first acid-base method that also uses the indicator as a tracer for the total titrant added.

In this study, an automated TMT system uses a standardized mixture of HCl and bromocresol green (BCG) to analyze alkaline samples. We used simple solenoid pumps (with volume reproducible to only 10%) to flush sample and make additions of titrant, while simultaneously determining total indicator concentration and pH from measurements of the absorbance in a stirred optical cell. We analyzed Na_2CO_3 solutions in 0.7 m NaCl in order to test the TMT method for seawater TA applications. In addition, we titrated solutions of NaOH in 0.7 m NaCl and a seawater certified reference material (CRM), a standard widely used to verify the accuracy of seawater alkalinity systems (Dickson, 2001).

2.2 Calculation of the titrimetric equivalence point

In TMT, we determine TA using a mixture of strong acid (HCl) and weak acid (bromocresol green). Throughout this document, the subscript a/i denotes the HCl-indicator mixture and m is concentration in mols per kilogram solution (m = mol kg-soln^{-1}). As explained in Section 1.3, TA is an analytically accessible parameter describing the excess of proton acceptors over proton donors, with donor and acceptor defined by selecting a threshold value for the equilibrium constant of each acid-base pair in the

35

sample. In TMT, the titrant contains another acid-base species (the indicator) in addition to HCl and indicator species must therefore also enter the proton balance. During a titration, the excess of proton acceptors is represented by

$$\frac{Acy \cdot M_{a/i} - TA \cdot M_s}{M_{a/i} + M_s} = \sum_{i=1}^{n} [HA_i] - \sum_{j=1}^{m} [B_j] \qquad 2.1$$

where Acy is the acidity of the a/i titrant due to both HCl and indicator, $M_{a/i}$ is mass of titrant added, M_s is sample mass, and TA is total alkalinity of the sample. The right hand side of Equation 2.1 represents the difference proton donors (HA) and acceptors (B) in a titration mixture containing n donors and m acceptors. We classified proton acceptors as bases formed from weak acids with a dissociation constant $K \leq 10^{-4.5}$ at 22°C and ionic strength, $I = 0.7\ m$, and proton donors as acids with $K > 10^{-4.5}$, at 22°C and $I = 0.7\ m$. This definition[29] requires addition of the term [HI] (singly protonated indicator) to the proton balance.

In the analysis, titrant is pumped into a stirred flowcell filled with the sample. The mixture of titrant and sample occupying the flowcell at any given time has a constant internal mass (assuming that sample and titrant have matching ionic backgrounds), M_T,

$$M_T = M_{a/i} + M_s. \qquad 2.2$$

Substitution of M_T into the left side of Equation 2.1 gives

$$\frac{Acy \cdot M_{a/i} - TA \cdot M_s}{M_T} = Acy \frac{M_{a/i}}{M_T} - TA \frac{M_s}{M_T}. \qquad 2.3$$

---

[29] For this study it was convenient to use slightly different criteria for the threshold K value, than suggested by Dickson (1981) (see section 1.3). Of all the equilibria used in this study, this definition only affects that of BCG. Measured TA is not affected by changing definitions, so long as one or the other definition is consistently used. The reasoning for this redefinition, is 1) K_1 crosses the threshold value at $I \sim 0.5$, and all experiments were carried out on the side of I where HI would otherwise be considered a proton donor and 2) it seems counterintuitive to regard HI in the zero level, since its protons effectively contribute to the titration of TA.

36

The mass ratios in Equation 2.3 can be thought of as dilution factors of the titrant ($f_{a/i}$)

and sample (f_s)

$$f_{a/i} = \frac{M_{a/i}}{M_T} \text{ and } f_s = \frac{M_s}{M_T}.$$ 2.4

The dilution factor $f_{a/i}$ is calculated from the ratio of total indicator concentration in the

flow cell, $[I]_T$, to the total indicator concentration in the a/i titrant, $[I]_{a/i}$, which is in turn

equal to the ratio of acid equivalents added, $[H^+]_{added}$, to initial titrant concentration, Acy,

$$f_{a/i} = \frac{M_{a/i}}{M_T} = \frac{[I]_T}{[I]_{a/i}} = \frac{[H^+]_{added}}{Acy}.$$ 2.5

The relationship described by Equation 2.5 is the primary innovation of TMT: the

indicator determines the amount of acid equivalents added while simultaneously

establishing the equilibrium position (pH) of the titration mixture. Utilizing the indicator

as a tracer eliminates volumetric measurements, shifting the burden of performance to the

spectrophotometer.

Equation 2.6 represents the alkalinity balance used to determine TA for a TMT of

a seawater sample

$$TA \cdot f_s + [H^+] + [HI^-] + [HSO_4^-] + [HF] - $$
$$[OH^-] - 2[CO_3^{2-}] - [HCO_3^-] - Acy \cdot f_{a/i} = 0$$ 2.6

where HI^- represents the singly protonated form of BCG. Using each species'

equilibrium expressions, mass balances, and the fact that $f_{a/i} + f_s = 1$, Equation 2.6

rearranges, giving

37

$$TA \cdot (1 - f_{a/i}) + [H^+] + [HI^-] + \frac{S_T \cdot (1 - f_{a/i})}{1 + \dfrac{K_s}{[H^+]}} + \frac{F_T \cdot (1 - f_{a/i})}{1 + \dfrac{K_F}{[H^+]}} - \frac{K_w}{[H^+]} -$$

$$\frac{2 \cdot C_T \cdot (1 - f_{a/i}) \cdot K_1 \cdot K_2}{[H^+]^2 + K_1 \cdot [H^+] + K_1 K_2} - \frac{C_T \cdot (1 - f_{a/i}) \cdot K_1 \cdot [H^+]}{[H^+]^2 + K_1 \cdot [H^+] + K_1 K_2} - Acy \cdot f_{a/i} = 0$$

2.7

where $C_T = [H_2CO_3^*] + [HCO_3^-] + [CO_3^{2-}]$, K_1 and K_2 are the first and second

dissociation constants of $H_2CO_3^*$ (see footnote 3), respectively, K_s is the dissociation

constant of HSO_4^- and K_F is the dissociation constant of HF. Total sulfate, S_T, and total

fluoride, F_T, are calculated from their conservative relationship with salinity.

Temperature dependent equilibrium constants (except for the indicator) were taken from

DOE (1994). K_1 and K_2 in 0.7 m NaCl were taken from Dyrssen and Hansson (1973).

For Na_2CO_3 and NaOH samples, $S_T = F_T = 0$. $[I]_T$, $[H^+]$ and $f_{a/i}$ are calculated from

absorbance data, as described below, leaving TA and C_T as the two unknowns in

Equation 2.7. From Equation 2.7, TA and C_T are then calculated from a set of

absorbance and temperature data using a non-linear least squares calculation (NLLS) (see

Section 1.5.3) which minimizes the sum of the squares of the residuals, $\Sigma residual^2$, by

iteratively optimizing TA and C_T. The Excel spreadsheet used to calculate TA contains a

combination of cell formulas and Visual Basic routines to perform the NLLS. This

spreadsheet is described in detail in the appendix (Section B.2). The key in using the

NLLS approach is to begin with only a slightly undetermined problem and collect a

sufficient number of measurements in the most trusted range of the instrument and

chemical model to allow convergence on the actual value. The total alkalinity TMT, in

this case, has two unknowns (TA and C_T) and ~25-30 different equations (one for each

titration point).

38

Although an estimate of C_T is necessary in the NLLS calculation, it must only be constrained to a reasonable range because 1) the residual is highly sensitive to adjustments in TA, while less sensitive to changes in C_T and 2) changes in C_T have a skewing effect on the residual set while changes in TA are much closer to an equal, overall positive or negative shift of all residuals (compare error trends of TA and C_T in Figure 1.4). If C_T is not constrained to a reasonable range, the NLLS routine may assign it unreasonable values. For example, constraining C_T to a value of $\pm 20\%$ from a best guess, gives less than 1 μm error in TA, while solving for TA and C_T without any constraints may swing C_T to a rail value of $C_T = 0$ or $C_T = TA$, resulting in a ~5 μm error in TA. This insensitivity to C_T is due primarily to the pH range used, where nearly all of the carbonate species are in the zero level of the proton condition (H_2CO_3 or $CO_{2(aq)}$), and therefore do not enter into Equation 2.7. In practice, C_T is known in almost all oceanographic locations to well within 10%.

2.2.1 Calculation of $[I]_T$ and $[H^+]$ for a titration point

The calculations described above require individual concentrations of each form of the indicator for each titration point in order to calculate the total indicator concentration, $[I]_T$, and pH of the solution. BCG is a diprotic molecule with $pK_{1I} \ll 0.0$ (Aragoni et al., 1995) and pK_{2I} ~4.5 depending on the temperature, ionic composition, and pressure. Above a pH of ~0, only the second dissociation is important

$$HI^- \xrightleftharpoons{K_{2I}} H^+ + I^{2-}$$ 2.8
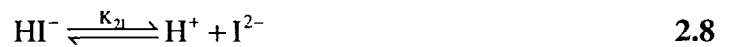
and from here on, we use $K_I = K_{2I}$. The equilibrium and mass balance equations are then

$$K_I' = \frac{[H^+][I^{2-}]}{[HI^-]}$$ 2.9

39

$$[I]_T = [HI^-] + [I^{2-}] \qquad\qquad \textbf{2.10}$$

where K_I' is the ionic strength dependent apparent dissociation constant (i.e. concentration constant). Spectrophotometric measurement of $[HI^-]$ and $[I^{2-}]$ allows calculation of $[H^+]$ from Equation 2.9. Using $[I]_T$ and $[I]_{a/i}$ with Equations 2.5 and 2.10 gives the dilution factors, $f_{a/i}$, and f_s.

As shown in Figure 2.1, the absorbance peaks of BCG are at $\lambda_{max} = 444$ nm for HI^- and $\lambda_{max} = 616$ nm for I^{2-}. Absorbance (A) at a particular wavelength (λ) is given by

$$_\lambda A = _\lambda \varepsilon_{HI} b[HI^-] + _\lambda \varepsilon_I b[I^{2-}] \qquad\qquad \textbf{2.11}$$

where ε is molar absorptivity of each species at wavelength λ and b is the pathlength. In general, the indicator spectra overlap and therefore $_\lambda A$ is a combination of the two forms at each analytical wavelength. The wavelengths 440 and 620 nm are used throughout the remainder of the paper (see Section 3.2). Indicator species are then calculated using

$$[HI^-] = \frac{_{440}A \, _{620}\varepsilon_I b - _{620}A \, _{440}\varepsilon_I b}{_{440}\varepsilon_{HI} b \, _{620}\varepsilon_I b - _{440}\varepsilon_I b \, _{620}\varepsilon_{HI} b} \qquad\qquad \textbf{2.12a}$$

$$[I^{2-}] = \frac{_{620}A \, _{440}\varepsilon_{HI} b - _{440}A \, _{620}\varepsilon_{HI} b}{_{620}\varepsilon_I b \, _{440}\varepsilon_{HI} b - _{440}\varepsilon_I b \, _{620}\varepsilon_{HI} b}. \qquad\qquad \textbf{2.12b}$$

As seen in Equation 2.12, for a mixture of two molecules with overlapping absorbance spectra at two analytical wavelengths, the numerical solution of the speciation requires four molar absorptivity values (one at each wavelength for each molecule). As described in Section 3.4, we determine εb rather than ε, because pathlength is not certain.

40
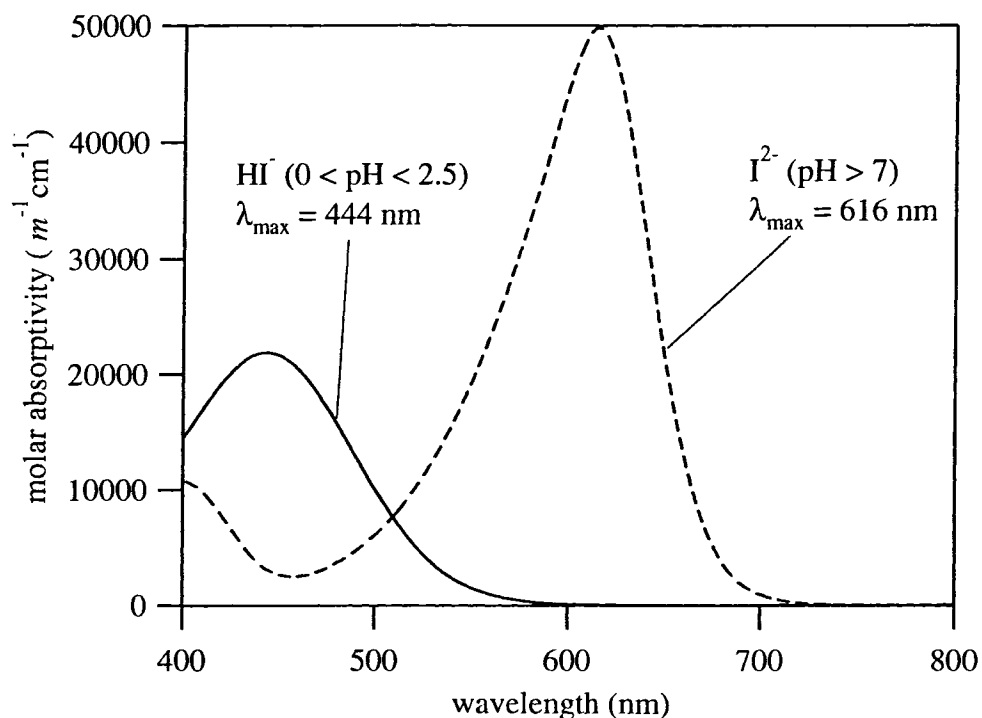
Figure 2.1 Absorbance spectra of singly protonated and fully de-protonated bromocresol green. Absorbance maxima are at 444 nm and 616 nm for HI^- and I^{2-}, respectively. Indicator concentration ($\sim$30 μm) is the same for both spectra. These scans were obtained on a Cary 300 with a spectral bandpass of 1 nm and optical pathlength of 1 cm. As described in Appendix C, BCG molar absorptivities may vary slightly between dye lots.

2.3 TMT theoretical model and mixing design

The most complex aspect of modeling any titration is calculating the speciation

(pH) of the sample-titrant solution at any given point. With the exception of the simplest

of cases, calculating the pH of a titration mixture requires numerical convergence on the

value $[H^+]$. The simplest approach is Newton's Method, in which a polynomial function,

$f([H^+])$, and its derivative are used to iteratively approximate the root of the function.

For several reasons, Newton's Method is undesirable. First, the iterations bog down

spreadsheets when calculating pH for a sizeable number of points. It is truly frustrating

to model a large problem, say, 1000 points using Newton's Method in a spreadsheet with

circular references. Second, it is susceptible to divergence errors (see e.g. 'the weak acid

problem' in Butler, 1998). A far better approach to solving the pH for a complex mixture

41

is to call a Visual Basic program from Excel, perform the convergence and return a value to the spreadsheet. The Visual Basic program I used for all titration models was given to me by Dr. Andrew Dickson (Scripps Institution of Oceanography). It uses the program 'ZEROIN'; a combination of bisection, secant, and inverse quadratic interpolation methods based on Forsythe (1977)

Modeling TMT has an added complexity: mixing. Almost all of the experiments presented in this document used active mixing, requiring a fairly simple dilution model. It would shortchange our past work on TMT, however, if the chronology of its development were completely skipped over. Static mixing was pursued for 2-3 years before active mixing was adopted in a desperate effort to eliminate the mixing gradients that were theorized to exist in the optical flowcell. Here, I will give a brief discussion of the major problems associated with a static mixing design, and argue the need for active mixing.

A static mixing design involves some sort of mixing chamber without moving parts, such as a mixing coil(s), elbow(s), braided tubing, etc. that serves to mix plugged flow. Active mixing uses a mixed chamber (containing a stirbar or impellor) at some point along the flow path. Active mixing assured us that there were no concentration gradients within the optical flow cell. Earlier studies showed that gradients between the source fiber and the return fiber optic led to deviations from Beer's Law (see below). Secondly, the mixing model for a well-stirred cell is simple, and agrees accurately and reproducibly with observed data. Finally, active mixing helps reduce any dead volume within the reaction chamber, guaranteeing rapid and complete flushing of each new sample.

42

In practice, the difference between active and static mixing is enormous. For example, consider in a typical flow injection analysis (FIA) in which a solution of C is injected into a flowing stream of water. The dilution factor is $D = [C]/[C]_o$, where $[C]$ and $[C]_o$ are the concentrations of C in the flowing stream and in the original solution, respectively. In Figure 2.2, D is approximated for a well-mixed chamber and a flowing stream, using the Tanks-In-Series model (Levenspiel, 1972). The curves shown in Figure 2.2 were generated by selecting
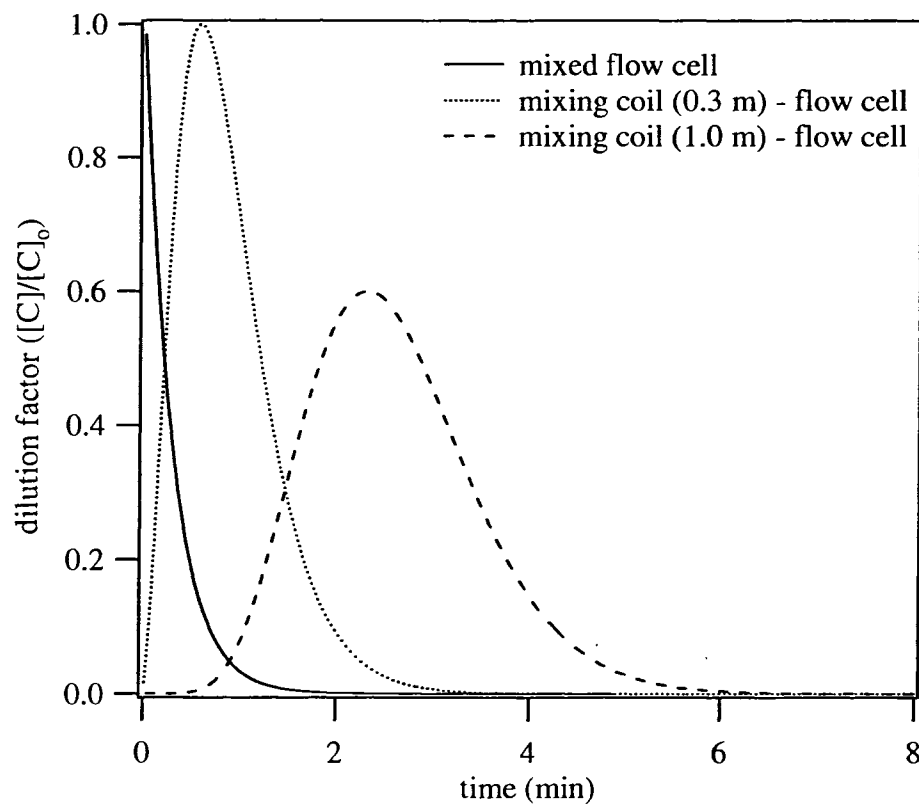
Figure 2.2 Mixing model for active and static designs of a ~10 µL flowcell. The flowcell flushes at a rate of 1.5 mL/min (a 50 µL pump pulse every 2 sec.). The dispersion is controlled by factors such the coil length, inner radius and flow rate. For typical FIA, as the mixing coil length increases, the dilution factor peak decreases. Peaks for the two mixing coils are normalized to 1 and 0.6 because, in practice, the volume of a/i injected into the flow line resulted in similar conditions.

the number of well-mixed tanks in a flow system. Not completely obvious from Figure 2.2 is the important characteristic that *no section of a static design is completely mixed,*

43

while active mixing provides a finite section which is almost perfectly mixed (i.e. the mixing chamber). Measurement points along a mixing coil/flowcell dilution curve necessarily correspond to finite volumes of the flow system and, hence, finite concentration gradients. A stirred flow cell, on the other hand, represents an infinitesimal volume of the mixing curve shown in Figure 2.2. Analysis of a mixed solution within a mixing chamber is thus the only approach free of concentration gradients.

Adapting the model shown in Figure 2.2 to the SAMI is accomplished by first calculating the volume of the SAMI plumbing, setting a flow rate from the expected number of solenoid actuations per unit time, then dividing the SAMI flow line into theoretical, well-mixed sections. For example, taking the flow rate as 1.5 mL/min with a 1 m mixing coil and a tank volume of 50 μL (solenoid pump volume), produces the dashed curve in Figure 2.2, which corresponds to about 9 tanks. This type of mixing model can then be incorporated into a titration model, and used to generate pH and absorbance data, as shown in Figure 2.3.

The titration model shown in Figure 2.3 does not account for the concentration gradient between the fiber optics in a flowcell, but an evaluation of the absorbance gradient effect is straightforward using both Figures 2.2 and 2.3. For example, a 10 μL interval of the system (i.e. the flowcell) corresponds to a time of 0.0067 minutes at a flow rate of 1.5 mL/min. The useful section of Figure 2.3 is the tailing edge where both forms of indicator are present (pump pulse 30-50), and dispersion is best (compared to the leading edge). At the point where the absorbances are roughly equal, the dilution factor (D) is approximately 0.4. From the mixing model (Figure 2.2), a time transient of 0.0067 where D ~ 0.4 corresponds to a change in D of ~0.005. This implies a pH gradient of

44

0.05, and absorbance gradients of 0.013 for both $_{440}A$ and $_{620}A$. Similarly, to achieve

absorbance
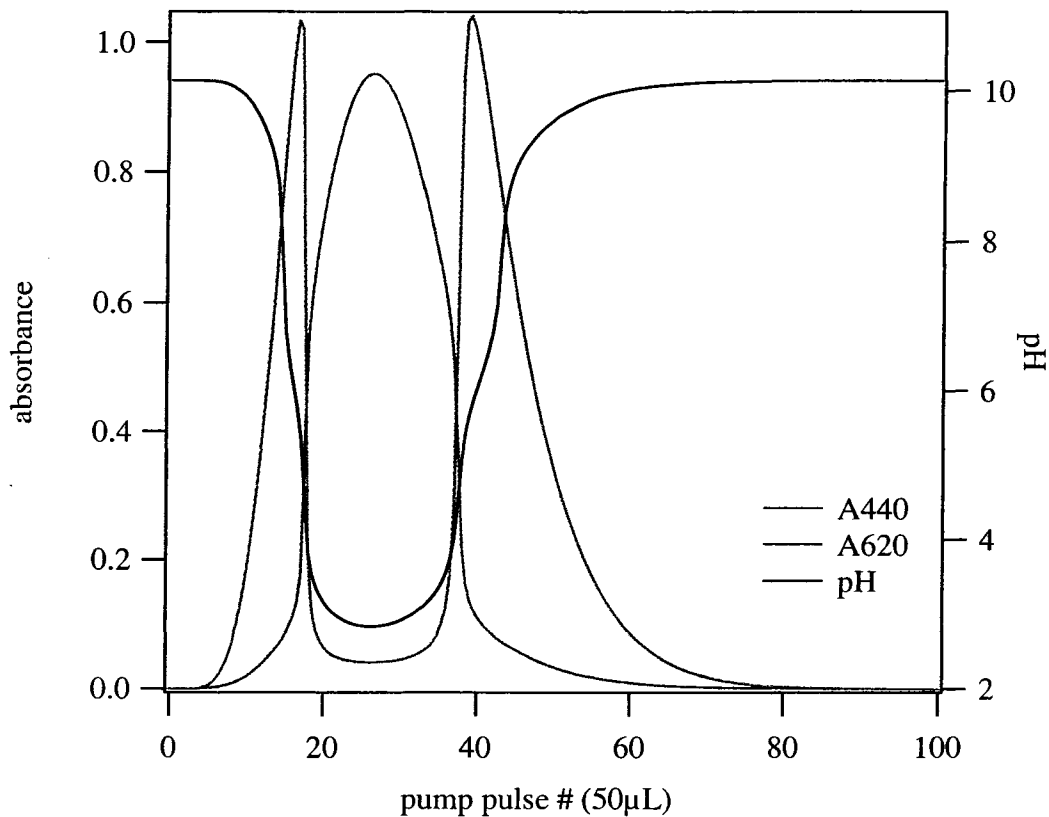
Figure 2.3 Theoretical titration data, generated using the 1.0 m mixing coil dilution curve shown in Figure 2.2. Pump pulse 100 corresponds to a time of 4.5 minutes on Figure 2.2. This type of model is a useful guide to solution preparation (i.e. a:i) and choice of nominal pump volumes, based on system volume.

gradients (during a titration) of ≤ 0.001 using this flow design, the model predicts that the

flowcell volume should be no more than 0.85 μL. Achieving a sufficient signal to noise

ratio (s:n) on a sub-microliter flowcell presents a serious challenge due to optical

throughput losses and was not attempted in this research. Because a titration occurs, both

analytical wavelengths pass through a steep inflection. Consequently, a flowcell-based

TMT has much larger absorbance gradients than an FIA analyte peak. Simply flushing a

plug of indicator, without acid, through the same system with a natural (alkaline) carrier

stream (e.g. to measure pH) results in an absorbance gradient of 0.008 where D ~ 0.4.

45

For a stirred flowcell, a simplified mixing model was used to examine the sensitivity of TMT precision and accuracy to different parameters. We used a mass balance for instantaneous addition of titrant followed by perfect mixing. It is therefore assumed that the composition of the solution pumped out of the mixing cell is equal to that of the mixing cell before the titrant pulse that displaces it. The theoretical total indicator concentration used in the titration model is calculated using approximate numbers for M_T (nominal mass of internal flow cell solution) and M_p (nominal mass of a pulse):

$$[I]_p = \frac{[I]_{p-1} \times M_T + [I]_f \times M_p - [I]_{p-1} \times M_p}{M_T} \qquad \textbf{2.13}$$

where I_{p-1} and $[I]_p$ represent the total concentration of the indicator before and after pump number p, respectively, and $[I]_f$ is total concentration in the solution being pumped into the flowcell. As shown in Figure 2.4, this mixing model agrees reasonably well with observed dilution data. The error shown in Figure 2.4B is relatively small compared with the errors expected for modeled vs. observed static mixing in FIA. The model therefore serves as a good approximation to evaluate instrumental response to factors such as absorbance noise and acid to indicator ratio (discussed in Section 2.3.1). Equation 2.13 is also useful to evaluate pump performance from experimental data. Dividing Equation 2.13 by $[I]_f$ gives the dilution factor D on the left side, and solving for the pump volume (or mass) gives

$$M_p = \frac{D \times M_T \times [I]_f - [I]_{p-1} \times M_T}{[I]_f - [I]_{p-1}}. \qquad \textbf{2.14}$$

46
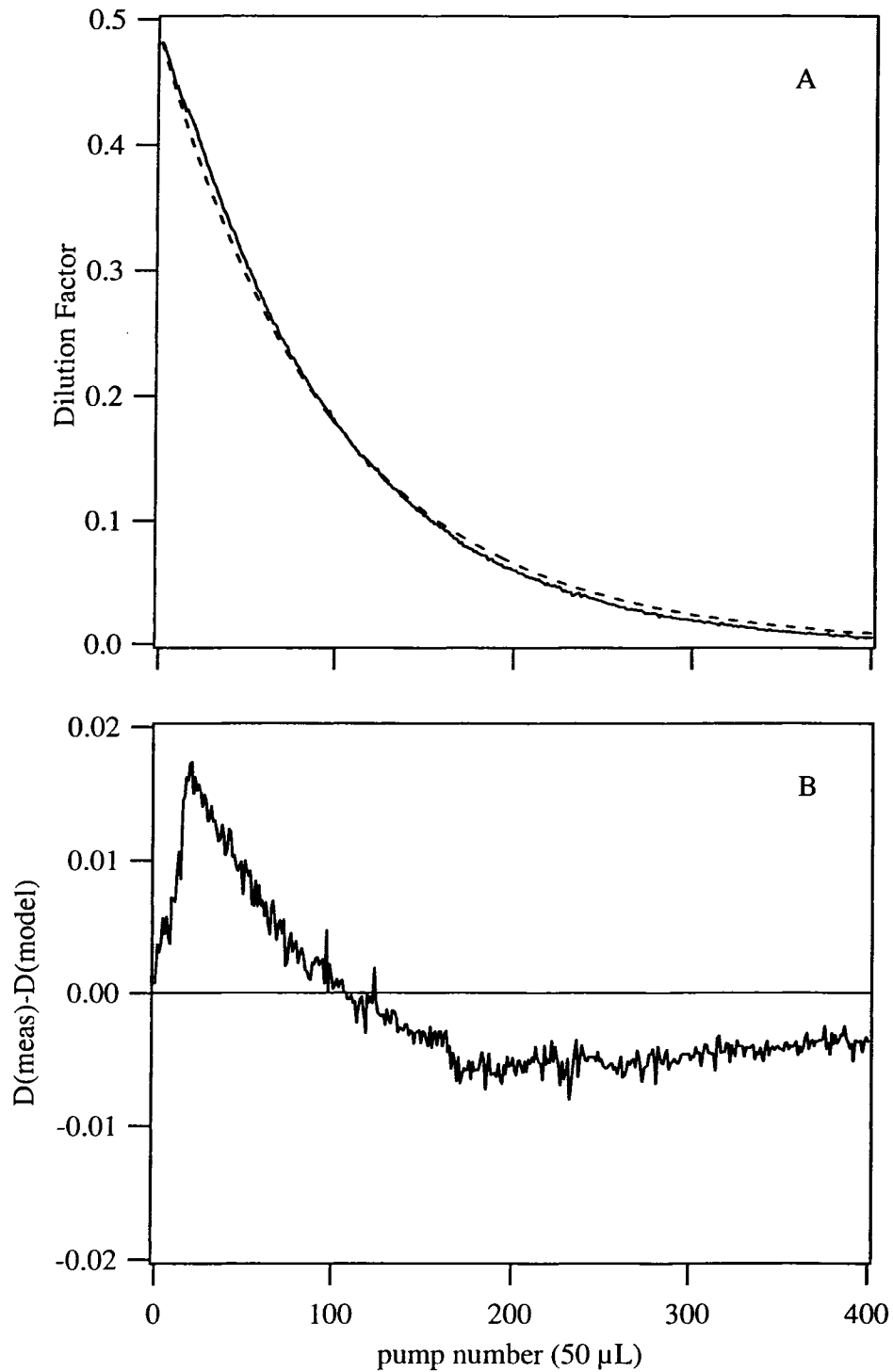
Figure 2.4 A) Observed dilution factor (solid line) from total indicator concentration, and theoretical dilution factor (dashed line) for flushing out a stirred flowcell from the peak of an a/i slug with a 50 μL pump. B) Dilution factor error between observed data and the mixing model.

47

Solving the set of observed dilution data shown in Figure 2.4A for the pump volume

using Equation 2.14, gives a running set of volumes dispensed by the solenoid pump. As

seen in Figure 2.5, the volume dispensed by the 50 μL pump is very noisy.
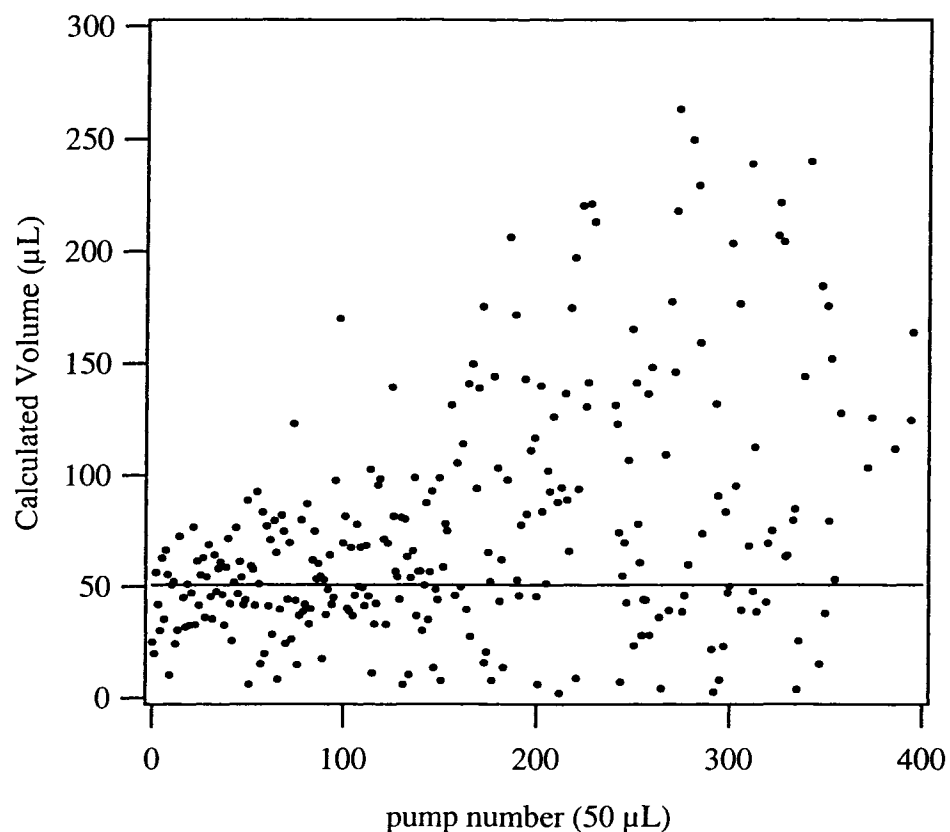
Figure 2.5 Solenoid pump volumes, calculated using Equation 2.14. The average of the first 150 pumps is shown as a horizontal line. This pump was a 50 μL BioChem Inc. pump.

The increasing noise with pump number in Figure 2.5 is due to absorbance noise as $_{440}A$

drops below 0.05 around pump 150 (absorbance data not shown). The average of the

first 150 pump pulses was 51 ± 30 μL. A similar calculation with an 8 μL pump resulted

in an average of 7.9 ± 12 μL (n = 78). Pump accuracy and precision do not, in principle,

influence titration accuracy and precision. Figure 2.5 serves to verify that the residual

noise is unaffected by pump noise, because, as shown below, the residuals exhibited very

low noise levels. It should be noted that a solenoid pump's performance is highly subject

48

to its operating conditions. For example, raising a 10 L bag of solution ~1 m above the solenoid pump will cause it to dispense a greater amount than its rated nominal volume. Similarly, using a great deal of backpressure over enough pump cycles can have the opposite effect, reducing the pump's nominal dispense.

2.3.1   Results from the theoretical model

The theoretical model is useful for individually estimating the TA error resulting from systematic errors in equilibrium constants, molar absorptivities, pathlength, temperature, absorbance, concentrations and the variables associated with solution preparation and random errors associated with absorbance noise. Using the dilution model for a tracer monitored titration in a stirred flowcell (Equation 2.13), the equilibrium speciation of the titration mixture was calculated for each point (Figure 2.6A). Next, absorbance data were calculated from molar absorptivities and the concentration of each form of the indicator (Figure 2.6A, colored lines). Figure 2.6B shows the residual trends based on systematic absorbance errors of 0.0005 and residual noise resulting from ±0.0005 absorbance noise.   Systematic and random errors were applied to the absorbances and other parameters, and then TA was calculated in a separate spreadsheet. As described below (Section 2.4, Appendix D), estimation of the combined systematic errors cannot be carried out using the simplistic approach described here, due to the offsetting effects of different variables. The model was most useful for approximating the effects of random absorbance error on TA. This "Monte Carlo" approach is carried out by generating a random array of absorbance noise at both analytical wavelengths, adding the noise values to the generated absorbances, and using the resulting values to calculate TA. This calculation is then repeated 20 times for each

49
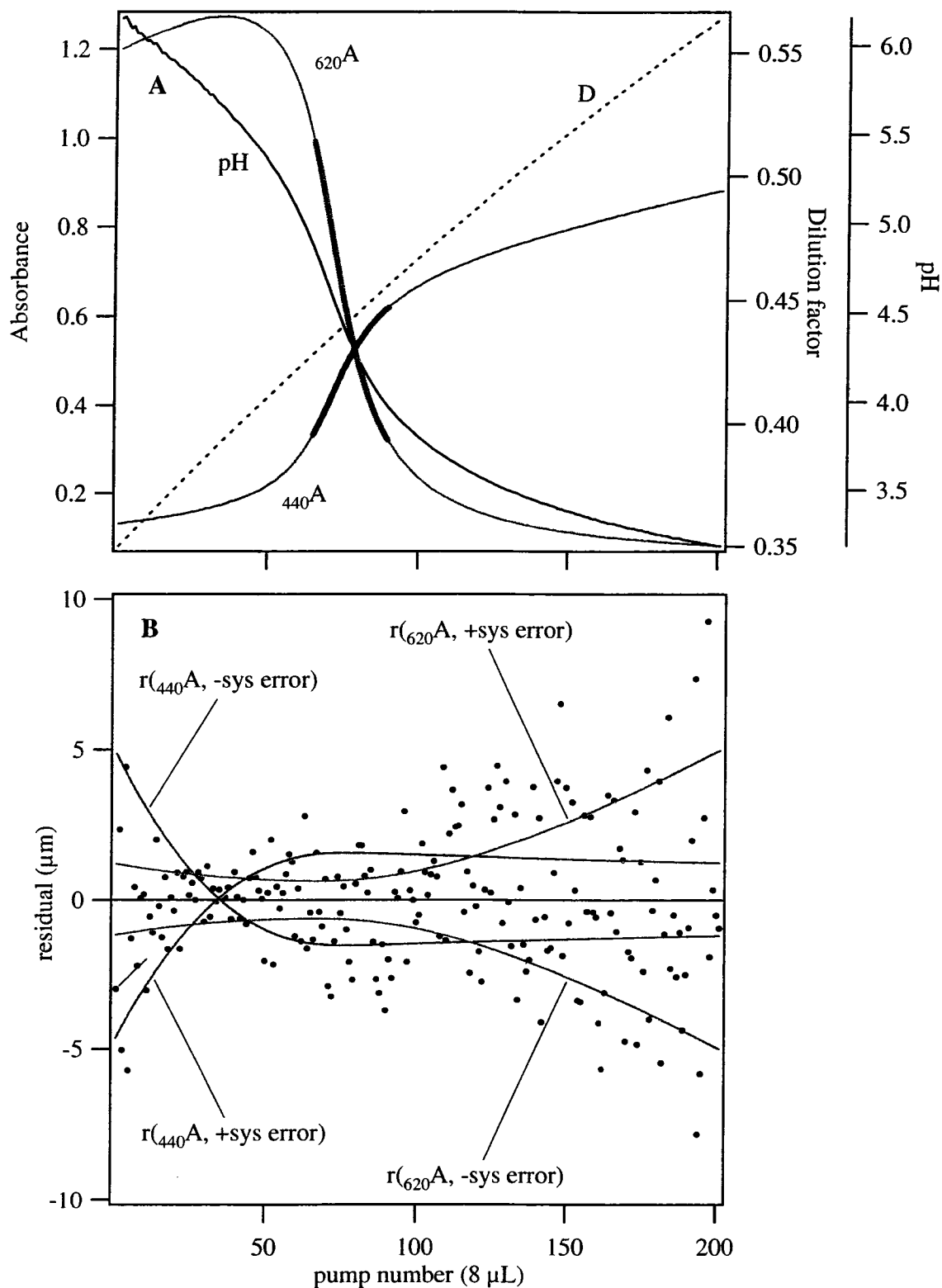
Figure 2.6 (A) Theoretical dilution, pH, and absorbances for a TMT of Na_2CO_3. Regions of absorbance that fall within the pH range 4-5 are highlighted in bold, and correspond to ~30 points. (B) TA errors resulting from systematic absorbance errors (lines) and random absorbance noise (dots). The magnitude of all errors was 0.0005 au.

50

scenario to obtain an average TA error, based on random noise. Following this method, Figure 2.7 was generated using 11 different absorbance noise levels with 20 iterations each. As seen in Figure 2.7, as absorbance precision deteriorates TA precision quickly degrades, reaching errors of $\sim \pm 1\%$ at absorbance precision of $\sim \pm 0.001$.
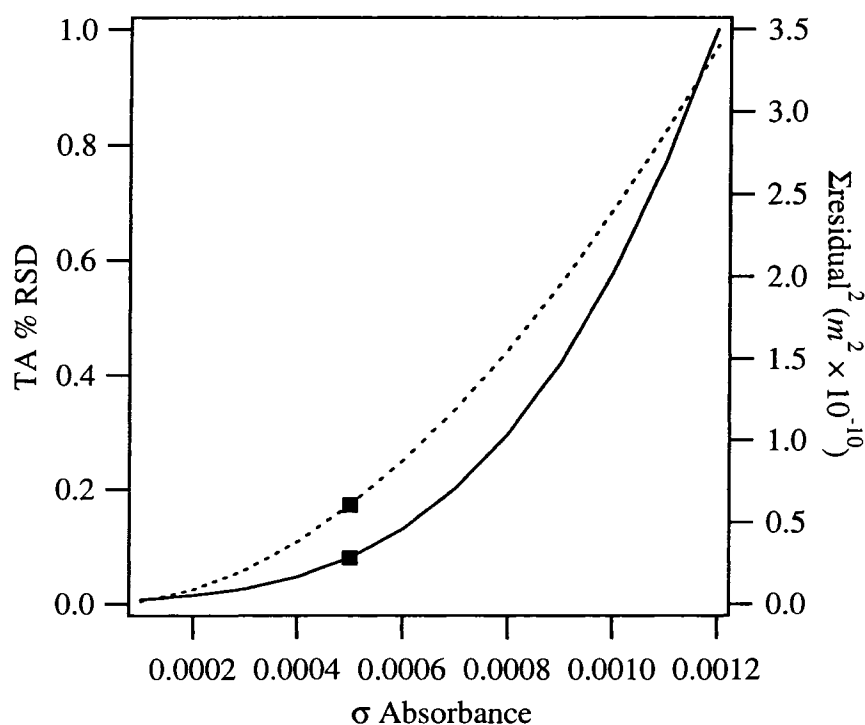
Figure 2.7 Precision plots of TA %RSD (solid line) and the sum of ~30 squared residuals, $\Sigma residual^2$ (dotted line), showing the instrumental performance in relation to absorbance precision. Based on this plot and the desired TA precision of 2 μm (0.1% RSD) the benchmark for absorbance precision was set at ± 0.0005 or better. Squares correspond to the ± 0.0005 absorbance precision, calculated for the region of 30 points shown in Figure 2.6, as described in the text. Based partly on this plot and partly on experimental data (see text) the maximum acceptable $\Sigma residual^2$ was set to $\leq 7 \times 10^{-10}$.

Temperature errors are also a source of random error. Thermostating fluctuations affect precision because the temperature dependence of each constant (especially indicator $K_I{}'$) is not perfectly known. The temperature of the flowcell is stable to $\pm 0.15°C$. Indicator $K_I{}'$ could potentially introduce noise under these conditions. For example, a 2 kJ/mol error in the $\Delta H°$ used to calculate the temperature dependence of $K_I{}'$ could result in a $\Delta pK_I{}'$ error of ~0.0002 (i.e. the difference in the magnitude of $pK_I{}'$

51

correction for a 0.15 °C temperature change), leading to a ~0.3 μm error in calculated TA. Noise from the ΔH^o error will increase with temperature fluctuations, making accurate enthalpy values an important factor during future TMT-based field deployments, where temperature is not controlled. Based on these predictions, it may be necessary to determine a more accurate, temperature dependent enthalpy of reaction for the second dissociation of BCG (see Section 3.5, below), or thermostat to better than ±0.05°C in order to optimize the precision. The temperature dependence of ϵb is relatively insensitive to this magnitude of temperature instability. Even a 20% error in the temperature dependence of ϵb (slope of ϵb vs. temperature) results in ≤ 0.1 μm error in TA over ±0.15°C.

Sensitivity to systematic errors (accuracy) was examined both numerically, using the titration model described in this section, and by propagation of error (see the uncertainty analysis in Section 2.4). Indicator $pK_1{}'$ errors of +0.001 and +0.010 lead to TA errors of +2 and +15 μm, respectively. TA errors due to errors in the titrant concentration (Acy) are dependent on the dilution factor. With $f_{a/i}$ ~0.5, a 10 μm error in Acy leads to 11-14 μm TA error. Accuracy errors due to Acy will decrease with decreasing dilution factor, but limits in indicator solubility and optical pathlength restrict $[I]_T$ to a narrow range, and titrant pump volume constrains the number of titration points achievable at lower dilution factors. Temperature accuracy errors result in offsetting errors from $pK_1{}'$ and ϵb. For example, a thermistor error of +0.5°C results in a TA error of -1.6 μm due to $pK_1{}'$ and +3.3 μm due to ϵb for a combined error of +1.7 μm. Systematic absorbance errors of ±0.001, or conversely, ϵb errors of ~ 0.15% lead to TA errors of up to 6 μm (Figure 2.6B). Based on these sensitivity studies, it is clear that very

52

high quality absorbance data, along with accurately known temperature dependence of pK_1' are required to achieve the desired TA precision and accuracy.

Because we used interference filters with a finite bandpass (see Section A.2.2), an absorbance measurement uses a distribution of wavelengths extending over about ± 20 nm (FWHM = 10nm) from the center wavelength of the interference filters. Since the molar absorptivity of BCG is also changing over these wavelengths (Figure 2.1), the resulting absorbance may slightly deviate from Beer's law with changing concentration. These deviations increase with differences in the center wavelength of the interference filter and the peak absorbance wavelength of each form of indicator, i.e. as $| d\varepsilon/d\lambda |$ increases. Theoretically, systematic absorbance errors due to polychromatic light are ≤ 0.001 a.u. in the range of absorbance used in this study. Therefore, according to the theoretical model (Figure 2.6B), accuracy errors in TA, induced by polychromatic light, should be minor. The linearity of the optical system is discussed in more detail in Section A.2.2. In general, the absorbance repeatability and accuracy of the optical system described below (Section 3.2) were shown to be adequate (Section A.2.2.5).

2.4 Uncertainty calculations

As mentioned in the previous section, combined systematic errors for TA were evaluated using a spreadsheet error propagation calculation that simultaneously considers all variables without their offsetting errors. The guidelines used for calculating uncertainty, U, and combined standard uncertainty, U_c, are discussed in greater detail in Appendix D. Here, Kragten's method is applied to the titration of seawater TA, specifically for TMT, and the results are discussed. As described in Appendix D,

53

preliminary uncertainty calculations for ε, $[I]_{stock}$ and Acy were necessary before calculating the U_c of a TMT.

The uncertainty analysis of a multipoint tracer monitored titration of seawater is shown in Figure 2.8 (see Terminology for descriptions of each parameter). The most important feature of this figure is that the parameters contributing to the U_c vary, depending on the pH of the solution. The estimated errors in temperature, salinity, K_W,
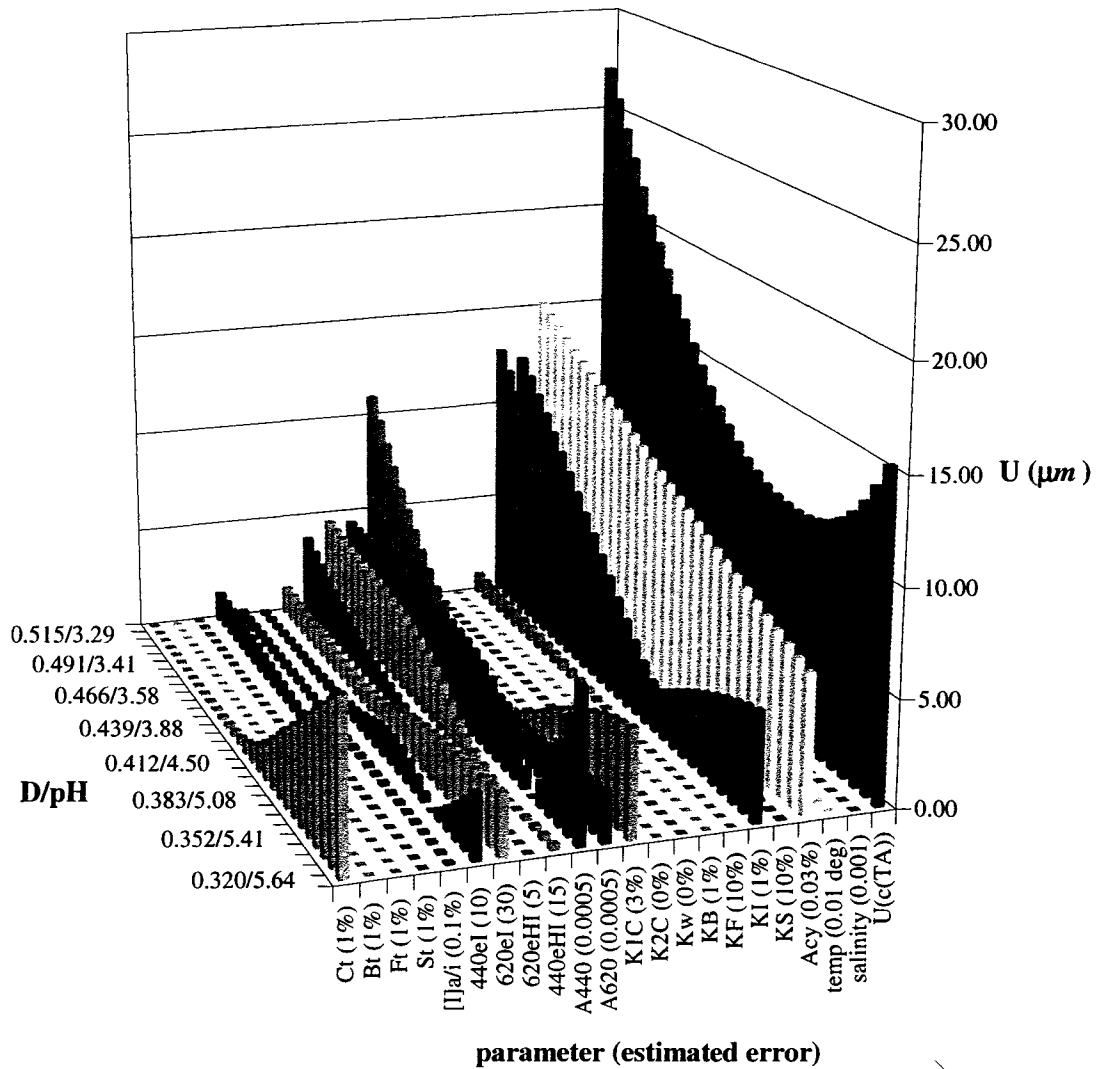
Figure 2.8 Sensitivity analysis for a tracer monitored titration of seawater total alkalinity. The left axis shows the progression of a titration; as dilution factor, D, increases pH decreases. On the bottom axis, the estimated error of each parameter is shown in parenthesis. e is molar absorptivity. The vertical axis is the uncertainty (error) in TA. The purple bars (far right) represent the combined standard uncertainty in TA.

54

K_{2C}, K_B, B_T, and F_T lead to an insignificant error in TA at all points in the titration. Temperature errors become significant around $\pm 0.05°$, as discussed in Section 2.3.1. K_B, B_T and K_{2C} play a minor role because the pH range of the titration is far removed from the equilibrium where the species $B(OH)_4^-$, and CO_3^{2-} exist in appreciable amounts. Uncertainty in titrant concentration (Acy) has a steadily increasing contribution as the titration progresses. Errors in K_S and, to a lesser extent, K_F become significant at pH < 4.5. C_T and K_{1C} contribute at pH > 4.5, where HCO_3^- is an important term in the alkalinity balance. The indicator equilibrium constant (K_I) has a minimum at pH = pK_I. As pH departs from pK_I, the K_I uncertainty contributions are roughly equal at ± 0.5 units. pH differences > 0.5 units from the pK_I, lead to greater errors at low pH because errors in $[H^+]$, calculated using K_I, weigh more heavily on the residual value at low pH.

Uncertainties due to the spectrophotometric parameters (absorbance and molar absorptivity) are shown in Figure 2.9. Absorbance errors at both channels (620 and 440 nm) exponentially increase the uncertainty at each pH extreme where their respective forms of indicator vanish. The 440 nm channel has a minimum that corresponds to the pH where both forms of indicator are present, due to its importance in the measurement of $[I^{2-}]$ in addition to $[HI^-]$. Molar absorptivities follow the general trend that $_\lambda\varepsilon_{HI}$ and $_\lambda\varepsilon_I$ are most important at low and high pH, respectively. At low to mid pH $_{440}\varepsilon_I$ steadily increases with $[I^-]$ (not shown) reaching a maximum around 4.7, which is a convolution of increasing errors due to the importance of $[I^{2-}]$ in measuring $[I]_T$ and decreasing errors due to a diminishing importance on the 440 nm wavelength in measurement of $[I^{2-}]$. After reaching a minimum at pH ~ 5.4, $_{440}\varepsilon_I$ again increases because of the amplified

55

dependence on measurement of $[I^{2-}]$ for total indictor concentration and, hence, dilution factor.
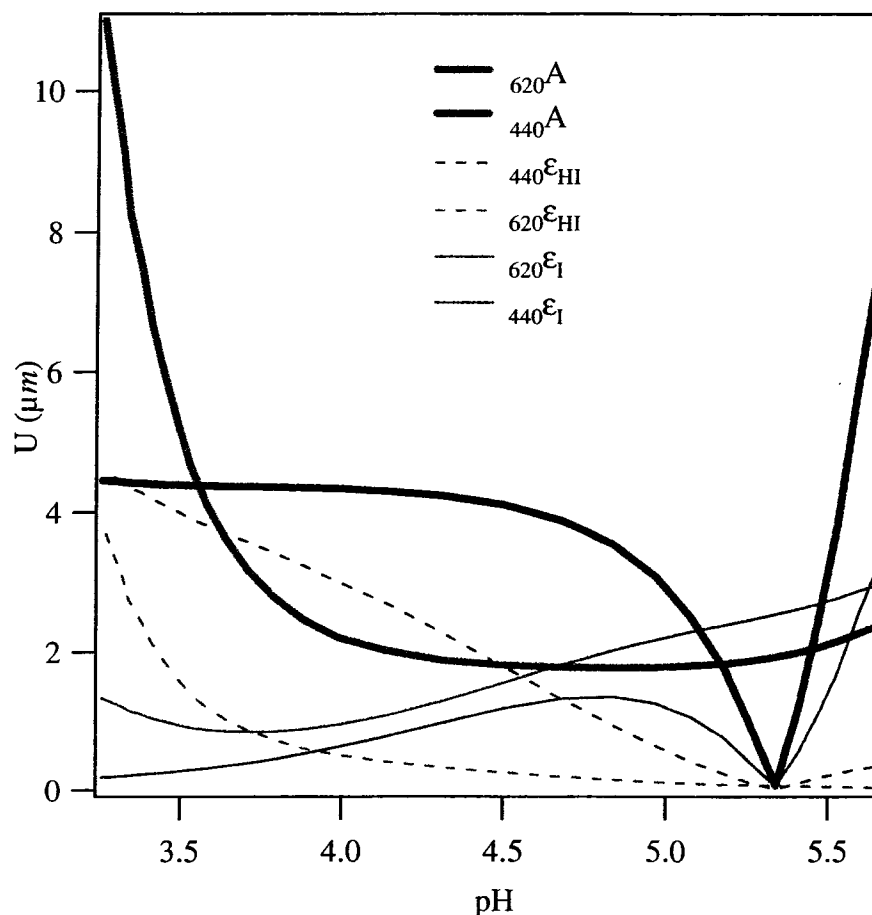
Figure 2.9 Uncertainties for the spectrophotometric parameters absorbance (solid bold lines) and molar absorptivity, from Figure 2.8. Values specific to the HI^- and I^{2-} species are given dashed and solid thin lines, respectively.

2.5 Summary

Sections 2.1 and 2.2 developed the theory and equations behind TMT and

Sections 2.3 and 2.4 used these equations in theoretical models to explore the sensitivity

of calculated TA to the different titration parameters. The most important information

revealed by the models is (1) for TA precision of ~2 μmol kg-soln^{-1}, the

spectrophotometer must operate with a precision of better than ±0.0005 AU and (2) the

combined systematic errors in a TMT of seawater TA may lead to an overall systematic

error of up to ~1%. High accuracy (~0.1%) seawater TA measurements by TMT, will

56

therefore require an adjustment based on a CRM. The first requirement (optical stability and precision) is addressed in Section 3.2 and described in greater detail in Appendix A (Section A.2). The second point is addressed in greater detail below in Section 3.5.

57

Chapter 3   Experimental Aspects of TMT

This chapter describes various laboratory procedures and introduces the

instrumental design used in TMT.

3.1   Solution Preparation

All solutions were prepared gravimetrically and corrected for air buoyancy.

Samples were immediately transferred from the preparation vessel to gas-impermeable

bags to limit evaporation and gas exchange during sampling. Solutions containing

indicator were carefully shielded from light and stored in bags. NaCl (biological grade

certified, Fisher Lot 041477) was added to all solutions except indicator stock to set ionic

strength, I, to seawater levels ($I = 0.700$ m).

Each alkalinity sample was prepared in a 7.5 L LDPE carboy, mixed for > 1 hour

and drained into a 10 L sterilized, inert, gas-impermeable bag (SCD, TC Tech). Sodium

carbonate TA standards were prepared using anhydrous Na_2CO_3 (Alfa Aesar Puratonic,

99.997% purity); dried at 200°C for 3 hrs and stored in a dessicator until use. Na_2CO_3 in

NaCl was prepared to ~0.0020-0.0025 equivalents kg-soln^{-1} by adding ~0.77-0.93 g

Na_2CO_3, ~7000 g H_2O, and ~297 g NaCl. NaOH samples were prepared from Fisher

standard NaOH (N/10 certified; N = 0.10030 mol L^{-1}, ρ = 1.0027 g/mL). NaOH in NaCl

was prepared to ~0.00235 mol kg soln^{-1} by adding ~175 g NaOH, 7000 g H_2O and ~306

g NaCl. The certified reference material (CRM) is filtered and sterilized seawater,

prepared and certified in Andrew Dickson's laboratory (Dickson et al., 2003).

A stock solution of BCG was prepared by dissolving ~2 g of NaHBCG (dye

content ~90%, dye purity ~95.4%, Sigma Aldrich dye lot 01920DI) in ~2400 g water to

give $[I]_{stock}$ ~1 × 10^{-3} m. The stock was stored in an amber glass jug. All other indicator

solutions were prepared from weighed masses of this stock[30].

Titrant was prepared from Fisher standard HCl (N/10; N = 0.09980 mol L^{-1}, ρ =

0.9998 g/mL) and BCG stock by adding ~450 g stock, ~150 g HCl, ~6000 g H_2O, and

~281 g NaCl. Titrant was stored in a 10 L bag (SCD, TC Tech) and wrapped in black

plastic to prevent light exposure.

Solutions of I^{2-} and HI^- were prepared for εb measurements. The procedures for

accurate preparation of these solutions are described in Appendix D. The pH was

controlled by adding accurate masses of 0.1 M HCl or 0.1 M NaOH. $[H^+]$ was calculated

using a model that accounted for the presence of indicator. The calculated pH was 2.4

and 10.6 for the HI^- and I^{2-} solutions, respectively. pH was also verified with a Ross

combination electrode (calibrated to NIST standards) which agreed to 0.1 unit for both

solutions. Due to the large difference in I between the electrode buffers and the

solutions, agreement of 0.1 unit is reasonable.

3.2 Titration apparatus

Solutions were titrated with the setup shown in Figure 3.1. This apparatus

consists of (1) the fluid sampling system (a/i titrant and alkalinity sample bags; pumps;

tubing; stirred flowcell), (2) an optical system (light source; fiber optics; flowcell; light

detection system), (3) a pc, microcomputer/datalogger and power supplies, and (4) a

water bath. Batch measurements are fully automated, requiring an operator only to

reload samples. Sample and titrant bags are connected to 250 µL and 8 µL per pulse

solenoid pumps (Bio-Chem Inc.), respectively. The pump outlets merge at a low dead

---

[30] Using a single stock solution eliminates problems associated with intra-dye lot inhomogeneities or inter-dye lot inconsistencies (i.e. dye purity, dye content), giving internally consistent results; it does not, however, address the issue of experimental reproducibility between separately prepared stock solutions.

volume tee, which connects to the inlet of a stirred optical flowcell with ~5 mL internal volume. All tubing leading up to the flowcell is 1.00 mm ID PEEK. As discussed in Section 2.3, the flow design is based on *active* mixing.

The flow cell has an integrated water manifold for temperature regulation (Figure 3.1). The outer cell surface is insulated with double-sided foam mounting tape and 4 mm thick cork. The manifold is connected to a water bath (Thermo Neslab; $\pm 0.01^{\circ}C$). The tubing (1/4" ID Tygon) connecting the water bath to the flow cell was equipped with two Nylon T-connectors with septums and wrapped in foam insulation. The PEEK tubing that connects the Upchurch tee (Figure 3.1) to the flow cell was sealed into the Tygon tubing through the two septums (not shown in Figure 3.1). This further improved thermostating because it reduced contact between the inlet tubing and the ambient air to a very small area at the flowcell entrance. A thermistor, installed in the flow cell inner chamber, directly monitors temperature of the titration solution with $0.01^{\circ}C$ resolution. The internal temperature was stable to around 0.10-$0.15^{\circ}C$. As discussed above, this level of temperature stability affects precision, but using temperature-dependent equations for εb and all equilibrium constants adequately reduced the temperature sensitivity.

The optical system and analog electronics used in this study are similar to those described by DeGrandpre et al. (1995) with some modifications. The optical system consists of a tungsten-halogen source with optical feedback (Custom Sensors), 1000 μm core fused silica fiber optics (Edmond Scientific), a 3-way fiber optic bundle splitter (FiberTech Optica), and a three channel spectrophotometer built from dual bandpass

60

filters (Intor) and Si photodiodes (S2386-45K, Hamamatsu) interfaced to a custom-built

analog amplification board (Sunburst Sensors LLC). The center wavelength (CWL) of
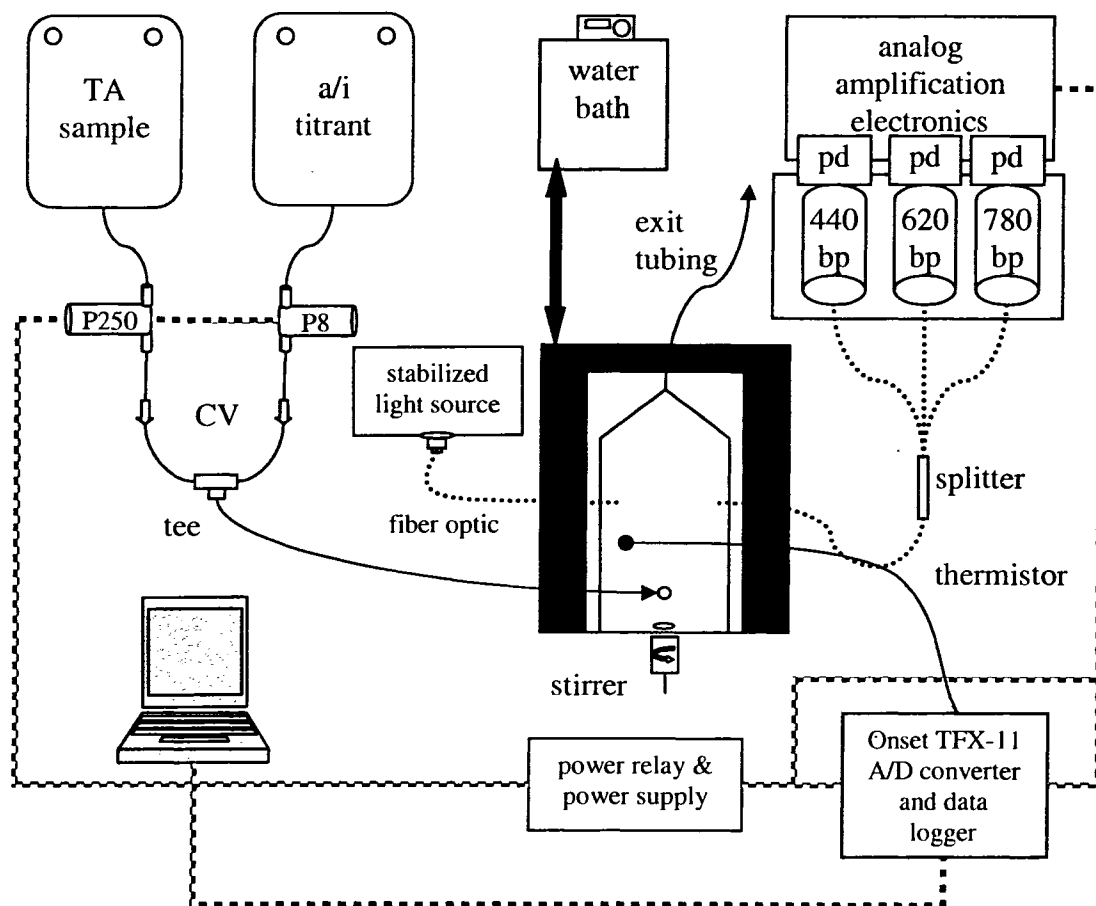
Figure 3.1 Schematic of titration apparatus. Sample and titrant are pumped by 250 μL (P250) and 8 μL (P8) solenoid pumps. Check valves (CV) prevent reverse breakdown of pump seals. Each pump's output is coupled to a low dead volume tee which connects to the flow cell below the light path. Light is collected at the return fiber and split to three dual bandpass filters (bp). The photocurrent in each photodiode (pd) is converted to voltage and amplified using a two-stage inverting op-amp design. The resulting voltage is then digitized and logged by the TFX-11. Water bath temperature is set at 22.0°C and connected to a built-in manifold in the flow cell. The temperature of the titration mixture is also directly monitored by a thermistor. A magnetic stir bar is sealed into the flow cell by an acrylic base plate, with a stirring motor mounted directly below.

the bandpass filters was only available on 5 nm intervals, so the filters were selected to

match peak absorbance wavelengths (PWL) of BCG as closely as possible (440 nm and

620 nm CWL filters for 444 nm and 616 nm PWL, respectively). The full width at half

maximum (FWHM) of the bandpass filters is 10 nm. Absorbances measured at a

reference channel (780 nm) were subtracted from the analytical absorbances to account

61

for baseline offsets (see Section 3.7). Adding a second identical filter to each channel guarantees a very high rejection of off-band radiation. At each channel, a photodiode is mounted on the other side of the two filters and directly connected to the analog board. Improvements in the optical design and additional signal averaging, increased the S/N from ~3000 to ~5000 (~0.0001 au) where it is limited primarily by the resolution of the 12 bit A/D converter. A TFX-11 microcomputer (Onset Corp.), controls pumps, analog to digital conversion and data acquisition.

As discussed above, very stable and precise absorbances (<0.0005 a.u.) are required for this application. Absorbance reproducibility better than ±0.001 au is very difficult to achieve on a single beam instrument. The highest quality data requires a very short time between blank and sample, but our system records absorbance several minutes after the blank during both titrations and ϵb measurements. A non-absorbing reference wavelength (i.e. 780 nm, Figure 2.1) provides short-term corrections for source noise and air bubbles, but cannot account for the wavelength dependent drift exhibited by a tungsten light source over minute-long periods (Section A.2.1.1). We therefore used a light source stabilized by optical feedback. The source exhibited very little drift over the time intervals between blank and sample (drift ~0.0001 a.u./hour).

3.3 Absorbance measurements

For a single absorbance measurement (e.g. for ϵb measurements), the setup shown in Figure 3.1 was slightly altered. The tee and 8 mL pump were removed and a 3-way selection valve (Upchurch) was connected to the 250 µL pump entrance. The 3-way valve was then connected to blank and sample solutions. The operating programs for absorbance measurements are described in Appendix B. First, the valve was positioned

62

to a blank solution and ~ 110 mL was flushed through the flow cell. Next, a blank was recorded, the valve was switched to the indicator solution and followed by a ~ 110 mL flush of the indicator sample while continuously monitoring the signal intensities. This procedure verifies a 100% flush.

3.4 Determination of εb

Accurate indicator molar absorptivities and pathlength are crucial parameters for accurate and precise performance. Because we do not know the exact pathlength in our custom flow cell, the combined value, εb, is determined by recording the absorbance of indicator solutions (see Section 3.1) directly in the cell, rather than on a benchtop spectrophotometer. εb values must be re-determined for each disassembly-reassembly of the flow cell because of slight changes in the positioning of the fiber optics. It is also critical that pathlength does not change during sample measurements. To determine absorbance/pathlength stability, we monitored the absorbance of a single solution over long time periods and compared εb values measured on freshly prepared solutions on different days. The εb is extremely stable, as shown below.

Numerous subtle problems arise in accurately measuring εb. εb depends upon ionic strength, indicator assay (dye content and dye purity), temperature, brand of spectrophotometer (i.e. spectral bandpass, type of wavelength selection) wavelength accuracy, wavelength repeatability, % stray light, and optical pathlength. Because εb is dependent on so many system specific parameters, researchers should beware of values reported by others. εb is quantified by measuring the absorbance of a solution in which the pH is set to maximize a single form of the indicator. For BCG, we first measured the absorbance of a basic solution (pH ~10), where $[I^{2-}]:[HI^-] > 1 \times 10^6$. At low pH, it is

63

impossible to fully isolate one form of BCG. The other two absorbance measurements

(at 440 and 620 nm) on acidified indicator (pH ~2) must be corrected for the presence of

I^{2-} using Equations 2.9 and 2.10 and the εb values of I^{2-} calculated in the first step. The

temperature dependence of εb is determined by recording absorbances at different

temperatures.

3.5 Indicator pK_I'

An accurate indicator pK_I' is very important in the calculation of $[H^+]$ (Equation

2.7, Figure 2.8) and, consequently, TA. Despite equal ionic strengths, a Na_2CO_3 standard

prepared in NaCl background requires a different pK_I' value than a seawater CRM due to

the formation of fewer ion pairs (Dyrssen and Hansson, 1973). Because there is no

reliable data reported for the pK_I' of BCG in 0.7 m NaCl, we relied on our own

approximation for this value. We used data reported by others (Byrne et al., 1988;

Breland and Byrne, 1993; King and Kester, 1989) to obtain a pK_I' for the TMT of a

CRM.

The pK_I' in NaCl background was determined by titrating a Na_2CO_3 standard on

the TMT system and iteratively refining TA and pK_I' to minimize the value $\Sigma residual^2$.

Using several preliminary titrations we found pK_I' (NaCl) = 4.475 (I = 0.700 m;

22.00°C). The pK_I' at 25°C on the *free* H^+ scale in molal units at salinity = 35 ‰ was

reported by Byrne and coworkers in seawater (4.435) and synthetic seawater (4.4166),

and by King and Kester in seawater (4.410). We calculated TA for the CRM using all

three of these values, converted to the concentration scale mol kg-soln^{-1}, titration

temperature (see below), and corrected to the CRM salinity as described by Yao and

Byrne (1998). At the same temperature (e.g. 22.0° C) pK_I'(NaCl) is ~0.03 units higher

64

than pK_I'(seawater), depending on which literature value is chosen for the seawater

constant. From a qualitative standpoint, this trend seems correct, because the ions present

in seawater should associate with H^+ and I^{2-} decreasing their activity and driving the

dissociation reaction in Equation 2.8 and increasing K_I' in seawater.

The pK_I' temperature dependence of BCG has not been reported. The following

procedure was used to calculate the pK_I' at the temperature measured during a titration in

each medium: (1) accept a value for pK_I' at ionic composition identical to and

temperature at or near that of the medium in which the titration is to occur and (2), use

the enthalpy of reaction, ΔH°, for dissociation of BCG, along with the accepted K_I' in the

van't Hoff equation to calculate the dissociation constant at the titration temperature.

Because all work in this study was done over a relatively narrow temperature range, it is

assumed that ΔH° is constant with temperature. The ΔH° for BCG is found by observing

changes in the absorbance ratio of a mixture of HI^- and I^{2-} as temperature is varied.

ΔH° was estimated by first generating theoretical R(T) values between 20°–30° C

using

$$R(T) = \frac{_{620}A(T)}{_{440}A(T)} = \frac{_{620}\varepsilon_I b(T)\left(\dfrac{[I_T]}{1+\dfrac{[H^+]}{K_I(T)}}\right) + {_{620}}\varepsilon_{HI} b(T)\left(\dfrac{[I_T]}{1+\dfrac{K_I(T)}{[H^+]}}\right)}{_{440}\varepsilon_I b(T)\left(\dfrac{[I_T]}{1+\dfrac{[H^+]}{K_I(T)}}\right) + {_{440}}\varepsilon_I b(T)\left(\dfrac{[I_T]}{1+\dfrac{K_I(T)}{[H^+]}}\right)} . \qquad \textbf{3.1}$$

In Equation 3.1, $[H^+]$ is calculated as a function of temperature using an equilibrium

model, $\varepsilon b(T)$ is calculated from the equations previously determined for effective molar

absorptivities and $K_I(T)$ is calculated using the van't Hoff equation

65

$$K_1(T) = K_1^\circ e^{\left[\frac{\Delta H}{R}\left(\frac{1}{T^\circ} - \frac{1}{T}\right)\right]}.$$ 　　　　　　　3.2

where K_1° was estimated at temperature T° during the Na_2CO_3 titration described above.

Next, data were collected for $R = {}_{620}A/{}_{440}A$ at varying temperatures (20-30°). The ΔH°

used in Equation 3.1 to calculate $K_1(T)$ (Equation 3.2) is then adjusted until the generated

slope of R(T) vs. T matches the empirical slope (Figure 3.2). Similarly, $[H^+]$ was

modeled for acidified seawater, R(T) was generated using the same set of temperature-

dependent εb values determined in NaCl, and R(T) data from Breland and Byrne (1993)

were used to find ΔH° in seawater. The literature K_1° value used to calculate ΔH° is

arbitrary because the range of reported pK_1' values has a negligible effect on the slope

calculated. Breland and Byrne reported a slope of R(25)/R(T) vs. T of 0.00907. Thus,

based on our own data for NaCl and a combination of our own data and that of Breland

and Byrne (1993) for seawater, we found that $\Delta H^\circ = 3.0$ kJ/mol for NaCl solutions and

$\Delta H^\circ = 2.5$ kJ/mol for the CRM. The pK_1' changes estimated are -0.0018 per °C in 0.7 m

NaCl and -0.0014 per °C in seawater. BCG's pK_1' is relatively insensitive to temperature,

compared to other sulfonephthaleins. For example, Yamazaki et al., (1992b) report $\Delta H^\circ =$

18.70±0.51 KJ/mol for Thymol Blue. The very low value of ΔH° for BCG is, perhaps,

the reason that researchers seem to have avoided measuring it. The R(25) correction of

Breland and Byrne (1993) circumvents reporting a discrete temperature dependence for

pK_1' by grouping the temperature dependence of molar absorptivity and pK_1' into a single

correction. Their approach involves observations of the changing absorbance ratio with

temperature, similar to the steps followed in this study. Breland and Byrne then simply

correct measured R values at all temperatures to 25°C. One potential problem with this

correction is that changes in R due to unpredicted phenomena (e.g. spectrophotometer

error, CDOM) would be erroneously corrected. In addition, their
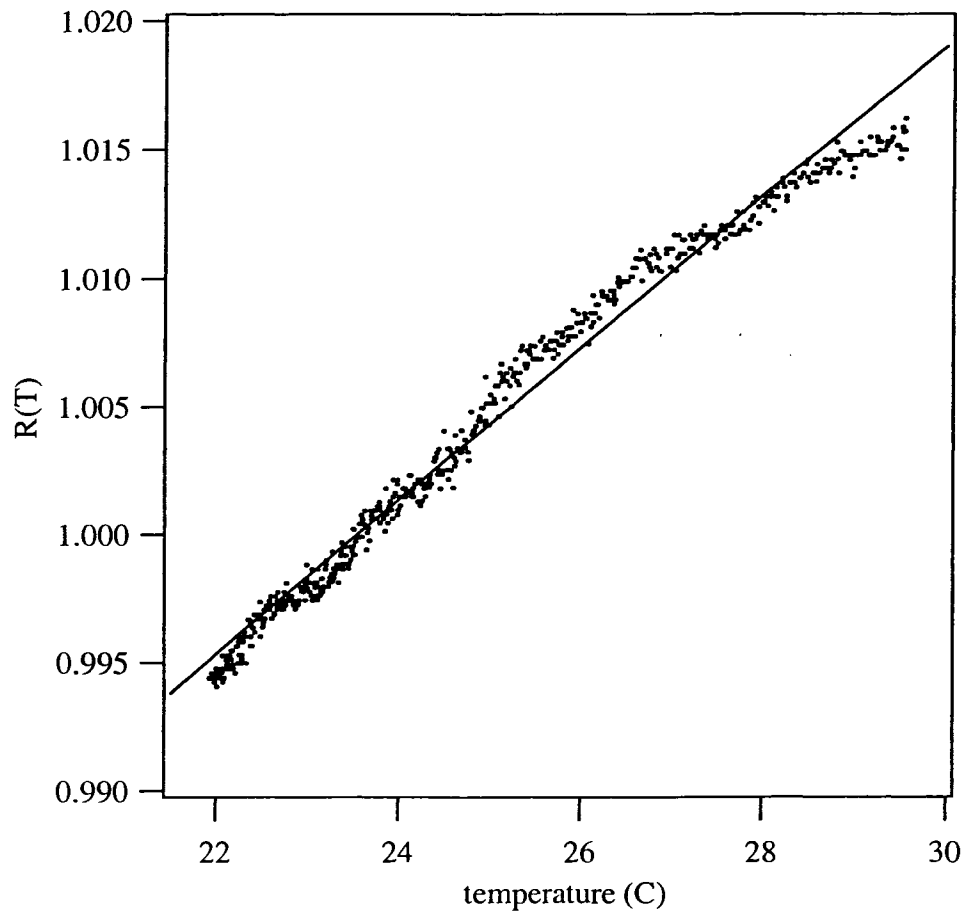
Figure 3.2 R(T) observed (dots) and R(T) generated (line) for BCG around the temperature at which titrations were carried out. The slope of the theoretical R values is matched to the observed slope by adjusting ΔH°.

R(25) correction is instrument specific and therefore does not apply to our custom-built

instrument, while pK_1' (T) should be universally consistent. In general it seems

worthwhile to determine temperature dependencies as rigorously as possible and report

thermodynamically relatable constants (e.g. Ramette, 1977), as they will be more useful

to other researchers using different instruments.

As mentioned above, the value of pK_1' used in this study for CRM (seawater)

titrations underwent some composition and concentration scale conversions to match the

67

titration conditions. Byrne et al. (1988), King and Kester (1989) and Breland and Byrne (1993) reported pK_1' on the molal scale for salinity = 35. Molal pK_1' is converted to the m scale using (DOE, 1994)

$$pK_1(\text{mol kg-soln}^{-1}) = pK_1(\text{mol kg-H}_2\text{O}^{-1}) - \log(1 - 0.001005 \times S).\qquad 3.3$$

Equation 3.3 can only be used for the salinity at which the molal pK_1' values were reported at (i.e. S = 35). A salinity correction for BCG (Yao and Byrne, 1998) accounts for compositional changes in the ionic medium

$$pK_1(S) = pK_1(35) + 0.002578(35-S).\qquad 3.4$$

There are several alternative ways of evaluating K_1'. In this section, we have discussed two approximation methods; one based on standard titrations in our own lab, and another based on simple adjustments to literature values. Neither of these approaches could be regarded as an authentic 'measurement' of K_1', however. The most rigorous approach to measuring an equilibrium constant involves equilibrating an equimolar solution of the acid-base pair to be studied with a hydrogen electrode for a direct measurement of the hydrogen ion activity, where the acid-base pair under examination is the primary buffer system of the solution. Due to various experimental difficulties, this method has never been reported on BCG[31]. The 'next best' approach involves dissolving a small amount of the indicator in a well-characterized buffer system (i.e. an acid-base pair that has an equilibrium constant traceable to a hydrogen electrode), of ~1000 times greater concentration than the indicator. A spectrophotometric measurement on this solution along with a calculated [H^+] gives the K_1 value of the indicator[32]. A somewhat

---

[31] this experiment is difficult with all sulfonephthalein indicators because they do not dissolve to sufficiently buffer the solution. In addition, the indicators are not very pure and may be reduced in the presence of hydrogen (Bates, 1970).
[32] molar absorptivity values are also required for this calculation.

68

more robust version of this approach involves preparing a number of buffered solutions of differing pH, measuring absorbance spectra on each solution, and using this overdetermined set of data to solve for a 'best-fit' K_I. Alternatively, Breland and Byrne (1993) calculated [H^+] directly from masses of HCl added to an indicator solution. The most obvious buffer system for BCG is acetic acid-sodium acetate. Values of K_a' for acetic acid in 0.70 M NaCl at 25°C were reported by Harned and Owen (1958) and Kilpatrick and Eanes (1953). Agreement of these values is ~0.006 pK units. Yamazaki et al. (1992a, 1992b) used the acetic acid buffer system at several pH values to measure K_I' of BCG at varying ionic strengths. Because Yamazaki et al. used a different ionic media (potassium nitrate), focusing mostly on resolving the trend in I, we were reluctant to use the pK_I' values reported by them. Furthermore, Yamazaki et al. were unable to achieve agreement better than 0.01 between calculated pH and pH measured by an electrode, calibrated using acetate buffers. The resulting uncertainty in the pK_I' of BCG, measured in an acetic acid-sodium acetate buffer is therefore around 0.01; due to the uncertainty in acetic acid pK_a' and the uncertainty in pH of a mixture of BCG and acetic acid-sodium acetate. In conclusion, it seems that several researchers have measured the pK_I' for BCG with much higher precision than accuracy but a thorough, systematic study of this equilibrium constant in seawater media has not been reported. To achieve the desired accuracy, TMT requires a pK_a accurate to ~0.001 (see Section 2.3.1), but, as described above, indicator pK_a determinations are typically accurate to ~0.01. Consequently, high accuracy (~2 μmol kg-soln^{-1}) seawater A_T measurement by TMT will require a slight adjustment to the indicator pK_a, based on preliminary CRM titrations.

3.6 Titrant Acy

Accuracy ultimately depends upon the titrant concentration, Acy. As pointed out earlier, Acy is the *acidity* of the titrant, due to both the HCl and the indicator in the mixture. We used Na_2CO_3 as the primary standard for assigning Acy. The reliability of this procedure is thus only as accurate as the purities of the standard and any salt added to the standard solution and the accuracy with which solutions are prepared. Because there may be impurities, as an independent verification with another primary standard, NaOH in NaCl (~ 0.2 m, $I = 0.7$ m) was standardized against potassium hydrogen phthalate in NaCl ($I = 0.7$ m) and used to titrate the a/i mixture with an electrode and highly accurate syringe pump. The strong acid and weak acid equivalence points were located using Gran's method (Pankow, 1991). The Fisher certificate of analysis for the NaCl lot used in this study reports a test value for free acid (as HCl % w/w) of 0.0020%, corresponding to 32 μmol H^+ per mol NaCl. This protic impurity could account for up to 23 μm error in Na_2CO_3 standards from the 0.7 m NaCl background. As shown below, with a blank correction for the NaOH standardization[33] and providing for a 25 μm acidic impurity in the NaCl used to prepare Na_2CO_3 standards, values of Acy agree.

As described by Pankow (1991), Gran plots are well suited for the titration of a mixture of strong and weak acid by strong base. The approach involves using data before, after or between equivalence points, but not at or near an equivalence point. A function is derived for each section of data, and plotted against the mass or volume of titrant added. In the case of a strong acid-weak acid mixture, there are four regions of the titration curve that could potentially generate a linear Gran function (Table 3.1). In Table 3.1, M_o is the mass of the sample, M_t is the mass of titrant added and M_s and M_w represent the mass of

---

[33] 0.7 m NaCl titrated with the standard NaOH gave 31 mol H^+/mol NaCl (a 22 μm acidic impurity)

titrant required to reach the strong acid and weak acid equivalence points, respectively. A plot of each function (column 1) vs. M_t over the range indicated (column 2), is linear and can be extrapolated to the point on the x-axis corresponding to either M_s or M_w. A NaOH titration of the HCl-BCG mixture (used to titrate TA) does not permit the use of F2 or F3 because, relative to HCl, the concentration of BCG is very small. The mass difference between M_s and M_t is therefore small making it difficult in practice to achieve a sufficient number of titration points in the region $M_s<M_t<M_w$ (see Table 3.1). We therefore used F1 to locate the HCl equivalence point and F4 to locate the HBCG equivalence point.

Table 3.1 Gran functions for the titration of a strong acid-weak acid mixture by strong base.

Function	Description
$F1=(M_o+M_t)10^{-pH}$	gives M_s, using data where $M_t<M_s$
$F2=(M_t-M_s)10^{-pH}$	gives M_w, using M_s obtained from F1 or F3 and data where $M_s<M_t<M_w$
$F3=(M_w-M_t)10^{pH}$	gives M_s, using M_w obtained from F2 or F4 and data where $M_s<M_t<M_w$
$F4=(M_o+M_t)10^{pH}$	gives M_w, using data where $M_t>M_w$

Before titrating the acid-indicator mixture for Acy, it was first necessary to standardize the strong base titrant. The NaOH-NaCl mixture[34] was prepared from ~30.35 g NaCl, ~8.3 g NaOH and ~ 1000 g H_2O to give [OH⁻] ~ 0.2 m and I = 0.700. Acidic standards were prepared from the primary standard potassium hydrogen phthalate (KHP) by weighing out ~4.3 g NaCl, ~0.3 g KHP and ~100 g H_2O. The concentration of NaOH in the titrant was carefully chosen so that the same syringe barrel (10 mL) could be used to titrate both KHP standards and acid-indicator titrant while, at the same time, allowing for appropriate amounts of both KHP and a/i to be weighed out with minimal analytical

---

[34] It is always important to hold ionic strength constant when using an electrode's response to generate a Gran plot.

error. As described in Appendix E, the syringe barrel was volume calibrated and the correction was applied to all Gran plots in this study. Figure 3.3 shows a typical electrode titration of KHP by OH^-. The NaOH standardization gave $[OH^-]_{std} = 0.18091$
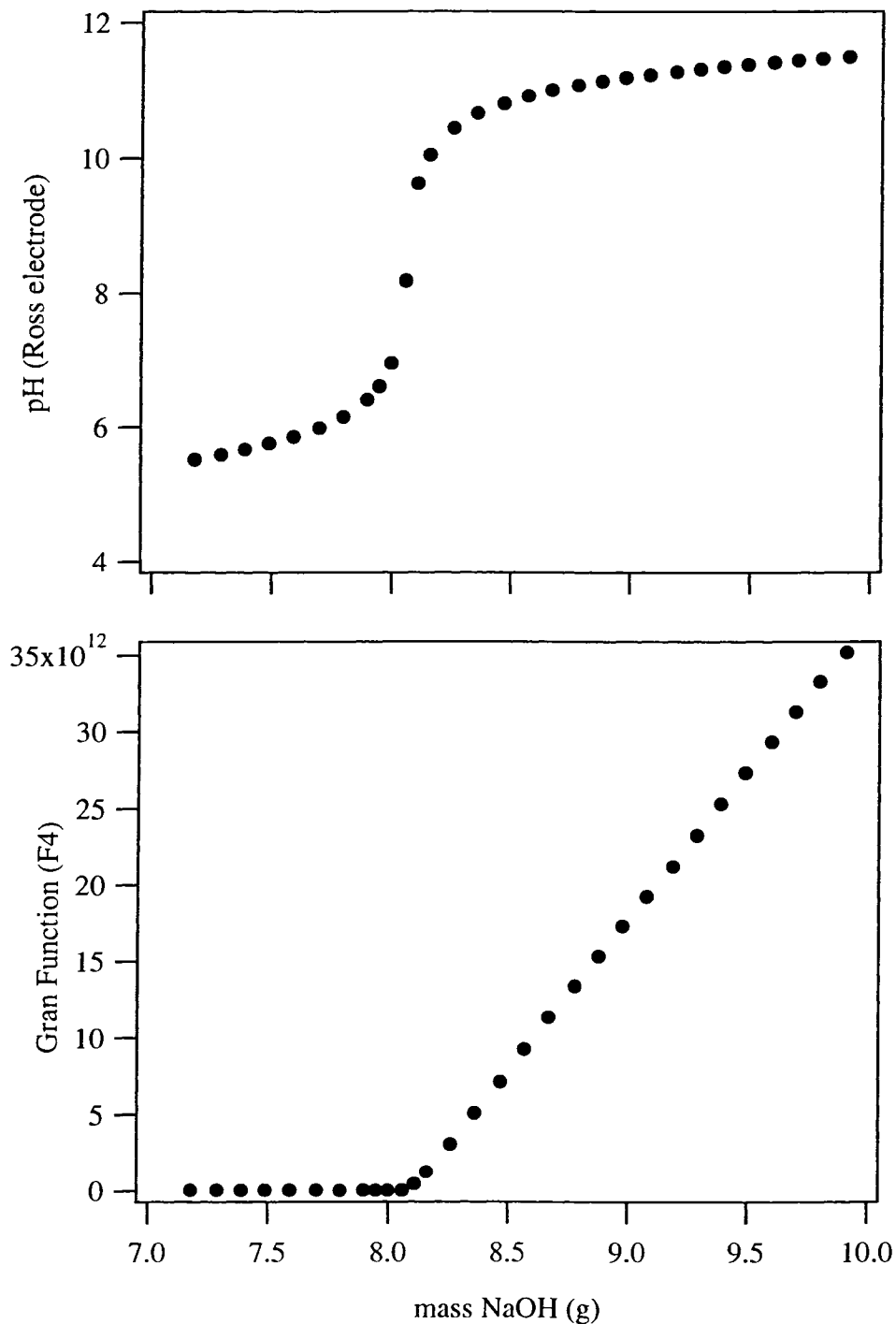
Figure 3.3 (Top) pH profile and (Bottom) Gran plot (F4, Table 3.1) for a KHP standard titrated by ~0.2 m NaOH.

72

±0.00016 m (n = 5), with a NaCl blank of +22 μm. As described above, this blank magnitude is in good agreement with the Fisher COA.

The acid-indicator mixture was titrated using the NaOH, standardized as described above. As shown in Figure 3.4, F4 deviates from linearity at high pH values leading to errors of up to ~100 μm and, for this reason, F4 was restricted to values where pH < 10.9. The nonlinearity is probably a characteristic of the electrode response (e.g. alkaline error). The NaOH titrations gave Acy = 2247±5 μm (n = 4), with HBCG = 121±7 μm and HCl = 2126±6 μm. The value for Acy is in close agreement with that obtained by Na_2CO_3 standardization of the titrant when the carbonate standard is corrected for the acidic impurity of a NaCl blank (Acy = 2244 μm). The indicator concentration, however, is overestimated by ~60 μm. One possibility for this inconsistency is the fact that monoprotonated BCG is in equilibrium with both I^{2-} and, to some extent, H_2I (Figure 3.4, pH < 3). These reactions go against the Gran Function F1 assumption that $[H^+]$ increases linearly with each titrant addition.

As mentioned above, F2 and F3 are potentially useful in the calculation of other values such as the indicator's equilibrium constant. A full analysis of all four Gran functions[35] also allows calculation of the NaOH titrant concentration (the F1 slope), the weak acid (BCG) apparent equilibrium constant (the F2 slope and the reciprocal of the F3 slope), and K_w' (titrant concentration divided by the F4 slope). The data shown in Figure 3.4 were obtained using 0.1 g titrant additions. At this resolution, two points were usually obtained in the region where $M_s<M_t<M_w$ and F2 and F3 are therefore not shown

---

[35] It should be pointed out that the Gran functions are not entirely independent of each other. As such, the values derived for a particular parameter may not necessarily be considered independent measurements. For example, the strong acid ep must first be obtained using F1 or, alternatively F4 & F3 before F2 can be used to calculate the weak acid ep (see Table 3.1 and Pankow, 1991).

73
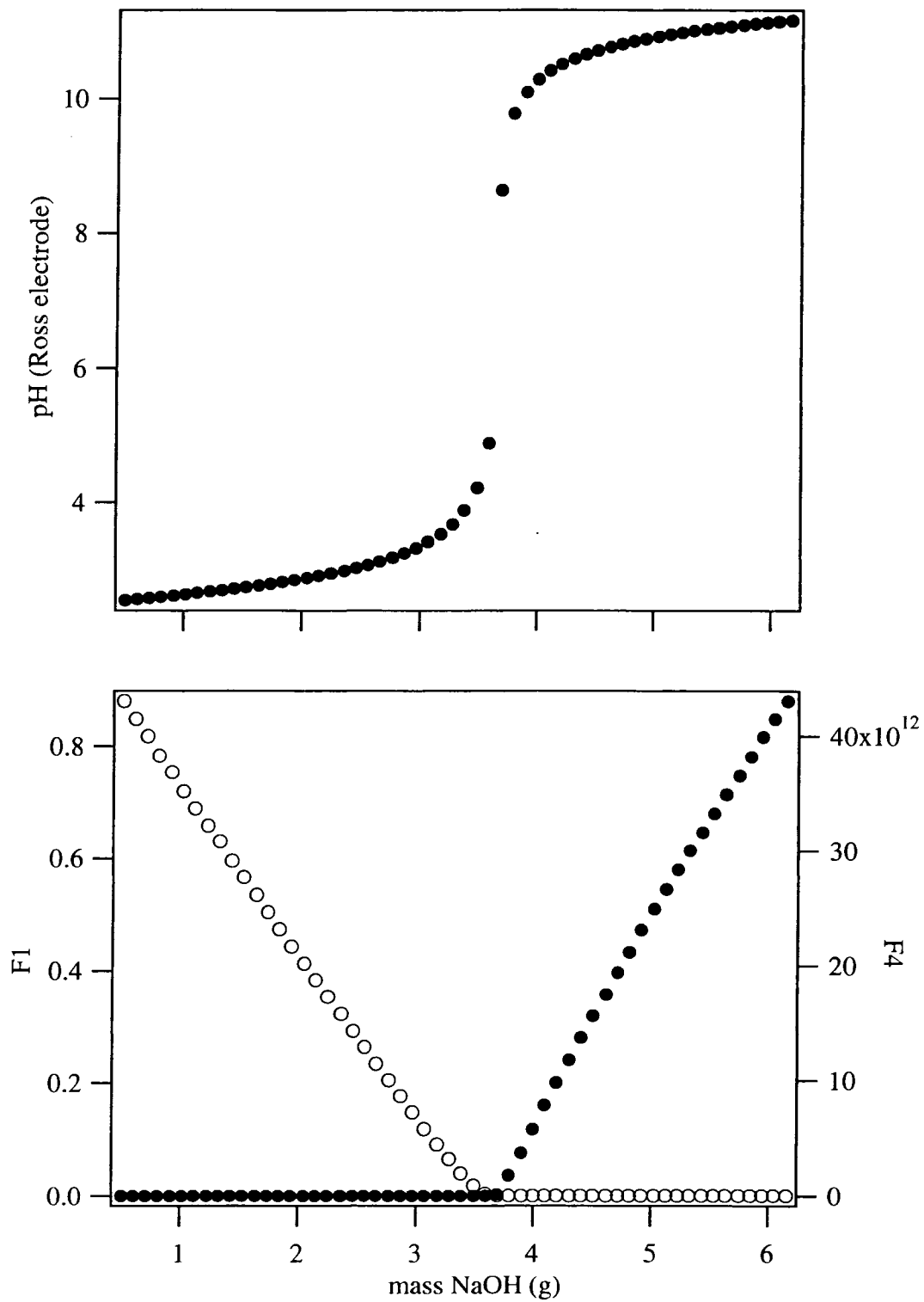
Figure 3.4 (Top) pH profile and (Bottom) Gran plots (F1, empty circles and F4, filled circles) for a titration of the acid-indicator by ~0.2 m NaOH.

74

in Figure 3.4. Increasing the number of points obtained for F2 and F3 from 2 to ~20 points could be accomplished by titrating an acidified solution of about 15-20 times greater indicator concentration (i.e. the saturation limit of an HI^- solution; $[I]_T \sim 0.001$ m). Decreasing the titrant step size will also increase the number of points, but titration time becomes impractical as step size passes below ~0.05 g.

3.7 Reference Absorbance

The absorbance value recorded at a nonabsorbing wavelength is commonly subtracted from the analytical absorbance. In many cases this procedure is perfectly valid. For example, small baseline shifts (both positive and negative) always result from removal and replacement of a sample cuvette in a conventional spectrophotometer. In flowing systems, baseline changes can result from air bubbles. As a correction for air bubbles, direct subtraction of a reference wavelength is somewhat questionable because there is a wavelength-dependent scattering at the air-water interface. Similarly, light source drift is not perfectly corrected using a reference absorbance (see Section A.2.1). Over the course of many different optical and flow design changes, it became apparent that every system used in this study exhibited a reproducible positive absorbance at the reference wavelength (i.e. > 740 nm). For example, a design similar to Figure 3.1 was used to obtain an absorbance profile of a titrant pulse, followed by alkaline sample flushing (Figure 3.5). It is clear from Figure 3.5 that the reference absorbance follows a reproducible trend. The 780 nm absorbance has a broad peak following the center of the a/i pulse (i.e. the HI^- form), as well as two distinct peaks aligned with the appearance of the I^{2-} form of indicator. Most peculiarly, the tail of the reference absorbance always takes several minutes to disappear, even after 99% of the a/i pulse is flushed out of the

75

flowcell. A stray light source of the reference absorbance is unlikely because the data

shown in Figure 3.5 were obtained using dual bandpass filters to reduce off-band

radiation to a very small quantity[36]. Absorbance from a changing concentration of H_2O

(H_2O weakly absorbs light at 780 nm) due to pH changes is not responsible for reference

absorbance. This was verified by performing the exact same experiment as shown in

Figure 3.5, in the absence of indicator. During the indicator-free titration, all three

absorbance channels remained stable within ±0.0002 au.
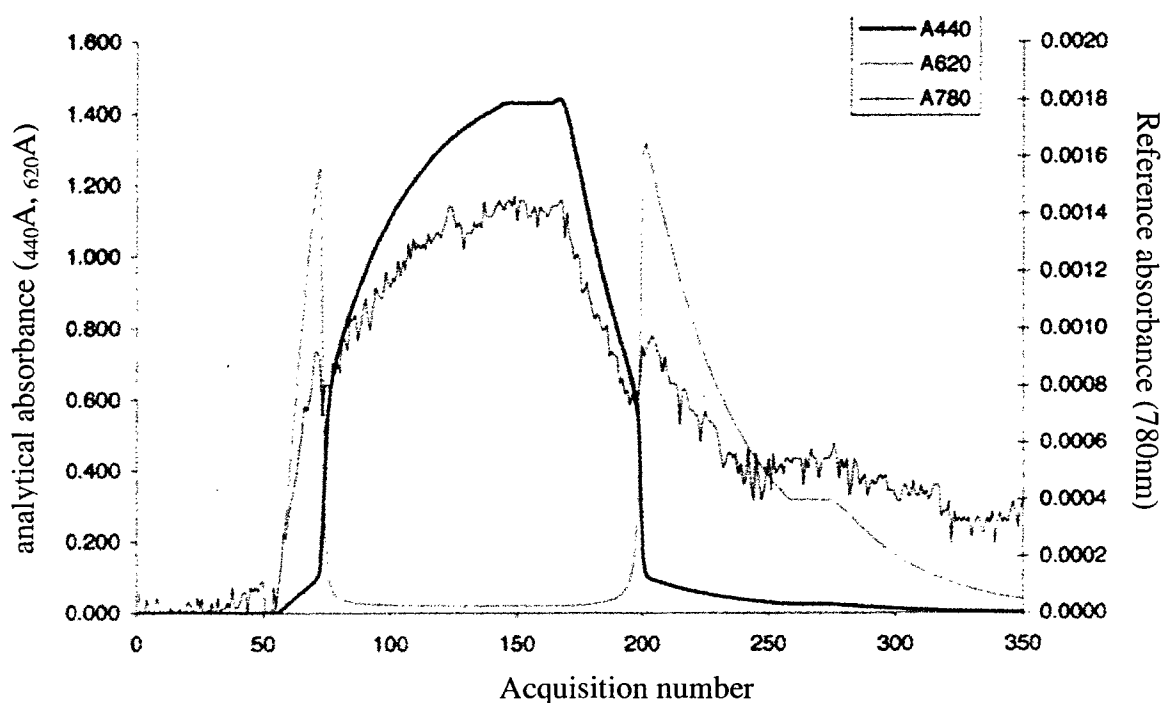
Figure 3.5 Absorbance profiles as acid/indicator is flushed into the stirred flow cell filled with alkaline sample, then flushed out by the subsequent alkaline sample. Flat regions at ~150 and 260 are where the Kloehn pump aspirated a full syringe volume. Total time was ~8 minutes. The light source was a warm white STAR LED (Section A.2.1.2).

A CCD array (Ocean Optics USB2000; Section A.4.3) and diode array (Agilent

8453; Section A.4.4) spectrophotometers were used to investigate the reference

---

[36] If stray light is the culprit of this reference absorbance, it must be a combination of a broad range of wavelengths because $_{780}A$ shows trends of both 440 nm and 620 nm light.

76

absorbance in more detail[37]. Because source drift of a similar magnitude is commonly encountered, it was imperative to let each spectrophotometer lamp warm up for >1 hour and frequently monitor blank absorbance drift thereafter.

We first attempted to verify the data in Figure 3.5 using a tungsten lamp and CCD array monitoring 444, 616, and 780 nm. The LED was replaced by a tungsten lamp to improve s:n at 780 nm on the CCD array (see Figure A.41). Using the CCD array, Figure 3.5 was verified. This finding further suggests that the reference absorbance is not due to stray light. Figure 3.5 was once again verified after placing a 780 nm bandpass filter in line with the return fiber optic leading to the CCD array. With the 780 nm filter in line with the CCD array, the CCD dark signal count at every channel outside the range 770-790 nm equaled the blank signal count (i.e. there was zero detectable stray light using this setup). Figure 3.5 was also reproduced at low (I = 0.004) and high (I = 0.7; NaCl) ionic strength. Finally, the Figure 3.5 experiment was carried out several times, monitoring wavelengths > 780 nm and it was found that the entire non-absorbing baseline (750-900 nm) has a similar positive peak when the a/i pulse passes through the stirred flowcell. Finally, we returned to the original interference filter-based design, replacing the dual 780 bp filters with dual 900 nm bp filters and, once again, reconfirmed Figure 3.5.

Baseline absorbance was also inspected on the diode array. Using a 1 cm glass cuvette, the absorbance of several acidified indicator solutions was measured (Table 3.2). A comparison of experiments 1 and 2 proves that the reference absorbance is not due to the tail region of the I^{2-} spectrum (λ_{max} 616 nm). Although I^{2-} is present in a small amount at pH ~ 2.4 (experiment 1) and decreasing concentrations of a/i exhibit a linear

---

[37] Although the Cary 300 was the most stable spectrophotometer available (because of its double beam design), it is not capable of resolving change of <0.001 au in the spectrum past about 740 nm, because its photomultiplier tube is less sensitive in this region, giving it a noise of ±0.001 or greater in the NIR.

$(r^2 = 0.999)$ relationship in reference absorbance (experiments 1a-1c) at pH ~ 10

(experiment 2), where the I^{2-} peak is many times greater than at low pH (experiment 1),

$_{800}A$ is several times lower. It appears from experiments 1 and 2 that $_{800}A$ increases with

increasing indicator concentration, but this apparent dependence upon $[I]_T$ is not present

when the pH is further decreased, as seen in experiment 3. Instead, the absorbance is

quite constant over a range of concentrations. Decreasing pH to 0.0 results in, perhaps, a

slight increase in $_{800}A$ (Experiment 4). The slightly higher $_{444}A$ for the most acidic

sample may be due to a change in refractive index, η, of the solution (compare

Experiments 3a and 4). The presence of H_2I in the more acidic sample might also be

responsible, but similar experiments with better matched ionic strengths showed

Table 3.2 Concentrations, pH, and absorbance measurements of indicator solutions at varying concentrations and pH. Columns 2 and 3 are calculated from solution preparation data; columns 4-6 were measured on the HP 8453 diode array. These measurements were designed to investigate the reference absorbance ($\lambda > 750$ nm) anomaly. exp = experiment; NR = not recorded. Concentrations (column 2) are in μm.

exp	$[I]_T;[HI^-];[I^{2-}]$	pH	$_{444}A$	$_{616}A$	$_{800}A$
1a	70.0;69.4;0.6	2.4	1.5454	NR	0.0029
1b	35.0;34.7;0.3	2.4	0.6696	NR	0.0011
1c	18.0;17.4;0.1	2.4	0.3218	NR	0.0001
2a	23.2;0.0;23.2	10.1	0.0925	1.0806	0.0007
2b	13.8;0.0;13.8	10.1	0.0541	0.6472	0.0004
2c	8.5;0.0;8.5	10.1	0.0337	0.3993	0.0003
3a	52.8;52.6;0.2	1.9	1.1162	0.0117	0.0015
3b	38.4;38.3;0.1	1.9	0.8137	0.0090	0.0015
3c	29.1;29.1;0.0	1.9	0.6042	0.0068	0.0016
4	50.4;50.4;0.0	0.0	1.3717	0.0054	0.0019
5	39.4;39.4;0.0	1.8	0.8569	0.0033	0.0003

conflicting results (see Section C.1). With further acidification, absorbance from H_2I is

expected to appear at pH < 0, but this involves a significant departure from the ionic

strengths expected in this work and was not explored. One last experiment is shown in

78

Table 3.2 (#5), in which the acidified indicator was prepared in a solution of 10%

methanol. Interestingly, in the presence of methanol, $_{800}A$ is diminished to nearly zero. It

was subsequently observed that $_{800}A$ of a 10% methanol solution did in fact exhibit a

slow, positive drift at a rate of 0.0002 au min^{-1}, settling to ~ +0.001 after 3-4 minutes. It

is commonly known that sulphonephthalein indicators are more soluble in methanol than

water, and that the order of increasing indicator solubility is generally $H_2I < HI^- < I^{2-}$

(Kolthoff, 1937). Qualitative studies were carried out in which a cuvette was allowed to

stand with an acidic or basic solution of indicator for several minutes, then emptied and

thoroughly washed with deionized water. Next, methanol was added to the cuvette and

absorbance was monitored for several minutes. When basic solutions were tested, the

baseline remained very stable over this period. On the contrary, acidic tests revealed a

slowly growing spectrum with peaks centered at 444 and 616 nm.

Based all of the evidence described above, it is hypothesized that the reference

absorbance is due to indicator adsorbed on the glass surface of both cuvette and fiber

optic and that the optical properties of adsorbed indicator retain a certain degree of pH

dependence. Further, there is a kinetic control on the adsorption, which is dependent on

the nature of the solvent[38].

Based on the Fresnel equation, a larger difference in η leads to more reflective

loss (Ingle and Crouch, 1988). Adsorption of a sulfonephthalein molecule is expected to

increase η_{glass} at the two liquid-glass interfaces inside the flow cell. Since η_{fiber} (~1.5) >

$\eta_{saltwater}$ (~1.3398), reflective loss should increase with adsorption and appear as a positive

optical absorbance. Based on the set of Fresnel equations for this optical system, the

---

[38] This statement is based on two observations: 1) the lingering reference absorbance described above for
Figure 3.5 and 2) time-dependent drift in reference absorbance for the acidic indicator in 10% methanol
solution (see text).

79

reference absorbance (Figure 3.5) is equivalent to an increase in η_{glass} of 0.042 and 0.029 in acidic and basic solutions, respectively. The evidence presented here does not necessarily apply to sulphonephthalein indicators in general, especially those that operate at a high pH. Nonetheless, researchers conducting high precision pH measurements with indicators should be aware of this issue.

The reference absorbance over the absorbance range used to calculate titrations is ~ 0.0005. This value significantly contributes to the accuracy of the measurement (±20 μm), but precision is not affected because the reference absorbance is very reproducible. In practice, the correction for this effect is lumped into the titrant standardization (Section 3.6).

3.8 Titrations

All titrations were carried out with the water bath set to 22.0°C. A titration begins with a ~110 mL flush of the alkaline sample. After a blank (100%T) reading is obtained from this solution, the 8 μL titrant pump delivers a pretitration volume (~1.5 mL in 90 sec with 0.5 sec pulses) to move the titration closer to the equivalence point. The microcomputer constantly monitors absorbance and spectrophotometric pH, comparing real-time values with preset limits for the remainder of the titration. Next, titrant is added in medium increments (~150 μL in 10 sec with 0.5 sec pulses) to save time while reducing the pH to ~6. Titrant is then added in single 8 μL increments with a 0.5 sec pause for stirring and a data point is recorded for each addition. The titrations are not dependent on the exact volume delivered, but small volume increments are required to obtain enough titration points for the NLLS calculation. When the solution in the mixing

chamber reaches pH = 3.5, data acquisition stops and the 250 μL sample pump begins the next flush. The sample flush and titration require 14 and 2.5 minutes, respectively.

We evaluated accuracy and precision with the high salinity alkaline standards described above (Section 3.1). The titration data were imported into Excel for filtering and calculation of TA. The absorbance data are filtered according to preset limits on reference absorbance (i.e. optical blank), analytical absorbance range, pH range and magnitude of the residual value. The first filter removes any point where $_{780}A > 0.0015$. Then all data are removed that fall outside of the range $3.5 < pH < 3.8$ and $0.1 < A < 1.0$. TA is then calculated from the resulting set of residuals. If any point's squared residual value exceeds 2.5×10^{-11} (corresponding to a residual error of 5 μm) the point is deleted. With these points removed, TA is recalculated. If, after the recalculation, $\Sigma residual^2 > 7 \times 10^{-10}$ then the entire titration is rejected. The $\Sigma residual^2$ limit is obtained using the theoretical model (Section 2.3) in combination with experimental observation. Several iterations using random absorbance noise at both optical channels show that as absorbance approaches ± 0.0012, $\Sigma residual^2$ approaches 3.5×10^{-10} (Figure 2.7). Because it is common to observe a few residual outliers per titration, or slight residual nonlinearities (see Section 4.3, below), the number 7×10^{-10} was selected as an acceptable upper limit for the sum of squared residuals from 25-30 titration points. Manual rejection of titration data was always avoided to retain the automated nature of the system.

81

Chapter 4 Results and Discussion of Tracer Monitored Titrations

This chapter presents the results of the measurements described in Chapter 3, and

briefly summarizes a few similar experiments that were not discussed in Chapter 3,

including results from previous prototype designs (Section 4.4.1) and the validity of

temperature corrections (end of Section 4.4.2).

4.1 Absorbance Precision and Stability

Absorbance reproducibility is controlled by absorbance noise and absorbance

drift. Before titrating samples, the optical system's absorbance reproducibility was

evaluated by recording replicate absorbance measurements on an indicator solution. This

step served to verify that precise values of εb and absorbance could be obtained and that

pathlength did not change with time. Absorbance reproducibility was tested by running

full system flushes of a blank (0.7 m NaCl) and an I^{2-} solution (19 μm I^{2-}, pH = 10.6, 0.7

m NaCl) repeatedly back-to-back. The flush time leads to approximately 14 minutes in

between recording blank and sample. Figure 4.1 shows that the stability of replicate

absorbance measurements is around ±0.0003 a.u. at 0.7 a.u. (RSD = 0.04%; n = 34).

Based on our model predictions (Figure 2.7), 0.04% a.u. precision leads to 0.024% (0.6

μm) TA precision, which is adequate for seawater TA analysis. The range of absorbance

in Figure 4.1 (~0.001 or ~3σ) corresponds to about 10 μm.
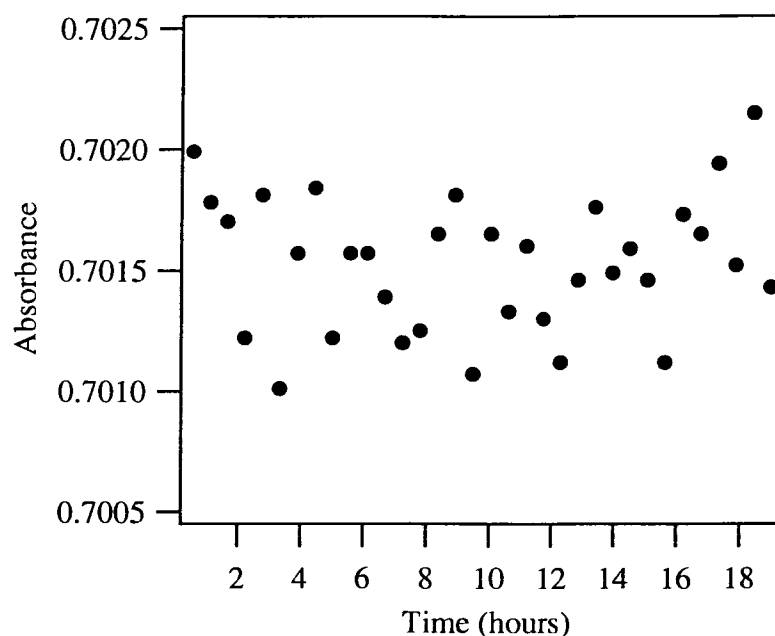
Figure 4.1 Absorbance precision and stability of the optical detection system (Figure 3.1). Absorbance reproducibility was tested by running full system flushes of a blank (0.7 m NaCl) and an I^{2-} solution (19 μm I^{2-}, pH = 10.6, 0.7 m NaCl) repeatedly back-to-back for ~19 hours. A complete flush of the flowcell takes approximately 14 minutes; leading to 28 minutes per absorbance measurement (blank followed by sample). The 1σ measurement precision of the instrument is ±0.0003 (n = 34) at 620 nm when A = 0.7015 (RSD = 0.04%).

4.2 εb

The εb values were re-determined frequently because every time the cell is

disassembled, the pathlength changes. For comparative purposes, the set of εb values

used in the stirred flowcell titrations described in Section 3.8 are given here (Table 4.1).

Table 4.1 Bromocresol green temperature dependent εb values, εb(T), T in Celsius.

$_{620}\varepsilon_I = 36373 - 63.03(T-21.76)$
$_{440}\varepsilon_I = 2598 - 1.22(T-21.88)$
$_{620}\varepsilon_{HI} = 34$
$_{440}\varepsilon_{HI} = 15898 - 15.44(T-21.81)$

The temperature dependence of each εb is assumed to remain constant and was therefore

not re-determined each time the cell was disassembled. Based on a long-running number

83

of repeated εb measurements following various changes to the experimental design, some

of common changes observed in εb are summarized in Table 4.2.

Table 4.2 Experimental changes and their corresponding effects on εb.

experimental/design change	corresponding change in εb
repeated absorbance measurements on the same solution (i.e. for temperature dependence tests)	≤0.04%
different solutions from the same indicator stock solution (i.e. for accurate εb at a single temperature)	0.1%
prepare new indicator stock from same dye lot	0.3%
prepare new indicator stock from different dye lot	5%
flow cell disassembly-reassembly	1-10%
different flow cells	20% and up

4.3 Titration Data

Figure 4.2A shows the absorbance data collected during a single titration.

Indicator species (Figure 4.2B, right axis) are calculated using Equation 2.12. $[H^+]$

(Figure 4.2B left axis) is calculated from Equation 2.9. Carbonate species (Figure 4.2B

left axis) are calculated from the CO_2 equilibrium equations (Table 1.1), $[H^+]$, and C_T.

pH is also shown (Figure 4.2C) to illustrate the dynamic range of BCG. Following

Figure 4.2C, the first large pretitration pulse brings the titration solution to a pH of 6.0-

6.5. Since this is about 2 units higher than the pK_I' of BCG, the absorbance is high at

620 nm and low at 440 nm (Figure 4.2A). In fact, almost all of the 440 nm absorbance

just after the blank (data acquisition number < 20) is actually due to the I^{2-} form of BCG

which weakly absorbs at this wavelength (Figure 2.1). As titrant is added, the decreasing

pH reflects the increasing acidity of the mixture inside the flow cell. In Figure 4.2A and

4.2C the overlapping absorbance and pH range used to calculate TA is outlined in boxes.

pH limits typically determined the residual cutoff at both ends of the titration. After

filtering, absorbance and dilution factor ($f_{a/i}$) ranged from 0.12-0.58 a.u. and 0.40-0.60,

84
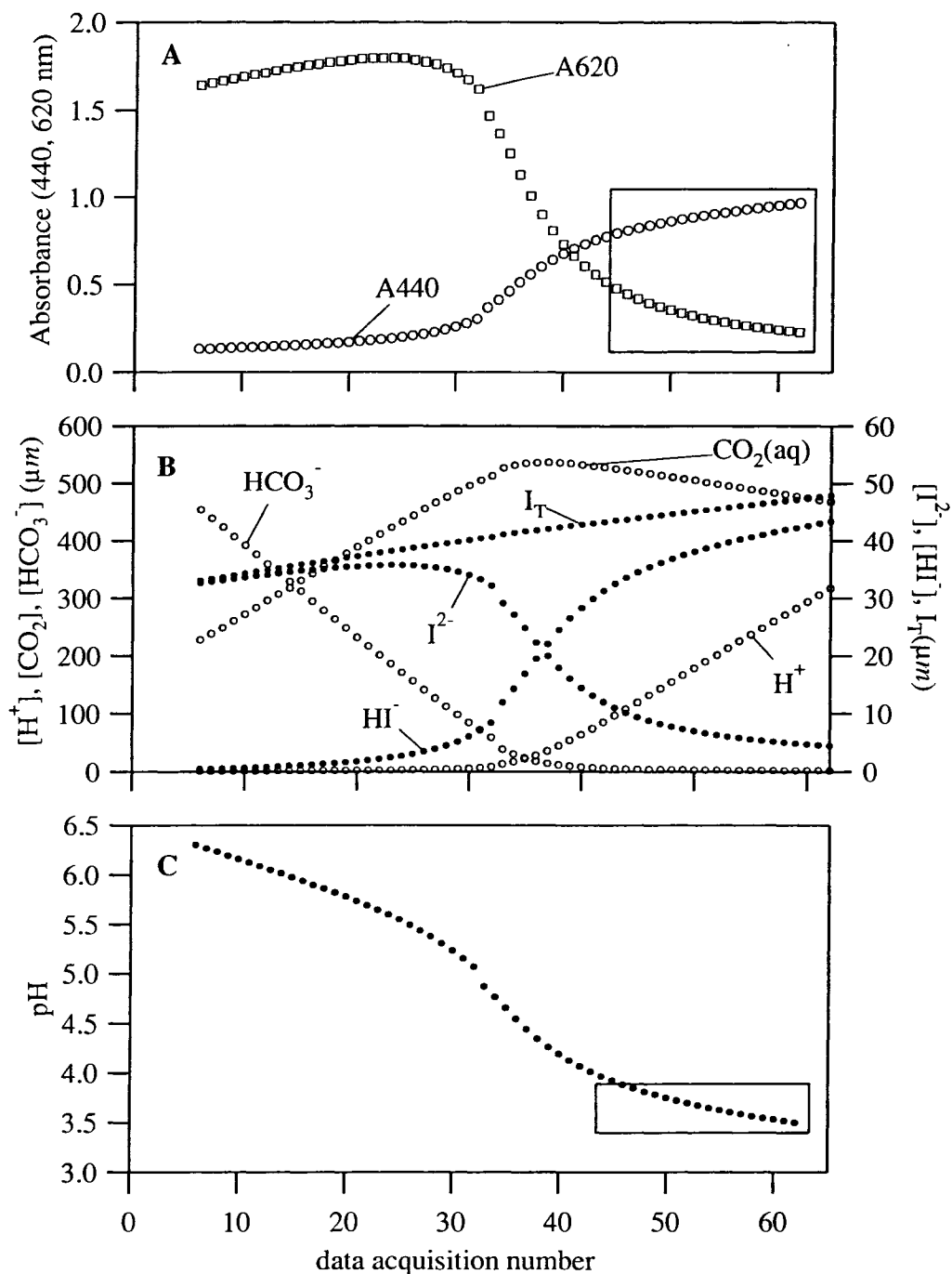
Figure 4.2 Measurement profiles for a single titration. (A) absorbance data are collected at analytical wavelengths of 440 nm and 620 nm, near the absorbance peaks of BCG. (B) Speciation of the titration is shown for all molecules or ions present in significant amounts. (C) pH calculated from absorbance data. Rectangles are drawn around the overlapping absorbance and pH ranges used to calculate TA. The first 5 points (not shown) are blank values. Each data acquisition is the set of measurements (absorbances and temperature) recorded following the addition of a/i.

respectively, depending on the sample TA. For example, when TA ~2000 μm, $_{440}A =$ 0.46-0.54, $_{620}A = 0.12$-0.21, $f_{a/i} = 0.40$-0.55; and when TA ~2500 μm, $_{440}A = 0.50$-0.58,

85

$_{620}A = 0.13\text{-}0.23$, $f_{a/i} = 0.46\text{-}0.60$. Figure 4.3 shows the residuals calculated using

Equation 2.7 for a single titration (Figure 4.2). The pH was restricted to a narrow range

because the residual set was not flat over the selected absorbances. The cause of the

residual trends at high and low pH is unclear (Figure 4.3). Nonlinear behavior at pH > 4.0

may be due to H_2CO_3 dehydration, while at pH < 3.5 may be due to spectrophotometer

absorbance limits. The section of residuals with least slope and values near zero

corresponds with the optimal overlap in absorbance and pH ranges (Figure 4.3, insert;

Figure 4.2, boxes).
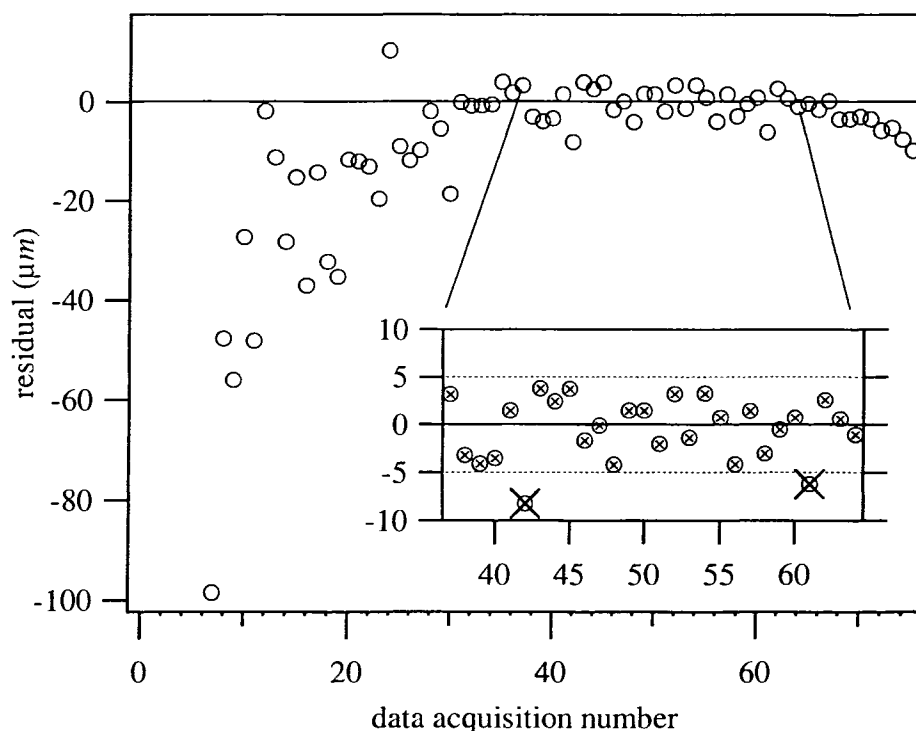
Figure 4.3 Residuals for a single titration calculated using Equation 2.7, as described in Section 2.2. The entire set (circles) was filtered to the overlapping range $3.5 < \text{pH} < 3.8$ and $0.1 < A < 1.0$ (circles with small $\times$, insert). Secondary filters reject points where $_{780}A > 0.005$ or residual$^2 > 2.5 \times 10^{-11}$ (circles with large $\times$, insert). A typical set of data is narrowed down from the initial 60-70 points to ~20 points. As sample TA increases, the absorbance range and pH range remain the same, but the dilution factor and hence total indicator concentration operate over different ranges (see text).

86

Residual outliers within the optimal pH and absorbance range are most likely due to air bubbles. Air bubbles in the flow cell are not identifiable directly from the analytical absorbance data, but rather, manifest through increased noise at the reference channel. The filtering described above typically resulted in less than 5 rejected measurement points for accepted titrations. Greater than 5 outliers (increased air bubbles) usually resulted in rejection of the analysis due to exceeding the $\Sigma residual^2$ limit. We found that adding backpressure at the cell outlet to eliminate air bubbles, while effective, resulted in impractical flush times.

4.4 Total Alkalinity Replicates: Accuracy and Precision

Below, a brief summary of past instrumental configurations is given, followed by a discussion of results from the working system shown in Figure 3.1.

4.4.1 Results from previous designs

The titration system described above (Figure 3.1) is the final version of many similar prototypes with varying components and configurations. Each system was first evaluated for titration reproducibility. Accuracy was therefore not a major concern in early stages of development, because high precision was extremely difficult to achieve. The original flow design consisted of a static mixing section[39] and conventional SAMI flow cell or a 4 µL z-cell (Ocean Optics). Figure 4.4 shows results from a typical set of flow cell titrations. It is clear from Figure 4.4, that both precision and accuracy of flow cell-based titrations are very poor. The data shown in Figure 4.4 represent the best performance achieved by static mixed flowcell titration. At the flow cell volumes (~4-20 µL) and mixing volumes (~0.5-10 mL) used in all of these studies, there is a color

---

[39] types of static (i.e. no moving parts) mixers tested include 1-10 m coils, 1-4 elbows (drilled out) and ASI™ mixers.
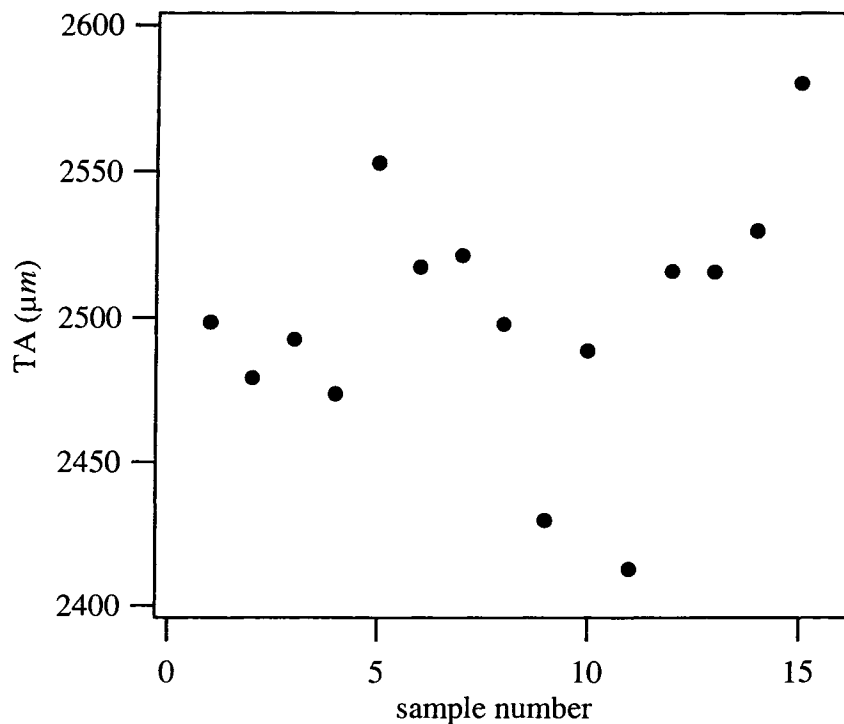
Figure 4.4 A series of titrations using a 4 µL z-cell (Ocean Optics). Precision is ~50 µ*m* with an accuracy error of ~300 µ*m*.

gradient in the flow cell, leading to substantial errors in Beer's Law calculations (Section 2.3). The best empirical evidence for this color gradient is the observation that residuals of apparently equal dilution factor disagree by up to 400 µ*m* (Figure 4.5). As seen in Figure 4.5, the curve of total indicator concentration and dilution factor is not calculated correctly as the large pH gradients (corresponding to equivalence points) pass through the flow cell. The absorbance profile appears as one would expect (see Figure 2.3), but large errors appear in the $[I]_T$ profile (Figure 4.5, bottom).

Because of the poor performance of static mixed flowcell titrations, we built a stirred optical cell. A Kloehn syringe pump(s) (Versa Pump 6; 5 & 10 mL syringes; 6-way distribution valve) was used in the initial testing of the active stirring design. One pump can control a complete titration (sample aspiration, sample dispense, titrant

88

aspiration, titrant dispense), but we also tried using two pumps to isolate titrant and

sample. A great advantage of a Kloehn pump is that,
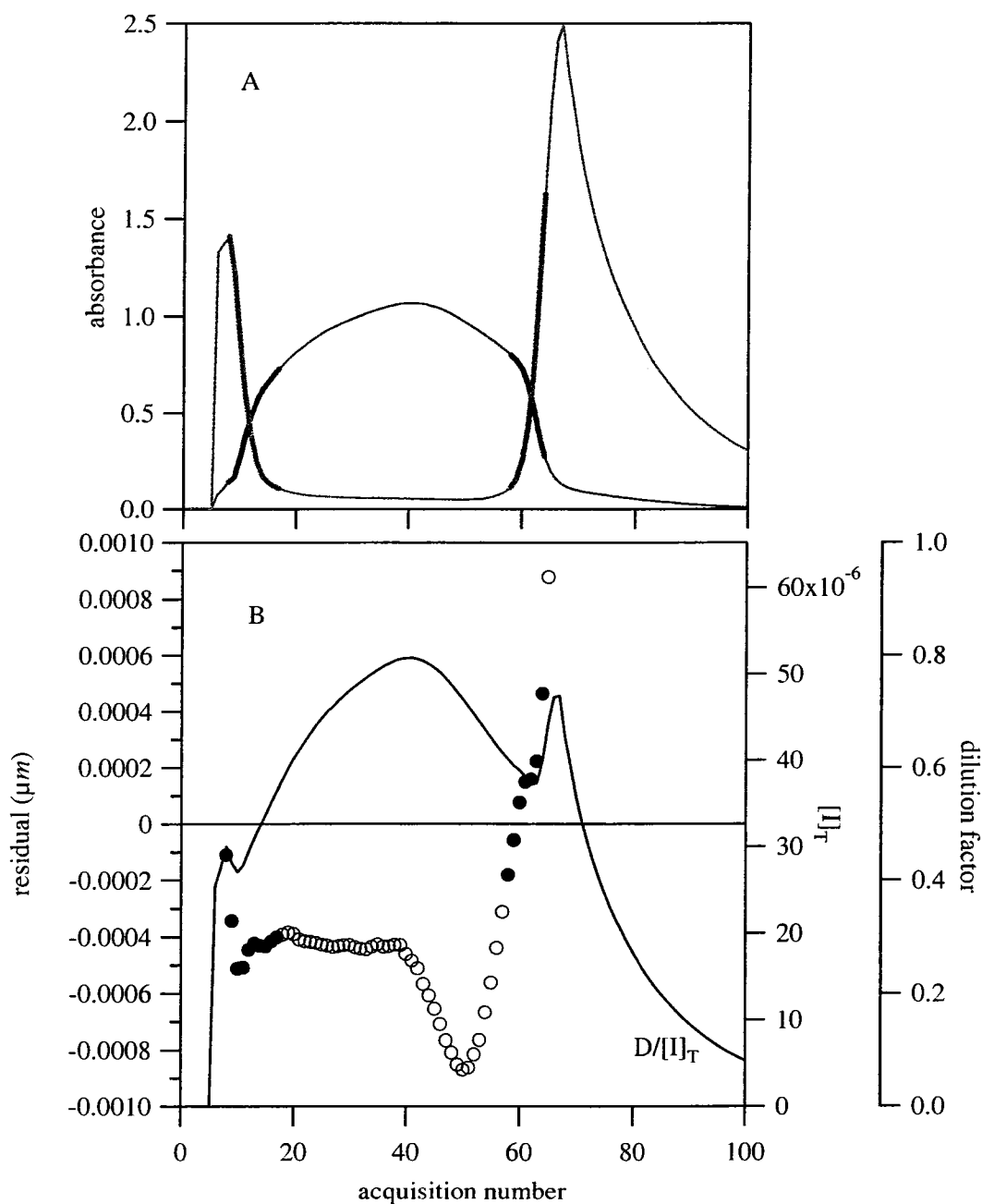
Figure 4.5 Data collected (A) and calculated (B) during a typical flow cell titration using a static mixer. (A) Absorbance is shown at 620 nm (red) and 440 nm (blue) for an entire flush of acid-indicator titrant in a flowing line of alkaline sample; bold sections are where 0.1<A<2.0. (B) total indicator and dilution factor (right axes, line) and residual (left axis, open circles) are calculated for every titration point; filled circles on bottom are the residuals corresponding to the bold sections on top.

89

during method development, nominal a/i dispense volume is easily altered. This allows

testing of parameters such as Acy:[I]$_{a/i}$, titration cell volume, and the number of titration

points collected within a specific pH range. As shown in Figure 4.6, the dual pump
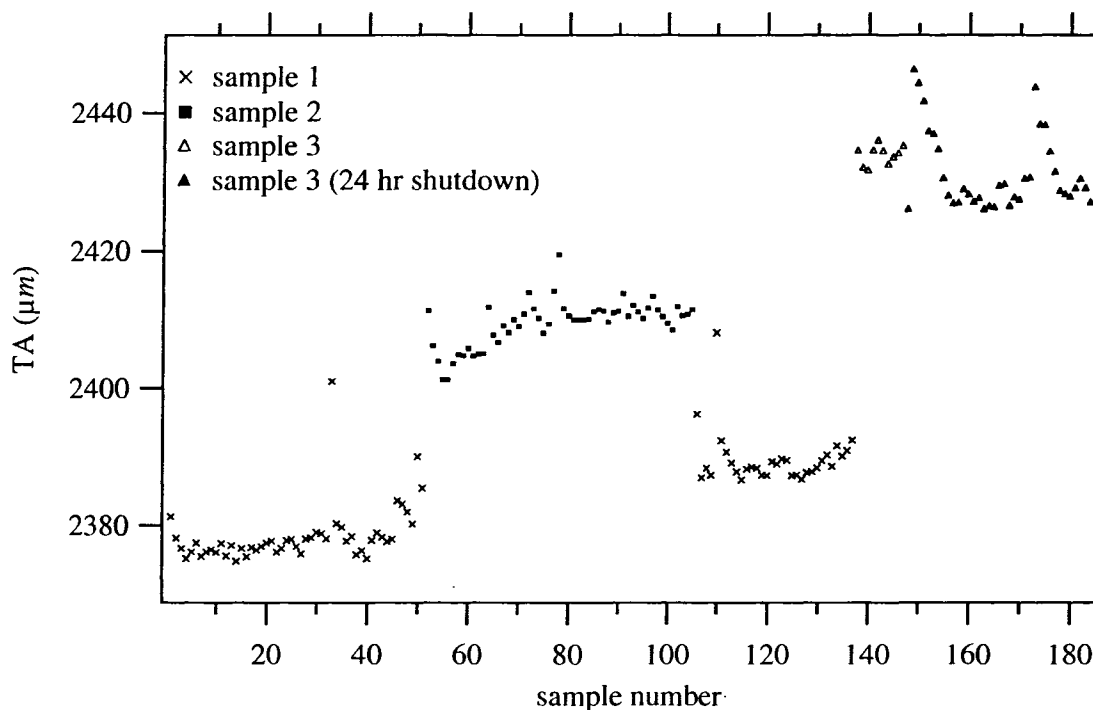
Figure 4.6 Results of stirred flow cell titrations when titrant and sample are propelled by a Kloehn pump. Three samples of different TA were titrated using separate Kloehn pumps for sample and titrant, in continuous mode, with a 24 hr system shutdown at sample 145.

configuration is, at times, capable of good precision, but suffers unpredictable drifts. The

general upward trend shown in Figure 4.6 is not a result of temperature or blank drift

(data not shown). Nor, is this trend a drift in the sample composition[40]. At sample 145,

the system was shut down for 24 hours. The lamp and water bath were turned on and

allowed to stabilize for an hour before sample 146. Upon close inspection under a weak

microscope, indicator crystals were observed on the inner surface of the syringe barrel

and Teflon plunger of the Kloehn pump. The acidified indicator in the titrant likely

---

[40] Na_2CO_3 standards are generally not stable for more than a week; their stability varying with the container material. For the SCD TC Tech bags used throughout this study, the TA rate of drift is estimated to be -1 μm day^{-1}.

90

adsorbs onto the *glass* syringe barrel[41] and is scraped off by the plunger. Over time, crystals build up and are periodically released causing drift and noise. Crystal formation may also alter the a/i composition by lowering $[I]_{a/i}$ while the titrant sits in the syringe. Attempts to flush the syringe between titrations by using a single pump for a/i and alkaline sample delivery resulted in similar, unpredictable drift. Other researchers working with sulfonephthalein dyes for seawater pH measurements also encountered this problem with Kloehn pumps (Husheer, 2001). Consequently, we replaced the Kloehn pumps with solenoid pumps (Biochem Inc.), which have inert wetted surfaces (PEEK and EDPM).

4.4.2 Results from the working prototype

Here, we present the titrations obtained using the apparatus shown in Figure 3.1. From the original set of 316 titrations, 37 were rejected because their $\Sigma residual^2$ value exceeded 7×10^{-10}. Table 4.3 and Figure 4.7 show the results of the remaining 279 titrations performed on 13 different samples. Eleven Na_2CO_3 standards ($I = 0.7$ m, NaCl) with ~50 μm increments over the range 2000-2500 μm were analyzed, encompassing the entire oceanic range of TA (Millero et al., 1998). A NaOH standard and seawater CRM were also titrated (see Section 2.1). Figure 4.8 shows the linearity of the instrumental response, along with 1σ error bars. Standard deviations for each sample ranged from $\pm 0.6_4$ to $\pm 2.7_4$ μm (Table 4.3, column 4). The TMT response is linear ($R^2 = 0.9999$) over the oceanic range of TA, and thus requires no manipulation of the response (e.g. calibration curve) beyond assigning pK_1', Acy and εb. Table 4.3 gives the measured and standard TA values for each solution. Based on the pooled standard deviation of these

---

[41] See also section 3.7.

Table 4.3 Results of 279 titrations on TA (units in μm) The pooled standard deviation for the entire set is 2.1 μm. CRM superscripts refer to the literature reference from which BCG pK_1' was taken: B-Byrne et al., 1988; BB-Breland and Byrne, 1993; KK-King and Kester, 1989.

Batch	n	measured average	sd	prep TA	error
$Na_2CO_3(1)$	28	1998.1	1.6_3	1989.3	+8.8
$Na_2CO_3(2)$	15	2044.8	0.6_4	2040.7	+4.1
$Na_2CO_3(3)$	25	2095.0	1.6_4	2093.7	+1.3
$Na_2CO_3(4)$	27	2150.1	2.2_9	2145.2	+4.9
$Na_2CO_3(5)$	29	2200.3	2.6_5	2195.5	+4.8
$Na_2CO_3(6)$	24	2252.4	1.7_6	2250.9	+1.5
$Na_2CO_3(7)$	24	2300.4	2.1_2	2301.4	-1.0
$Na_2CO_3(8)$	30	2353.3	2.2_5	2352.3	+1.0
$Na_2CO_3(9)$	19	2399.8	2.7_4	2401.4	-1.6
$Na_2CO_3(10)$	23	2453.4	1.6_4	2454.9	-1.5
$Na_2CO_3(11)$	26	2504.1	2.4_7	2507.3	-3.2
NaOH	7	2349.8	2.1_5	2347.4	+2.4
[B]CRM#68	2	2217.5	1.6_2	2233.7	-16.2
[BB]CRM#68	2	2227.8	1.8_4	2233.7	-5.9
[KK]CRM#68	2	2211.0	2.3_1	2233.7	+22.7

279 titrations, the 1σ precision is ± 2.1 μm (0.1%) and accuracy is ± 4.0 μm (~0.2%). The

sensitivity of the calculation to indicator pK_1' is shown by calculating three different TA

values for the CRM, using the three different literature values for the pK_1' described in

Section 3.5 (Table 4.3). The values calculated for the CRM span a TA range of ~40 μm.

As explained in Section 2.3.1, the extreme sensitivity to indicator pK_1' is a result of its

importance in the residual (Equation 2.7) where [H$^+$] is calculated using Equation 2.9.

The best agreement between the known CRM TA and our measurement is from the pK_1'

reported by Breland and Byrne (1993), but we expect that a new, determination-

calibration of this constant will be required before applying the method in a seawater

study (see Section 3.5).

92

TA (µm)

2550 — 2550
2500 — 2500
2450 — 2450
2400 — 2400
2350 — 2350
2300 — 2300
2250 — 2250
2200 — 2200
2150 — 2150
2100 — 2100
2050 — 2050
2000 — 2000
1950 — 1950

● Na₂CO₃ primary standard
△ NaOH secondary standard
○ CRM

0   40   80   120   160   200   240   280

titration number
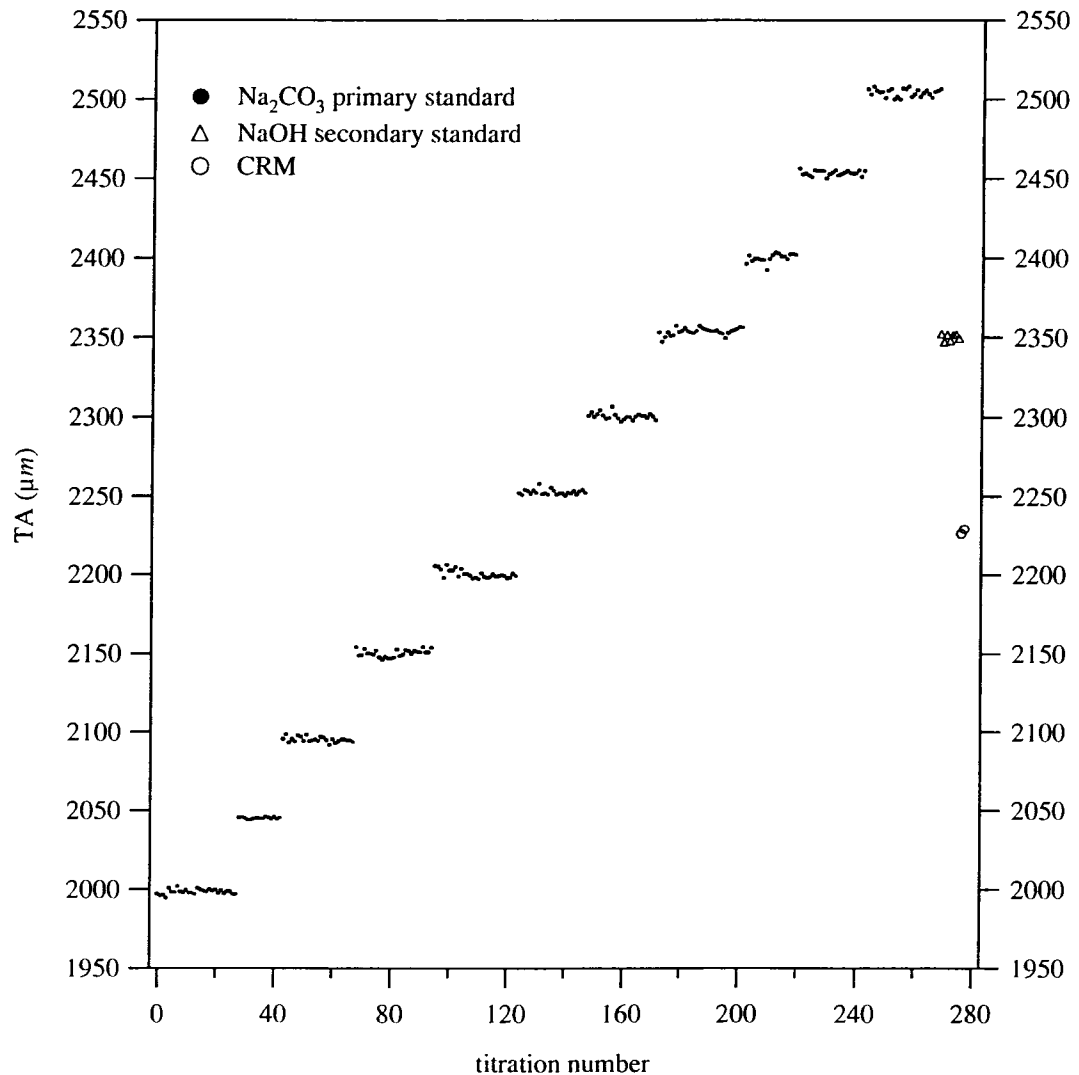
Figure 4.7 Results from 279 titrations spanning the range of observed seawater total alkalinity values. The primary standard Na₂CO₃ was used as the principal analyte in this study. A NaOH secondary standard was run to verify the accuracy. The method was also checked against a seawater certified reference material (CRM). Note that samples were not run in order of increasing or decreasing TA (see Figure 4.9B).

Figure 4.9 shows the errors between measured and standard TA values as a function of TA and time for the set of 279 titrations (Figures 4.7 and 4.8) plus an additional 7 titrations at day 42 (TA = 2283 µm) for a total of 286. The errors skew from positive to negative as TA increases (Figure 4.9A). The samples were not run in sequence of increasing or decreasing TA and Figure 4.9B shows that the trend is clearly

93
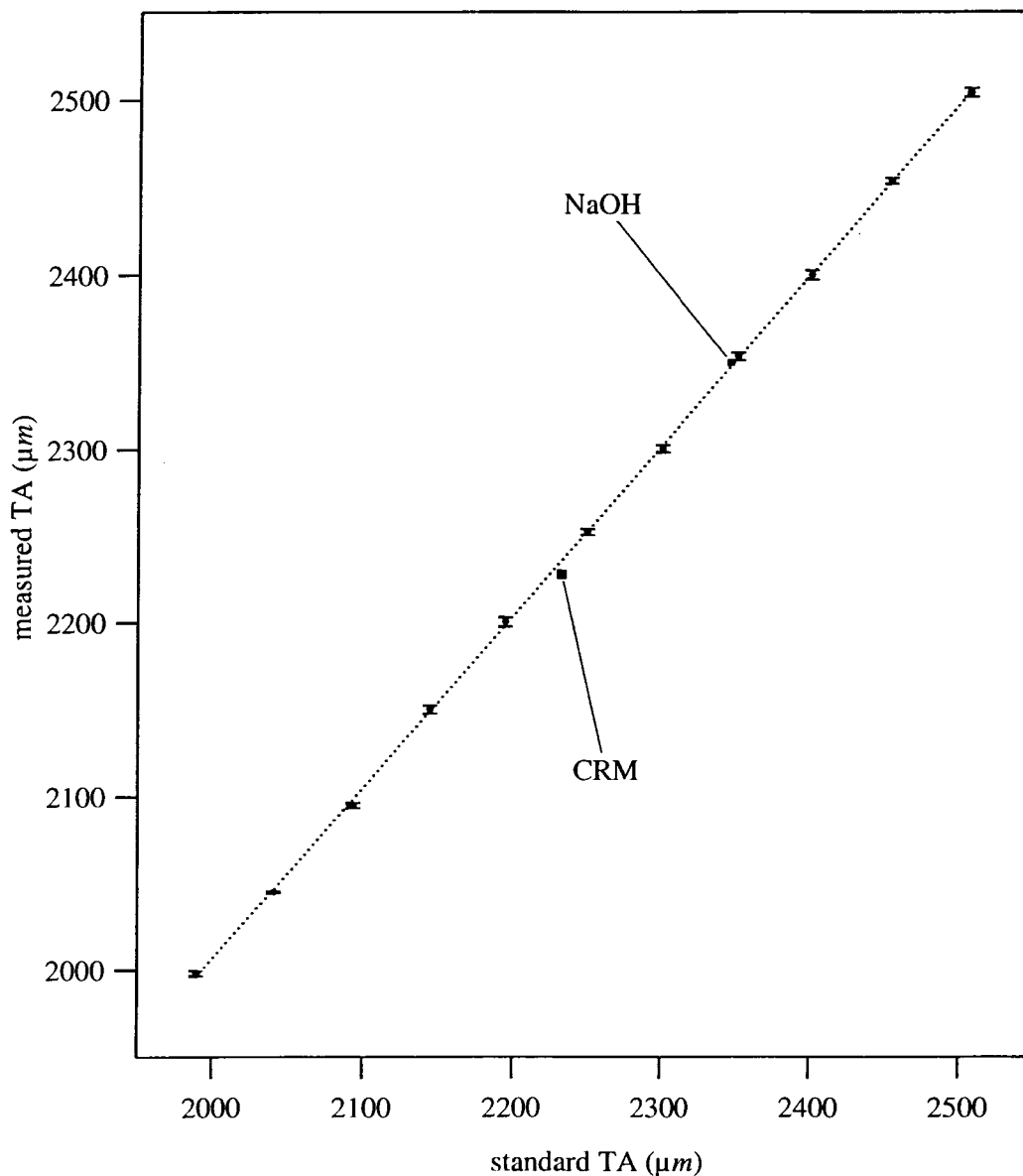
Figure 4.8 Results from Figure 4.7 averaged with errors show the linear response $(R^2 = 0.9999)$ of the TMT method. Standard TA is calculated from the solution preparation, as described in Section 3.1.

not due to a time-dependent drift. The negative trend is most likely due to a protic

impurity in the titrant because this effect should vary with TA. For data as plotted in

Figure 4.9A, acidic impurities would result in negative skewing and basic impurities

result in positive skewing as TA increases, according the model described in Section 2.3.

Because the titration operates at increasing dilution factors with increasing TA, a protic

94
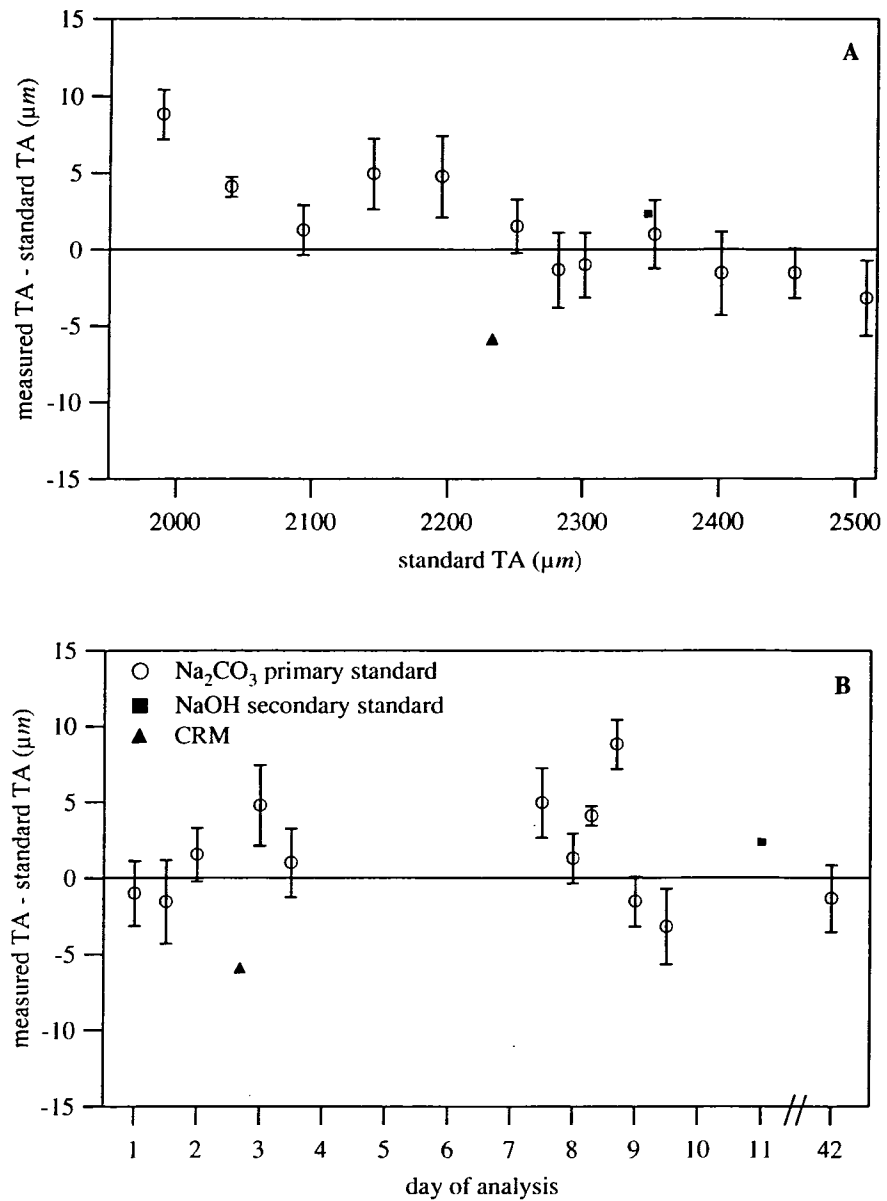
Figure 4.9 TA errors (from data in Figures 4.7 & 4.8) relative to (A) standard TA and (B) time of analysis. Error bars are shown for the carbonate standards. A Na_2CO_3 standard, freshly prepared and measured 42 days after the sampling began, shows that the system is extremely stable over long time periods without calibration (graph B).

impurity that causes $f_{a/i}$ to change will have a different effect at a different dilution factor, similar to a conventional titration with an error in the Acy value (see e.g. Section 1.5.3, Figure 1.4). Acy error on the order of 20 μm results in a similar trend, estimated using our model. The observed errors in Figure 4.9A are actually less than 20 μm because the

95

impurity was also present in the standards used to assign Acy (Section 3.6). As expected, the zero crossing shown in Figure 4.9A (~2250-2350 μm) corresponds closely with the solution used to assign Acy (Na_2CO_3 #7, 2301.4 μm). As mentioned in Section 3.6, independent measurement of Acy also revealed an acidic impurity in the NaCl of ~ 20 μmol kg-soln^{-1}. Another possible source of this error, although less likely, is a protic impurity in the ~10% w/w optically inactive fraction of the indicator.

For an estimate of TMT performance in the absence of the titrant impurity, we applied a correction of -1.9 μm per 100 μmol kg-soln^{-1} of TA to the data shown in Figure 4.9A. The corrected data (Figure 4.10) are randomly distributed about the zero line over

$$TA_{corrected} = TA_{measured} (1+0.0184)-43.1$$
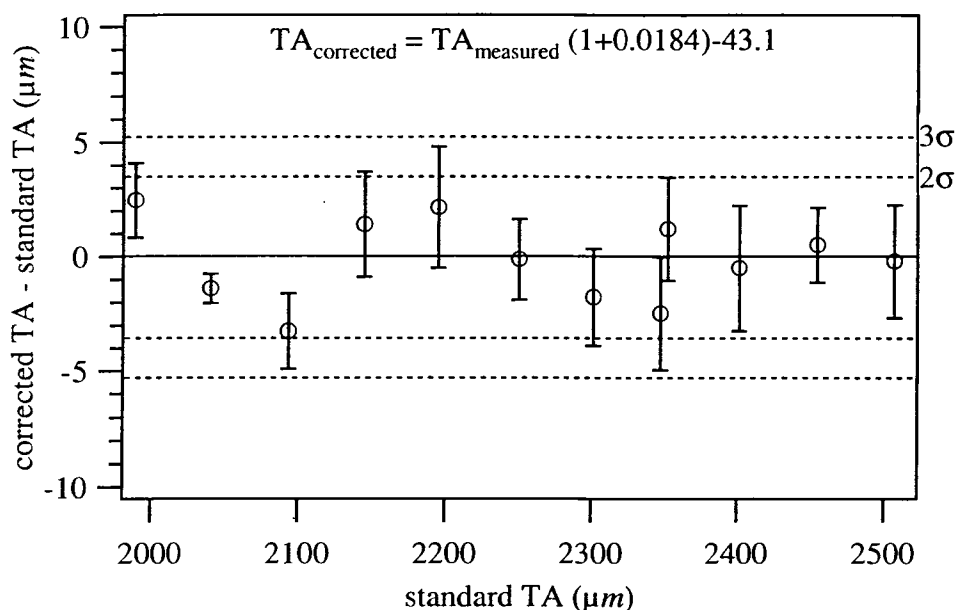
Figure 4.10 TA data corrected for the NaCl impurity. A linear regression ($r^2 = 0.8$) of the data in Figure 4.9A was used to apply the correction (equation shown in figure).

the range 2.5 to -3.3 with a standard deviation of 1.7 μmol kg-soln^{-1}. All 1σ error bars shown are greater than the 99% confidence intervals and all error bars fit into the 99.7% ($\pm 3\sigma$) probability distribution from the mean. With this correction, the measurements shown in Figure 4.8 are accurate to 0.1%. However, based on Figure 4.10, it is not

correct to claim that a single seawater titration would be accurate to 0.1% because the 99% confidence intervals for a single measurement are much greater than the 1σ error bars shown for the averaged data.

The system achieved excellent accuracy and precision over the 11 days that the initial samples were analyzed and exhibited no detectable drift after more than a month. As shown in Figure 4.9B, 42 days after the first sample analysis, a new Na_2CO_3 standard was measured with accuracy and precision of 0.06% and 0.10 %, respectively. All results were obtained with the same batch of titrant, without redetermination of εb or Acy, implying that the optical bandpass and pathlength are very stable. The absence of a time dependent drift also demonstrates that the titrant solution is chemically stable. Since the system is capable of fully automated drift-free operation (limited only by titrant consumption) the 10 L titrant bag used in this study could potentially titrate continuously for about five weeks, calibration-free, supplying over 3000 titrations on 16.5-minute intervals; or a little over four months at an hourly frequency.

In the approach to building an autonomous instrument, a few major issues stand out. For in situ operation, temperature cannot be thermostated, and can fluctuate by several degrees each day and by more than $10°C$, seasonally. The temperature dependence of each constant used in the residual calculation is known, and it is therefore possible to account for the effects of temperature on the thermochemical properties of the titration mixture. This aspect has been partially investigated in the laboratory (Figure 4.11). The 30 titrations shown in Figure 4.11A were carried out at three different water bath settings[42] (Figure 4.11B). For uncorrected values, the temperature used in the TA

---

[42] Flow cell temperature does not perfectly match the water bath because the ambient air influences the temperature of the flow cell. This effect is particularly evident as the water bath temperature becomes

97
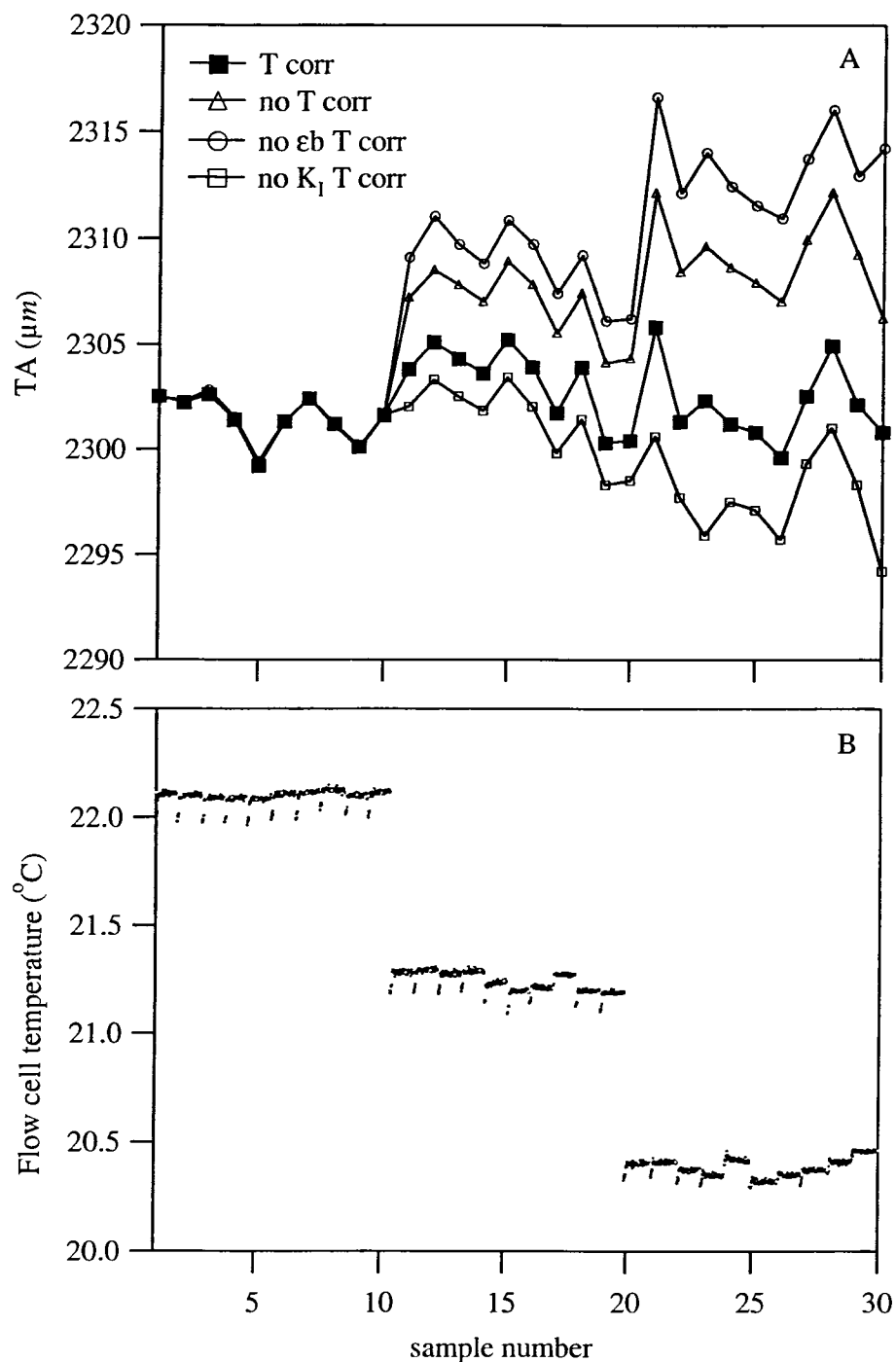
Figure 4.11 TMT performance under fluctuating temperature conditions. (A) 30 continuous titrations of a Na_2CO_3 standard; 1-10 at 22°; 11-20 at 21°; 21-30 at 20°). Filled squares are the data set calculated using temperature corrections as described in the text. Empty markers represent the same set of titrations, as calculated without the specified corrections. (B) a continuous record of temperature inside the flowcell during the titrations (temperature during flushing not shown). Downward spikes in temperature occur at the beginning of a titration when pretitration pulses begin.

significantly cooler or warmer than the air; i.e. room T was ~22°C, and points 20-30 sit 0.4-0.5° higher than the water bath, with considerably greater noise (Figure 4.10B).

98

calculation was held constant from the first titration point, hence the close agreement for all calculations of the first ten titrations. The corrected titration data (Figure 4.11, Top, filled squares) are very stable ($1\sigma = \pm1.7 \ \mu m$, n = 30) over the large ~2° temperature changes. As explained in Section 2.3.1, with no temperature correction, the errors due to K_I' and εb offset each other somewhat. This effect is apparent in Figure 4.11 where uncorrected titrations show less error than titrations corrected for K_I' temperature changes. Conversely, when only εb is corrected, the error is negative. These errors are summarized in Figure 4.12.
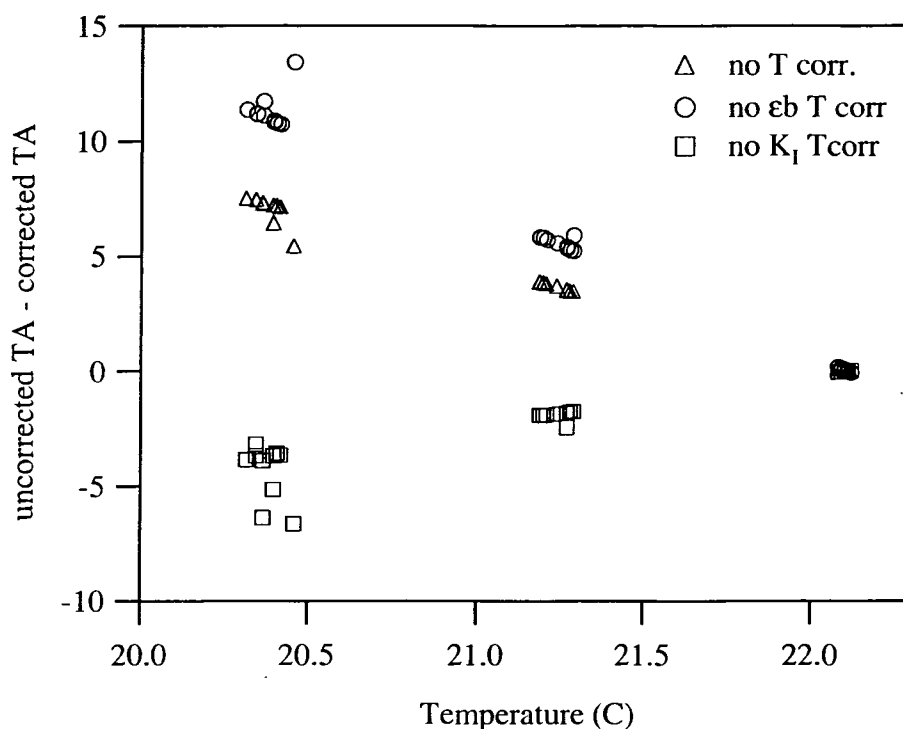
Figure 4.12. Temperature-induced errors in TA, from Figure 4.10. Error values were calculated by subtracting each of the three uncorrected data sets (Figure 4.10A, empty markers) from the corrected data set (Figure 4.10A, filled squares). The trends for no correction, no εb correction and no K_I' correction are -4.1, -6.5 and +2.5 μm °C^{-1}, respectively.

4.5 Conclusions

Using TMT we obtained highly precise and accurate, drift-free measurements with an automated titration system using low precision pumps. Rather than volume, mass

99

or flow reproducibility, the sample-to-sample reproducibility depends instead upon quality of absorbance measurements (precision and stability). This result is exciting because it offers a simplified approach to automated titrations. The accuracy and precision of the technique were established as ~0.2% and 0.1%, respectively for carbonate standards in the range 2000-2500 μm, corresponding to the observed ocean range of TA. The apparatus we built is fully automated, with sample throughput of about 90 day^{-1}. Sampling time is mostly limited by flushing of the flow cell, so it should be possible to apply TMT in higher speed titrations. As shown in Figure 1.1, the TMT TA analysis rivals the limits of existing techniques for seawater TA titration. Performance of better than 1 μm precision has been achieved in shore-based laboratories by both spectrophotometric (Yao and Byrne, 1998) and potentiometric (Dickson et al., 2003) procedures, but both require meticulous quantification of either volume or mass. At-sea precision of ±2 μm is unsurpassed.

Although ±2 in ~2300 μm (0.1%) can be considered ultrahigh precision for any titration, there remains some room for improvement in performance. Because flush time dictates the time between analyses, a more efficient flow design could easily triple the sample throughput. A static mixing design is better suited to unattended operation because it is lower power and requires fewer moving parts. Unfortunately, incorporating a static mixer into TMT is difficult because the method is highly dependent on Beer's law calculations, which are not valid across concentration gradients. Removal of CO_2(aq) in the acidified sample (e.g. by stripping with N_2) would make C_T ~ 0, eliminating errors in TA due to our estimation of C_T; but is an impractical complication of the system. Future

100

flow cells designed to minimize bubbles[43] should improve the precision. A diode array

spectrophotometer offers an alternative method of $[I]_T$ calculation, via the isosbestic

wavelength. The analytical wavelengths would also correspond closely with the peak

absorbance wavelengths (~1 nm), which would allow inter-comparison between different

instruments using the same type of diode array and pathlength and also allow direct

instrumental verifications such as wavelength and photometric accuracy.

Using theoretical corrections, TMT has proven to be very robust under large

temperature changes (Section 4.4.2). The other major issues for field deployments are

light source stability and power consumption. Because the goal of this research was a

proof-of-concept, power consumption is not addressed here. As shown above (e.g.

Figure 2.6), light source stability is crucial, but very difficult to achieve (see Section

A.2.1). The highly stable lamps used in this study were most important during single

absorbance measurements (ϵb characterization) because this involved full cell flushing

(i.e. 14 minutes between blank and sample). Because these measurements would be

carried out in the lab, prior to a field study, mooring-based titrations would require 2-3

minutes of very stable lamp performance. This level of stability would probably be

achievable if the lamp was left on continuously (even with changing ambient

temperatures), but the power draw of an uninterrupted tungsten lamp presents a problem.

Even the stabilized lamps used in this study (Section A.2.1) undergo significant warm-up

drifts. One promising alternative is optically stabilized LEDs. A simple LED-

---

[43] A debubbler can help minimize preexisting bubbles but CO_2 bubbles (from outgassing) are also a serious concern. The desorption rate of CO_2 in TMT is controlled by stirring speed, temperature and degree of supersaturation (Hikita and Konishi, 1984). Bubble formation, however, is also highly dependent on surface roughness, which dictates the number of nucleation sites (e.g. pits, scratches). It has been shown that hydrophobic surfaces (e.g. Delrin) produce a much greater abundance of bubbles than hydrophilic surfaces (e.g. glass), due to the differences in contact angles (the main control of bubble entrapment) of a liquid front traveling over the different materials (Hey et al., 1994).

101

photodiode design, developed by Anfalt and Graneli (1976) achieved good stability

(0.003 au) for long periods (hours) with varying temperature. Given the enormous

advances in semiconductor technology over the past 30 years, achieving optical stability

of < 0.0005 au for short periods of time using an LED-photodiode design should be a

matter of choosing the right components and putting them together.

Another important point is that TMT is not limited to acid-base systems and can

be generalized for use in other types of titrations. The tracer can be either an inert

chromophore or an indicator that also serves as the sensing mechanism for the titration.

In the latter, the primary requirement is that all forms of the indicator absorb light so total

indicator concentration may be observed at any point in the titration from the sum of the

different species (e.g. protonated + unprotonated; complexed + uncomplexed; reduced +

oxidized). Several redox indicators exhibit a color change from blue to red when

reduced. Many metal ion indicators have an absorbance spectrum in the visible region

for both the free indicator and the indicator-metal ion complex. For example, a titration

analogous to the one presented here could be accomplished by adding a quantitative

amount of Calmagite (a metal ion indicator with colored complexed and uncomplexed

forms) to standardized EDTA and titrating Ca^{2+}. TMT also extends beyond absorbance

spectrophotometry to fluorescence (provided that the excitation source remains constant

and low concentrations are used where concentrations are calculated directly from

fluorescence emission power (Skoog and Holler, 1998)) since indicators with two

fluorescing forms are commonly used in acid-base, redox, and metal ion titrations. If

using an inert tracer, an alternative method (e.g. electrode) for observations on the

equilibrium position of the titration would be required. In theory, a potentiometric

102

counterpart to TMT may even be possible, if ion selective electrodes could be used to

quantify the tracer species. We plan to test TMT in redox or complexometric titrations in

the future to verify the general applicability of the method. In the near term, we plan to

field test the TMT system, measuring TA from shipboard underway seawater and

continue working toward a fully autonomous TMT sensor for seawater TA.

Appendix A   Instrumental Design Details

The following appendix provides detailed information related to some instruments and instrumental components used during the development of TMT. These discussions, schematics and experiments will mostly serve as a guide to others in the DeGrandpre lab, or those attempting to reproduce the TMT system described in Chapters 1-4.

A.1   Stirred fiber optic flow cell schematics

A stirred, thermostated, fiber optic flowcell was the crux of TMT. In Chapter 3 the flow cell was described, but only with simple drawings for illustrative purposes. This section shows the schematics that I designed and Big Sky Machining followed while manufacturing the flowcell (Figures A.1-A.6). Cell orientations and accessory names are labeled in red, beginning with the front side of the cell, as viewed from the face on which the stirring motor is mounted. The sides of the cell are labeled: front = Side A; back = Side B; left = Side C; right = Side D; top = Side E; bottom = Side F. The bottom of the cell (Figure A.3) has an o-ring groove which forms an axial (face) seal with an o-ring and the bottom base plate (Figure A.4). Liquid flow is from the backside (Side B, Figure A.1) through the top (Side E, Figure A.3). The light path is from left to right (Side C to Side D, Figures A.1 and A.2). All fittings are externally threaded knurled nuts. Fitting ports are 10-32 coned, except for the temperature probe ports which are ¼-28 flat bottom. For simplicity, fittings are not explicitly shown in the flow cell drawings and ports are drawn to show basic dimensions only. More detailed machining specifications for the fitting ports (Upchurch Scientific) are included following the flow cell schematics (Figures A.5 and A.6). Other accessories not shown include base plate screws, motor mount screws,
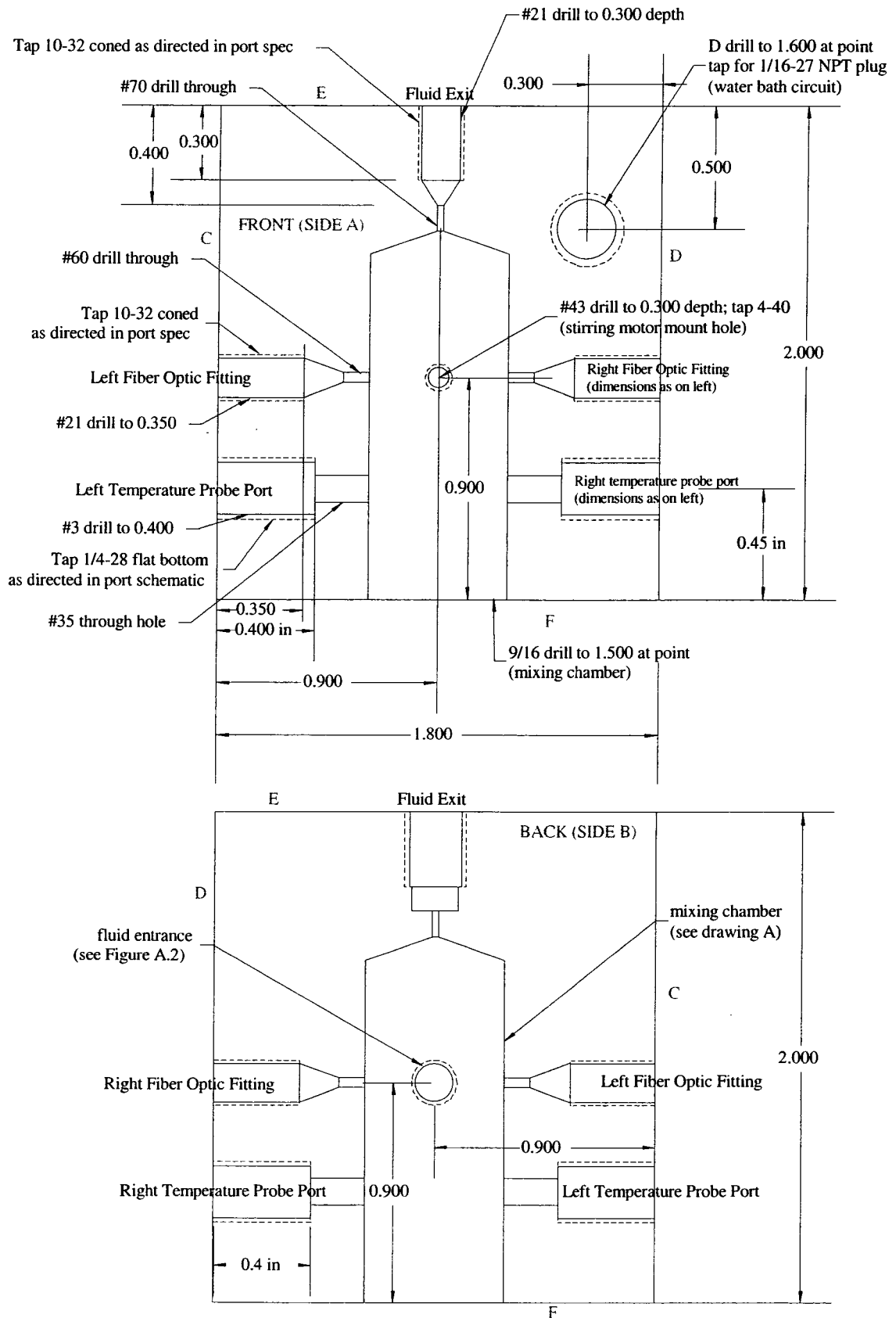
Figure A.1 Machining schematics for front (side A) and back (side B) of the stirred flowcell.

105
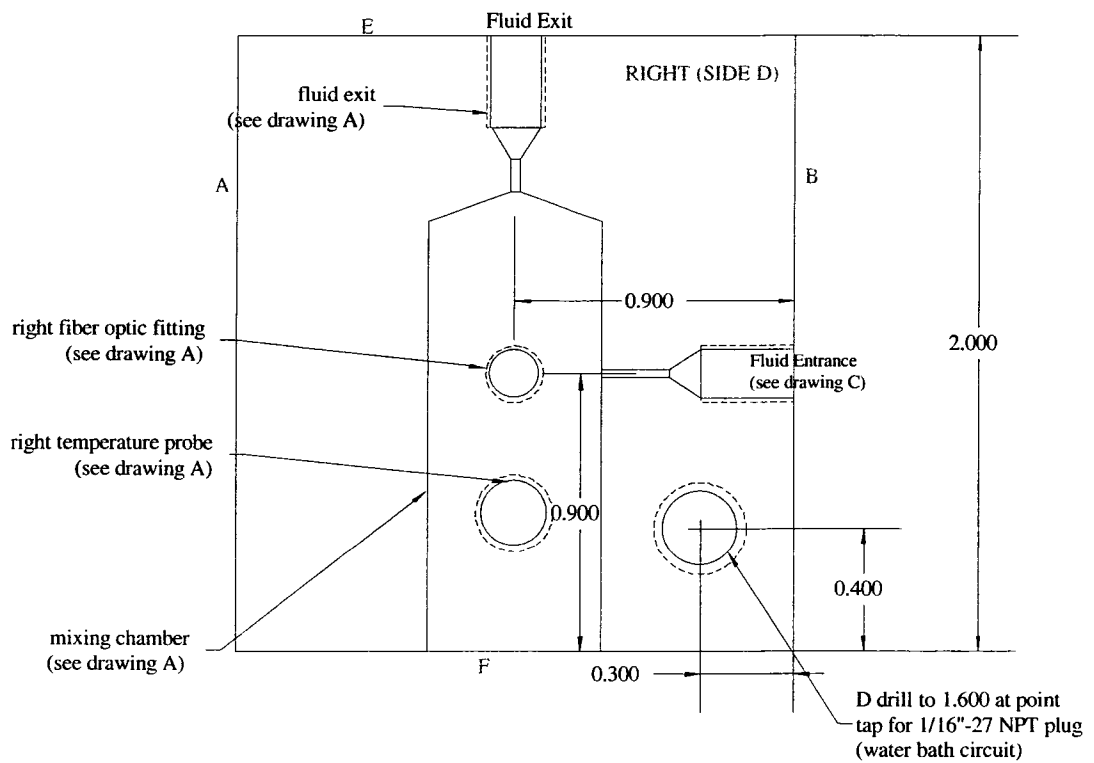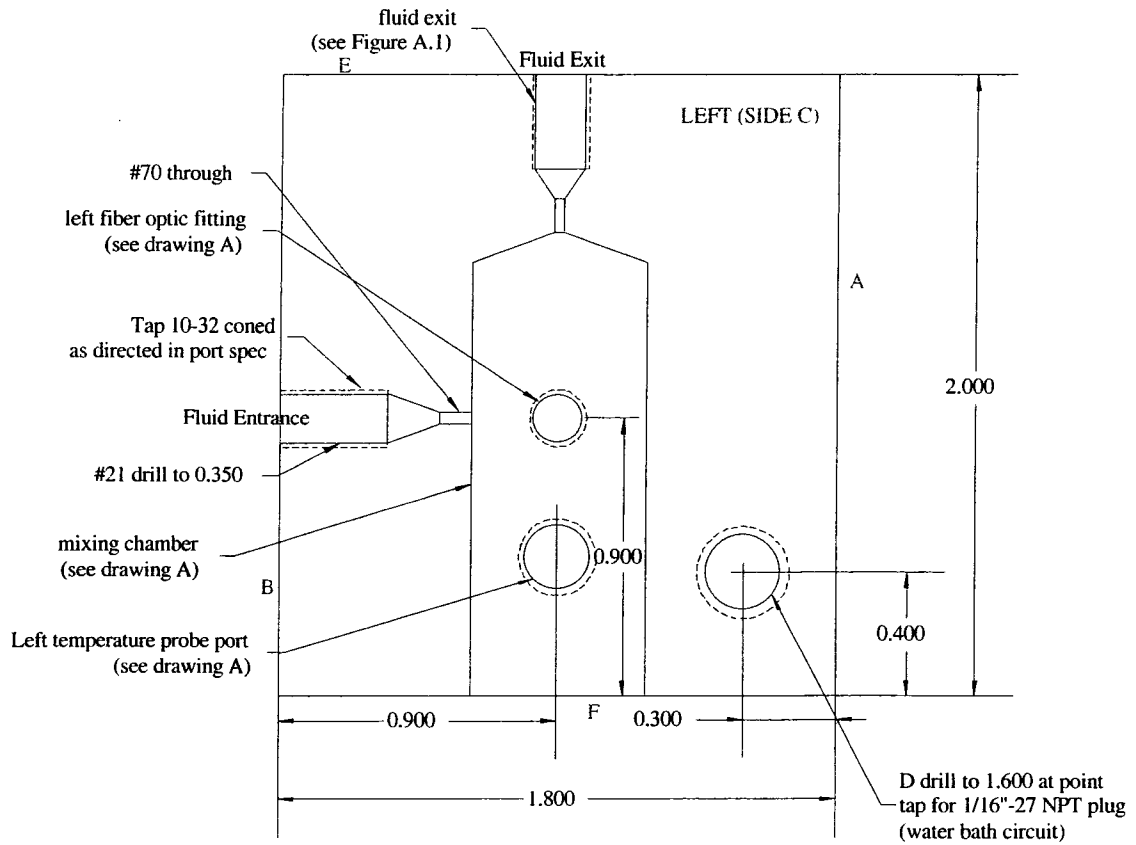
Figure A.2 Machining schematics for left (side C) and right (side D) of the stirred flowcell.

106
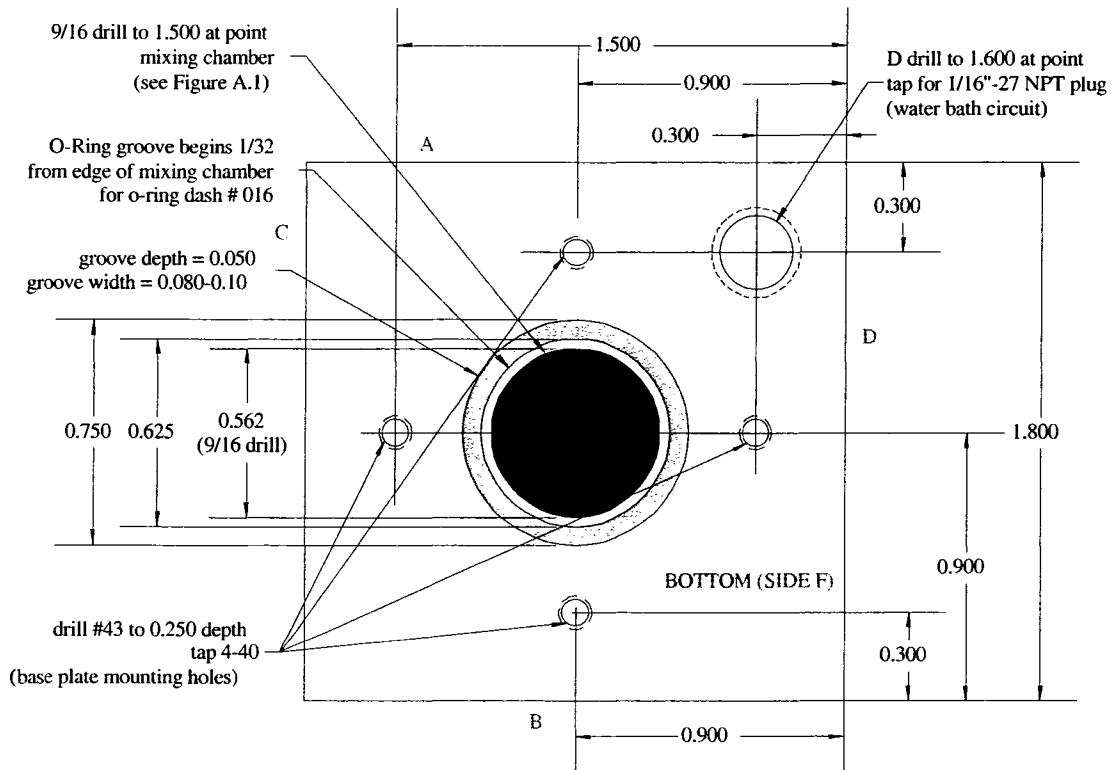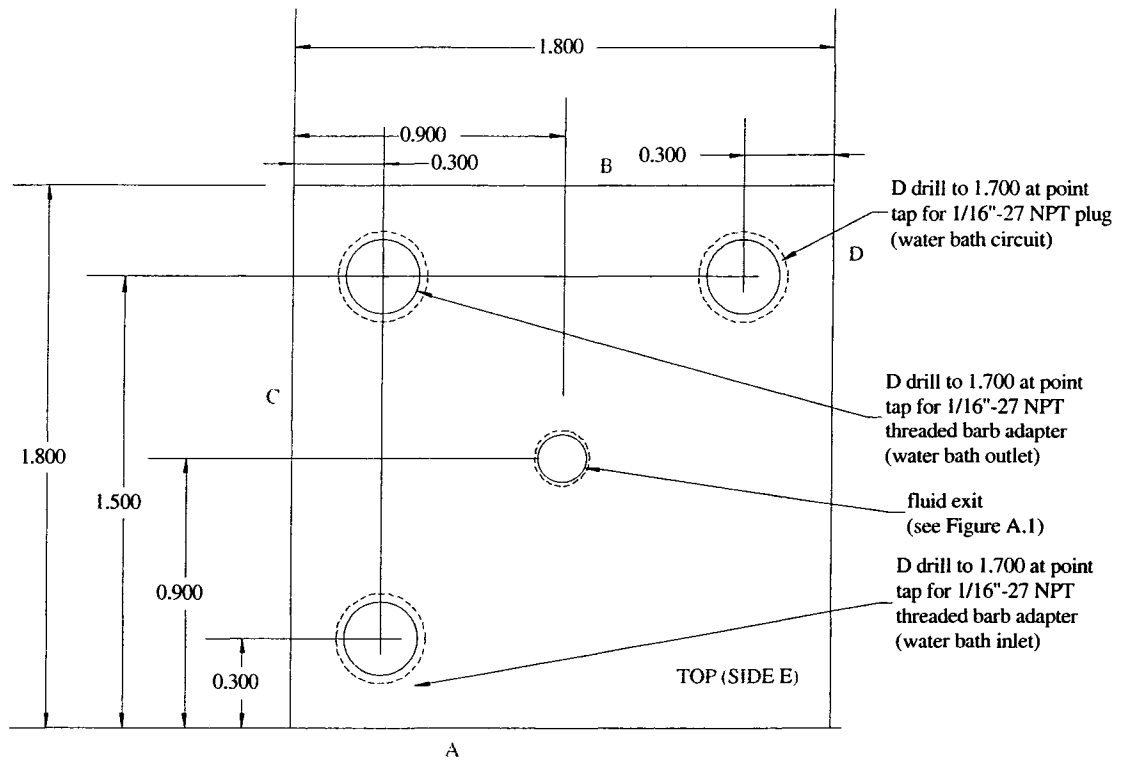
Figure A.3 Machining schematics for top (side E) and bottom (side F) of the stirred flowcell.

107
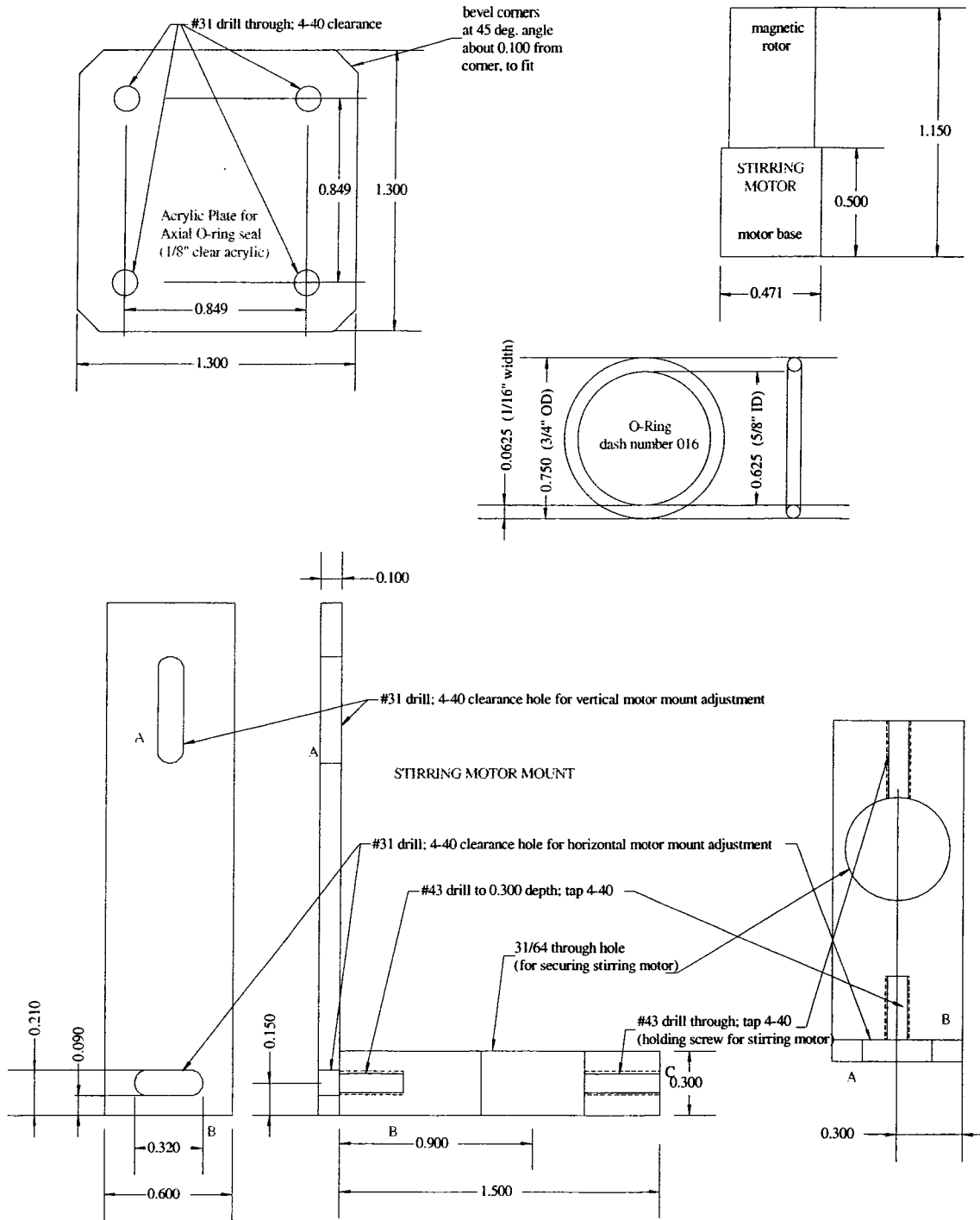
Figure A.4 Machining schematics for flow cell accessories

108
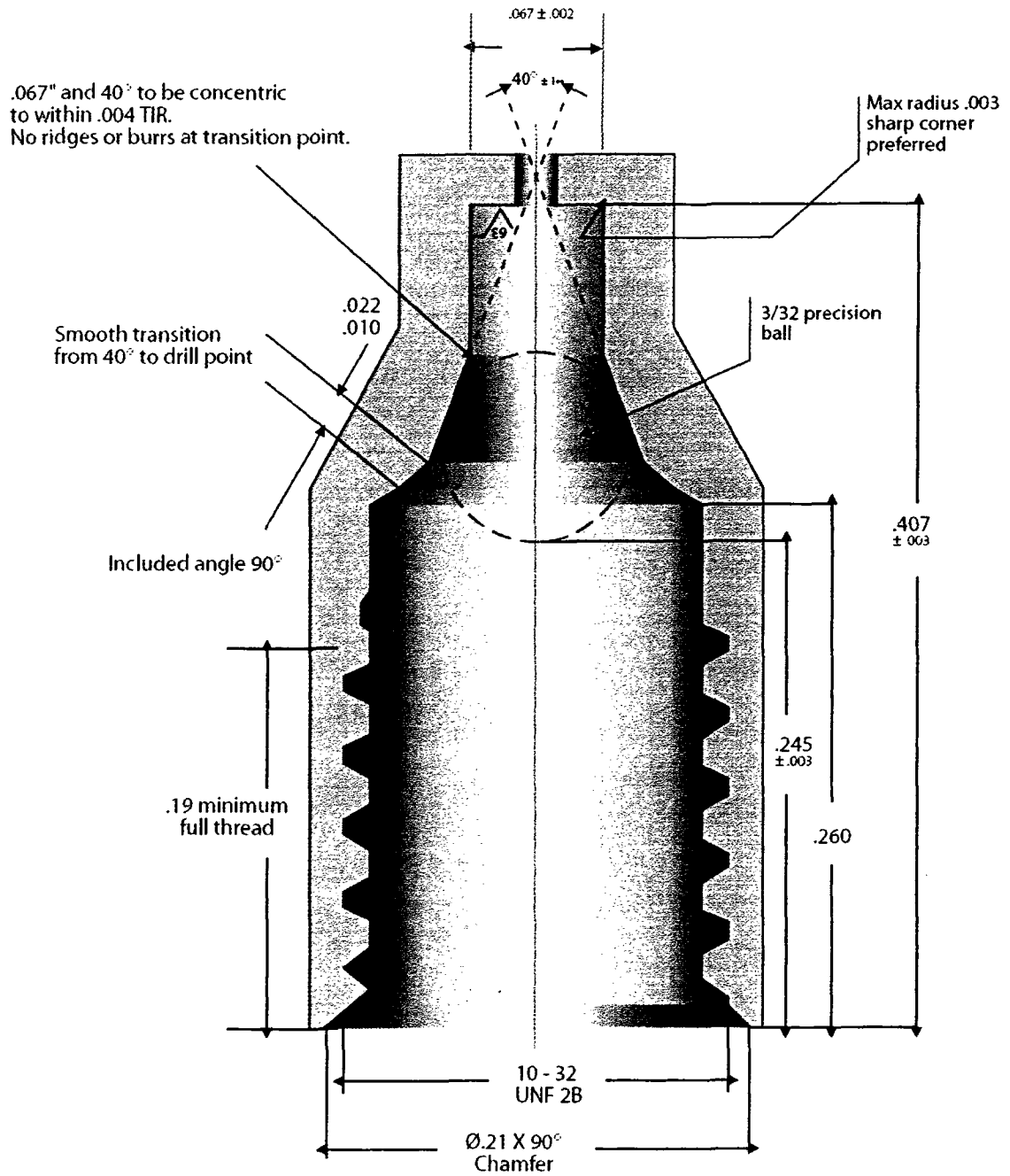
Figure A.5 10-32 coned port specifications (figure used with permission from Upchurch Scientific).

109
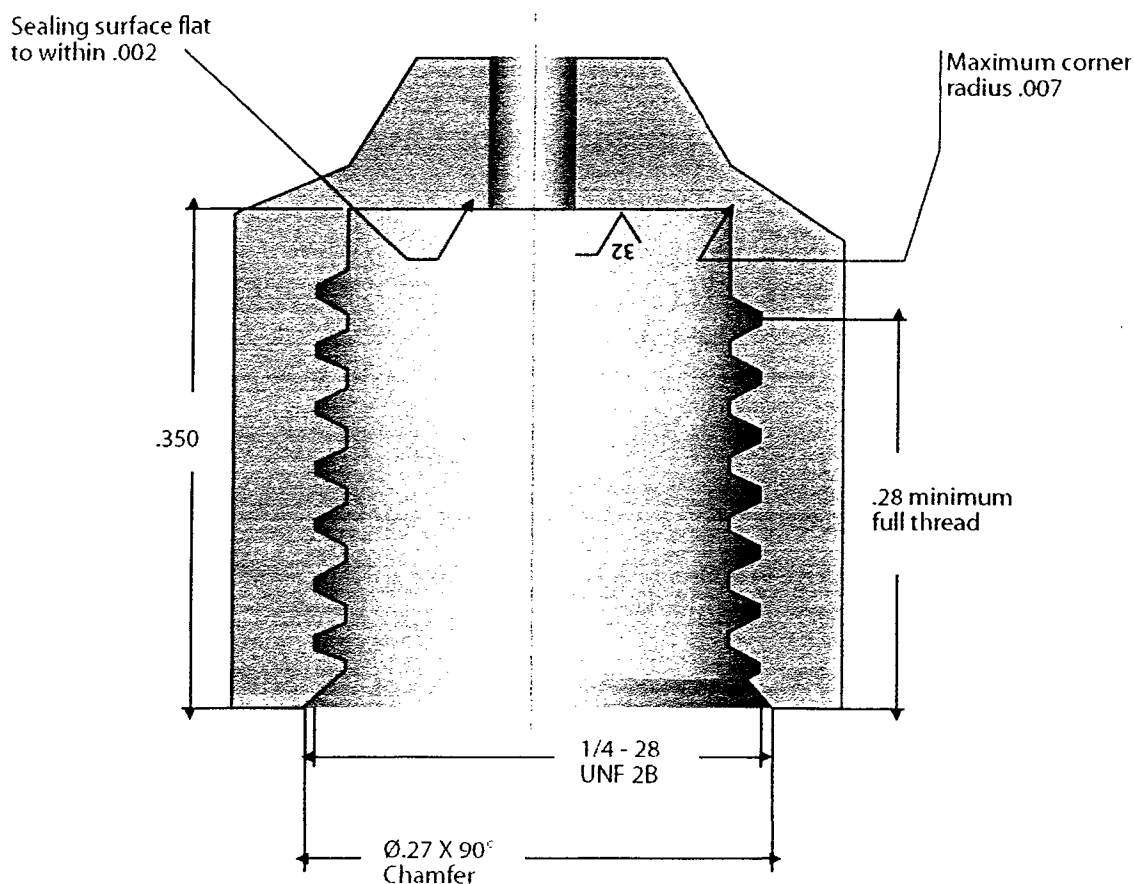
Figure A.6 ¼-28 flat bottom port specifications (figure used with permission from Upchurch Scientific).

tubing, NPT plugs and barbs (for the water bath circuit), the Teflon micro stirbar, cell

insulation (double sided foam mounting tape and cork). Wetted surfaces include black

Delrin™ (polyoxymethylene aka acetal; flow cell body), acrylic (base plate), fused silica

(fiber optics), PEEK (polyetheretherketone; ferrules and tubing), Buna-N (butadiene

acrylonitrile; o-rings). The internal volume of the stirred chamber is approximately 6.1

mL.

A.2 Optics

The optical system described in Section 3.2 was evaluated for photometric

accuracy (i.e. absorbance linearity), lamp performance (i.e. blank drift, emission

110

intensity), detector noise, stray light, and wavelength accuracy. Here, the details of these experiments are described and their results discussed.

A.2.1 Types of light sources: intensity and spectral emission

For UV-Visible (UV-VIS) spectrophotometry, the three categories of light sources that produce a continuum across the visible spectrum are tungsten lamps, xenon flash lamps and white light emitting diodes (LEDs). The technology of white LEDs is relatively new compared to the tungsten lamp, which has a long history of development. Consequently, tungsten sources are used almost universally in precision UV-VIS spectrophotometry. As an alternative to the tungsten lamp, white LEDs were tested. Flash lamps were not explored in this study. Ultimately, the tungsten lamp served as the primary light source in the final stages of instrument development, although the LEDs showed promise for future applications

A.2.1.1 Tungsten Lamps

Tungsten lamps consist of a glass-encapsulated filament under vacuum or in the presence of a halogen gas such as I or Br. Tungsten-halogen lamps burn hotter and longer than tungsten-vacuum lamps due to a continuous process whereby W is deposited on the inner glass of the bulb, where it reacts with the gas to re-vaporize and then re-deposit on the W filament. Figure A.7 shows a spectrum of the SAMI tungsten source after passing through a fiber optic flowcell (Gilway 4115-1B T-¾ subminiature lens-end lamp, 5V, 110 mA). The emission spectrum of a tungsten lamp closely follows Planck's radiation law of blackbody emission. In Figure A.7, fiber optic attenuation and detector sensitivity skew the peak *transmission* wavelength to a shorter value than the peak *emission* wavelength. The blackbody model describes the intensity of emitted light as a

111

function of frequency (or wavelength), temperature, and several universal physical

constants (Ingle and Crouch, 1988). Figure A.8 illustrates how
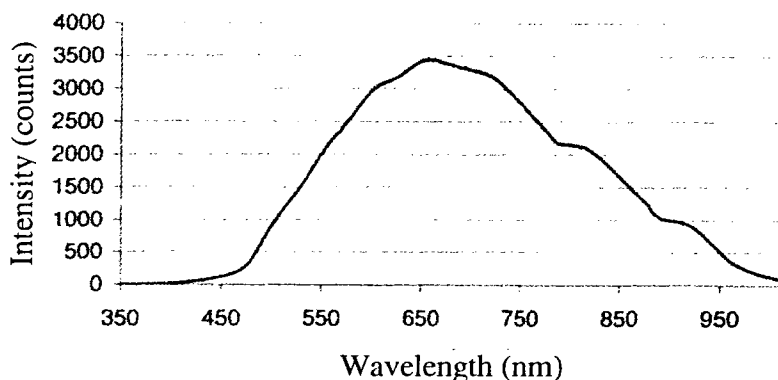
Figure A.7 Spectrum of the SAMI light source at 5V, 110 mA. The detector was an Ocean Optics USB2000 CCD array spectrophotometer (5 sec integration time). Fiber optic attenuation and detector sensitivity skew the peak *transmission* wavelength to a shorter value than the peak *emission* wavelength.

the emission spectrum of a tungsten lamp varies with increasing filament temperature[44].

This shift is particularly important at the sparsely emitting shorter wavelengths ($<$ 500

nm), where a higher lamp operating current can increase optical throughput several times.

Figure A.8B shows the increase in lamp intensity (at the analytical wavelengths used in

this study) for changes in color temperature (i.e. operating current). The rule of thumb

for the SAMI light source is +~1.25 V (25% increase in operating voltage) = +~10 mA

(8% increase in operating current) = +~200°K (8% increase in color temperature) = ~90%

decrease in lamp lifetime. The SAMI light source is rated at 40,000 hours, so it should

not be overrun by more than about 1.5 V (i.e. operating voltage $<$ 6.5 V)[45]. Gilway does

not report exact color temperatures for their lamps, so it is difficult to say exactly what

the color temperature of the SAMI source is at its rated operating voltage. Instead,

---

[44] A more thorough, but more complicated, analysis accounts for the nonideality of a real source (i.e. a graybody).
[45] I have run it as high as 7.2 V without immediate failure, but the expected lifetime at this high voltage is only a few hundred hours.

112
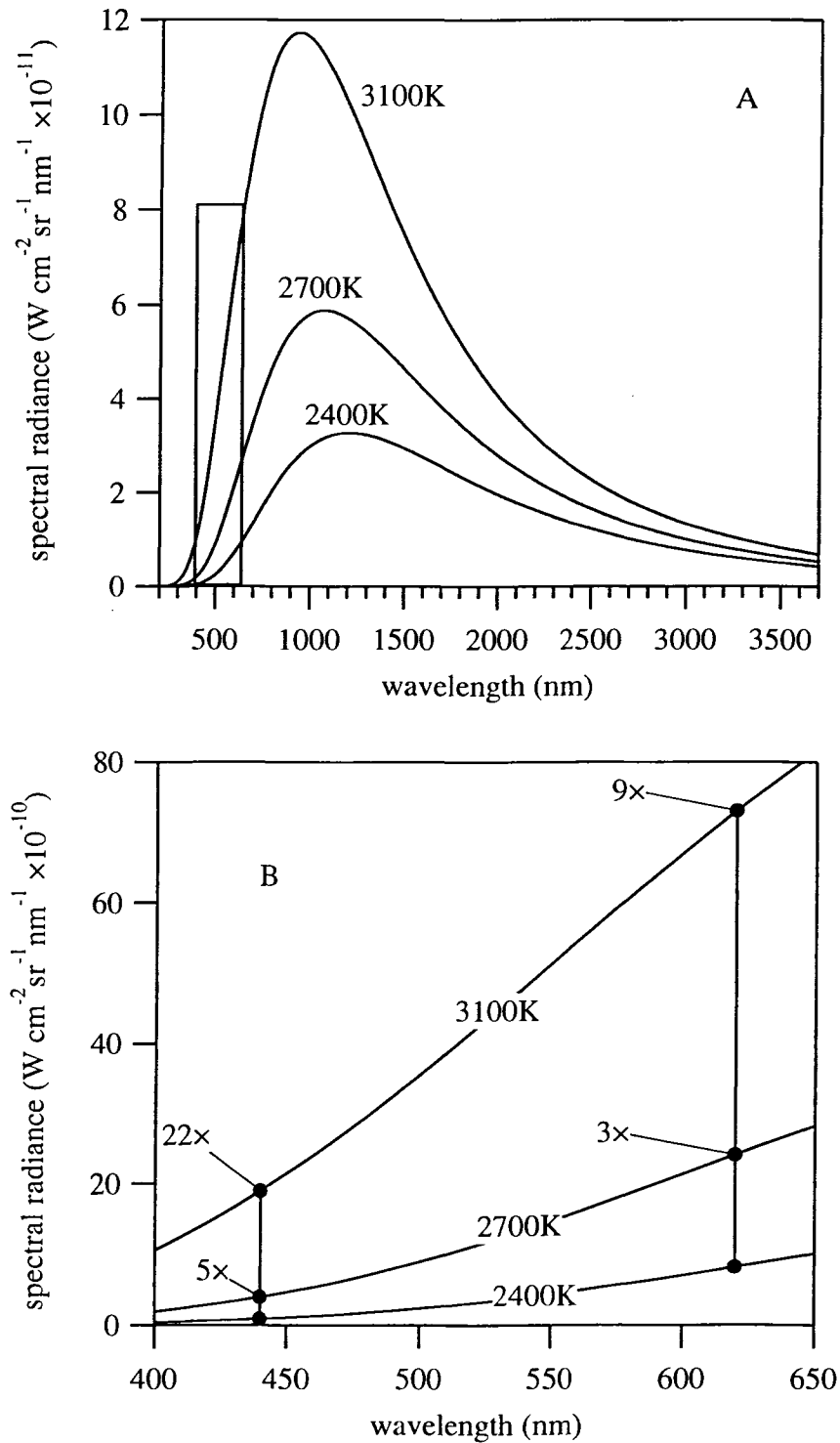
Figure A.8 (A) The changing emission spectrum of a blackbody emitter, as calculated from Planck's radiation law as a function of wavelength. (B) Expanded view of the region covering the two analytical wavelengths 440 and 620 nm. Increases in optical intensity due to changes in color temperature (i.e. operating current of a tungsten lamp) of the blackbody are labeled as multiples of the lowest color temperature (2400K).

113

Figure A.8B is an attempt to bracket the highest and lowest temperatures expected for this type of lamp. Based on these figures, it is reasonable to say that adjustments to the SAMI light source operating voltage within a safe range could be expected to raise the signal at 440 nm by at least 3 times, but no more than 20 times. Similarly, the 620 nm channel will not increase by much more than 5 times.

Tungsten lamps exhibit drift due to multiple forcings. As elements age over hundreds of hours of operation, emission at all wavelengths decreases. More subtly, however, are the effects of ambient temperature and heat sink efficiency on the light source. Because it is not possible to draw heat away from a lamp at a perfectly constant rate, the filament never reaches a true thermal equilibrium with its environment. Thus, as room temperature changes or the heat sink temperature fluctuates, careful observations will reveal a constantly changing emission spectrum. We therefore carried out several light signal monitoring tests using various configurations of tungsten-halogen lamps. These studies used the same interference filter spectrophotometer shown in Figure 3.1 with blank solution in the flowcell and different lamps connected to the source fiber optic. In some cases the flowcell was bypassed, and this is noted in figure captions. Figure A.9 shows the enormous dependence of lamp emission upon the character of the material in direct contact with the lamp. It is also clear from Figure A.9 that thermal lamp drift is, to some degree, wavelength dependent. As seen in Figure A.10, the reference value ($_{780}A$) undercorrects at $_{620}A$ and overcorrects at $_{440}A$, leading to positive and negative absorbance errors, respectively. At the 440 nm channel, a 780 nm reference wavelength corrects for 70-90% of the drift, leaving up to 0.004 au uncorrected.
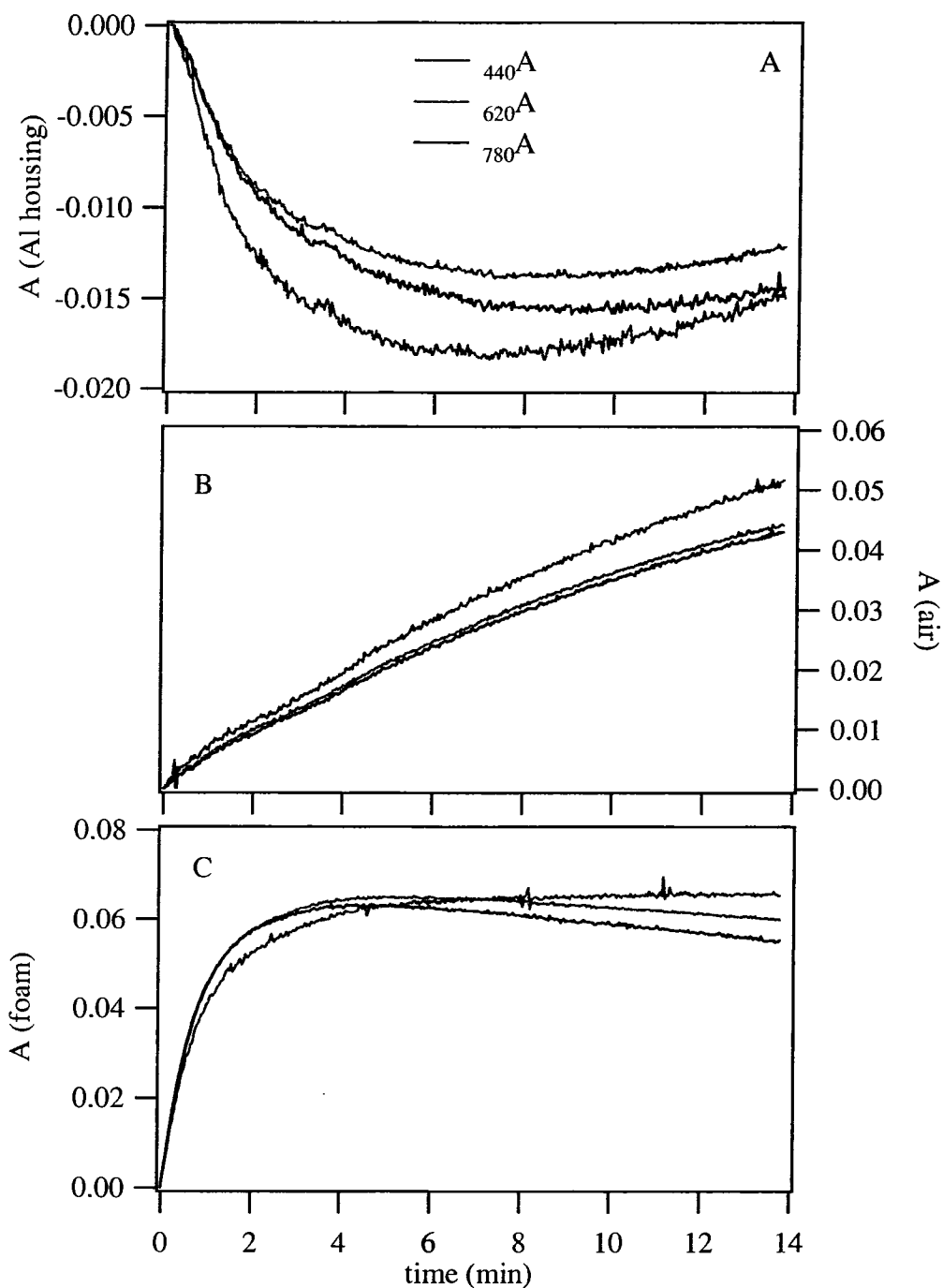
Figure A.9 Tungsten (SAMI) lamp drift from a cold startup while in (A) an aluminum housing, (B) no housing, open to ambient air, and (C) surrounded by a foam block. A is absorbance. The flowcell was bypassed in this study.

High precision absorbance measurements thus require (1) a substantial lamp warm-up time with a suitable heat sink, (2) a wavelength-dependent drift correction such as a blank reference beam (e.g. double beam spectrophotometer) (3) an electronic

115

feedback loop that maintains a constant source intensity by continuously adjusting the lamp's drive circuit on a frequency much higher than the lamp drift or (4) blank-to-blank sampling times much shorter than the lamp drift. During this project, all four of these options were explored.
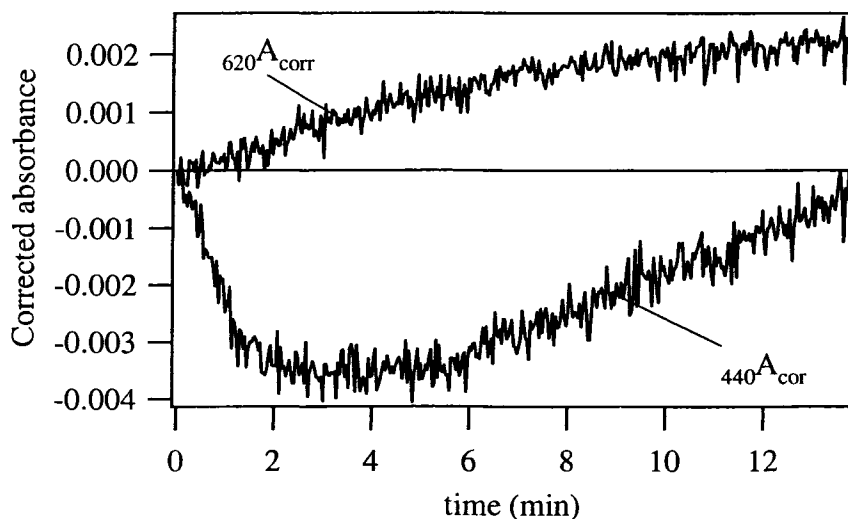
Figure A.10 Analytical absorbances from Figure A.9A, corrected by subtracting the 780 nm reference absorbance.

As a first approximation, it was useful to explore the highest stability that could be expected from the SAMI tungsten lamp in an Al housing. Figure A.11 represents the best performance achievable by a SAMI light source and housing. On several occasions, it was found that the SAMI lamp in its aluminum housing drifts at a rate of less than ~ 0.0001 au min^{-1} after complete warm-up. Although reasonably stable over extended periods (e.g. Figure A.11, the one hour period between hours 6 and 7), the SAMI lamp can potentially generate large errors when absorbance is recorded more than a minute after the blank, because subtracting the absorbance drift at a reference wavelength does not necessarily correct for drift at another wavelength (Figure A.10). Also, the lamp's relatively weak intensity at 440 nm requires a very high gain setting. Consequently, it is

116
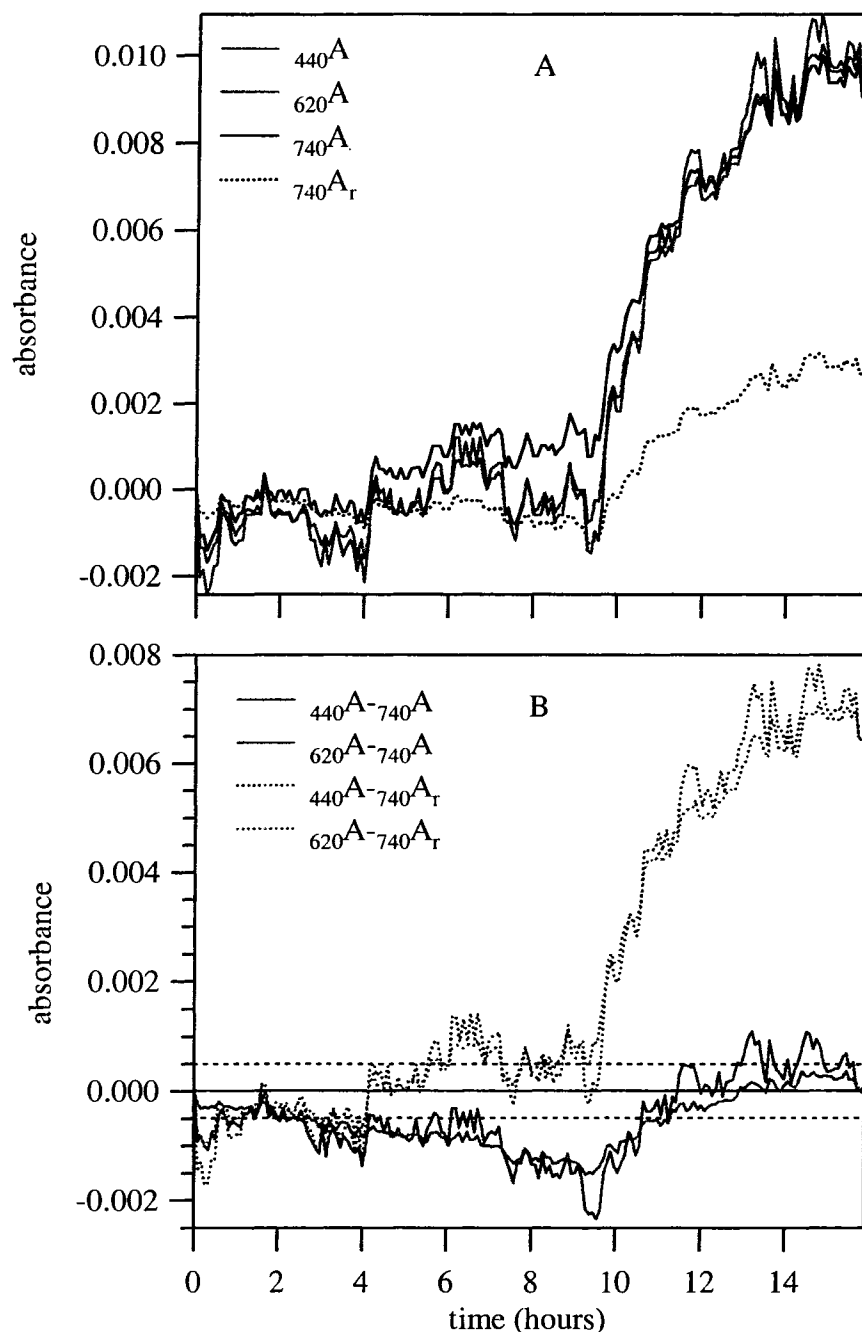
Figure A.11 Time series of blank SAMI lamp drift. The source is a Gilway tungsten lamp in aluminum housing. (A) For the first three absorbance values listed in the legend, light passes through a flow cell with DI, with 1 pump per data acquisition point. A hole, drilled radially into the lamp housing also allows direct monitoring of the lamp at 740 nm ($_{740}A_r$, dotted line). (B) Analytical absorbances, corrected by the usual 740 nm channel (solid lines) and the radial 740 nm channel (dotted lines). Black dashed lines represent the maximum tolerance in absorbance error, between blank and sample, required for TA measurements by TMT ($\pm$0.0005).

very difficult (if not impossible) to routinely achieve sub 0.0005 au precision using the

conventional SAMI optical design.

117

The second option was crudely tested by drilling a hole into the SAMI aluminum housing at a 90° angle and directly monitoring the lamp's intensity at a narrow wavelength range using a filter photodiode (Intor) and an additional analog amplifier. Three tests were performed using 440, 620 and 740 nm filter photodiodes. Only the experiment with the 740 nm filter photodiode is shown (Figure A.11). As shown in Figure A.11, reference absorbance tracks analytical absorbance better through the flowcell than radially at the source. With 440 and 620 nm (instead of 740 nm) filter photodiodes mounted 90° from the source, radial corrections were no better than that shown in Figure A.11. In general, no matter which wavelength was monitored at the 90° lamp mount, the radial channel exhibited similar but less pronounced drift on both short and long time scales[46]. Long-term blank monitoring (Figure A.11) reveals two distinct types of lamp behavior. After warmup, lamp emission may stabilize for long periods, such as the first eight hours recorded in Figure A.11. A lamp will also undergo random, long, drifting interludes characteristic of the intensity loss one might expect to observe as a light source ages, such as the last eight hours recorded in Figure A.11. Unstabilized lamp behavior is therefore unpredictable and frequent blanks must be taken on fairly short intervals. Calculating a running absorbance (Figure A.12) on the continuous time series of lamp drift (Figure A.11) helps establish the acceptable time limit that must be achieved between blank and sample.

As shown in Figure A.12, if frequent blanks are recorded, even an unstabilized lamp can achieve excellent performance. In fact, the level of drift shown in Figure A.12A is nearly good enough to provide the level of TA precision required for the stirred

---

[46] An interesting follow-up experiment would be to build a special aluminum housing for the SAMI tungsten lamp with fiber optic couplers at 0° and 90°, and monitor the wavelength dependence of the spatial radiation pattern of this lens-end lamp.

flow cell titrations presented in Chapters 3 and 4. The caveat is that εb is extremely

difficult to measure with this light source, because it takes 15 minutes to flush out the

flow cell and accurate εb values demand absorbance precision better than 0.0005 (Section

2.3). A more sophisticated correction approach, such as a true double beam instrument,

provides a more reliable correction to lamp drift over minutes to hours, but, due to the
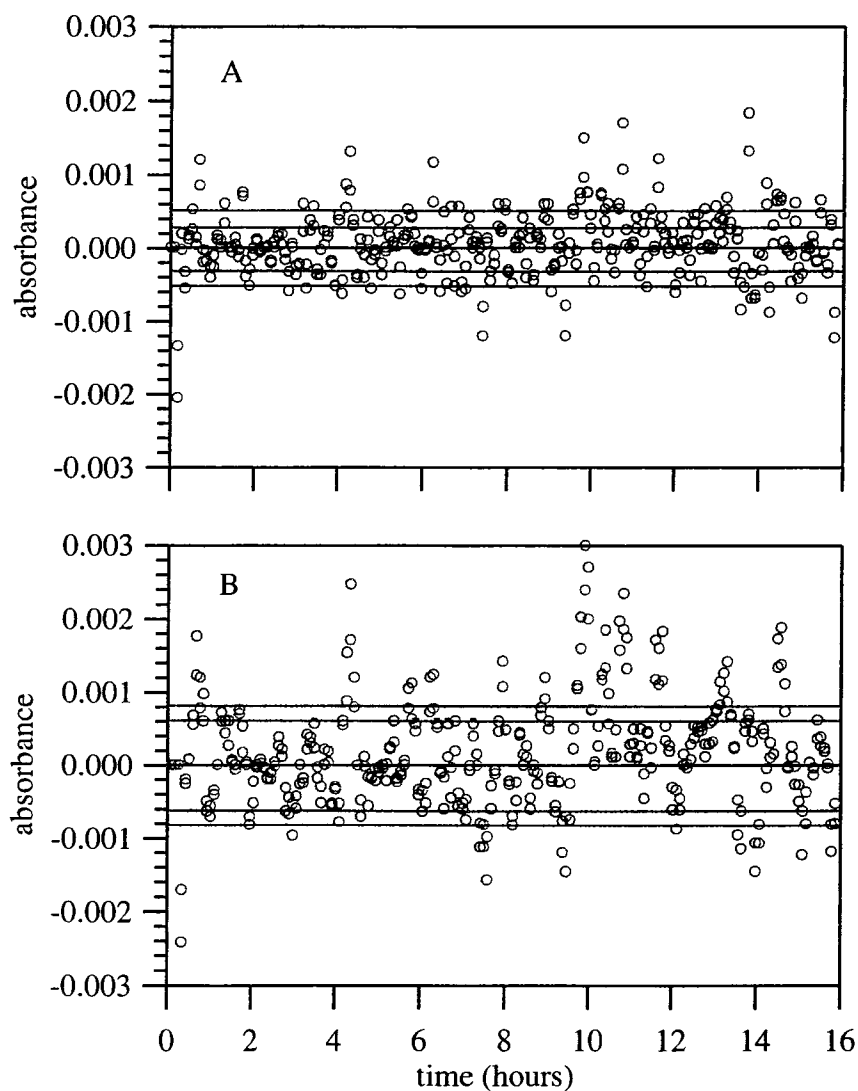
Figure A.12 Running absorbance values for data shown in Figure A.11. (A) 5
minute periods and (B) 15 minute periods. Red and blue represent 620 nm
and 440 nm, respectively. The 1σ (n~180) standard deviation values are
5min: ±0.0005 (440 nm) ±0.0003 (620 nm); 15min: ±0.0008 (440 nm),
±0.0006 (620 nm).

119

complexity of such a setup (building a second flow cell and more complicated optical

detection system) this approach was deemed impractical. Two types of electronic

feedback loops are available for tungsten lamps: current feedback and optical feedback.

Current feedback involves using a simple op-amp loop that holds the drive current of the

lamp at a constant value. Optical feedback requires monitoring an optical signal at a

narrow bandpass (similar to the experiment shown in A.11), digitizing the signal, and

adjusting the lamp's current to hold the digitized optical signal at a constant value.

Intuitively, optical feedback will maintain the most stable lamp emission, but its

complexity and expense makes it undesirable unless no other approach can obtain the

required instrumental stability. As shown in Figure A.13, a current stabilized
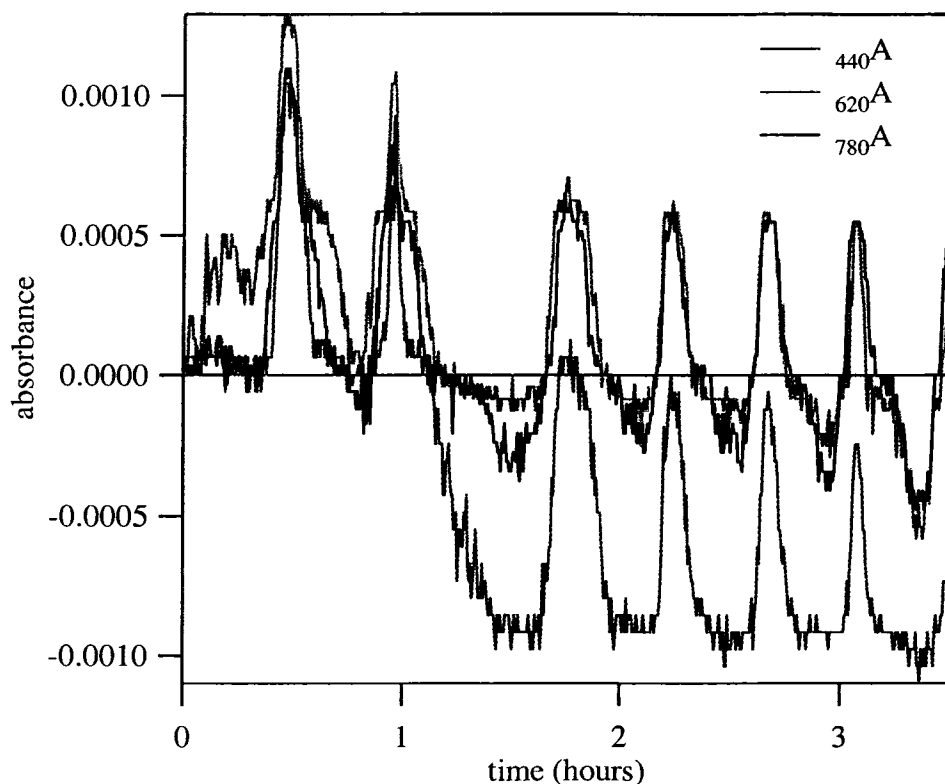
Figure A.13 Time series of a current-regulated tungsten halogen lamp (CDI-TTL). Cycling is due to room temperature fluctuations (not shown).

120

tungsten-halogen source (Control Development Inc., CDI-TTL) achieves much greater stability over long periods than the SAMI lamp (Figure A.11). The temperature-driven cycles of the current-regulated lamp pose a similar problem as an unregulated source because if a blank is taken in a trough and an absorbance measurement is recorded at a peak, there is a potential for absorbance errors of up to 0.001. An optically stabilized lamp (XLamp, Custom Sensors), achieves better stability, but temperature effects are still obvious (Figure A.14). As seen in Figures A.13 and A.14, the effects of ambient
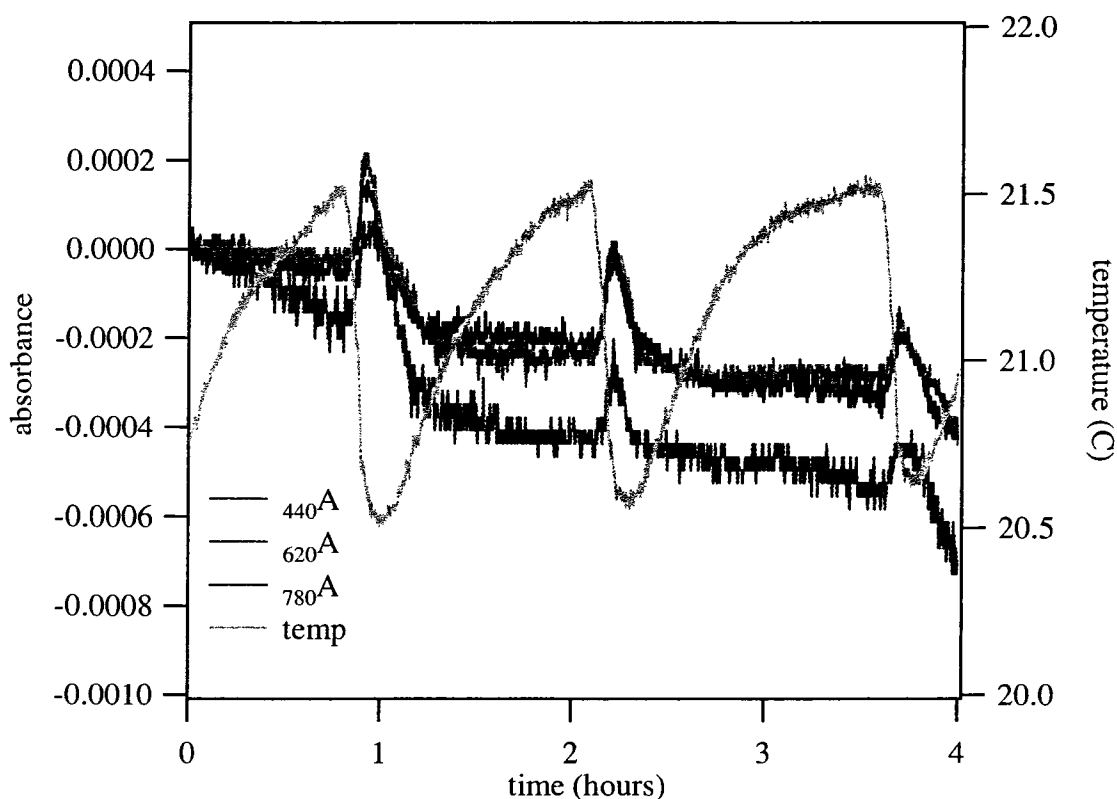
Figure A.14 Time series of an optically regulated tungsten halogen lamp (XLamp, CSI). Emission fluctuations are clearly due to the room temperature cycles.

temperature remain significant, even on 'regulated' lamps. One final measure that can be taken to prevent this type of behavior is sealing the lamp in its housing into a NEMA (National Electrical Manufacturers Association) box, in an attempt to isolate the lamp from the ambient air temperature fluxes. Figure A.15 shows a time series of the optically

121

stabilized XLamp in a NEMA box after allowing several hours to reach a thermal

equilibrium. Even in the NEMA box, temperature influences the lamp intensity, but with
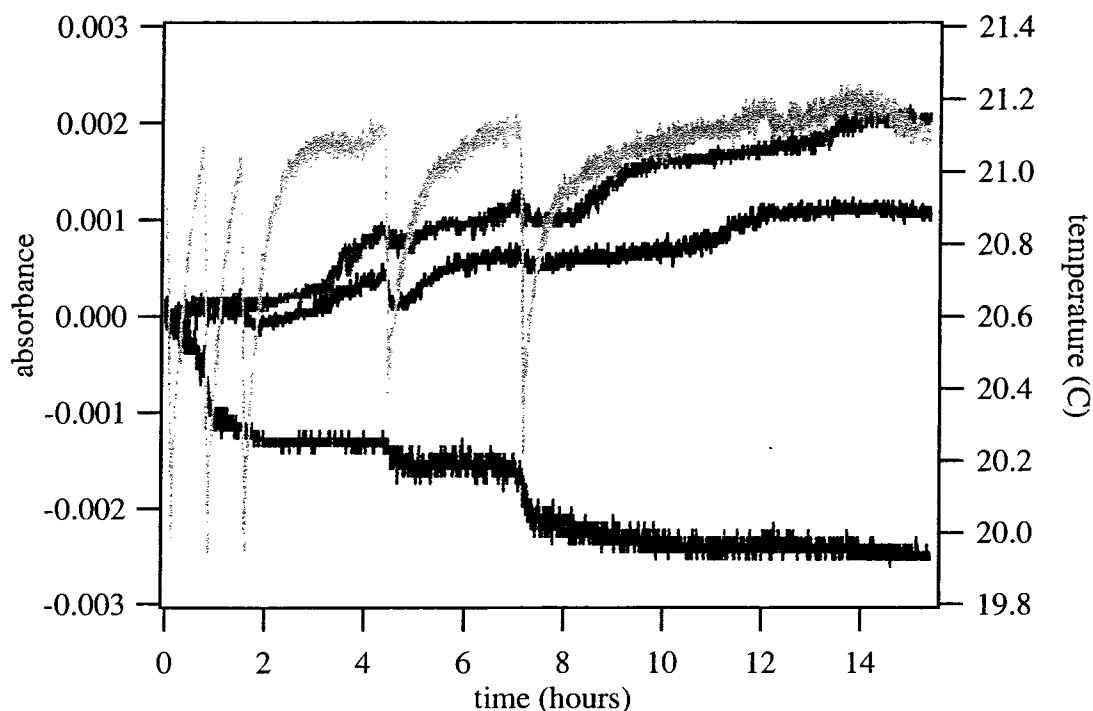
Figure A.15 Time series of an optically stabilized tungsten halogen lamp in a NEMA box (XLamp, CSI). See legend in Figure A.14. The effect of room temperature cycles is still apparent, but with an differing effect on the lamp intensity (Figure A.14). Even with the optimal lamp performance shown here, blanks should be recorded on intervals no greater than 30 minutes (see Figure A.16). If the room temperature changes a new blank should be recorded.

the opposite effect. As shown in Figure A.16, the running absorbance stability is far

greater than that of the unstabilized SAMI tungsten lamp (Figure A.12).

With sufficiently short (< 5 min) intervals between blank and sample, the

emission of the optically stabilized lamp is so constant that the absorbance precision will

be limited by factors other than lamp emission including analog to digital resolution and

small chemical differences between samples (Figure A.16A). As the time between blank

and sample increases, the temperature fluctuations in the XLamp (Figure A.15) are

evident in the running absorbance values, although they remain very low (Figures A.16B

& A.16C).

122
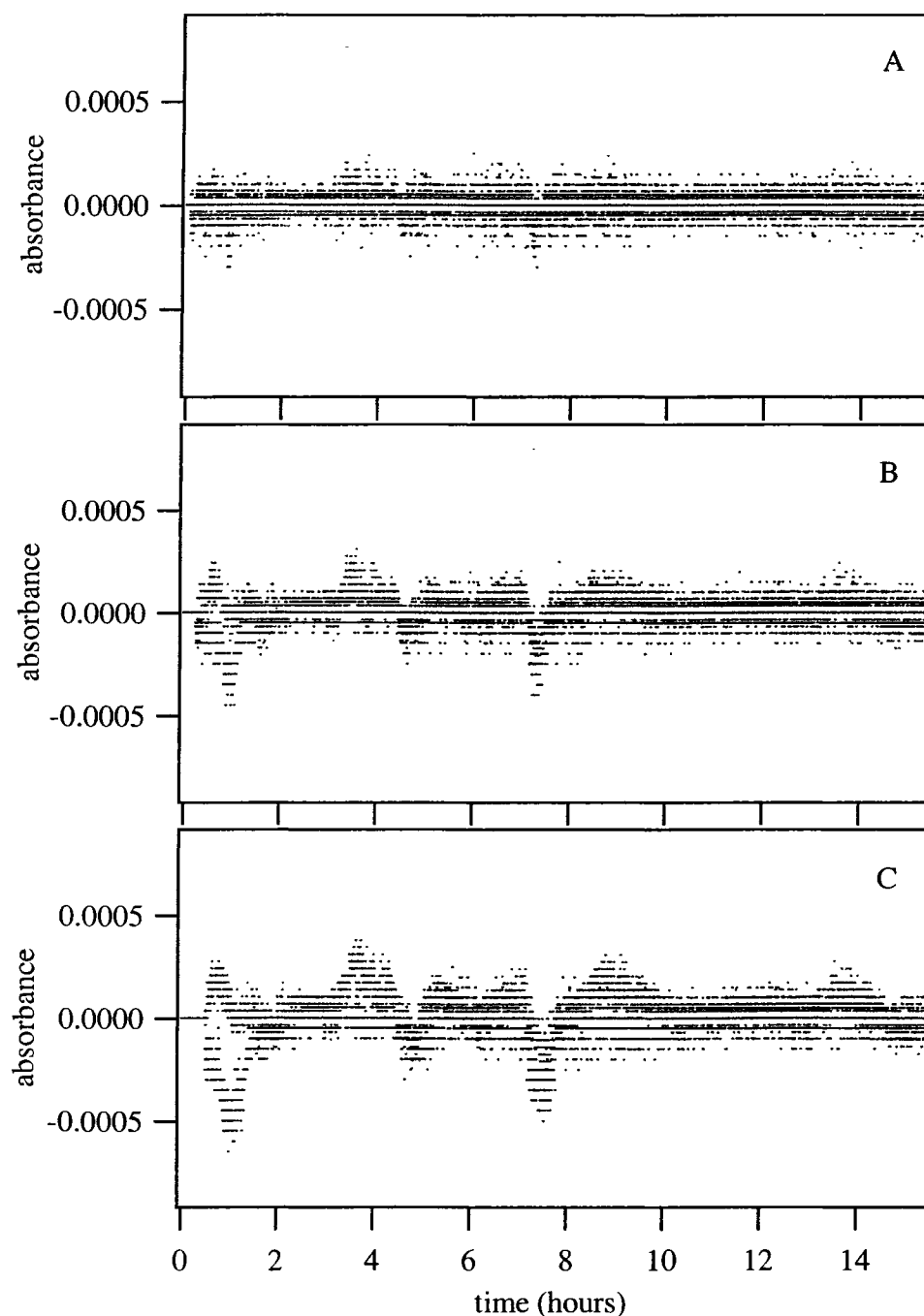
Figure A.16 Running absorbance values for data shown in Figure A.15. (A) 5 minute periods (B) 15 minute periods and (C) 30 minute periods. Red and blue represent 620 nm and 440 nm, respectively. The 1σ (n~4000) standard deviation values are 5min: ±0.00006 (440 nm), ±0.00006 (620 nm); 15min: ±0.00008 (440 nm) ±0.0003 (620 nm); 30 min: ±0.00011 (440 nm), ±0.00008 (620 nm). See Figure A.15 for temperature record.

123

The most apparent features of the experiments with stabilized lamps (Figures A.13-A.15) are that temperature effects are nearly impossible to eliminate, and wavelength-dependent drift is inevitable. In the case that a double beam design is impractical, corrections by a non-absorbing 'reference' wavelength should always be made with caution. In general, subtracting absorbance at a reference wavelength from analytical absorbance works for short term baseline errors caused by air bubbles[47] or, in the case of a conventional benchtop instrument, cuvette displacement. However, the wavelength-dependent lamp drift, present in all these Figures (A.9-A.15) cannot be fully corrected by a reference wavelength, to the level of absorbance accuracy and precision (i.e. <0.0005) required for precise TA measurements (Section 2.3.1). It seems then, that, even with the most painstaking efforts, a single beam instrument is fated to sustain periodic absorbance drifts ≥ 0.0005 hr^{-1}. Section A.2.1.3 below summarizes the performance of all light sources tested and gives some concluding remarks about them.

A.2.1.2 Light Emitting Diodes

Historically, LED-based instruments were limited because all available LEDs emitted a narrow (± 10 nm) band of wavelengths. An LED instrument for multiple absorbance wavelengths would therefore require multiple LEDs, with emission PWL corresponding to the absorbance peak of the sample. This meant that the LEDs installed in a particular instrument were specific to a particular sample or technique[48]. The biggest drawback about this configuration, however, is the use of multiple sources. Considering the difficulty involved in stabilizing a single source, it seems highly probable that a

---

[47] Light scattering by air bubbles is also wavelength dependent, so the best approach is eliminating air bubbles altogether.
[48] This is similar to the configuration used in this study, where bandpass filters select narrow regions of the spectrum.

124

multi-LED source would be more susceptible to drift-induced absorbance errors[49]. The invention of the first white LED changed little. This was because early white LEDs were simply a combination of red, blue and yellow LEDs giving the appearance of a white source to the human eye, but still made up of three different sources. Several companies introduced single element white LEDs in the late 1990's (e.g. Gilway, Archer, Lumex) but their spectral emission was too weak to provide sufficient optical throughput for precision absorbance measurements. An important step in LED spectrophotometry came when Lumileds Lighting (Agilent-Phillips subsidiary) introduced the ultra bright white Luxeon™ STAR LED. The Luxeon LED operates by overlaying a 440 nm LED with an organic phosphor. The resulting spectrum consists of a continuum of wavelengths from about 410-750 nm, with a bright, narrow peak at 440 nm, a minimum at 470 nm, and a broad maximum at 550 nm trailing off to nearly zero emission by 750 nm (Figure A.17). More recently, Luxeon began marketing warm white LEDs, which closer approximate a blackbody emission spectrum (Figure A.18). Both STAR LEDs have similar peak emission power. The bright white and warm white STAR have approximately 10 and 2 times higher optical throughput, respectively, at 440 nm than the SAMI Gilway lamp. Both have comparable intensity at 620 nm and 10-20 times lower throughput at 780 nm.

Several experiments were carried out on both types of STARs to evaluate their applicability to spectrophotometry. Variables included type of heat sink, temperature of heat sink and forward voltage/operating current. Because there is a color shift associated

---

[49] It is relatively straightforward to build a multi-LED source with separate optical feedback channels at each LED and a fiber optic coupler that mixes the modes of light into a single homogenous source, but the blank absorbance stability of this type of circuit has not yet been investigated with the same rigor as was done for the tungsten sources in section A.2.2.1. It nonetheless holds great promise for future SAMI applications.

125

with any change in junction temperature, a heat sink is required for all LEDs. Initially,

the LED was attached to a relatively large aluminum block, several times greater than the
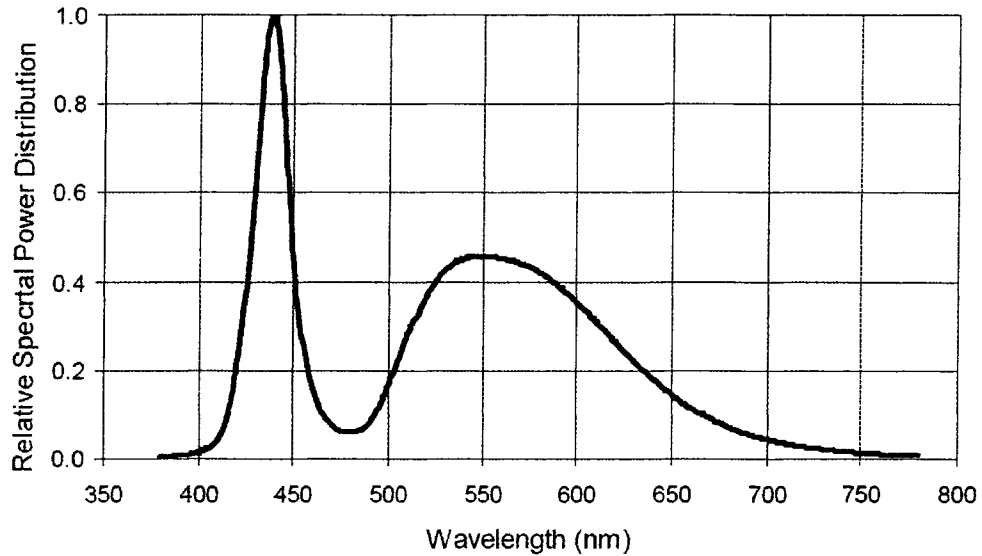
Figure A.17 Luxeon STAR emission spectrum (figure used with permission from Lumileds Lighting, Luxeon Technical Datasheet DS47).
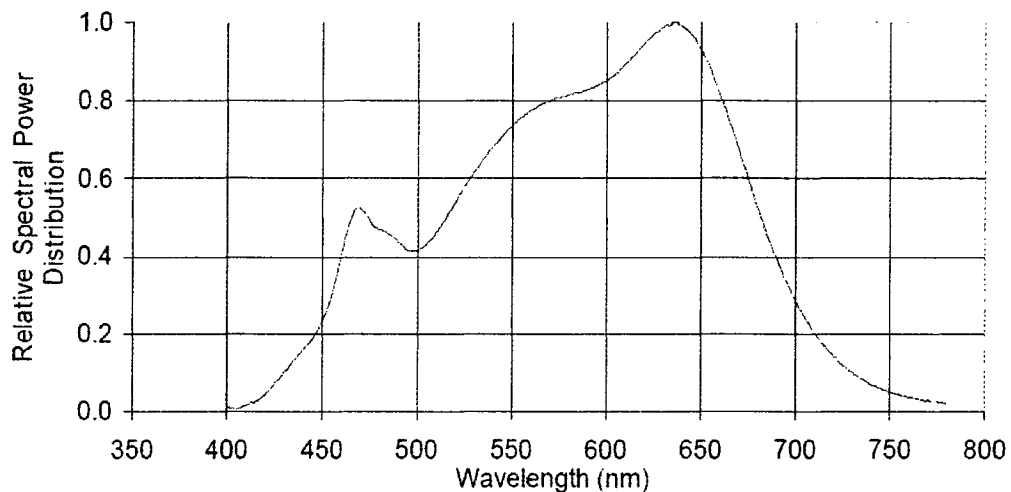
Figure A.18 Luxeon warm white STAR emission spectrum (figure used with permission from Lumileds Lighting, Luxeon Technical Datasheet DS47)

minimum size suggested in Luxeon's Thermal Design Guide (Luxeon Application Brief

AB05). STAR LEDs are designed such that heat travels from the semiconductor junction

through the PCB to the Al heatspreader (a flat-bottom plate). This design prevents direct

heat flow between the junction and the ambient air. Therefore, if the LED is connected to

126

an appropriate heat sink, small air temperature changes have little effect on the emission because they must first change the temperature of the heat sink. Figure A.19 shows the stability of a warm white STAR over a 52 minute period. The experiment shown in Figure A.19 was repeated a number of times at different operating current and heat sink temperature. STAR optical drift patterns are highly sensitive to the operating current and the temperature of the heat sink. The LED quickly burns out if powered above the
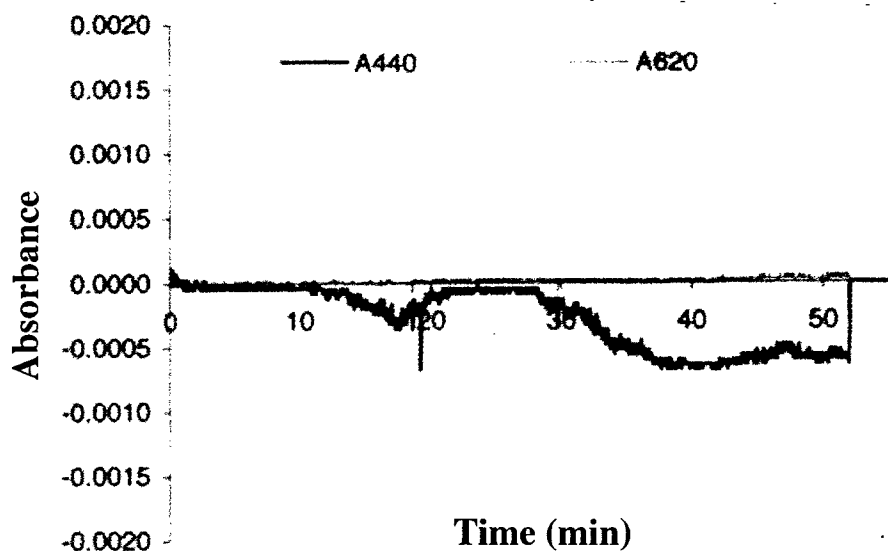
Figure A.19 Warm white STAR LED emission stability through a thermostated flowcell filled with water. Operating at 310 mA and 3.5 V on a temperature-controlled heat sink at 21°C. The 780 nm channel is not shown, because it closely overlapped the 620 nm channel. No reference correction was used.

maximum rating of 350 mA at 3.5 V. The 440 nm channel (i.e. the driving LED) shows increasingly anomalous behavior when powered below 280 mA at 3.3 V. The temperature controlled heat sink was the base plate of an Ocean Optics CUV-UV 1 cm cuvette holder attached to a water bath. The 440 nm absorbance trend shown in Figure A.19 follows the ambient temperature patterns (not shown). It is unfortunate, but not surprising that the temperature sensitivity is different between the two emission sources (blue 'driving' LED and phosphor). As a result, drift patterns are often observed at one

127

channel only, or in opposite directions. In general, the unpredictable behavior of STAR

LEDs makes them a questionable choice for spectrophotometery. On the other hand, the

drift is very small <0.001 hr^{-1}, and over short times (<10 min), incredibly stable at all

wavelengths. In addition, the optical throughput is very high at short wavelengths,

offering a higher s:n than a tungsten lamp[50].

A.2.1.3 Light sources: conclusions

Table A.1 summarizes the findings of the various light source tests (Section

A.2.1). In general, the optically stabilized tungsten halogen XLamp was the best source.

Table A.1 Drift (fully warmed up) characteristics of the light sources tested during this study, using the interference filter spectrophotometer and stirred flowcell. The noise for all measurements was detector-limited at ~ ±0.0002 au. The maximum observed range is the absolute value of the largest difference between two blank intensities for the times denoted in parenthesis (i.e. calculated from running absorbance values).

Light Source	drift (au hr^{-1})	maximum observed range	
		$_{440}A$(5min)	$_{440}A$(15min)
SAMI Tungsten (Al housing)	0.0020	0.0021	0.0030
CDI-TTL (current stabilized)	0.0010	0.0010	0.0010
XLamp (optically stabilized)	<0.0005	0.0003	0.0004
STAR (white LED)	<0.0010	0.0005	0.0006

The current-stabilized lamp (CDI-TTL) would probably perform better if isolated from

the ambient (room) temperature swings. The SAMI tungsten lamp drifted at the highest

rate. The white LED is promising, but its unpredictable wavelength-dependent drift

patterns raise concern. In general, the time in-between recording a blank and a sample

measurement is the most critical aspect of achieving precision absorbance measurements.

Because this time is controlled by flow rate and flushing efficiency the type of light

source used must provide stable operation over the required period. Because of the

---

[50] From a tungsten lamp to a STAR bright white LED the noise problems toggle between a problematic 440 nm channel using the tungsten lamp and a problematic 740-780 reference wavelength region using the LED. In this respect only, the tradeoff is in favor of the LED, because the reference wavelength is not a critical part of the measurement (i.e. if care is taken the reference channel is not required).

128

superior performance of the XLamp in these studies, it served as the primary light source during most of the titrations and εb measurements presented in Chapters 3 and 4.

A.2.2 Effects of polychromatic radiation at the detector

Because Beer's Law is derived for monochromatic light, wavelength selection using broad bandpass filters may result in deviations from linearity. The weighting method described below was used to theoretically predict these deviations for sulfonephthalein-type absorbance peaks. The magnitude of error is controlled by two factors: 1 – bandpass and 2 – range of molar absorptivities of the absorber over the bandpass. As a general rule, such deviations become negligible when the FWHM (or effective bandwidth) of the filter is less than 1/10 the FWHM of the absorption peak (Ingle and Crouch, 1988). The peak wavelength of each filter should also closely match the peak wavelength of the absorption peak. This helps minimize the range of molar absorptivities over the bandpass. The ratio of the FWHM for the 620 nm bandpass filters used in this study (FWHM = 10 nm) and the absorption peak for BCG I^{2-} ($\lambda_{max} = 616$ nm, FWHM = 80 nm) is 1/8. Since this ratio is slightly greater than desired, and the λ_{max} is not perfectly matched, deviations due to polychromatic radiation must be considered, and are discussed below.

A.2.2.1 Bandpass filters & Cary 300 intercomparison

We used a spectrophotometer built from bandpass filters (Figure A.20) to measure absorbance on neutral density filters in the absorbance range 0.3-2.2. Because of its broad bandpass at each channel (FWHM = 10nm), an interference filter-based spectrophotometer cannot be directly evaluated for photometric and wavelength accuracy using standards. An indirect assessment of these interference filters was therefore carried

129

out by comparison with the benchtop spectrophotometer (Cary 300 or Agilent 8453). If the Cary operates with good photometric and wavelength accuracy over the range of the spectrum used by the SAMI, absorbance spectra obtained on the Cary can be used as a secondary standard reference
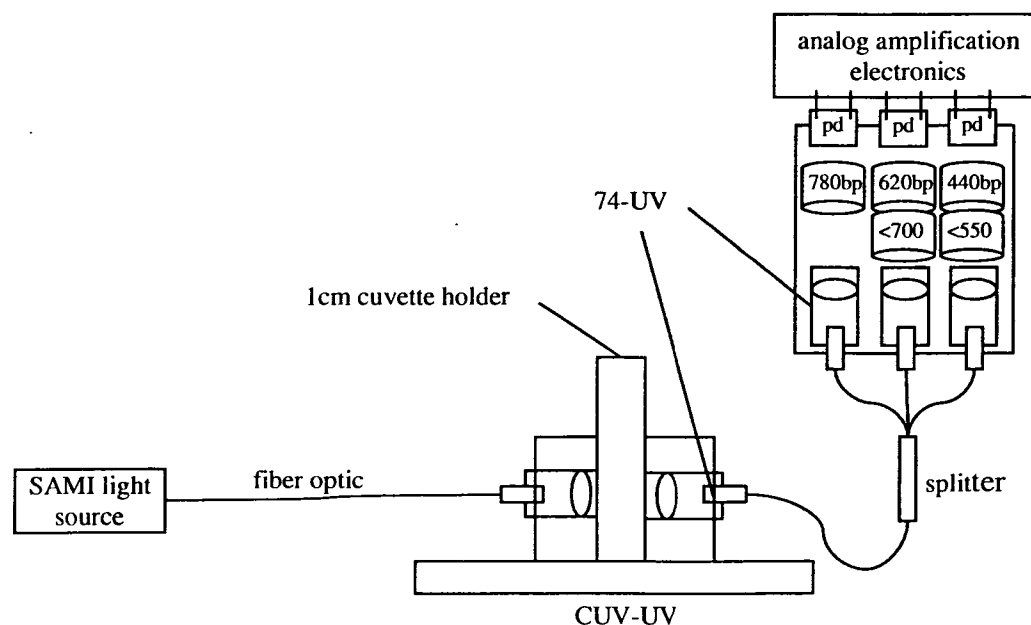
Figure A.20 Optical setup for the interference filter-based spectrophotometer used in the intercomparison experiment.

for SAMI absorbances. Comparison between the two instruments requires manipulation of Cary absorbance spectra, as described below. Because absorbance measurements on this system require very little time (< 1 min) between blank and sample, the SAMI light source (fully warmed up) provided sufficient optical stability.

Absorbance measurements on photometric standards are made by first recording a blank intensity with an open optical path. Next, a photometric standard is placed in the 1 cm cell holder (always in the same orientation) and the absorbance is recorded. For interference filter-based absorbance measurements of photometric standards (Figure A.20), an Ocean Optics CUV-UV 1 cm cell holder with fiber optic collimating lenses was used. Photometric standards are scanned on the benchtop instruments using the

130

conventional 1cm cell holders. For interference filter scans on the Cary and 8453, custom filter holders were built to ensure reproducible placement of an interference filter in the optical path. Replicates of blank followed by absorbance were made for all Cary and SAMI measurements for calculation of standard deviations.

A.2.2.2 Photometric and wavelength standards

Photometric standards (i.e. neutral density filters) were used to verify that the custom-built optical design is capable of a linear response over increasing optical absorbances. The purpose of wavelength standards in this study was to certify the spectrophotometer used for scanning interference filters. Interference filter scans were made to verify their center wavelength (CWL) and to obtain %T values for spectral weighting (Section A.2.2.3). Before this study, it was generally accepted that molar absorptivity ratios obtained on the Cary were valid for all SAMI-CO_2's. Therefore, a central goal in scanning the interference filters was to test the hypothesis that molar absorptivities or their ratios were instrument-specific values.

The photometric standards used throughout this study consist of six NIST-traceable neutral density (Schott glass) filters (Starna Inc. RM-1N2N3N, RM-N1N35N). Certified absorbance values of the photometric standards are reported for narrow regions of the spectrum (1 nm). For this reason, SAMI absorbance measurements on the photometric standards are not directly comparable to the certified absorbance values. As shown in Figure A.21 each filter absorbs a continuum of light across the visible spectrum with varying efficiency and wavelength dependence. The approximate % transmittance (%T) values are 1, 3, 10, 20, 30 and 50 %, corresponding to absorbances of ~2.0, 1.5, 1.0, 0.7, 0.5, 0.3 au.

131
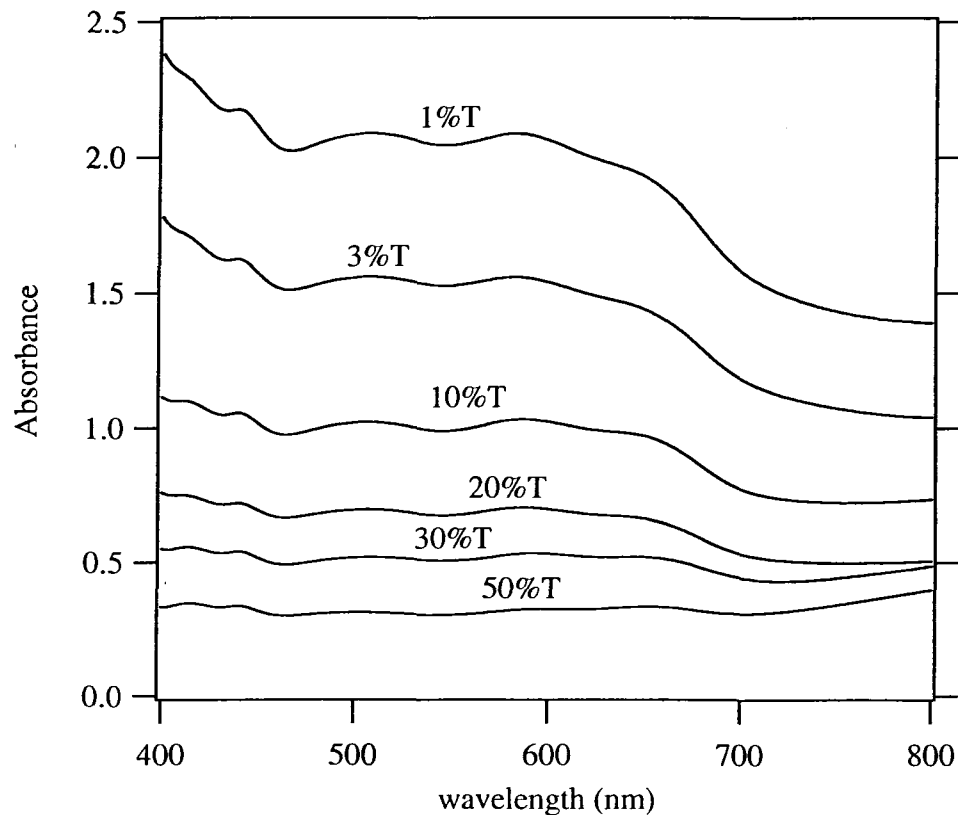
Figure A.21 Cary 300 Scans of the six photometric standards. Certified absorbance values are reported at 440.0, 465.0, 546.1, 590.0, and 635.0 nm.

Because interference filters cannot resolve wavelength standards (e.g. well-characterized emission lines or narrow absorbance peaks) a benchtop spectrophotometer (calibrated to a wavelength primary standard) served as a secondary standard in CWL measurements. Both the Cary 300 and Agilent 8453 run automatic internal wavelength accuracy tests by locating deuterium peaks at (486.0, 656.1 nm). A fiber optic coupler was also built for the 8453 (A.4.4), so it was straightforward to check wavelength accuracy on this instrument with a Hg-Ar line source (Ocean Optics HG-1). After the benchtop spectrophotometer passed this verification, an interference filter was scanned on the spectrophotometer, and assigned a CWL based on the peak transmission wavelength registered by the benchtop instrument.

132

Interference filters are prepared as large plates and then cut into hundreds of small pieces, each secured by a metal ring to preserve the exact cavity spacing (i.e. bandpass) of the original plate. According to the manufacturer (Intor, personal communication), CWL varies by 1-2 nm between each filter plate. In addition, CWL may vary by 1-2 nm, depending on the location from which a filter is cut out of a single plate. Achieving good reproducibility of a filter scan is challenging and, although it is unlikely to observe CWL shifts between replicate scans of the same filter, very small changes in the orientation of the filter in the light path of the scanning instrument can result in up to a 20% difference in normalized %T at ±4-5 nm from the CWL. For this reason, a filter holder was machined for the Cary, which vastly improved the reproducibility of replicate scans, reducing the difference in normalized %T at wavelengths ±10 nm from the CWL to <1%. Because each filter is slightly different (Figure A.22), the section of the Cary scan used to calculate indicator molar absorptivities (TMT) or their ratios (SAMI-pCO$_2$, pH) should be matched to each instrument using a %T scan of the exact filters in that instrument[51]. For example, a Cary absorbance scan of BCG I^{2-}, weighted by the two different filter scans shown in Figure A.22, differs by ~0.005 au.

Distortions of the bandpass may also result from the addition of short or long-pass filters to reduce stray light. As shown in Figure A.23, if the additional filter has a skewed transmission across the wavelengths of the bandpass filter, the combination of the two filters is distorted from that of the original the bandpass filter alone. In this case the distortion effect is relatively small (note the expanded scale on the insert in Figure A.23),

---

[51] Alternatively, absorbance measurements of indicator solutions can be made directly on each instrument...the approach ultimately taken in this study.

133

but such effects should always be considered during instrument design. A similar effect

is possible due to the varying wavelength sensitivity of a photodiode (see below).

Periodic verification of interference filter CWL is an important quality control

protocol. Due to minute expansions or contractions of the cavity spacing over time[52], an

interference filter may change CWL by 0.3-0.45 nm yr^{-1} (Andover Corp., CATA001-

PDF, Rev B., 2002). Given the harsh conditions encountered in the field, deployed

instruments should periodically be disassembled for interference filter tests.
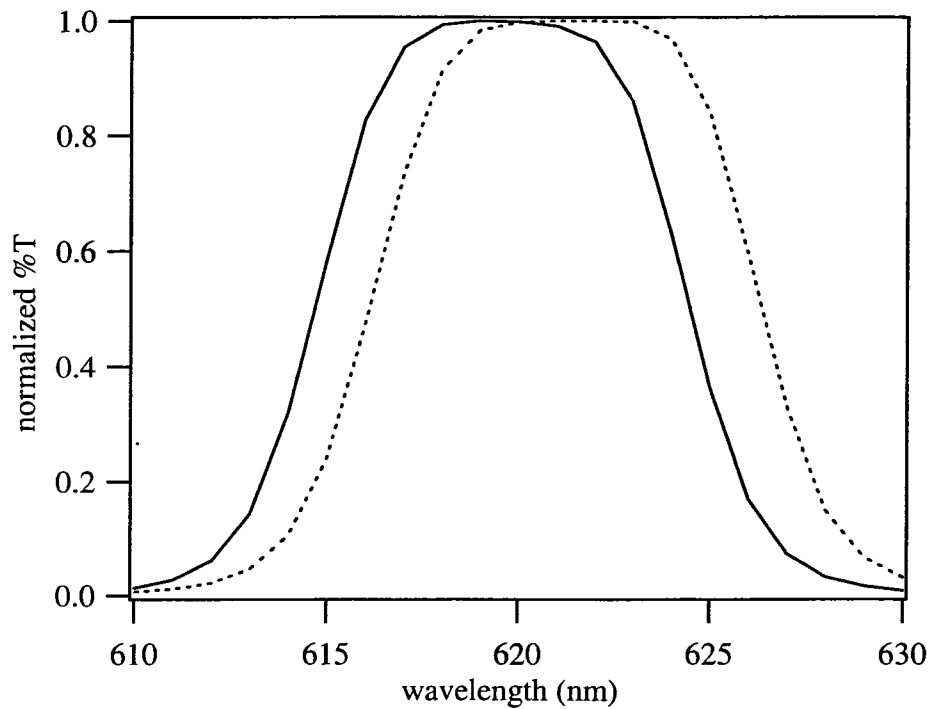
Figure A.22 Scans of two different 620 nm bandpass filters (Intor). The CWLs are 619 nm (solid line) and 621 nm (dashed line).

---

[52] This effect is exacerbated by frequent temperature fluctuations.
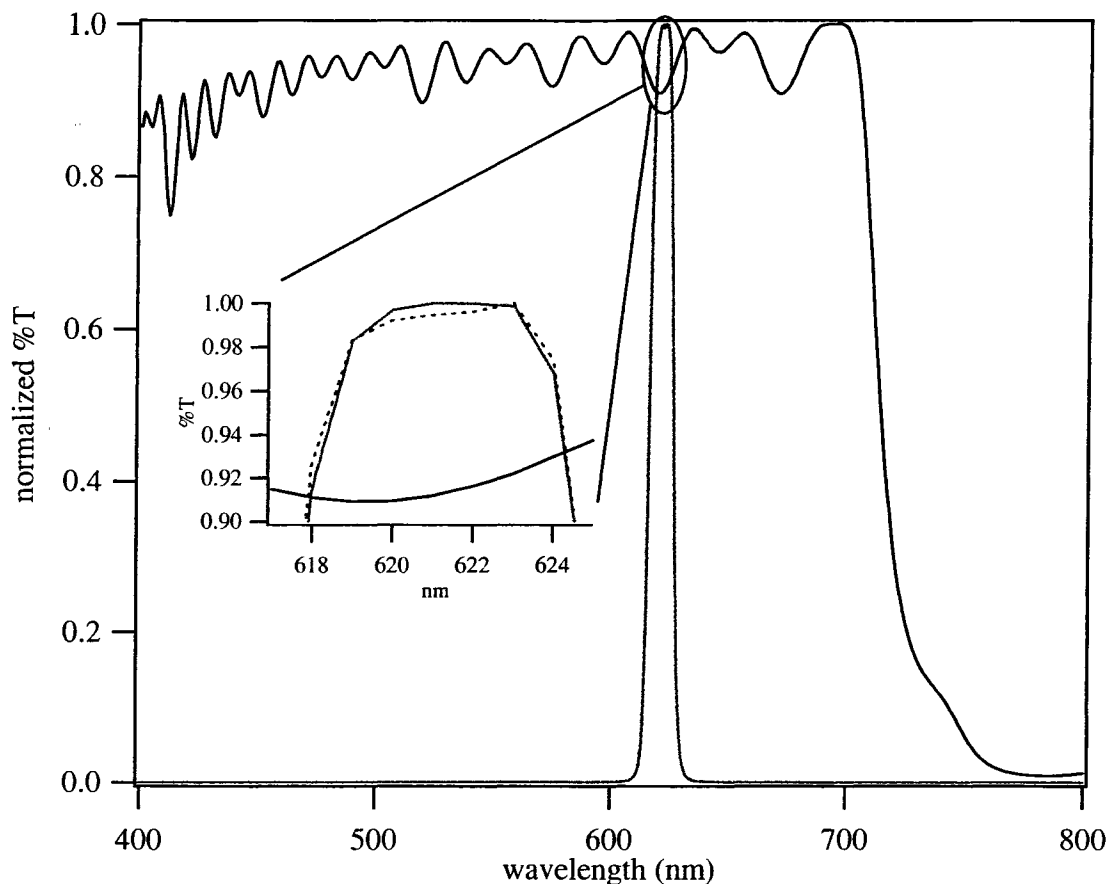
Figure A.23 A short-pass filter (black) placed over a 621 nm bandpass filter (red line) results in a distortion of the bandpass (dashed red line, inset).

A.2.2.3 Spectral weighting

A validation procedure was developed for the bandpass filter-based

spectrophotometer. The procedure involves scanning a photometric standard on a

benchtop UV-VIS and measuring the absorbance on the custom instrument (as described

in Section A.2.2.1). The bandpass filters are also scanned on the UV-VIS. After some

transformations (described below), absorbance measurements of the two instruments are

compared.

First, absorbance spectra recorded by the Cary are converted to %T for every 1

nm value. This is required because the TFX-11 is programmed to average dark, blank,

and sample digital voltage signals before absorbance is calculated for the interference

filter instrument. Next, Cary %T values for each wavelength ($\%T_\lambda$) are multiplied by a

135

spectrum of weights (W_λ) ranging from 0 to 1. The weights are obtained from a

normalized %T spectrum of the bandpass filter, previously obtained on the Cary. %T

must be weighted because the polychromatic light passed by a bandpass filter has a

distinct rejection slope (see Figure A.22). The absorbance value measured by the filter-

photodiode combination is therefore a result of absorbances spanning a range of different

wavelengths, resulting mostly from light at the peak wavelength of the interference filter,

and to a lesser extent from light at wavelengths extending to about ±10 nm from the peak

wavelength. A weighted average is calculated for the %T sample spectrum, using

Equation A.1,

$$\%T_W = \frac{\sum\limits_{400}^{800} W_\lambda T_\lambda}{\sum\limits_{400}^{800} W_\lambda} . \qquad\qquad \textbf{A.1}$$

$\%T_W$ is then converted back to absorbance ($_wA_{440}$ or $_wA_{620}$). This value is now

comparable to absorbance measured on the SAMI. For completeness, one may also

consider the wavelength dependent sensitivity of the detector by applying a normalized

spectrum of its wavelength sensitivity to the absorbance spectra, analogous to the

weighting method described here (see Section A.3.4.3, below).

A.2.2.4 Theoretical deviations due to polychromatic radiation

Calculations using interference filter scans and the molar absorptivity spectrum of

BCG illustrate the importance of bandpass and why measurements on one instrument

should generally not be expected to hold on an instrument with a different bp. Using the

molar absorptivity spectrum of BCG, several theoretical absorbance spectra were

generated (Figure A.24). As described in Section A.2.2.3, the normalized spectrum of an

interference filter was used to weight the absorbance spectra collected on the Cary. The

136
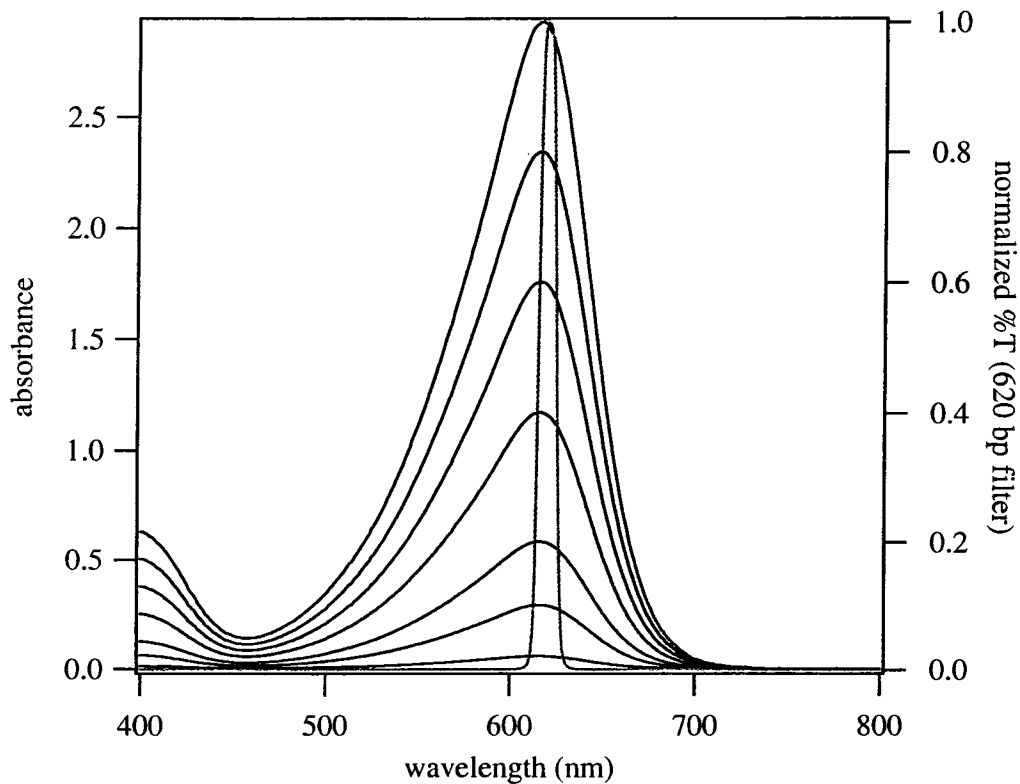
Figure A.24 Theoretical absorbance spectra (black lines, left axis) generated using molar absorptivities of BCG I^{2-} and seven arbitrarily chosen concentrations of indicator. The normalized spectrum of a 620 nm bandpass interference filter is also shown (red line, right axis).
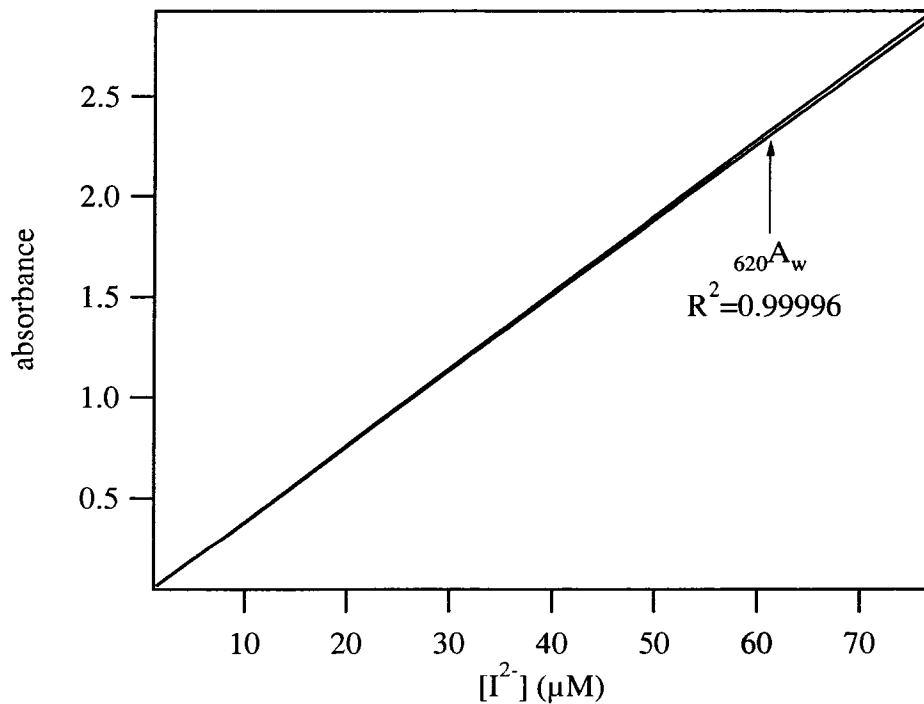
Figure A.25 Theoretical linearity plot for a single wavelength and a weighted portion of the spectrum (slightly lower line). Deviations from linearity are not readily apparent using this type of plot.

137

Cary absorbance value for the wavelength corresponding to the peak transmission wavelength of the filter, $_{620}A$, compared to the weighted absorbance value $_{620}A_w$ provides a drastic example of the difference between instruments. The deviation from linearity (Figure A.25) is small, but the difference between absorbance at 620 nm and the weighted absorbance is significant (Figure A.26). For example, absorbance errors of the magnitude shown in Figure A.26 result in spectrophotometric pH errors of 0.005-0.01, depending on the absorbance value and the channel (440 or 620 nm) at which the error occurs.
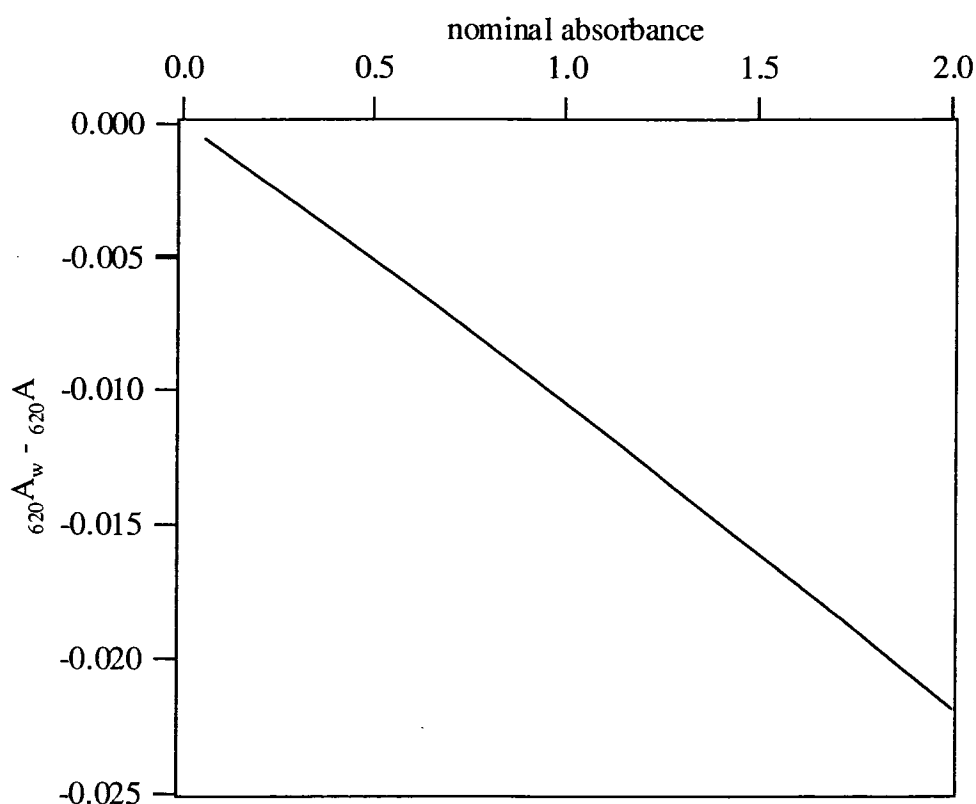
Figure A.26 The difference between absorbance at a single wavelength and a weighted portion of the spectrum.

A.2.2.5 Interference filter spectrophotometer-Cary intercomparison

Cary 300 scans were compared to absorbance measurements obtained with an interference filter spectrophotometer (Figure A.20). Figure A.27 shows the difference

138

between absorbance measurements on these two instruments, after the Cary data were weighted, as described in Section A.2.2.3. Because neutral density filters ranged from 0.3-2.2 au (Figure A.21) a BCG I^{2-} solution was used to collect absorbances below this range (Figure A.27, filled markers). Weighting the spectra typically moved the Cary absorbance value at the interference filter's peak wavelength ~0.001–0.002 au closer to the value measured using the filter-photodiode combination. The dashed lines in Figure A.27 represent the uncertainty (reported by Starna) in the photometric standards. With the exception of the 440 nm measurements on the 2 and 1.5 au filters, the absorbances
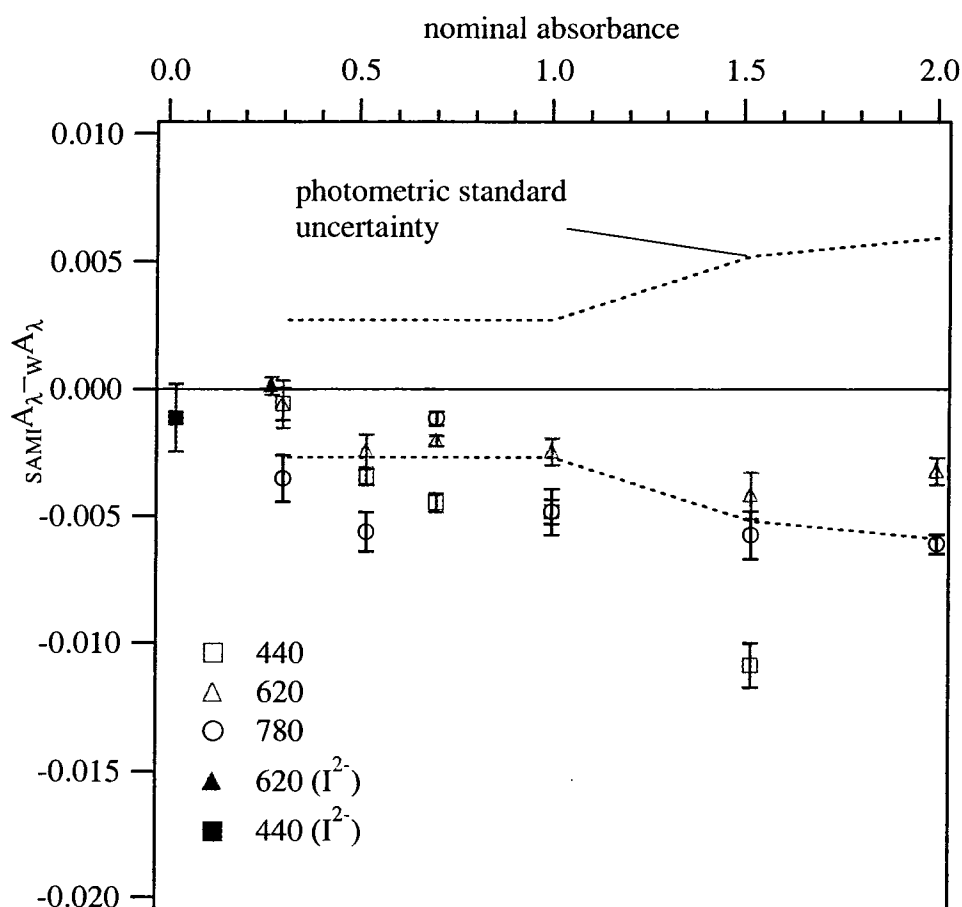
Figure A.27 Difference between absorbance measured by an interference filter spectrophotometer and Cary spectra, weighted using scans of the interference filters. Photometric standards were used for A = 0.3-2.0 (unfilled markers) and a solution of bromocresol green was used for measurements below 0.3 au (filled symbols). The A ~ 2.0 measurement for the 440 channel is not shown because it was limited by digital readout noise.

139

obtained on the filter-photodiode combination agreed to within ± 0.006 au. Due to digital

readout noise at the 440 channel, precision of the A ~ 2.0 standard was 0.017. There was

an insignificant difference between Cary spectra weighted with the full interference filter

scan versus the region of the scan ±20 nm from the filter's λ_{max}. In general, all three

channels measure absorbance ~0.005 au lower than weighted Cary spectra. In addition,

the 440 nm channel appears to have a negative trend. Because the trends between 0.1-1.0

(the range used by the instrument during titrations) show no drastic nonlinear behavior

(Figure A.27), we concluded that absorbance measurements for concentration

calculations from Beer's law would hold, given that absorbance was constrained to

values < 1.0; but that it would be necessary to measure all εb values on the custom-built

instrument, because absorbances used to calculate εb must be accurate to better than

0.0005 (see Section 2.3.1).

The effect of collimation at both the CUV-UV holder and the interference filter

(see Figure A.20) was also investigated (Figure A.28). Collimation effects at the cell

holder were tested by taking blank and absorbance measurements on photometric

standards, then adjusting the 74-UV barrel by ~ 1 mm or less to give an overall

throughput change of 25% and re-measuring blank and absorbance. Collimation at the

interference filter was tested by measuring absorbance with and without the 74-UV lens.

Adjusting the lens at the 1 cm cell holder typically resulted in a small, constant

absorbance shift (0.0005-0.001) for absorbances below 1.5 (data not shown). The effect

of collimation at the interference filter (Figure A.28) is more pronounced than at the

sample.

140
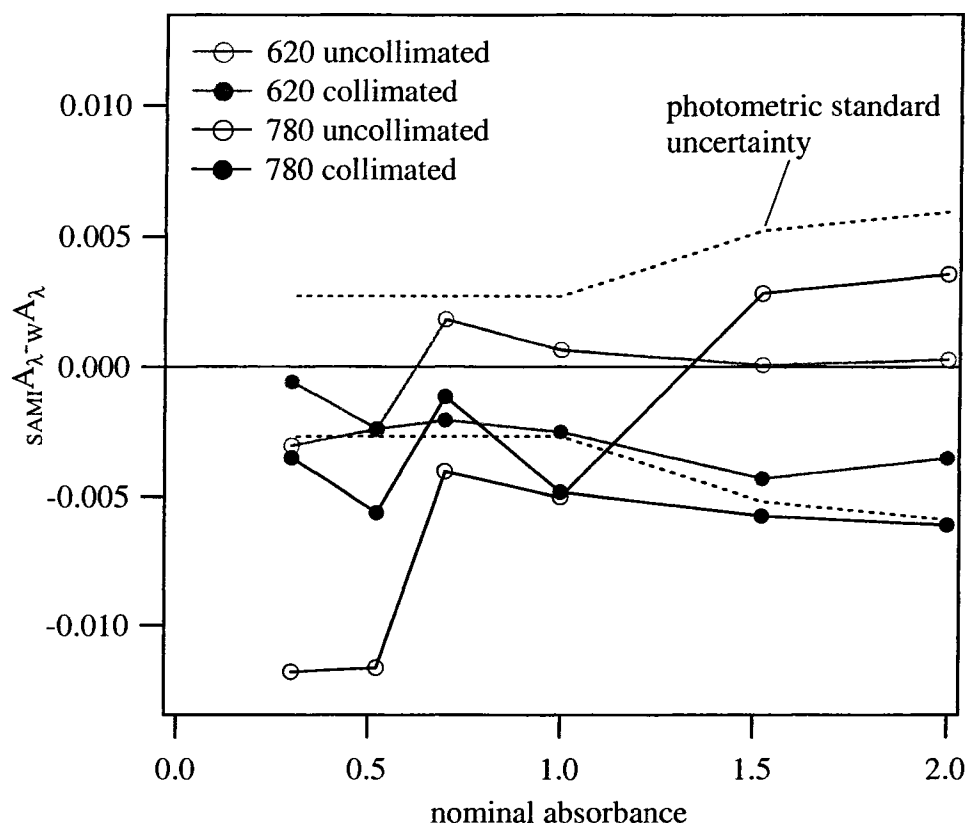
Figure A.28 Effect of collimation at the photodiode interference filter as the difference between absorbance of photometric standards, measured by an interference filter spectrophotometer, and Cary spectra, weighted using scans of the interference filters. Filled circles (data from Figure A.27) represent measurements where a fiber optic collimating lens (74-UV, Ocean optics) was placed in front of the interference filters. For empty circles, the lenses were removed so light passed from the bare tip of a fiber through an interference filter, to a photodiode.

A.2.3 Fiber optics

A.2.3.1 Types of fibers

The type, size and condition of fiber optics, used at both the source and detector ends of the flow cell, greatly influence the optical throughput. Between the lamp and Si of each channel's photodiode, there are nine optical interfaces where reflective losses occur. Based on the Fresnel equation (see e.g. Ingle and Crouch, 1988), a perpendicular beam of light passing through the optical system (Figure 3.1) should lose about 25% of its intensity. This calculation is based on the difference between refractive index (η) at

141

each interface[53]. For the short lengths of fiber used in this application (<1 m) light

attenuation by the fiber is far less critical than the type of fiber and its condition. In

general, all fiber faces should be inspected for scratches and cracks under a microscope

and polished at a near-perfect $90°$ angle. Polishing can increase optical throughput by up

to an order of magnitude. The fiber's numerical aperture defines the acceptance/exit

angle of light and is important for calculations involving spatial arrangement of the fiber

and detector (see Section A.3.4.1 below). Although plastic (polymethylmeth-acrylate,

PMMA) fiber optics are far more flexible and cheaper, they transmit less light than glass

(fused silica) fibers (Figure A.29). For example, typical attenuation values for a plastic

and glass fiber at 620 nm are ~200 db/km and ~3 db/km, respectively. Over a 1 m

distance, these levels of attenuation result is optical absorbances of 0.02 (5% loss) and

0.0003 (0.07% loss) for plastic and glass fibers, respectively. Early on, many experiments

were carried out using plastic fibers and/or a plastic fiber optic splitter but, based on

Figure A.29, glass fibers were used exclusively for later experiments. Because we used a

large, stirred flow cell, the issues associated with flushing are different than the issues

faced when using a low-volume fiber optic channel (i.e. a conventional flowcell). With

active stirring, dead volume is not a concern. Rather, flush time is the central issue that

causes problems[54]. Alternatively, low-volume fiber optic channels may suffer significant

errors due to tiny 'dead volume' pockets that slowly diffuse into the analyte solution. For

these reasons, very large fibers (1000 μm) were used to maximize optical throughput,

with no concern over dead volume.

---

[53] For this approximate calculation, refractive index is taken as wavelength-independent quantities of:
$\eta_{saltwater}$ = 1.3398; η_{fiber} = 1.5; η_{air} = 1.003. The percent loss is about 4.03% and 0.32% at the air-fiber and fiber-saltwater interfaces, respectively.
[54] Alternatively, FIA pioneers used stirred mixing chambers, but soon after, switched to static mixing because their priority was always speed, not ultra-high precision (Ruzicka, 1988).

142
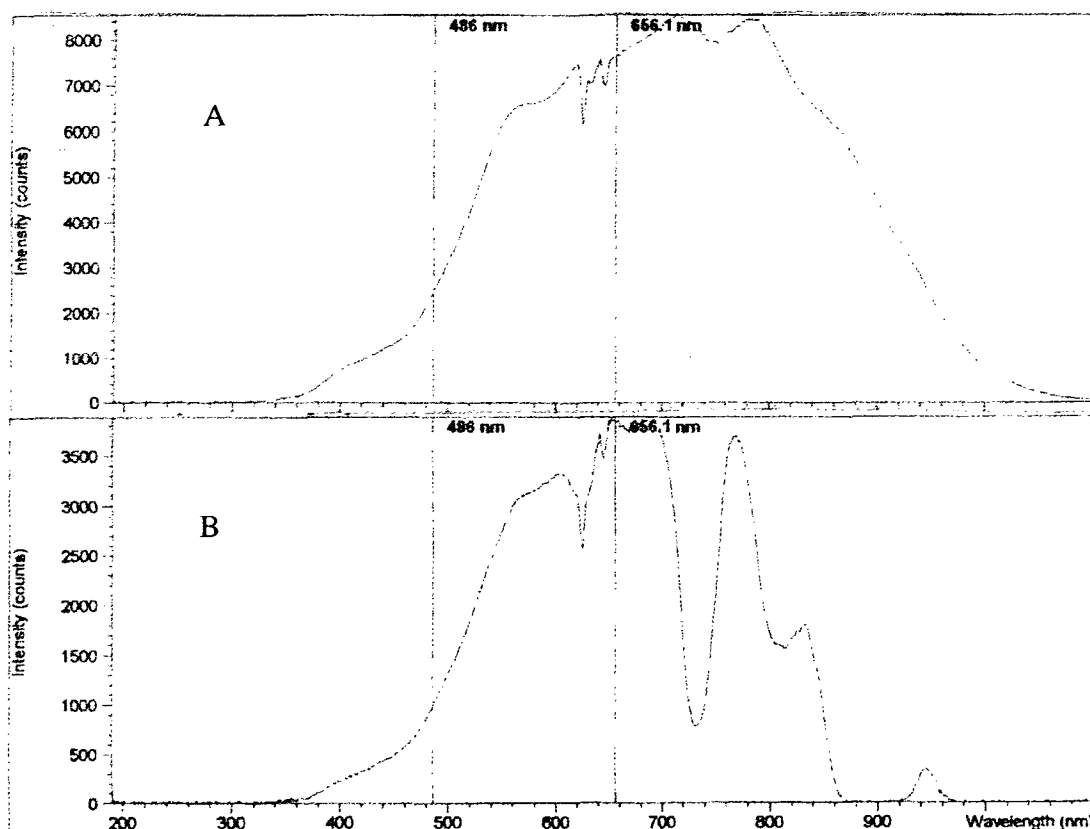
Figure A.29 Spectral attenuation of (A) fused silica and (B) plastic (PMMA) fiber optics. The optical configuration was tungsten lamp → source fiber → stirred flow cell with deionized water → return fiber → Agilent 8453 diode array spectrophotometer. The peak intensities are not directly comparable because the cell was disassembled to change fibers, which results in pathlength changes. In general, fused silica fibers have higher throughput (see text). The important features to note are (1) the large attenuation at ~735 nm and the reduced transmittance in the NIR, due to water uptake by the PMMA (Avakian et al., 1984). Plastic also attenuates light in the UV, but this feature is not apparent here because a tungsten lamp was the only light source used. Attenuation is wavelength dependent but, in general, plastic fibers attenuate 5-10 times more light than glass fibers. The vertical deuterium calibration lines are also shown.

A.2.3.2 Fiber optic lenses

A 74-UV fiber optic lens (Ocean Optics) was used for testing throughput and collimation effects on absorbance values. A discussion of the collimation experiments is given in Section A.2.2.5. The 74-UV unit contains a 5 mm diameter f/2 fused silica Dynasil lens with a 10 mm focal length. One end accepts an SMA 905 fiber optic and the other end terminates with a 3/8-24 external thread. Collimation of the lens requires very small adjustments of the SMA barrel (held in place by a set screw). It is therefore ineffective to calculate the distance between the fiber tip and the lens that would be

143

required for collimation, because the unit cannot be adjusted to this exact distance using length measurements by hand. The practicable procedure is as follows: (1) Couple an SMA 905 terminated fiber to a light source and plug the SMA end into the 74-UV lens. (2) Tightly secure the 74-UV and point it at a $90°$ angle to a surface 1-2 m away. (3) In dim light, adjust the SMA barrel until the circular spot has very crisp edges.

It was hoped that inserting a lens before each interference filter would increase optical throughput by cutting down on photodiode overfill (Section A.3.4.1). In practice the throughput gain from collimation was mitigated by reflective loss at the lens. Addition of a 74-UV lens reduced throughput by ~40%.

A.3 Electronics

This section details certain aspects of the SAMI electronics including some electronic design changes and elementary investigations of the components.

A.3.1 Shielding analog components

Electronic components are in close proximity inside the SAMI housing. Several controlled experiments revealed that moving the analog board away from the other components or turning the lamp circuit off reduces the detector noise. It was hypothesized that components on or connected to the power relay board (e.g. switching regulators, coils, and lamp circuit) might induce noise on the analog light detection electronics. In an effort to reduce detector noise, I tested the electronic shielding properties of several different materials by carefully wrapping the analog board in the material, reassembling the SAMI and monitoring dark signals. One of the most effective materials was a metallic bag used to hold SAMI reagents. Consequently, all SAMIs are now deployed with an analog shield made of a moderately thick aluminum alloy.

144

A.3.2 Analog signals

When no light strikes a photodiode, the digital signal recorded at its analog output (after amplification) is the dark signal. One must account for dark signals during both blank and sample measurements. It is good practice to calculate the theoretical dark signal, based on the photodiode amplification circuit (Figure A.30) and compare this value to that measured in the absence of light. The equation describing the output of this circuit is

$$\frac{V_{in}}{R_{in}} + \frac{V_{ref}}{R_{ref}} = \frac{V_{out}}{R_{fb2}}$$

A.2

where V_{in} is the voltage output from stage 1 (left side), V_{out} is the output analog voltage (after amplification), V_{ref} is an added bias voltage to ensure that dark signals are positive, R_{in} is the input resistor between stages, R_{ref} is the resistor at the voltage reference and R_{fb2} is the second stage feedback resistor. A capacitor, placed in parallel with the feedback resistor (Figure A.30), removes most of the ac noise caused by the switching regulators (not shown), input voltages, and thermal fluctuations in the feedback resistors. From Equation A.2 it is straightforward to calculate the theoretical dark signals ($V_{in} = 0$), given the values of the feedback resistor (R_{fb2}), reference resistor (R_{ref}) and the voltage reference (typically 2.48 V; LM385). From a purely theoretical point of view, the overall gain (V_{out}/V_{in}) is not readily calculable because it is not a simple problem to rearrange Equation A.2 to solve for V_{out}/V_{in}. In practice, it is necessary that the designer begin with an approximate value for the photocurrent, based on the optical throughput, and estimate V_{in} using $V_{in} = -I_{photocurrent}R_{fb1}$.

145
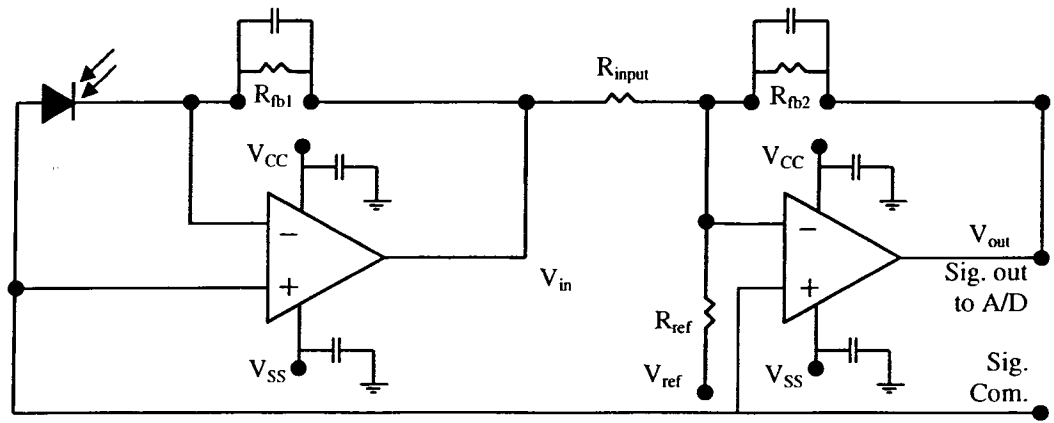
Figure A.30 Diagram of SAMI analog amplification board for a single photodiode. The first inverting op-amp stage (left) converts the photocurrent to a voltage and changes the sign. The second stage further amplifies the voltage and changes the sign again, giving a positive voltage to the A/D converter of 0-5 volts.

Another important aspect this circuit is the RC time constant of the feedback resistors, which dictates the response time between a change in photocurrent and output voltage. The time constant, in seconds, for each op-amp is the product of the feedback resistor's value in ohms and the feedback capacitor's value in farads. The response times are calculated to be ~1 sec at the first stage and ~0.004 sec at the second stage. Direct measurements of the response time were made by monitoring the output voltage with an oscilloscope and manually blocking then unblocking the light launching into a source fiber optic. Using this technique, the response time was measured as 2-3 sec. As described in Section A.3.5.2, switching regulators can be removed for benchtop applications. In this case, the feedback capacitors can also be taken out, reducing the response time no almost nil. It was found that when using a split power supply to power the op-amps, at least one capacitor should be left in parallel with a feedback resistor; otherwise, dark signal noise roughly triples. Therefore a fast response time (<< 1 sec) is achieved, without compromising precision, by removing the first stage parallel feedback capacitor and leaving a 0.10 μF cap at stage two. Table A.2 gives typical SAMI analog

146

gain configurations along with theoretical and experimental dark signal values for each

channel. The larger disagreement between theoretical and observed values at the 440

Table A.2 Common SAMI optical channel gain configuration and the corresponding dark signals. Photodiodes are S2386-44K (Hamamatsu). s.d. is standard deviation

channel	R_{fb1} (MΩ)	R_{fb2} (kΩ)	R_{ref} (kΩ)	V_{out} theor. dark (digital value)	V_{out} meas. dark (digital value)	digital s.d. (n = 300)
440	100	715	10000	0.177 (2324)	0.201 (2302)	1.0
620	100	40.2	402	0.248 (3251)	0.245 (3213)	0.7
780	50	40.2	402	0.248 (3251)	0.245 (3216)	0.6

channel is probably due to the difference in gain between 440 and the other two channels.

At high enough gain, the dark current of a photodiode becomes detectable and potentially

problematic. As described in the next section, a more through study of the A/D

converter's voltage accuracy was also carried out, as this could be another source of

error.

A.3.3 Tattletale TFX-11 voltage accuracy

Voltage accuracy, particularly a linear voltage response, is critical for accurate

and linear optical absorbance measurements. The voltage accuracy of the Tattletale

TFX-11 was tested using a variable DC power supply and a digital volt meter (Fluke 87

True RMS Multimeter) readable to 0.0001 V (Figure A.31). In this setup, the DC power
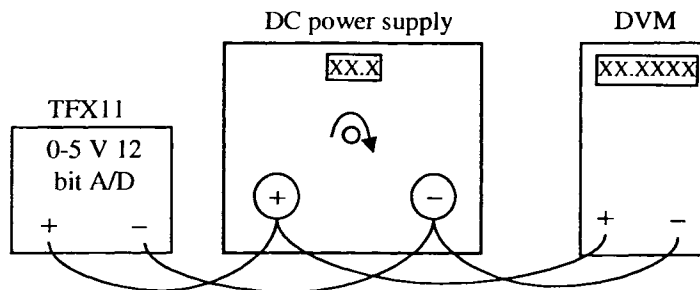
Figure A.31 Setup for simultaneously monitoring the same voltage using a TFX11 and a digital volt meter (DVM; Fluke 87 True RMS Multimeter).

147
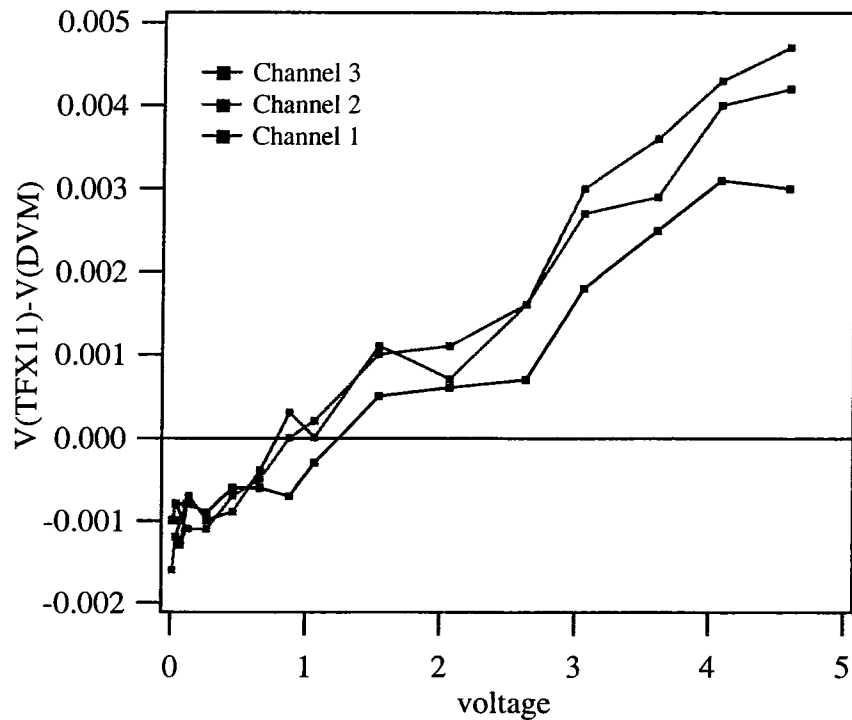
Figure A.32 Voltage disagreement between a Fluke 87 digital multimeter and Onset TFX11 datalogger.
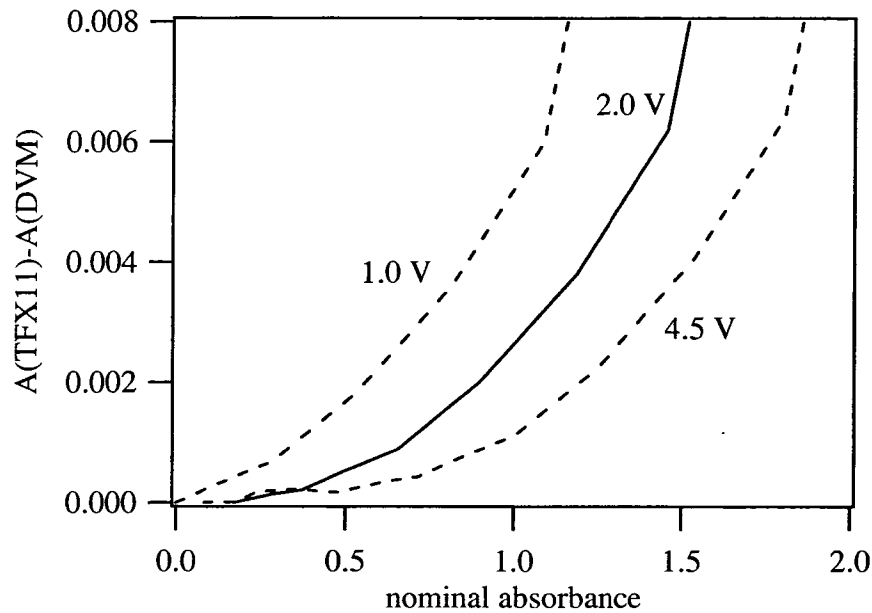
Figure A.33 The magnitude of absorbance error between the TFX11 and DVM depends on the voltage, V_o, during blank measurement of I_o. A typical V_o is 2.0 V (~27,000 digital counts). As shown by the dashed lines, raising the V_o to 4.5V by increasing optical throughput lowers absorbance error. Similarly, lowering V_o, by decreasing optical throughput increases absorbance errors.

148

supply simulates optical signals over the range of voltages characteristic of the amplified

photocurrent signal (converted to voltage) shown in Figure A.30 as V_{in}. The magnitude of

voltage error shown in Figure A.32 has a varying effect on measured absorbance through

digital readout, based on the blank voltage, I_0. Figure A.33 shows the absorbance (A = -

log(V/V_0)) calculated using the channel 2 data from Figure A.32.The data in Figure A.33

indicate that a threshold value should be set for the minimum V_0 or I_0 recorded during a

blank measurement. Furthermore, a maximum absorbance should also be set, based on

I_0. If the voltage accuracy (or error) of the readout electronics is known, an approximate
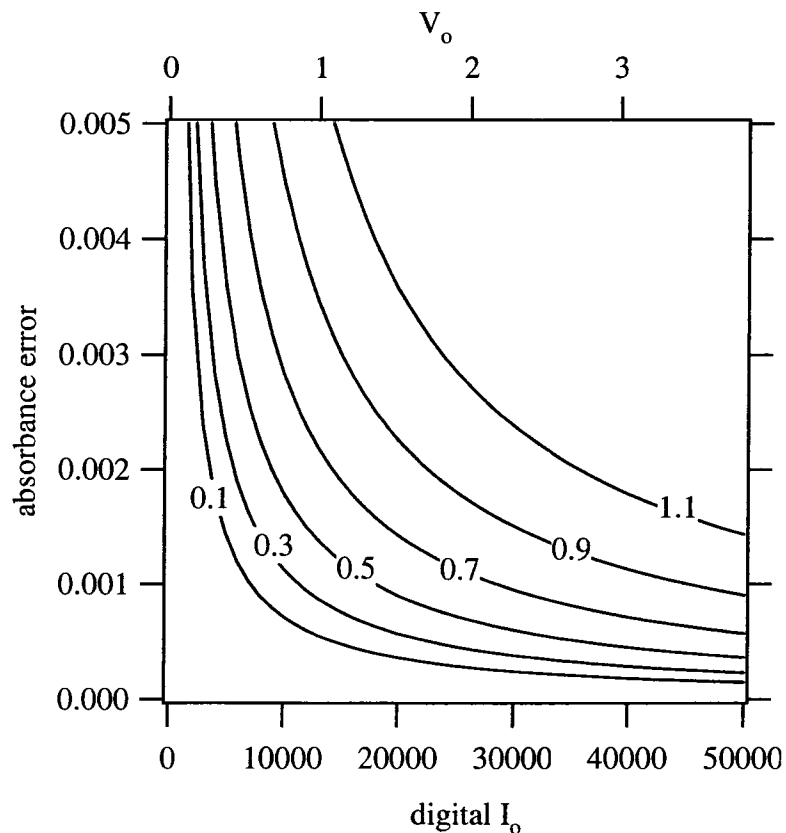
Figure A.34 Analog to digital readout errors. This graph helps set tolerances for minimum I_0 and maximum absorbance, given the desired maximum absorbance error. Based on optical throughput and gain settings, or observations, an I_0 (or V_0) is chosen on the x-axis. Drawing a vertical line up from the I_0 gives the maximum absorbance allowed (labeled lines) for the absorbance error limit desired (vertical axis). This graph represents a 0.001 volt error on a 12-bit A/D converter with a 0-5 V range (i.e. the TFX11).

149

value of the blank intensity can be used to examine the resulting absorbance error (Figure A.34). Because it is impractical to change gain every time the optical design is slightly altered, I_o tends to vary between experiments, which in turn shifts the absorbance range over which the TFX11 can be expected to operate properly.

A.3.4 Photodiodes

Hundreds of different photodiodes are commercially available from scores of different companies. Hamamatsu is the leading manufacturer of high quality OEM photodiodes and these studies were almost exclusively carried out using their products. Several important factors one should consider when choosing the right photodiode are discussed below.

A.3.4.1 Filling active area

If a photodiode is to be illuminated by an un-focused and un-collimated fiber optic, it is desirable to place the fiber at a distance from the photodiode such that the active area is filled, but not *over* filled (Figure A.35). Over filling a photodiode's active
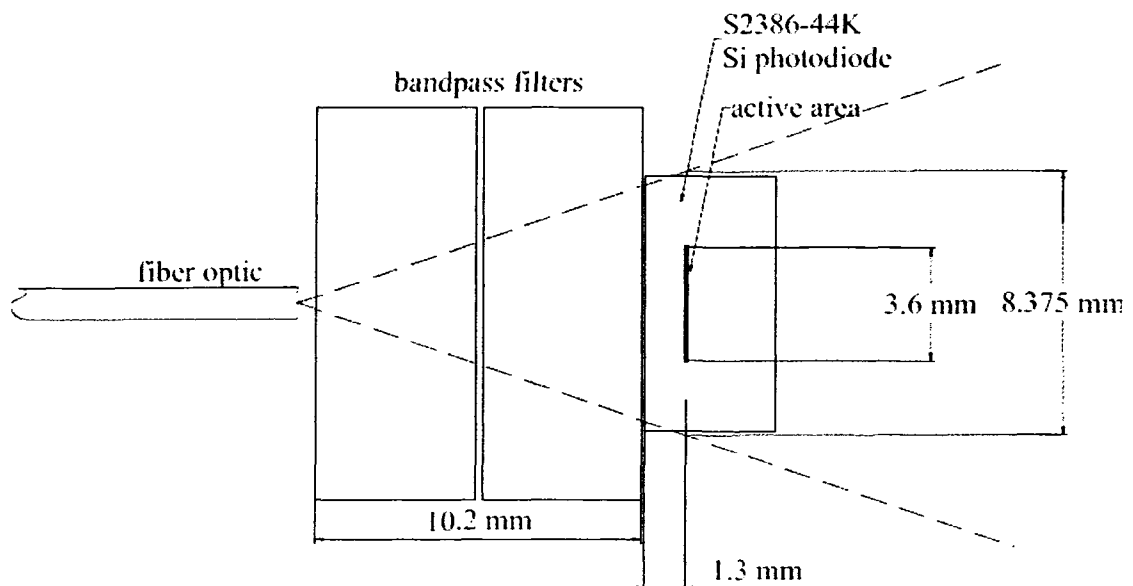
Figure A.35 Geometry of filling the active area of a photodiode. In this case, due of overfilling, more than 50% of the signal is lost. Values used in the calculation were $NA_{fiber} = 0.43$, $\theta_o = 19°$, $n_o = 1.34$.

150

area compromises performance by reducing optical throughput. Often, it is not possible to butt a fiber up against the photodiode's protective glass cover, because optical filters must go in-between. Simple geometrical calculations show that the dual bandpass filter configuration used in this research overfills the active area (Figure A.35).

A.3.4.2 Dark signals

In theory, there is no dark current flowing through a photodiode unless a reverse voltage bias is applied (e.g. high frequency and very high speed response applications) (Hamamatsu, KSPD0001E01). Nonetheless, at very high gain a small signal may appear, which is difficult to explain otherwise (Section A.3.2). SAMI dark signal noise is due mostly to amplifier readout noise, which is comprised of signal processing noise and resolution limits of the A/D converter (Ingle and Crouch, 1988). The most important component of the signal processing noise is the Johnson noise, due to thermal electrical noise.

A.3.4.3 Wavelength sensitivity

Depending on their semiconductor material, photodiodes have different wavelength sensitivities. Most Si photodiodes exhibit peak sensitivity in the NIR (~960 nm), while compound semiconductor (e.g GaP, GaAsP) photodiodes are most sensitive from 600-700 nm. These properties can be exploited to reduce stray light, but won't increase optical throughput because compound semiconductor photodiodes have an overall lower light sensitivity[55].

---

[55] Earlier versions of the SAMI used GaP photodiodes at 434 nm to reduce stray light. Due to anomalous behavior at this (very high gain) channel, the GaP photodiode was eventually replaced by a Si photodiode with an optical filter to eliminate NIR stray light. It is unlikely that the anomalous behavior was due to faulty photodiodes, but rather, was probably related to poor soldering techniques that damaged the analog components. A systematic study of the anomalous GaP behavior was never conducted.

151

Wavelength sensitivity also may play a secondary role in the absorbance errors discussed in Section A.2.2.4. If the wavelength sensitivity of a photodiode is changing at a steep rate over the wavelengths passed by a bp filter, the absorbance value measured at that channel may suffer a bias toward the wavelengths of higher sensitivity on the photodiode. As a simple example, consider a photodiode illuminated by light comprised of two slightly different wavelengths of intensity $\lambda_1 I_o$ and $\lambda_2 I_o$. If both intensities drop by the same amount, the measured absorbance represents the true absorbance for both wavelengths. If the intensity at $\lambda 1$ remains constant and the intensity at $\lambda 2$ decreases, the measured absorbance will be lower than the actual absorbance at $\lambda 2$. This negative error is the well-known effect of stray radiation at a non-absorbing wavelength. If the detector is more sensitive to $\lambda 2$ (the absorbing wavelength) than $\lambda 1$ (the non absorbing wavelength), the negative error in the measured absorbance is reduced; likewise, with greater detector sensitivity at $\lambda 1$ than $\lambda 2$ the negative absorbance error is enhanced. Detector wavelength sensitivity can therefore be regarded as a reinforcing or reducing mechanism on the effects of stray light or polychromatic radiation. Given a sufficiently narrow spectral bandpass and low stray light, the effects of detector sensitivity to wavelength are negligible. The wavelength sensitivity of the photodiodes used in this project is shown in Figure A.36. Because stray light is very low (Section 3.7), the factors that dictate whether or not this sensitivity will be significant are interference filter bandpass and steepness of the absorbing medium over this bandpass. To test the sensitivity, two wavelengths passed by the interference filter were chosen, 618 and 622 nm. Based on the interpolated values of detector sensitivity (Figure A.36) and the observed difference in absorbance for the BCG I^{2-} peak between 618 nm and 622 nm, it

152

was found that the absorbance difference due to the detector sensitivity effect was

0.00005 au. No experiments were carried out to further test this effect, as it was shown to

be secondary, but in theory it exists and should therefore be kept in mind when

optimizing the performance of an instrument.
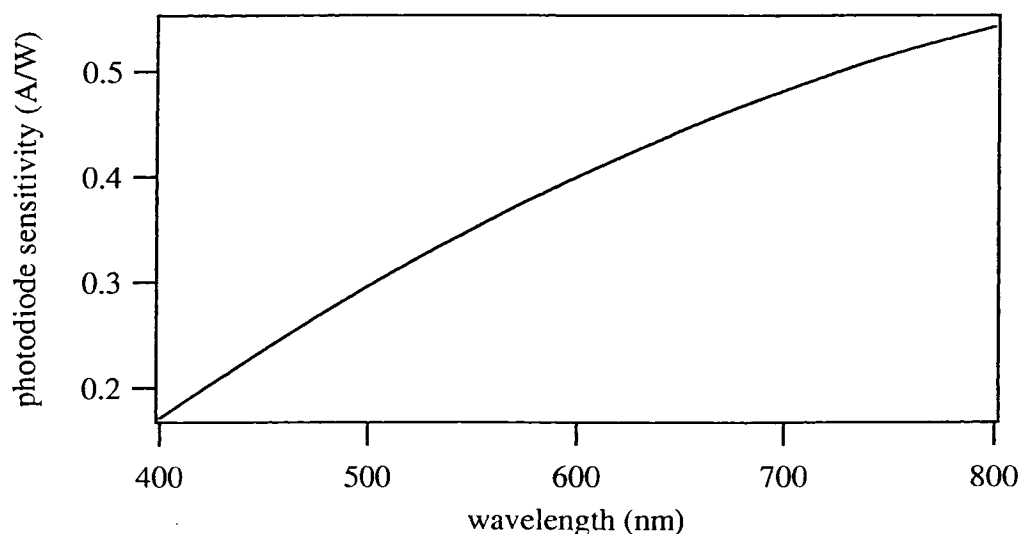
Figure A.36 The photosensitivity of Hamamatsu S2386 Si semiconductor material. This response curve was interpolated using several points in the visible spectrum, as reported by Hamamatsu (Cat No. KSPD1035E02). The equation fit to the points is A/W = -$1.074{\times}10^{-6}(\lambda^2)+2.2186{\times}10^{-3}$ (λ)-0.54514.

A.3.5 Operational amplifiers

A.3.5.1 Input offset voltage warm-up drift

When power is applied, all operational amplifiers undergo an input offset voltage

warm-up that affects the output voltage. Summarized from Horowitz and Hill (1989):

- Op-amp self heating can cause drift (pp 399).
- Low light levels may pose problems when using photodiodes, due to the op-amp's input offset voltage (on the bias voltage) in combination with the photodiode's dark resistance (pp 996).

Because the voltage change associated with this warm-up is very slight (Figure A.37), it

is typically an insignificant fraction of the input voltage and, therefore, does not

appreciably change the op-amp's output voltage. As seen in Figure A.38, at high gain the

warm-up is a serious problem.

153

INPUT OFFSET VOLTAGE WARM-UP DRIFT
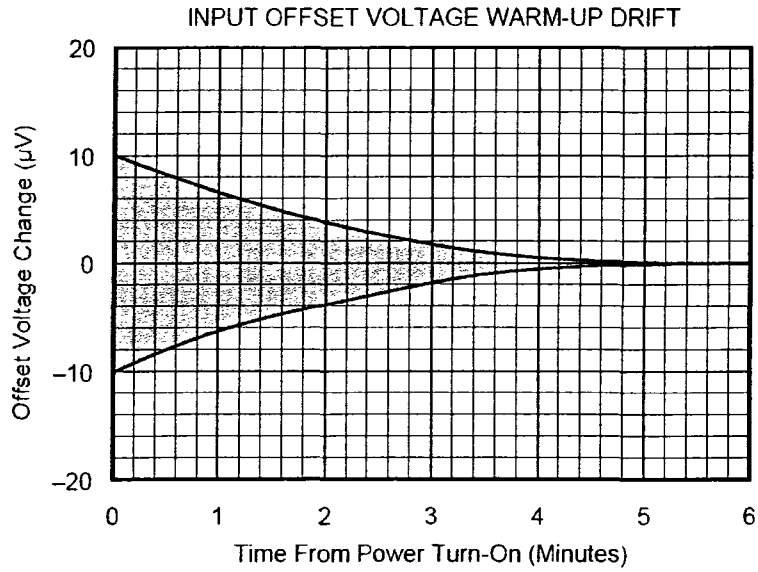
Figure A.37 OPA111 input offset voltage warm-up drift reported in the Burr-Brown datasheet[56].
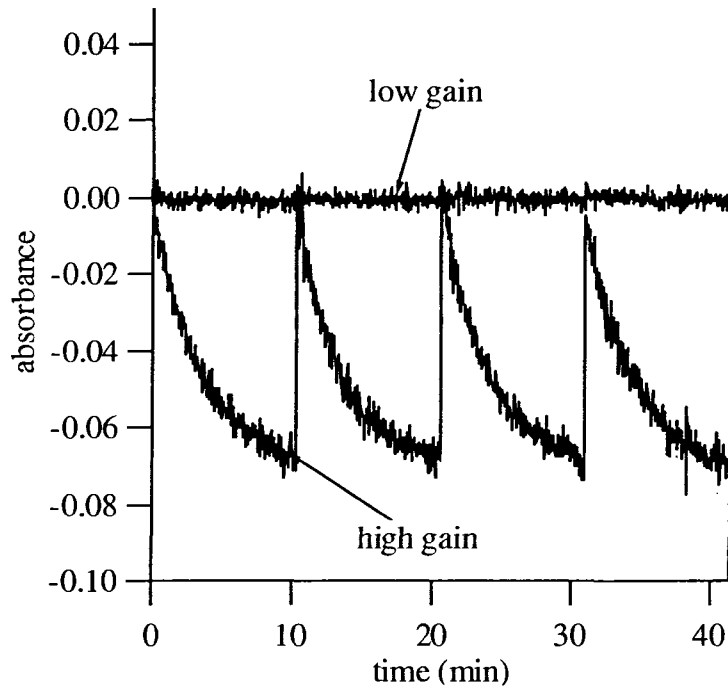
Figure A.38 The input offset voltage warmup drift expressed on the absorbance scale. On this graph 0.07 absorbance units is about 20 mV at the analog output. The op-amps were powered off and allowed to cool for 15 minutes at ~10, 20 and 30 minutes (the timescale is condensed to show only times when the op-amps were on). High and low gains correspond to the 440 and 780 nm configurations in Table A.2, respectively.

---

[56] The LT1097 op-amp (located at the second SAMI amplification stage also has a warm-up drift, but the large gain at the first stage makes the OPA11's drift most important.

The effect of this drift is not predictable. Different op-amps of the same type may exhibit quite different warm-up drifts in both positive and negative directions. The extreme case shown in Figure A.38 is the most drastic case encountered in our lab, but it is not of an unreasonable magnitude. Solving Equation A.2 for $V_{out} = V_{ref} + 0.020$ (see Figure A.38 caption), and using the typical resistors (Table A.2) gives a corresponding V_{in} change equal to ~25 μV, this is the calculated input offset voltage warmup drift for stage 2 (right side) in Figure A.30. In addition to gain, several factors affect the performance of op-amps including soldering temperature and ambient temperature. If a drift as dramatic as that shown in A.38 is observed, the analog board should be questioned, troubleshot and, possibly, replaced[57]. For the highest precision measurements, dark signals should be observed for warm-up drift and op-amps should be allowed to warm-up for an appropriate amount of time before the first absorbance measurement is recorded.

A.3.5.2 Switching regulator vs. split supply voltage

A switching regulator is an analog component that converts a voltage of single polarity (e.g. 0 to +12 V) into a pseudo split polarity of + and - voltages (e.g. -12 to +12 V). Most op-amps require a split power supply, and because SAMI's run off of the single supply of a battery pack, switching regulators furnish the positive and negative voltages. The high-frequency voltage swings in a switching regulator add noise to the analog circuit, making them an undesirable component in any precision circuit (Burr-Brown, R.

---

[57] The board used to conduct this particular experiment was exhibiting a low voltage error of ~60 mV at the 440 nm channel, hence the abnormally large change in absorbance units with dark signal drift (Figure A.38). Nearly every analog component shown in Figure A.30 was systematically replaced and the board was tested but no change in drift was observed. The component change with the most significant effect on this drift is lowering the feedback resistor R_{fb1}. During this study, similar drifts were observed on many other analog boards.

155

Gonzalez, personal comm.). For the benchtop study reported here, I removed switching regulators from the SAMI analog electronics and powered each op-amp with a benchtop split power supply (Mastech HY3003). As shown in Figure A.39, the split power supply gives much lower noise than a switching regulator. It has recently been shown that single supply op-amps achieve noise levels similar to the switching regulator-based design[58] (M. Seidel, pers. Comm.). Although no switching regulators are present in the single supply op-amp, the circuit itself is inherently noisier and the s:n is still compromised using this design (Maxim Application Note 656, 2000). Because this study required absorbance noise of ±0.0005 au or better, a split supply remains the best approach.
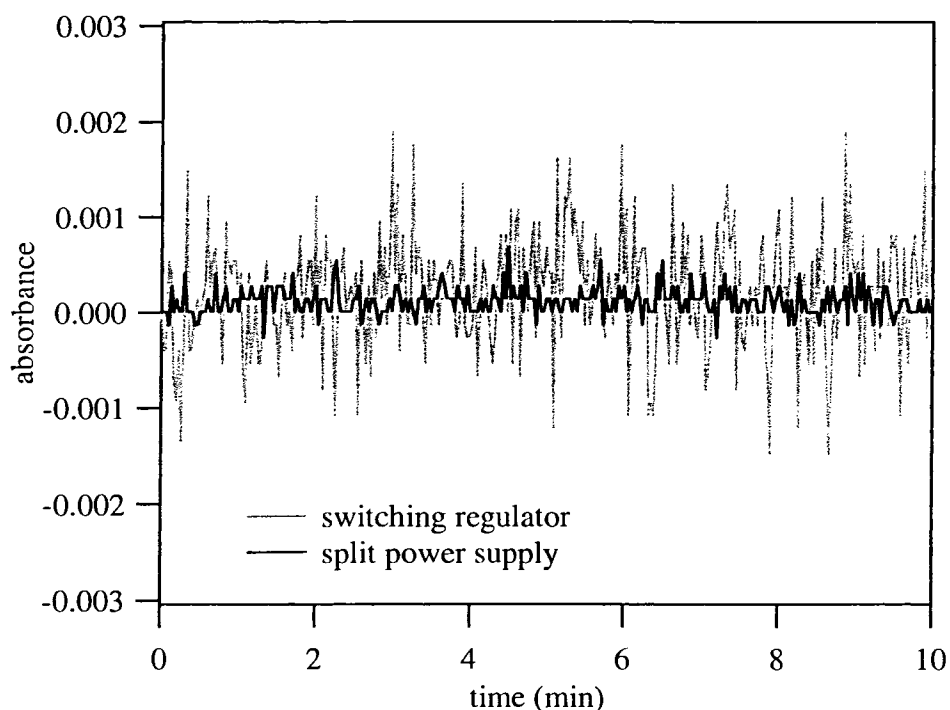
Figure A.39 The difference in dark signal noise between an op-amp powered by a switching regulator (MAX636, grey line) and a split voltage power supply (black line). The standard deviations (n = 300) correspond to ±0.0006 au and ±0.0001 au for the switching regulator and split supply, respectively.

---

[58] A third option that holds potential, but has not been explored is using a charge pump converter in place of the switching regulator.

A.4 Alternative components

A few devices were tested and never implemented as part of the titration system.

They are, however, worth mentioning for future reference.

A.4.1 Integrating a photodiode

The SAMI analog amplification circuit shown in Figure A.30 is commonly known as a transimpedance amplifier. In this configuration, a photodiode's photocurrent flows through a feedback resistor, producing an instantaneous voltage proportional to the photocurrent. A couple of drawbacks to this design are (1) changing the gain requires soldering in different feedback resistors, a serious detriment to the lifetime of the analog board and (2) input op-amp voltage may be imposed across the photodiode, causing linearity errors (Baker, 1997). An alternative to the transimpedance amplifier is a switching integrator. This design replaces the feedback resistor in a transimpedance circuit with capacitors and switches. The integrating amplifier operates by charging up a capacitor with the photocurrent when a switch is opened, and dissipating that charge when the switch is closed. Altering the analog gain then becomes a programming step rather than a soldering step. Although more convenient regarding gain optimization, integrating a photodiode requires a considerable amount of programming expertise (e.g. writing machine code for timing diagrams) and a detailed understanding of sophisticated electronic components (e.g. programmable gate arrays)

Attempting to circumvent the time required to build the integrating counterpart to the SAMI analog board, we purchased a DDC112 evaluation fixture (DEM-DDC112U-C) from Burr-Brown/Texas Instruments. The DDC112 is a 28-pin chip consisting of two integrating circuits and a 20-bit analog to digital converter (i.e. an integrating, charge-digitizing chip). The evaluation fixture holds the DDC112 on a DUT (device under test)

157

board, which connects to a PC-interface board, allowing convenient PC control using software provided by Burr-Brown. A battery of tests was run on the chip. Electrical current was injected into the board using (1) an illuminated photodiode connected directly to the DUT board (2) a 13 volt battery with a potentiometer and (3) a variable power supply (Mastech HY3003D). The battery and power supply were both connected to the DUT by BNC cables.

The DDC112 achieved very low RMS noise levels for single data acquisitions. For example, using a battery supply set to ~9V with Z2 = 1MΩ (see Figure 2 in DEM-DDC112U-C User Guide) and integrating 1024 times for 100 μsec each with a 300 pC maximum range gives an rms noise equivalent to a blank absorbance noise of ±0.000002 (s:n ~ 200,000). Noise begins to rise as the input current decreases, but very low levels were still achieved using illuminated photodiodes (Table A.3). The evaluation fixture

Table A.3 Signal:noise (s:n) and timing results for integrating a photodiode. The light source was a SAMI lamp and housing (Section A.2.1.1) operated at 5.0 V. I_T is integration time, t_{ac} is the total acquisition time (integration + processing) for 50 points. Photodiodes were Intor 440 nm filter-photodiode combined package (T5) or Hamamatsu 1226-44BK. The external integrating capacitors for each channel were set to give similar readout signals of ~70-80% of A/D saturation (see text).

Configuration	I_T (μsec)	t_{ac} (sec)	s:n 440	s:n 620
source fiber → 440nm filter-photodiode	500	< 1	26,600	NA
source fiber → flowcell → collection fiber → 440 nm filter-photodiode	100,000	16	11,000	NA
as above	50,000	8	8,600	NA
as above	10,000	1.5	1,200	NA
source fiber → flowcell → collection fiber → 3-way fiber splitter → 440 and 620 dual bandpass filters → 44BK photodiode	1,000,000	135	2,600	21,800
as above	100,000	15	1,900	17,100

Increasing optical throughput ↑

158

comes with factory-installed internal capacitors and an option to install external capacitors. For an integrating circuit, smaller capacitors charge up faster giving a full signal with less integration time. The tradeoff is noise. A smaller capacitor dissipates a smaller charge, resulting in a lower analog signal. In the PC control program, the range of current to be charge-digitized can be altered so that the digital signal remains at a maximum, but this does not make up for the lost analog signal. External capacitors were used for all experiments shown in Table A.3. As shown in Table A.3 s:n decreases with losses in optical throughput. The time required to achieve an acceptable s:n at the 440 channel for a flowcell configuration was impractically long (> 15 sec per acquisition) for a multipoint titration (Table A.3). As both integration time and number of points (for signal averaging) increase, processing time becomes a significant component of each acquisition time[59]. For example, the second configuration shown in Table A.3 required 5 seconds of integration time, but processed for 11 seconds. Unfortunately, separating the integration channels from each other (i.e. one acquisition with two different integration times) would require customizing the DUT board for independent integrating op-amps and rewriting the machine code[60]. Despite the complexity of this design, if acquisition time is a major concern, multi-channel integration offers advantages over semiconductor arrays (e.g. photodiode, CCD), which use shift registers (see also Section A.4.3 below). We concluded that designing a working absorbance-based spectrophotometer from the DDC112 would require resources in time and expertise that were not at our disposal. This experiment was, however, an important first look at the performance that could be expected using the available SAMI components and the vastly improved potential that

---

[59] Processing time compounds with longer integration times.
[60] Not a simple task, considering the complexity of the evaluation fixture.

photodiode integration may hold if, in the future, optical throughput is boosted by a factor of ten or more.

A.4.2 Photomultiplier tube

The short wavelength channel (430-440) on all SAMIs is problematic. In this region of the spectrum the intensity of a tungsten light source rapidly diminishes (Figure A.8) and all photodiodes are less sensitive (Figure A.36). Consequently, pushing the 440 nm channel amplifiers to the absolute limit of their gain increases the detector noise and augments other issues such as op-amp input offset voltage warm-up drift (Section A.3.5.1) and dark signal errors due to photocurrent (Sections A.3.2 & A.3.4.2). A photomultiplier tube (PMT, Hamamatsu H5784-01) was tested as an alternative light detector at the 440 nm channel because PMTs are much more sensitive than photodiodes, especially at shorter wavelengths.

The PMT was set up for resistance programming with a 10 kΩ potentiometer (pot, Digikey 5AG14BK-ND). Light signals from a SAMI tungsten lamp were collected on a flowcell blank for 12 minutes with the pot set at 1.15 kΩ. Using this configuration, signals were ~0 and 35,000 (2.7V) for dark and blank, respectively. As shown in Figure A.40, the blank absorbance noise was ±0.001 au. The ~0.001 au drift is probably due to the normal drift of the tungsten lamp (Section A.2.1.1). With a resistor in place of the potentiometer, the PMT noise was identical (Figure A.40B). Voltage programming was also investigated, but did not reduce the noise (data not shown). Because absorbance precision better than ±0.001 was required, PMT-based absorbance measurements were not further investigated.

160
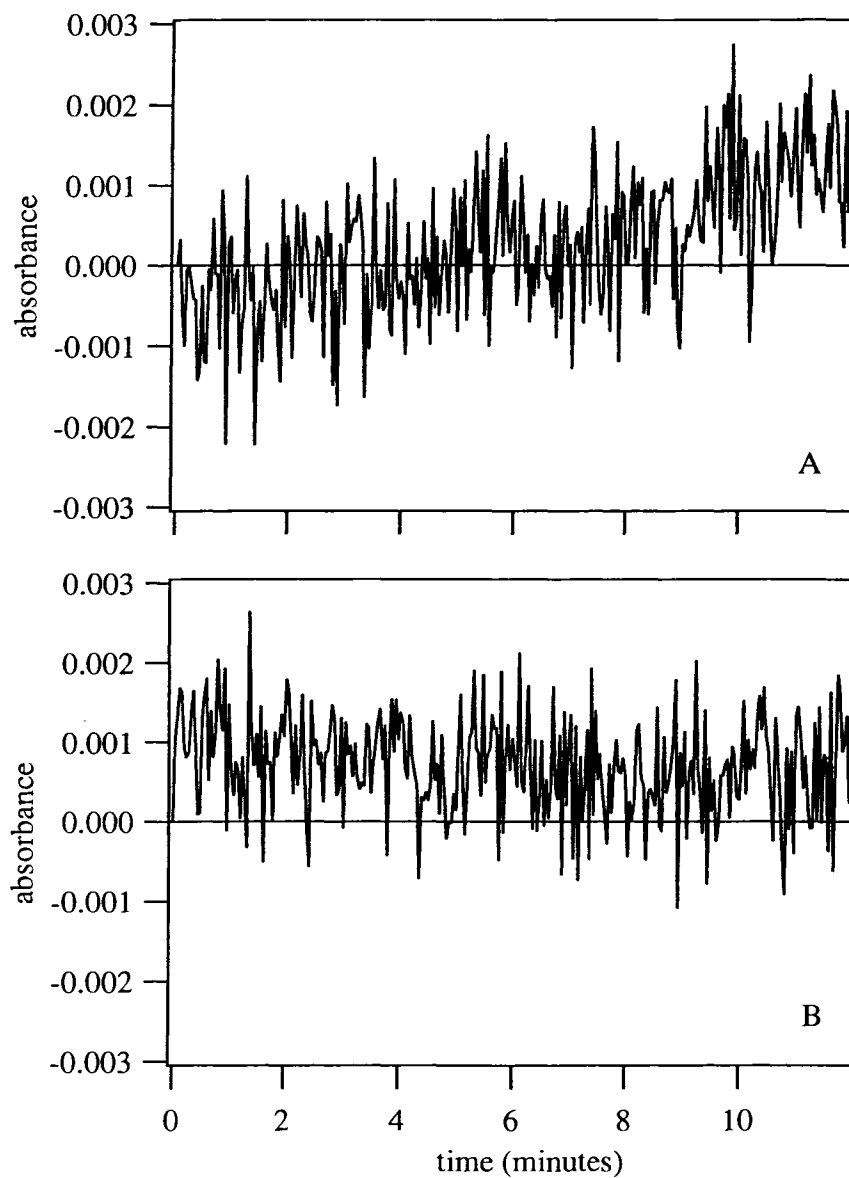
Figure A.40 PMT blank absorbance noise in resistance programming mode using A) a potentiometer and B) a soldered-in resistor. The PMT achieved precision around ±0.001 in both resistance and voltage programming mode.

A.4.3 CCD array

An Ocean Optics USB2000 (diffraction grating and charge coupled device array)

was evaluated as an alternative detection system. The purpose of testing an alternative

detector was driven mostly by the goals of reducing noise at the 440 nm channel and

discerning the cause of the reference absorbance (see Section 3.7). Figure A.41, shows

an absorbance snapshot of a blank solution on the stirred flowcell. At this optical

161
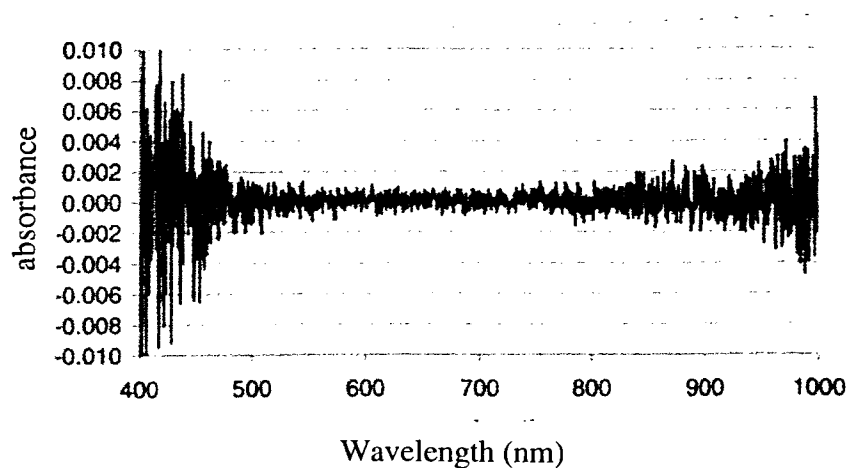
Figure A.41 Blank noise on the CCD array (Ocean Optics, USB2000). This snapshot was captured using the SAMI lamp at 5.0 V, a stirred flowcell filled with DIW, 1000 μm source and return fiber optics and a 600 μm CCD input fiber. Data were collected for 50 acquisitions with a 5 ms integration time each.

throughput the CCD achieved 1σ absorbance noise of ±0.0024 at 440 nm, ±0.0004 at 620 nm, and ±0.0004 at 780 nm using an integration time of 5 ms and 50 averages per acquisition over a 10 minute period where the lamp (SAMI Gilway) was not drifting. The electronic design of most (if not all) multielement semiconductor arrays, including the USB2000, is based on shift registers that readout the entire array of elements at the end of each integration period. Unfortunately, this limits all array elements to the same integration time, regardless of the fact that the light source greatly varies with wavelength. Consequently, as seen in Figure A.41, the array elements corresponding to wavelengths of low source emission intensity suffer far greater noise than the elements at peak emission intensity (Figure A.7). The noise at NIR wavelengths is also partly due to decreased CCD sensitivity in this region. The 5 ms integration time used to obtain Figure A.41 was chosen to get the peak element (660 nm) to 90% of the A/D converter's limit. Even a small increase in integration time, to achieve lower noise at 440 nm, would saturate the 660 nm element. Programming the array to collect back-to-back spectra with different integration times leads to a minimum of 20-30 sec in between subsequent titrant

162

additions due to a ~10 sec processing time per spectral acquisition. Consequently, any chemical changes that transpire in solution (e.g. minute titrant leakage into the flow cell, H_2CO_3 dehydration) over this interval will lead to measurement errors.

Because the CCD performance was significantly worse than the interference filter spectrophotometer at 440 nm, it was not further pursued as a replacement for the SAMI detection system. Nonetheless, as described in Section 3.7, the CCD played an important role during an investigation of the reference correction behavior.

A.4.4 Diode array spectrophotometer

The Agilent 8453 diode array spectrophotometer was used several times throughout this study[61] (Section 3.7, Figure A.29). All of these measurements required some modifications to the instrument. Because the experiments involved fiber optics running to a sensor (the flow cell) and returning to the detector, the central issue was how to couple light from our external light source into the system and not use the 8453 light source[62]. In effect, we wanted to use the 8453 detection system (diode array) but not the 8453 light source.

I first built a fiber optic detector coupler for the 8453. This piece (Black Delrin™) was machined to fit into the spectrophotometer's open-path sample chamber. The two-piece coupler consists of a base plate and an adjustable arm, tapped out for an Ocean Optics 74-UV lens (Section A.2.3.2). With this piece secured in the sample

---

[61] Although the data is not presented in this document, it was also used to carry out TMTs using the stirred flow cell.

[62] Custom Sensors & Technology offers a (high priced) fiber optic coupling system for the 8453. Our laboratory later purchased one, after the completion of these measurements, but it has never achieved throughput as high as what is possible with a bright external source and the simple approach described here.

163

chamber of the instrument, the return fiber optic is positioned directly in front of the detector lens.

The shutter is located on the source side of the sample chamber. The ChemStation software controlling the 8453 is written to collect dark signals during 10-20 second intervals when the shutter is closed. Because experiments using the 8453 were for temporary evaluations, it was impractical to take the time to reprogram the instrument[63]. The alternatives were therefore to (1) couple the 8453 light source into the flow cell system or (2) move the shutter to another location in the light path of the external source. Because we did not have the means to couple source light from the spectrophotometer into a fiber optic, the shutter was moved to the detector side of the sample chamber[64]. First, all of the 8453 covers were removed (see user manual) to reveal the source optics, detector optics and shutter assembly. The shutter assembly was then removed. Unfortunately, the shutter assembly's power cable is too short to reach around the sample chamber to the detector side, so a ten-pin extension cable was built. With the shutter assembly removed and the cable connected, the covers were replaced and the shutter was mounted externally in the sample chamber between the fiber optic detector coupler and the hole in the cover leading to the detector lens. This design, albeit crude, works surprisingly well. In fact, it is capable of providing much higher optical throughput than the commercially available add-on. Drawbacks include less stable components and nullification of the Agilent warranty if the instrument is damaged as a result of modification (e.g. miswiring of the shutter extension cable).

---

[63] this could be accomplished using the LabView VI's available from Agilent
[64] WARNING: This procedure requires some delicate work, can potentially damage the spectrophotometer, and is not covered in the Agilent warranty.

164

The diode array was not used for TMT for reasons similar to those described for

the CCD array (Section A.4.3). As shown in Table A.4, the low s:n at 440 nm is outside

the acceptable limit.

Table A.4. Agilent 8453 signal:noise at various wavelengths. To achieve this performance the SAMI lamp was overrun at 7.5 V (160 mA) and a shortened pathlength was used (~0.5 cm). These data were collected on the stirred flowcell filled with DIW and 600 μm core fused silica fiber optics.

λ (nm)	signal:noise
400	250
450	400
500	1200
600	2400
700	2800
800	3000

Appendix B   Programs, Models and Calculators

B.1   TFBASIC programs

TFBASIC is the programming language used to control the Tattletale TFX-11 (Onset Computer Corp.) dataloggers.

B.1.1   Signal monitoring (STABAVE)

The program STABAVE is a simple TFBASIC program that averages and records light or dark signals for stability tests. With some basic programming knowledge, STABAVE is easily altered to record at the desired interval, for a set length of time, with varying fluid control, such as intermittent pumping.

```
// ****************optical signal monitoring program**************
// ************************* STABAVE.TFB ************************
// ********************** WRITTEN BY T. Martz ********************
// ***************************************************************
//
// ***************** DEVICE POWER; INPUT/OUTPUT PINS ************
// LIGHT SOURCE, ANALOG BOARD, TFX-11 POWERED EXTERNALLY
// I/O(0) GENERIC 5 V SUPPLY
// I/O(1) GENERIC 12 V SUPPLY
// I/O(2) GENERIC 12 V SUPPLY
// I/O(3) GENERIC 12 V SUPPLY
// I/O(5) THERMISTOR POWER
// I/O(7) -OPEN-
// ************* ANALOG/DIGITAL CONVERSION CHANNELS *************
// CHAN(0)  = -OPEN-
// CHAN(1)  = 780 nm
// CHAN(2)  = 620 nm
// CHAN(3)  = 440 nm
// CHAN(4)  = -OPEN-
// CHAN(5)  = -OPEN-
// CHAN(6)  = -OPEN-
// CHAN(10) = TEMPERATURE
// ***************************** VARIABLES **********************
// CELLT! - TEMPERATURE
// TEMPSUM! - TEMPERATURE AVERAGE
// DSUM444, 620, 780 - DARK SIGNAL SUMS
// DARK444, 620, 780 - DARK SIGNAL AVERAGES, STD DEV
// SIG444, 620, 780  - LIGHT SIGNAL INTENSITIES
// LSUM444, 620, 780 - LIGHT SIGNAL SUMS
// LITE444, 620, 780 - LIGHT SIGNAL AVERAGES
// ***************************** COUNTERS ***********************
// F - MEASUREMENT SUBCYCLE COUNTER
// X - PUMP LOOP COUNTER
// Z - NUMBER OF MEASUREMENT CYCLES
// ***************************** CONSTANTS **********************

ONERR GOTOSLEEP // ERROR TRAP
```

166

```
T = 65 // NUMBER OF SIGNAL AVERAGES

GOSUB SETTIME
READRTC // get time from pic clock
CBREAK SHUTDOWN // sets CTRL-C destination

// *********************************************************************
// *********************** MAIN PROGRAM ****************************
// *********************************************************************
START:
      F = 0 // INITIALIZE SUBCYCLE COUNTER
      PCLR 0,1,2,3,4,6,7 // SHUT DOWN ALL DEVICES
      PSET 5 // THERMISTOR OFF

                  F = 5000 // NUMBER OF LIGHT SIGNAL CYCLES
            GOSUB RUNSAMI // MEASUREMENT CYCLE
STOP

// *********************************************************************
// ******************* END OF MAIN PROGRAM ***********************
// *********************************************************************


// ------------------------------------------------------------------
// ----------------------- SUBPROGRAMS ----------------------------
// ------------------------------------------------------------------


// *********************************************************************
// ********************** SIGNAL INTENSITY MEASUREMENT**************
// *********************************************************************
RUNSAMI:
      PCLR 5 // THERMISTOR ON

// -=-=-=-=-=-=-=-=-=-=- BEGINNING OF MEAS. LOOP =-=-=-=-=-=-=-=
      FOR Z = 1 TO F

      RTIME // TRANSLATES ? VARAIBLE TO ?() ARRAY
      PRINT "*************************************************"
      PRINT #02, "TIME =   ",?(2), ":",?(1), ":",?(2)
      STORE #2,?(2),?(1),?(0) // STORE TIME

// -=-=-=-=-=-=-=-=-=-=-=-=SAMPLE # COUNTER -=-=-=-=-=-=-=-=-=-=-=-=-
      PRINT "   ", Z // PRINT PUMP & MEAS. LOOP COUNTER
      STORE #2, Z // STORE COUNTER

// -=-=-=-=-=-=-=-=-=-=-=-=-= LIGHT SIGNALS -=-=-=-=-=-=-=-=-=-=-=-=
      SIG440 = 0 // INITIALIZE SIGNAL VARIABLES
      SIG620 = 0
      SIG780 = 0
      LSUM440 = 0 // INITIALIZE LIGHT SIG SUMMATIONS
      LSUM620 = 0
      LSUM780 = 0
      LITE440 = 0 // INITIALIZE LIGHT SIG AVERAGES
      LITE620 = 0
      LITE780 = 0
      FOR Q = 1 TO T
            SIG440 = CHAN(3)
            SIG620 = CHAN(2)
```

167

```
            SIG780 = CHAN(1)
        LSUM440 = LSUM440 + SIG440
        LSUM620 = LSUM620 + SIG620
        LSUM780 = LSUM780 + SIG780
        NEXT Q
        LITE440 = LSUM440/T // AVERAGE
        LITE620 = LSUM620/T
        LITE780 = LSUM780/T


// -=-=-=-=-=MEASURE TEMPERATIURE-=-=-=-=-=-=-
TEMPSUM! = 0
FOR P = 1 TO 50
    G = CHAN(10) // GET TEMPERATURE
    CELLT! = TEMP(G)
    CELLT! = CELLT!/100
    TEMPSUM! = TEMPSUM! + CELLT!
NEXT P
CELLT! = TEMPSUM!/50


// =-=-=-=-=-=-=-=-=-=-=-= PRINT AND STORE SIGNALS -=-=-=-=-=-=-=-=-
        PRINT "SIGNALS @ 440, 620, AND 780 nm and temp ";
        PRINT #5,LITE440," ",LITE620," ",LITE780, " "
           PRINT "TEMPERATURE = ", #.2F,ASFLT(CELLT!) // outputs TEMP *
100
        STORE #4,LITE440,#4,LITE620,LITE780, CELLT! // STORE LIGHT
SIGNALS

// =-=-=-=-=-=-=-=-=-=-=-= PUMPING COMMANDS -=-=-=-=-=-=-=-=-=-
// THE FOLLOWING EXAMPLES ARE COMMENTED OUT FOR NO PUMPING

//PUMP #3 TWICE EVERY TEN LIGHT SIGNALS
//IF Z % 10 = 0
//     FOR X = 1 TO 2
//          PSET 3
//          SLEEP 0
//          SLEEP 100
//          PCLR 3
//          SLEEP 0
//          SLEEP 100
//     NEXT X
//ENDIF


        WAITTIME = 1 // SECONDS BETWEEN SIGNALS
        GOSUB WAIT
   NEXT Z
// =-=-=--=-=-= SHUT OFF ALL DEVICES POWERED BY TFX-11 =-=-=-=-=-=-==
PCLR 0,1,2,3,4,6,7 // SHUT DOWN ALL DEVICES
PSET 5 // THERMISTOR OFF

RETURN

// **************************************************************************
// ************************ DELAY LOOP**************************
//*************************************************************************
WAIT:
        FOR R = 1 TO WAITTIME // WAITTIME IN SECONDS
              SLEEP 0
```

168

```
                SLEEP 100
        NEXT R
        RETURN


// ***********************************************************************
// ********************** SET CLOCK ***********************************
// ***********************************************************************
SETTIME:
        PRINT

        INPUT "ENTER THE HOUR          (0 - 23) "?(2)
        INPUT "ENTER THE MINUTE        (0 - 59) "?(1)
        INPUT "ENTER THE SECOND        (0 - 59) "?(0)
        STIME // SETS TIME CLOCK
        SETRTC // REAL TIME CLOCK
        U = 0 // ZERO BLANK CYCLE COUNTER
        RETURN


// ***********************************************************************
// ******************* CTRL-C DESTINATION ***********************
// ***********************************************************************
SHUTDOWN:
        PCLR 0,1,2,3,4,6,7 // shut down all devices
        PSET 5
        STOP // stops program and gives prompt
```

B.1.2   Absorbance measurement (ABSMEAS)

The flowcell absorbance measurements described in Section 3.3 are greatly

facilitated by an automated program that prompts the user for input. The program

ABSMEAS is a modification of STABAVE (Section B.1.1) that requires user input to

record measurements on alternating blank and sample solutions. ABSMEAS is written

specifically for the flow design shown in Figure 3.1.


```
// ************* FLOW CELL ABSORBANCE MEASUREMENT PROGRAM ***********
// ************************** ABSMEAS.TFB **************************
// ********************** WRITTEN BY T. Martz **********************
// ***********************************************************************
//
// ****************** DEVICE POWER; INPUT/OUTPUT PINS **************
// LIGHT SOURCE, ANALOG BOARD, TFX-11 POWERED EXTERNALLY
// I/O(0) GENERIC 5 V SUPPLY
// I/O(1) GENERIC 12 V SUPPLY
// I/O(2) 12 V SUPPLY FOR 250 uL SOLENOID PUMP
// I/O(3) GENERIC 12 V SUPPLY
// I/O(5) THERMISTOR POWER
// I/O(7) -OPEN-
// **************** ANALOG/DIGITAL CONVERSION CHANNELS ***********
// CHAN(0) = -OPEN-
```

169

```
// CHAN(1)  = 780 nm
// CHAN(2)  = 620 nm
// CHAN(3)  = 440 nm
// CHAN(4)  = -OPEN-
// CHAN(5)  = -OPEN-
// CHAN(6)  = -OPEN-
// CHAN(10) = TEMPERATURE
// ***************************** VARIABLES *************************
// CELLT! - TEMPERATURE
// TEMPSUM! - TEMPERATURE AVERAGE
// DSUM440, 620, 780 - DARK SIGNAL SUMS
// DARK440, 620, 780 - DARK SIGNAL AVERAGES, STD DEV
// SIG440, 620, 780 - LIGHT SIGNAL INTENSITIES
// LSUM440, 620, 780 - LIGHT SIGNAL SUMS
// LITE440, 620, 780 - LIGHT SIGNAL AVERAGES
// ***************************** COUNTERS *************************
// F - MEASUREMENT SUBCYCLE COUNTER
// X - PUMP LOOP COUNTER
// Z - NUMBER OF MEASUREMENT CYCLES
// ***************************** CONSTANTS ************************

T = 65 // NUMBER OF SIGNAL AVERAGES

GOSUB SETTIME
READRTC // get time from pic clock
CBREAK SHUTDOWN // sets CTRL-C destination
// *************************************************************
// ********************* MAIN PROGRAM *************************
// *************************************************************
START:
        F = 0 // INITIALIZE SUBCYCLE COUNTER
        PCLR 0,1,2,3,4,6,7 // SHUT DOWN ALL DEVICES
        PSET 5 // THERMISTOR OFF
FOR B = 1 TO 5 // number of replicate absorbance measurements
        // PROMPT USER TO SET UPCHURCH VALVE TO BLANK FOR FLUSH
        PRINT "SWITCH VALVE TO BLANK"
        PRINT " "
        INPUT "PRESS ANY KEY WHEN READY" KEY$,#1,0;
                WHILE KEY$ = ""
                SLEEP 0
                SLEEP 100
                INPUT "" KEY$, #1, 0;
                WEND

                GOSUB BLNKFLSH // BLANK FLUSH OF FLOWCELL
                        F = 20   // NUMBER OF LIGHT SIGNAL CYCLES
                                 // 1-10 ARE BLANK; 11-20 ARE SAMPLE
                GOSUB RUNSAMI  // MEASUREMENT CYCLE
NEXT B

STOP

// *************************************************************
// ********************* END OF MAIN PROGRAM ******************
// *************************************************************


// ------------------------------------------------------------
```

```
// ------------------------- SUBPROGRAMS --------------------------
// ----------------------------------------------------------------

// ***************************************************************
// ****************** SIGNAL INTENSITY MEASUREMENT****************
// ***************************************************************
RUNSAMI:
      PCLR  0,1,2,3,4,6,7
      PSET  5 // THERMISTOR OFF

// -=-=-=-=-=-=-=-=-=- BEGINNING OF MEAS. LOOP =-=-=-=-=-=-=-=
      FOR Z = 1 TO F

IF Z = 10
      GOSUB SMPFLSH // after recording ten blank intensities, the flow
                    // cell is flushed with absorbing sample
ENDIF
      PCLR  5
      RTIME // TRANSLATES ? VARAIBLE TO ?() ARRAY
      PRINT "*******************************************"
      PRINT #02, "TIME =   ",?(2), ":",?(1), ":",?(2)
      STORE #2,?(2),?(1),?(0) // STORE TIME

// -=-=-=-=-=-=-=-=-=-=-=SAMPLE # COUNTER -=-=-=-=-=-=-=-=-=-=-=-==
      PRINT "    ", Z // PRINT PUMP & MEAS. LOOP COUNTER
      STORE #2, Z // STORE COUNTER

// -=-=-=-=-=-=-=-=-=-=-=-=-= LIGHT SIGNALS -=-=-=-=-=-=-=-=-=-=-=-=
      SIG440 = 0 // INITIALIZE SIGNAL VARIABLES
      SIG620 = 0
      SIG780 = 0
      LSUM440 = 0 // INITIALIZE LIGHT SIG SUMMATIONS
      LSUM620 = 0
      LSUM780 = 0
      LITE440 = 0 // INITIALIZE LIGHT SIG AVERAGES
      LITE620 = 0
      LITE780 = 0
      FOR Q = 1 TO T
            SIG440 = CHAN(3)
            SIG620 = CHAN(2)
            SIG780 = CHAN(1)
      LSUM440 = LSUM440 + SIG440
      LSUM620 = LSUM620 + SIG620
      LSUM780 = LSUM780 + SIG780
      NEXT Q
      LITE440 = LSUM440/T // AVERAGE
      LITE620 = LSUM620/T
      LITE780 = LSUM780/T

// -=-=-=-=-=-=MEASURE TEMPERATIURE-=-=-=-=-=-=-=-=-
TEMPSUM! = 0
FOR P = 1 TO 50
    G = CHAN(10) // GET TEMPERATURE
    CELLT! = TEMP(G)
    CELLT! = CELLT!/100
    TEMPSUM! = TEMPSUM! + CELLT!
NEXT P
```

171

```
CELLT! = TEMPSUM!/50


// =-=-=-=-=-=-=-=-=-=-=-= PRINT AND STORE SIGNALS -=-=-=-=-=-=-=-=-
      PRINT "SIGNALS @ 440, 620, AND 780 nm and temp ";
      PRINT #5,LITE440," ",LITE620," ",LITE780, " "
      PRINT "TEMPERATURE = ", #.2F,ASFLT(CELLT!) // outputs TEMP * 100
      STORE #4,LITE440,#4,LITE620,LITE780, CELLT! // STORE LIGHT
SIGNALS

      WAITTIME = 1 // SECONDS BETWEEN SIGNALS
      GOSUB WAIT
   NEXT Z
// =-=-=-=-=-=-=-=-=-=-=-= SHUT OFF --=-=-=-=-=-=-=-=-=-=-=-=-=-=-=
PCLR 0,1,2,3,4,6,7
RETURN


// ***************************************************************
// ************************** DELAY LOOP**************************
//***************************************************************
WAIT:
      FOR R = 1 TO WAITTIME // WAITTIME IN SECONDS
            SLEEP 0
            SLEEP 100
      NEXT R
      RETURN


// ***************************************************************
// ************************** BLANK FLUSH ***********************
//***************************************************************
BLNKFLSH:
      FOR R = 1 TO 2000
            PSET 2
            SLEEP 0
            SLEEP 20
            PCLR 2
            SLEEP 0
            SLEEP 20
      PRINT R
      NEXT R
RETURN


// ***************************************************************
// ************************** SAMPLE FLUSH ***********************
// ***************************************************************
// PROMPT USER TO SWITCH UPCHURCH VALVE FROM BLANK TO SAMPLE
SMPFLSH:
PRINT "SWITCH VALVE FROM BLANK TO SAMPLE"
PRINT " "
INPUT "PRESS ANY KEY WHEN READY" KEY$,#1,0;
      WHILE KEY$ = ""
      SLEEP 0
      SLEEP 100
      INPUT "" KEY$, #1, 0;
      WEND

      FOR R = 1 TO 2000
```

172

```
                    PSET  2
                    SLEEP  0
                    SLEEP  20
                    PCLR  2
                    SLEEP  0
                    SLEEP  20
            PRINT  R
            NEXT  R
RETURN

// *********************************************************************
// ************************* SET CLOCK *********************************
// *********************************************************************
SETTIME:
        PRINT

        INPUT "ENTER THE HOUR              (0 - 23) "?(2)
        INPUT "ENTER THE MINUTE            (0 - 59) "?(1)
        INPUT "ENTER THE SECOND            (0 - 59) "?(0)
        STIME // SETS TIME CLOCK
        SETRTC // REAL TIME CLOCK
        U = 0 // ZERO BLANK CYCLE COUNTER
        RETURN

// *********************************************************************
// ******************** CTRL-C DESTINATION *****************************
// *********************************************************************
SHUTDOWN:
        PCLR 0,1,2,3,4,6,7 // shut down all devices
        PSET 5
        STOP // stops program and gives prompt
```

B.1.3 Solenoid pump titrations (STRCLTITR)

The program STRCLTITR is the main control program used to run titrations.

This particular version is written for the plumbing configuration shown in Figure 3.1.

Another significantly different titration program using Kloehn pumps is included at the

end of this appendix in Section B.1.4.

```
// ****************************STRCLTITR.TFB***************************
// ********** STIRRED FLOWCELL ·TITRATION PROGRAM (SOLENIOD PUMPS)****
// ********************** WRITTEN BY T. Martz ********************
// *********************************************************************
//
// ***************** DEVICE POWER; INPUT/OUTPUT PINS *************
// LIGHT SOURCE, ANALOG BOARD, TFX-11 POWERED EXTERNALLY
// I/O(0) GENERIC 5 V SUPPLY
// I/O(1) GENERIC 12 V SUPPLY
// I/O(2) 12 V SUPPLY FOR 250 uL BIOCHEM SOLENOID PUMP
// I/O(3) 12 V SUPPLY FOR 8 uL BIOCHEM SOLENOID PUMP
// I/O(5) THERMISTOR POWER
```

173

```
// I/O(7) -OPEN-
// *************** ANALOG/DIGITAL CONVERSION CHANNELS ***************
// CHAN(1) = 780 nm
// CHAN(2) = 620 nm
// CHAN(3) = 440 nm
// CHAN(10) = TEMPERATURE
// ***************************** VARIABLES *************************
// CELLT! - THERMISTER TEMPERATURE READOUT
// TEMPSUM! - TEMPERATURE AVERAGE
// DSUM440, 620, 780 - DARK SIGNAL SUMS
// DARK440, 620, 780 - DARK SIGNAL AVERAGES, STD DEV
// SIG440, 620, 780  - LIGHT SIGNAL INTENSITIES
// LSUM440, 620, 780 - LIGHT SIGNAL SUMS
// LITE440, 620, 780 - LIGHT SIGNAL AVERAGES
// ***************************** COUNTERS *************************
// X - PUMP LOOP COUNTER
// Z - MEASUREMENT SUBCYCLE COUNTER
// TITR - TITRATION MEASUREMENT COUNTER
// ***************************** CONSTANTS ************************
T = 50 // NUMBER OF SIGNAL AVERAGES
PUMP = 200 // NUMBER OF 8 uL PRETITRATION PUMPS
e1! = 0.0004 // MOLAR ABSORPTIVITY RATIOS
e2! = 2.2942
e3! = 0.1673
pka! = 4.5 // BROMOCRESOL GREEN pKa

GOSUB SETTIME
READRTC // get time from pic clock
CBREAK SHUTDOWN // sets CTRL-C destination
TITR = 0 // INITIALIZE MEASURMENT COUNTER


// *****************************************************************
// ************************* MAIN PROGRAM **************************
// *****************************************************************
START:
        Z = 0 // INITIALIZE SUBCYCLE COUNTER
        PCLR 0,1,2,3,4,6,7 // ZERO ALL I/O
        PSET 5 // THERMISTOR OFF

        GOSUB FLUSH // WAIT FOR END OF PURGE REPLY FROM KLOEHN

        TITR = TITR + 1

        GOSUB RUNSAMI // MEASUREMENT CYCLE

        IF TITR = 30 // NUMBER OF BACK TO BACK TITRATIONS
              STOP
        ENDIF
GOTO START

// *****************************************************************
// ********************* END OF MAIN PROGRAM *********************
// *****************************************************************


// ---------------------------------------------------------------
// ----------------------- SUBPROGRAMS ---------------------------
// ---------------------------------------------------------------
```

174

```
// ************************************************************************
// ********************* SIGNAL INTENSITY MEASUREMENT***************
// ************************************************************************

RUNSAMI:

        PCLR 5 // THERMISTOR ON
        GOTITR = 1
// -=-=-=-=-=-=-=-=-=- BEGINNING OF MEAS. LOOP =-=-=-=-=-=-=-=
WHILE GOTITR = 1
        RTIME // TRANSLATES ? VARAIBLE TO ?() ARRAY
        PRINT "***************************************************"
        PRINT #02, "TIME =  ",?(2), ":",?(1), ":",?(2);
        STORE #2,?(2),?(1),?(0) // STORE TIME


//-=-=-=-=-=-=--=-=-=-AFTER BLANK ADD PRETITRAITON=-=-=-=-=-=-=-=-=

IF Z = 6 // FIRST 5 SIGNALS ARE BLANK SIGS
        GOSUB PRETITRATION
ENDIF

// -=-=-=-=-=-=-=-=-=-=-=-=-= LIGHT SIGNALS -=-=-=-=-=-=-=-=-=-=-=-=-=
        SIG440 = 0 // INITIALIZE SIGNAL VARIABLES
        SIG620 = 0
        SIG780 = 0
        LSUM440 = 0 // INITIALIZE LIGHT SIG SUMMATIONS
        LSUM620 = 0
        LSUM780 = 0
        LITE440 = 0 // INITIALIZE LIGHT SIG AVERAGES
        LITE620 = 0
        LITE780 = 0

        FOR Q = 1 TO T
                SIG440 = CHAN(3)
                SIG620 = CHAN(2)
                SIG780 = CHAN(1)
        LSUM440 = LSUM440 + SIG440
        LSUM620 = LSUM620 + SIG620
        LSUM780 = LSUM780 + SIG780
        NEXT Q
        LITE440 = LSUM440/T // AVERAGE
        LITE620 = LSUM620/T
        LITE780 = LSUM780/T

IF Z < 5
B440 = LITE440
B620 = LITE620
B780 = LITE780
ENDIF

//CALCULATE REAL TIME ABSORBANCES AND pH

A440! = -LOG10((LITE440-3249.0)/(B440-3249))
A620! = -LOG10((LITE620-3247.0)/(B620-3247))
A780! = -LOG10((LITE780-3254.0)/(B780-3254))
```

175

```
RATIO! = A620!/A440!

IF RATIO! < e2!/e3! - 1.0
      pH! = pka! + LOG10((RATIO!-e1!)/(e2!-RATIO!*e3!))
ENDIF

IF A440! < 0.02
 pH! = 7
ENDIF

IF A620! < 0.02
 pH! = 7
ENDIF

// --=-=-=-=-=   FLOW CELL TEMPERATURE =-=-=-=-=-=-=-

TEMPSUM! = 0
FOR P = 1 TO 50
    G = CHAN(10) // GET TEMPERATURE
    CELLT! = TEMP(G)
    CELLT! = CELLT!/100
    TEMPSUM! = TEMPSUM! + CELLT!
NEXT P
CELLT! = TEMPSUM!/50

// =-=-=-=-=-=-=-=-=-=-=== PRINT AND STORE SIGNALS -=-=-=-=-=-=-=--=-
PRINT "   ACQUISITION # ", Z, " TITRATION # ", TITR // PRINT PUMP &
MEAS. LOOP COUNTER
PRINT ""
PRINT "TEMPERATURE = ", #.2F,ASFLT(CELLT!) // outputs TEMP * 100
PRINT ""
PRINT "   pH  =   ", #.5F,ASFLT(pH!)
PRINT ""
PRINT "               440        620        780"
PRINT "COUNTS          ", #5,LITE440,"      ",LITE620,"      ",LITE780
PRINT "ABSORBANCE      ",#.5F,ASFLT(A440!)," ",ASFLT(A620!),"
",ASFLT(A780!)
STORE #2, Z // COUNTER
STORE #4,LITE440,#4,LITE620,LITE780,CELLT! // STORE LIGHT SIGNALS

// =-=-=-=-=-=-ORDER TITRATION PUMP=-=-=-=-=-=

   IF A620! > 0.01

      IF A440! > 0.01
          IF pH! > 5.0
              FOR X = 0 TO 20 // MEDIUM TITR INCREMENTS
              PSET 3
              SLEEP 0
              SLEEP 15
              PCLR 3
              SLEEP 0
              SLEEP 15
              NEXT X
          ENDIF

              IF pH! > 3.0 // ERROR TRAP FOR LOW ABS VALUES
```

176

```
                          FOR X = 0 TO 1 // NUMBER OF TITR PULSES
                          PSET 3
                          SLEEP 0
                          SLEEP 15
                          PCLR 3
                          SLEEP 0
                          SLEEP 15
                          NEXT X
                     ENDIF


          ENDIF


      ENDIF


// =-=-=-=-=-=-END OF TITRATION SIGNAL=-=-=-=-=-=


      IF A620! > 0.01
         IF A440! > 0.01
               IF pH! < 3.5
                     IF pH! > 3.0 // ERROR TRAP FOR LOW ABS VALUES
                     GOTITR = 0 // STOP DATA ACQUISITION
                     ENDIF
               ENDIF
         ENDIF


      ENDIF


Z = Z + 1   // INCREMENT CYCLE COUNTER


WEND


WAITTIME = 5
GOSUB WAIT


RETURN


// *******************************************************************
// ************************** DELAY LOOP******************************
//*******************************************************************
WAIT:
      FOR R = 1 TO WAITTIME // WAITTIME IN SECONDS
            SLEEP 0
            SLEEP 100
      NEXT R
      RETURN


// *******************************************************************
// ************************ SET CLOCK ********************************
// *******************************************************************
SETTIME:
      PRINT

      INPUT "ENTER THE HOUR                (0 - 23) "?(2)
      INPUT "ENTER THE MINUTE              (0 - 59) "?(1)
      INPUT "ENTER THE SECOND              (0 - 59) "?(0)
      STIME // SETS TIME CLOCK
      SETRTC // REAL TIME CLOCK
```

177

```
      U = 0 // ZERO BLANK CYCLE COUNTER
      RETURN


// ***************************************************************
// ********************** CTRL-C DESTINATION *********************
// ***************************************************************
SHUTDOWN:
      PCLR 0,1,2,3,4,6,7 // CLEAR ALL I/O
      PSET 5
      STOP // stops program and gives prompt


// ***************************************************************
// ******************** FLOWCELL SAMPLE FLUSH ********************
// ***************************************************************
//USING A 250uL BIOCHEM PUMP POWERED BY I/O #2
FLUSH:
PRINT "SAMPLE FLUSH"
      FOR X = 1 TO 500 // # OF PULSES TO 100% FLUSH SHOULD BE FREQUENTLY
VERIFIED
         PSET 2
         SLEEP 0
         SLEEP 20
         PCLR 2
         SLEEP 0
         SLEEP 20
         PRINT X
      NEXT X
RETURN


// ***************************************************************
// ******************** PRETITRATION ADDITION*********************
// ***************************************************************
// USING AN 8uL BIOCHEM PUMP POWERED BY I/O #3

PRETITRATION:
      FOR X = 1 TO PUMP
         PSET 3
         SLEEP 0
         SLEEP 15
         PCLR 3
         SLEEP 0
         SLEEP 15
      NEXT X
RETURN
```

B.1.4 Kloehn pump titrations (TTKLOEHN)

During early development stages of the stirred flow cell, titrations were carried

out using a single Kloehn pump (with sample, titrant, and output all attached to the

distribution valve) or two Kloehn pumps (one for sample, one for titrant, joined by a

solenoid valve or Upchurch Tee). A Kloehn program (KLPTITR, Section B.4.2) was

178

written to control the pumps and give feedback to the TFX11. Hardwiring between the two microcomputers is described below (Section B.4.2). The program TTKLOEHN is the TFBASIC counterpart to KLPTITR (Section B.4.2). This program controls the TFX11 during titrations that use a Kloehn pump and involves giving feedback to the pump(s) as well as receiving input from the pump(s).

```
// *****************************TTKLOEHN.TFB**************************
// ***************STIRRED FLOWCELL - KLOEHN PUMP TITRATION CONTROL*****
// ********************** WRITTEN BY T. Martz  *********************
// ****************************************************************
//
// ****************** INPUT/OUTPUT PINS ***************************
// I/O(0) OUTPUT, INITIATES KLOEHN FLUSHING
// I/O(1) OUTPUT, INITIATES & STOPS KLOEHN PRETITRATION
// I/O(2) VALVE POWER OR OPEN IF USING A TEE
// I/O(3) OPEN
// I/O(5) THERMISTOR POWER
// ************* ANALOG/DIGITAL CONVERSION CHANNELS ***************
// CHAN(0) = INPUT FROM KLOEHN; SIGNALS END OF FLUSHING
// CHAN(1) = 780 nm ANALOG INPUT
// CHAN(2) = 620 nm ANALOG INPUT
// CHAN(3) = 440 nm ANALOG INPUT
// CHAN(4) = OPEN
// CHAN(5) = OPEN
// CHAN(6) = OPEN
// CHAN(10) = TEMPERATURE ANALOG INPUT
// **************************** VARIABLES ************************
// CELLT! - THERMISTER TEMPERATURE READOUT
// TEMPSUM! - TEMPERATURE AVERAGE
// DSUM440, 620, 780 - DARK SIGNAL SUMS
// DARK440, 620, 780 - DARK SIGNAL AVERAGES, STD DEV
// SIG440, 620, 780  - LIGHT SIGNAL INTENSITIES
// LSUM440, 620, 780 - LIGHT SIGNAL SUMS
// LITE440, 620, 780 - LIGHT SIGNAL AVERAGES
// **************************** COUNTERS ************************
// Z - NUMBER OF MEASUREMENT CYCLES
// **************************** CONSTANTS ************************
TITR = 0
T = 50 // NUMBER OF SIGNAL AVERAGES
DATAINT = 30 // MEASUREMENT INTERVAL IN MINUTES
PUMPTRANS = 0

//USE APPROXIMATE pKa and e VALUES FOR real time pH
e1! = 0.0004
e2! = 2.2942
e3! = 0.1673
pka! = 4.5

GOSUB SETTIME
```

179

```
READRTC // get time from pic clock
CBREAK SHUTDOWN // sets CTRL-C destination

// ***********************************************************************
// ********************** MAIN PROGRAM ***************************
// ***********************************************************************
START:
      Z = 0 // INITIALIZE CYCLE COUNTER
      PCLR 0,1,2,3,4,6,7 // ZERO ALL I/O
      PSET 5 // THERMISTOR OFF
      PUMPTRANS = 0

      PSET 2 // OPEN PORT TO TITRANT: PUMP 2
      WAITTIME = 1
      GOSUB WAIT
      PSET 1 // INITIATE KLOEHN PUMP # 2 A/I PURGE
      GOSUB FLUSHWAIT // WAIT FOR END OF PURGE REPLY FROM KLOEHN

      WAITTIME = 10 // WAIT FOR KLOEHN TO REACH DELAY LOOP
      GOSUB WAIT

      PCLR 2 // OPEN PORT TO SAMPLE: PUMP 1
      WAITTIME = 1
      GOSUB WAIT
      PSET 1 // INITIATE KLOEHN PUMP # 1 FLOWCELL SAMPLE FLUSH
      GOSUB FLUSHWAIT // WAIT FOR END OF FLUSH REPLY FROM KLOEHN

        TITR = TITR + 1

      GOSUB RUNSAMI // MEASUREMENT CYCLE

      IF TITR = 30 // set the number of continuous titrations
            STOP
      ENDIF
GOTO START

// ***********************************************************************
// ******************* END OF MAIN PROGRAM ***********************
// ***********************************************************************

// -----------------------------------------------------------------------
// ----------------------- SUBPROGRAMS --------------------------------
// -----------------------------------------------------------------------

// ***********************************************************************
// ********************* SIGNAL INTENSITY MEASUREMENT****************
// ***********************************************************************
RUNSAMI:

      PCLR 5 // THERMISTOR ON
      GOTITR = 1
// -=-=-=-=-=-=-=-=-=-=- BEGINNING OF MEAS. LOOP =-=-=-=-=-=-=-=
WHILE GOTITR = 1
      RTIME // TRANSLATES ? VARAIBLE TO ?() ARRAY
      PRINT "*************************************************"
      PRINT #02, "TIME =   ",?(2), ":",?(1), ":",?(2);
      STORE #2,?(2),?(1),?(0) // STORE TIME
```

180

```
//-=-=-=-=-=-=-=-=-=-=-NOTIFY KLOEHN BLANK IS RECORDED=-=-=-=-=-=-=-=-=-
=-=

IF Z = 6 // FIRST 5 SIGNALS ARE BLANK SIGS

        PSET 2 // OPEN VALVE TO A/I: KLOEHN PUMP #2
        WAITTIME = 1
        GOSUB WAIT

        PCLR 1 // INITIATE KLOEHN PRETITRATION
        GOSUB PULSEREPLY
        WAITTIME = 4
        GOSUB WAIT

ENDIF

// -=-=-=-=-=-=-=-=-=-=-=-=-= LIGHT SIGNALS -=-=-=-=-=-=-=-=-=-=-=-=-=
WAITTIME = 2
GOSUB WAIT
        SIG440 = 0 // INITIALIZE SIGNAL VARIABLES
        SIG620 = 0
        SIG780 = 0
        LSUM440 = 0 // INITIALIZE LIGHT SIG SUMMATIONS
        LSUM620 = 0
        LSUM780 = 0
        LITE440 = 0 // INITIALIZE LIGHT SIG AVERAGES
        LITE620 = 0
        LITE780 = 0

//AVERAGE T LIGHT SIGNALS
        FOR Q = 1 TO T
                SIG440 = CHAN(3)
                SIG620 = CHAN(2)
                SIG780 = CHAN(1)
        LSUM440 = LSUM440 + SIG440
        LSUM620 = LSUM620 + SIG620
        LSUM780 = LSUM780 + SIG780
        NEXT Q
        LITE440 = LSUM440/T
        LITE620 = LSUM620/T
        LITE780 = LSUM780/T

//SET BLANK VALUES
IF Z < 5
B440 = LITE440
B620 = LITE620
B780 = LITE780
ENDIF

//CALCULATE ABSORBANCE FOR REAL TIME DISPLAY AND
//pH-ABS LIMIT MONITORING
A440! = -LOG10((LITE440-3249.0)/(B440-3249))
A620! = -LOG10((LITE620-3247.0)/(B620-3247))
A780! = -LOG10((LITE780-3254.0)/(B780-3254))
```

181

```
//A440! = A440! - A780!
//A620! = A620! - A780!


RATIO! = A620!/A440!


IF RATIO! < e2!/e3! - 1.0
      pH! = pka! + LOG10((RATIO!-e1!)/(e2!-RATIO!*e3!))
ENDIF


IF A440! < 0.02
 pH! = 7
ENDIF


IF A620! < 0.02
 pH! = 7
ENDIF


// --=-=-=-=-=    FLOW CELL TEMPERATURE  =-=-=-=-=-=-=-=-=-


TEMPSUM! = 0
FOR P = 1 TO 50
     G = CHAN(10) // GET TEMPERATURE
     CELLT! = TEMP(G)
     CELLT! = CELLT!/100
     TEMPSUM! = TEMPSUM! + CELLT!
NEXT P
CELLT! = TEMPSUM!/50



// =-=-=-=-=-=-=-=-=-=-=-= PRINT AND STORE SIGNALS -=-=-=-=-=-=-=-=-
PRINT "   ACQUISITION # ", Z, " TITRATION # ", TITR // PRINT PUMP &
MEAS. LOOP COUNTER
PRINT ""
PRINT "TEMPERATURE = ", #.2F,ASFLT(CELLT!) // outputs TEMP * 100
PRINT ""
PRINT "   pH  =    ", #.5F,ASFLT(pH!)
PRINT ""
PRINT "              440      620      780"
PRINT "COUNTS         ", #5,LITE440,"     ",LITE620,"     ",LITE780
PRINT "ABSORBANCE    ",#.5F,ASFLT(A440!),"  ",ASFLT(A620!),"
",ASFLT(A780!)
STORE #2, Z // COUNTER
STORE #4,LITE440,#4,LITE620,LITE780,CELLT! // STORE LIGHT SIGNALS



// -=--=-=-=--ORDER KLOEHN PRETITRATION ADJUSTMENT-=-=-=-=-=-=-

   IF A620! > 0.01
      IF A440! > 0.01
          IF pH! > 5.1 // MUST MATCH ACQUISITION PUMP SETTING
                    PSET 1 // SIGNAL KLOEHN TO PUMP MED. ADJUSTMENT
                    WAITTIME = 1
                    GOSUB WAIT
                    PCLR 1 // SET SIGNAL LOW TO KEEP KLOEHN IN LOOP
                    WAITTIME = 2
                    GOSUB WAIT
```

182

```
                    ENDIF
                ENDIF
            ENDIF

// =-=-=-=-=-=- KLOEHN MED. TO SMALL PULSE TRANSITION=-=-=-=-=-=-=-=

IF pH < 5.1
        IF PUMPTRANS = 0
                PUMPTRANS = 1 // PERFRORM ONLY ONCE TO SWITCH KLOEHN LOOP
                PSET 1 // SIGNAL KLOEHN
                WAITTIME = 7
                GOSUB WAIT
        ENDIF
ENDIF


// =-=-=-=-=-=-ORDER KLOEHN TITRATION PUMP=-=-=-=-=-=

    IF A620! > 0.01

        IF A440! > 0.01

                IF pH! <= 5.1 // MUST MATCH PRETITRATION SETTING
                        IF pH! > 3.0
                         PCLR 1 // SIGNAL KLOEHN DATA ACQ. PUMP PULSE
                         WAITTIME = 1
                         GOSUB WAIT
                         PSET 1 // SET SIGNAL HIGH TO KEEP KLOEHN IN TITRLOOP
                         WAITTIME = 3
                         GOSUB WAIT
                        ENDIF
                ENDIF
        ENDIF

    ENDIF


// =-=-=-=-=-=-END OF TITRATION SIGNAL=-=-=-=-=-=

    IF A620! > 0.01
        IF A440! > 0.01
                IF pH! < 3.5
                        IF pH! > 3.0
                        GOTITR = 0 // STOP DATA ACQUISITION
                        PCLR 1 // STOP KLOEHN TITRATION
                        ENDIF
                ENDIF
        ENDIF
    ENDIF

WAITTIME = 1
GOSUB WAIT

Z = Z + 1  // INCREMENT CYCLE COUNTER

WEND
```

183

```
WAITTIME = 5
GOSUB WAIT

RETURN

// ********************************************************************
// *************************** DELAY LOOP******************************
//*********************************************************************
WAIT:
        FOR R = 1 TO WAITTIME // WAITTIME IN SECONDS
                SLEEP 0
                SLEEP 100
        NEXT R
        RETURN

// ********************************************************************
// ************************* SET CLOCK ********************************
// ********************************************************************
SETTIME:
        PRINT

        INPUT "ENTER THE HOUR            (0 - 23) "?(2)
        INPUT "ENTER THE MINUTE          (0 - 59) "?(1)
        INPUT "ENTER THE SECOND          (0 - 59) "?(0)
        STIME // SETS TIME CLOCK
        SETRTC // REAL TIME CLOCK
        U = 0 // ZERO BLANK CYCLE COUNTER
        RETURN

// ********************************************************************
// ******************** CTRL-C DESTINATION ***************************
// ********************************************************************
SHUTDOWN:
        PCLR 0,1,2,3,4,6,7 // CLEAR ALL I/O
        PSET 5
        STOP // stops program and gives prompt

// ********************************************************************
// ******************** WAIT FOR KLOEHN FLUSH**************************
// ********************************************************************
FLUSHWAIT:
PRINT "WAITING FOR BLANK OK FROM KLOEHN"

        WHILE PIN(0) = 1 // CHECK INPUT LINE FROM KLOEHN

                WAITTIME = 1
                GOSUB WAIT
        WEND
RETURN

// ********************************************************************
// ******************** WAIT FOR KLOEHN PUMP PULSE REPLY**************
// ********************************************************************
PULSEREPLY:
        WAITTIME = 2
        GOSUB WAIT
```

184

```
        PSET 1
        PRINT "PULSEREPLY, PSET 1, WAITING ON KLOEHN REPLY"
        WHILE PIN(0) = 1 // CHECK INPUT LINE FROM KLOEHN
              WAITTIME = 1
              GOSUB WAIT
        WEND
RETURN
```

B.2   Excel spreadsheets

After absorbance and titration data collection, calculations are carried out in five

linked Excel spreadsheets. Most of these calculations were described in Chapters 2 and

3. In order to fit a printable page, the spreadsheet format was altered from the working

version. In the original worksheets, the list of variables generally extends horizontally

across several pages. This layout provides much better organization and simplifies cell

copying for replicate solution preparations or titration point calculation. The cell

references throughout Section B.2 are consistent with each other. Because of the cell

transposition, Section B.2 cells do not correspond to the cell commands shown in the

Visual Basic program in the next section. Altering the program in Section B.3.1 to match

the illustrative cell format in Section B.2 would be confusing for the user, so B.3.1 is left

as it would be found in the working spreadsheet.

B.2.1   Titrant preparations

This worksheet contains values associated with the preparation of the acidified

mixture of indicator used to titrate alkaline samples. B.2.1 is not linked to any

worksheets for its values. The worksheet B.4.5, below, is linked to B.2.1 for the values

ACY and $[BCG]_0$.

A1	B	C	D
2		**INDICATOR STOCK**	
3	*parameter*	*value*	*cell formula*
4	solution	**6034A**	
5	dye lot	**01920DI**	

185

6	FW NaHBCG	720.02	
7	dye content	90%	
8	dye purity	95.4%	
9	g NaBCG	2.0000	
10	w H_2O + g BCG	2400.00	
11	m H_2O + BCG	2402.52	C8*((1-$C$20/$C$19)/(1-$C$20/1))
12	$[BCG]_{stock}$ mol kg-soln^{-1}	0.000993	(B8*B6*B7/B5)/((B10)/1000)
13	**STANDARD ACID**		
14	*parameter*	*value*	*cell formula*
15	Lot #	033175-24	
16	[HCl] mol L^{-1}	0.105380	
17	[HCl] mol kg^{-1}	0.1054	B15/B20
18	**CONSTANTS**		
19	*parameter*	*value*	*cell formula*
20	ρ NaCl	2.165	
21	ρHCl kg / L	0.9998	
22	ρ stock	0.99750	
23	ρ weights (g/ml)	8.000	
24	ρ air (g/ml)	0.001200	
25	FW NaCl	58.443	
26	indicator pka	4.470	
27	**SOLUTION CALCULATIONS**		
28	*parameter*	*value*	*cell formula*
29	solution	PREP	
30	stock	6034A	
31	$[BCG]_{stock}$ mol kg-soln^{-1}	9.9268E-04	B$11
32	w stock	450.00	
33	m stock	450.47	B31*((1-$B$23/$B$22)/(1-$B$23/$B$21))
34	w NaCl	280.90	
35	m NaCl	281.01	B33*((1-$B$23/$B$22)/(1-$B$23/$B$19))
36	w H_2O	6000.00	
37	m H_2O	6006.31	B35*((1-$B$23/$B$22)/(1-$B$23/1))
38	w HCl	150.00	
39	m HCl	150.16	B37*((1-$B$23/$B$22)/(1-$B$23/$B$20))
40	g soln	6887.95	B32+B34+B36+B38
41	$[BCG]_o$ mol kg-soln^{-1}	0.000065	(B30*B31)/B39
42	ACY = -TA (mol kg-soln^{-1})	0.002363	-(-B33/1000*$B$14-B27/1000*B25)/(B34/1000)
43	pH est.	2.64	pH_(B36,B35,B$37)
44	[H]	0.002299	10^-B38
45	[HBCG$^-$]	0.000064	B40/(1+Ki_/B43)
46	[BCG^{2-}]	0.000001	B40-B44
47	[Na$^+$]	0.697862	(B31*B30+B33/58.443*1000)/(B39)
48	[C^{l-}]	0.700092	(B37*B$15+B33/58.443*1000)/(B39)
49	ionic st	0.700160	0.5*(B43*(-1)^2+B45*(-2)^2+B44*(-1)^2+B46*(1)^2+B47*(-1)^2)

186

B.2.2 HI⁻ and I²⁻ solution preparation for εb measurement

This worksheet contains the preparation record of several pH controlled solutions of the I²⁻ and HI⁻ forms of BCG. The solutions are prepared analytically from the same stock solution. Upon preparation, absorbance measurements are made on each solution and recorded in another spreadsheet (not shown). Worksheet B.2.2 is not linked to any other worksheets in the example shown here. The worksheet where absorbance is recorded for each solution links to B.2.2 for the concentration values required to calculate εb. For the TA calculation shown on worksheet B.2.5, temperature-dependent equations for εb and K₁ were derived (Sections 4.2 and 3.5, respectively) and entered directly into B.2.5.

A1	B	C	D
2	INDICATOR STOCK		
3	*parameter*	*value*	*cell formula*
4	solution	6034A	
5	dye lot	01920DI	
6	FW NaHBCG	720.02	
7	dye content	90%	
8	dye purity	95.4%	
9	g NaBCG	2.0000	
10	g H2O + g BCG	2400.00	
11	m H2O + BCG	2402.52	B9*((1-$B$30/$B$29)/(1-$B$30/1))
12	[BCG]$_{stock}$ mol kg soln⁻¹	9.9268E-04	(B8*B6*B7/B5)/((B10)/1000)
13			
14	STANDARD ACID		
15	*parameter*	*value*	*cell formula*
16	Lot #		
17	[HCl] mol L⁻¹	0.100000	
18	[HCl] mol kg⁻¹	0.1010	B15/B20
19	STANDARD BASE		
20	*parameter*	*value*	*cell formula*
21	Lot #		
22	[NaOH] mol L⁻¹	0.100000	
23	[NaOH] mol kg⁻¹	0.1003	B15/B20
24	CONSTANTS		

187

25	parameter	value	cell formula
26	ρ stock	1.000	
27	ρ 0.100 M HCl	0.990	??double check??
28	ρ 0.100 M NaOH	0.997	??double check??
29	ρ NaCl	1.250	
30	ρ weights (g/ml)	8.000	
31	ρ air (g/ml)	0.001200	
32	[HCl] mol/L	0.0998	
33	[NaOH] mol/L	0.1000	
34	FW NaCl	58.443	
35	pka	4.479	
36	Ka	3.32E-05	
37	Kw (mol kg soln^{-1})	1.692E-14	
38	approx. $_{HI}\varepsilon_{440}$	21766	
39	approx. $_{I}\varepsilon_{620}$	47517	
40	**SOLUTION CALCULATIONS**		
41	parameter	value	cell formula
42	ε_{HI}		
43	solution	**prep**	
44	stock	**6034A**	
45	[BCG]$_{stock}$ mol kg soln^{-1}	9.9268E-04	
46	w stock	**28.0000**	
47	m stock	28.0294	B45*((1-$B$30/$B$29)/(1-$B$30/$B$25))
48	w NaCl	**28.30**	
49	m NaCl	28.32	B47*((1-$B$30/$B$29)/(1-$B$30/$B$28))
50	w H$_2$0	**600.00**	
51	m H$_2$O	600.63	B49*((1-$B$30/$B$29)/(1-$B$30/1))
52	wNaOH	**0.0000**	
53	m NaOH	0.0000	B51*((1-$B$30/$B$29)/(1-$B$30/$B$27))
54	w HCl	**40.0000**	
55	m HCl	40.0425	B53*((1-$B$30/$B$29)/(1-$B$30/$B$26))
56	g soln	697.03	B54+B52+B50+B48+B46
57	ρ soln kg L^{-1}	1.0150	
58	[BCG]$_T$ mol L^{-1}	0.000041	(B44*B46)/(B55/B56)
59	TA mol L^{-1}	-0.00584	(B46*B44+B52*(B$32/$B$27)-B54*(B$31/B$26))/(B55/B56)
60	pH	2.24	pH_(B58,B57,$B$34)
61	[H$^+$]	0.005797	10^-B59
62	[OH$^-$]	0.000000	B$36/B60
63	[HBCG$^-$] mol L^{-1}	4.0287E-05	B57/(1+B$35/B60)
64	[BCG^{2-}] mol L^{-1}	2.3064E-07	B57-B62
65	[Na$^+$]	0.69475	(B45*B44+B47/B$33*1000+B51*B$32)/(B55)
66	[Cl$^-$]	0.70044	(B53*B$31+B47/B$33*1000)/(B55)
67	ionic st	0.70052	0.5*(B60*(-1)^2+B63*(-2)^2+B62*(-1)^2+B64*(1)^2+B65*(-1)^2)

188

68	est λmax	0.8769	B37*B62
69	ϵ_i		
70	solution	**prep**	
71	stock	**6034A**	
72	[BCG]$_{stock}$ mol kg soln^{-1}	9.9268E-04	
73	w stock	**19.0000**	
74	m stock	19.0200	C73*((1-$C$31/$C$30)/(1-$C$31/$C$26))
75	w NaCl	**43.75**	
76	m NaCl	43.79	C75*((1-$C$31/$C$30)/(1-$C$31/$C$29))
77	w H$_2$0	**1000.00**	
78	m H$_2$O	1001.05	C77*((1-$C$31/$C$30)/(1-$C$31/1))
79	wNaOH	**5.0000**	
80	m NaOH	5.0053	C79*((1-$C$31/$C$30)/(1-$C$31/$C$28))
81	w HCl	**0.0000**	
82	m HCl	0.0000	C81*((1-$C$31/$C$30)/(1-$C$31/$C$27))
83	g soln	1068.86	C82+C80+C78+C76+C74
84	ρ soln kg L^{-1}	1.0150	
85	[BCG]$_T$ mol L^{-1}	1.7910E-05	(C72*C73)/(C83/C84)
86	TA mol L^{-1}	0.00049	(C74*C72+C80*(C$33/$C$28)-C82*(C$32/C$27))/(C83/C84)
87	pH	10.69	pH_(C86,C85,$C$35)
88	[H$^+$]	2.022E-11	10^-C87
89	[OH$^-$]	0.000837	C$37/C88
90	[HBCG$^-$] mol L^{-1}	1.0909E-11	C85/(1+C$36/C88)
91	[BCG^{2-}] mol L^{-1}	1.7910E-05	C85-C90
92	[Na$^+$]	0.70085	(C73*C72+C75/C$34*1000+C79*C$33)/(C83)
93	[Cl$^-$]	0.70036	(C81*C$32+C75/C$34*1000)/(C83)
94	ionic st	0.70064	0.5*(C88*(-1)^2+C91*(-2)^2+C90*(-1)^2+C92*(1)^2+C93*(-1)^2)
95	est λmax	0.8511	C39*C91

B.2.3 Alkaline sample preparation

This spreadsheet is used to track one or a series of artificial TA standards. It is not used with any of the other spreadsheet presented here to calculate TA, but it is an important aspect of the quality control process to have a record of all the steps involved in preparing the standard solutions used to test the titration method.

A1	B	C	D
2			**STANDARD BASE**
3	*parameter*	*value*	*cell formula*

189

4	Lot #		
5	[NaOH] mol L^{-1}	0.10030	
6	[NaOH] mol kg^{-1}	0.1000	B4/B8
7	**CONSTANTS**		
8	*parameter*	*value*	*cell formula*
9	ρNaOH kg L^{-1}	1.0027	
10	FW Na$_2$CO$_3$	105.988	
11	ρ Na$_2$CO$_3$ (g/ml)	2.532000	
12	ρ weights (g/ml)	8.000	
13	ρ air (g/ml)	0.001200	
14	FW NaCl	58.443	
15	ρ NaCl (g/ml)	1.250	
16	**CARBONATE SAMPLES**		
17	*parameter*	*value*	*cell formula*
18	solution	prep	
19	w Na$_2$CO$_3$	0.9300	
20	m Na$_2$CO$_3$	0.9303	B18*((1-$B$12/$B$11)/(1-$B$12/$B$10))
21	mols	0.008777	B19/$B$9
22	mols Alk	0.017555	B20*2
23	w NaCl	297.10	
24	m NaCl	297.34	B22*((1-$B$12/$B$11)/(1-$B$12/$B$14))
25	w H$_2$0	7000.00	
26	m H$_2$0	7007.36	B24*((1-$B$12/$B$11)/(1-$B$12/1))
27	g soln	7303.77	B25+B23-B19
28	TA	0.0024035	(B21+(B23/$B$13*$P$7))/(B26/1000)
29	Ct	0.001202	B20/(B26/1000)
30	pH	10.24	pHcalc_(B27,B28,K1_,K2_,KW_)
31	[H+]	0.000000	10^-B29
32	[OH-]	0.000295	KW_/B30
33	[HCO$_3^-$]	0.000295	(B28*K1_*B30)/(B30^2+K1_*B30+K1_*K2_)
34	[CO$_3^{2-}$]	0.000907	(B28*K1_*K2_)/(B30^2+K1_*B30+K1_*K2_)
35	[Na+]	0.698426	(B22/$B$13+2*B20)/(B26/1000)
36	[Cl-]	0.696022	(B22/$B$13)/(B26/1000)
37	ionic st	0.699333	0.5*(B30*(1)^2+B31*(-1)^2+B32*(-1)^2+B33*(2)^2+B34*(1)^2+B35*(-1)^2)
38	**NaOH SAMPLES**		
39	*parameter*	*value*	*cell formula*
40	solution	prep calc	
41	w NaOH	175.00	
42	mNaOH	175.18	B40*((1-$B$12/$B$11)/(1-$B$12/$B$8))
43	mols	0.017524	B41*B$5/1000
44	mols Alk	0.017524	B42*1
45	w NaCl	305.50	
46	m NaCl	305.75	B44*((1-$B$12/$B$11)/(1-$B$12/$B$14))
47	w H$_2$0	7000.00	

190

48	m H_2O	7007.36	B46*((1-$B$12/$B$11)/(1-$B$12/1))
49	g soln	7480.50	B40+B44+B46
50	TA	0.002343	B43/(B48/1000)
51	[Na+]	0.7011	(B44/$B$13+1*B42)/(B48/1000)
52	[Cl-]	0.6988	(B44/$B$13)/(B48/1000)
53	ionic st	0.7000	0.5*(B50*(1)^2+B51*(-1)^2)

B.2.4 TFX-11 recorded intensities

During titrations, the TFX-11 stores raw light intensities sequentially as five blank signals followed by a varying number of titration signals, determined by the preset limits of pH and absorbance. For each data acquisition point, the TFX-11 records the time, digital voltage at each of the three photodiodes, and temperature. Raw data is copied directly into spreadsheet B.2.4 and the first level of filtering takes place. Dark signals (previously measured) are first subtracted from all recorded digital voltages. The blank intensity is calculated by averaging the first five points (see TTKLOEHN, Section B.1.4). Absorbance is then calculated for each recorded titration point at each channel. Using the Excel IF command, points are excluded where $_{780}A$ exceeds a predefined limit. $_{780}A$ is subtracted from the remaining points. The worksheet B.2.5 is then linked to B.2.4 for further calculations. Because the worksheet is relatively simple, no example is shown.

B.2.5 TA calculation template

This is the final worksheet in the calculation of TA from raw light intensity data. Most of the calculations are embedded in worksheet cells. The NLLS calculation and final round of filtering is controlled by a VB macro (Section B.3.1). To save space in this section, calculation of only one data acquisition point is shown. In the working spreadsheet, the 22 values shown below (rows 34-66) are spread out horizontally and extended vertically to row ~300. Cell names (column E) are absolute references, used in several formulas. For example, setting cell A1 = TC is the same as setting A1 = D7.

191

A1	B	C	D	E
2	pH & ABSORBANCE RANGE OVERLAP			
3	3.00	< pH <	3.80	lowpH,highpH
4	0.10	< Abs <	1.50	lowA,highA
5	FLOWCELL MIXTURE PROPERTIES			
6	PARAMETER	VALUE	FORMULA	CELL NAME
7	T(C)	22.44	AVERAGE(rawdata!F46:F56)	TC
8	T(K)	295.59	B8+273.15	TK
9	S(sample)	NA		
10	ρ kg/L	1.015		
11	TITRANT COMPOSITION			
12	PARAMETER	VALUE	FORMULA	CELL NAME
13	ACY mol kg soln^{-1}	2.3627E-03	stock & titrant prep'!C42	Acy
14	$[I]_o$ mol kg soln^{-1}	6.4853E-05	'stock & titrant prep'!C41	Io_
15	CO_2 & H_2O EQUILIBRIMUM CONSTANTS			
16	PARAMETER	VALUE	FORMULA	CELL NAME
17	KC1 (mol kg soln^{-1})	9.2302E-07	2.8282E-8*(TC-25)+EXP(-13.82)	K1_
18	KC2(mol kg soln-1)	1.7828E-10	4.2585E-11*(TC-25)+EXP(-21.97)	K2_
19	Kw (mol Kg soln^{-1})	1.71E-14	EXP(-31.7)	Kw_
20	INDICATOR CHARACTERISTICS			
21	PARAMETER	VALUE	FORMULA	CELL NAME
22	Ki (mol kg soln^{-1})	3.33E-05	10^	Ki_
23			pKi*EXP(((3.00*1000)/8.3145)*(1/295.14-1/TK))	
24	pKi (at 22.00 C)	4.47900		pKa
25	$_{620}\varepsilon_I$	36330	36373-63.03*(TC-21.76)	E1i_
26	$_{620}\varepsilon_{HI}$	34		E2i_
27	$_{440}\varepsilon_I$	2597	2598-1.22*(TC-21.88)	E3i_
28	$_{440}\varepsilon_{HI}$	15888	15898-15.44*(TC-21.81)	E4i_
29	e_1	0.0021	E2i_/E4i_	e1e_
30	e_2	2.2866	E1i_/E4i_	e2e_
31	e_3	0.1635	E3i_/E4i_	e3e_
32	EXAMPLE CALCULATION FOR ONE DATA POINT			
33	PARAMETER.	VALUE	FORMULA	CELL NAME
34	acq #	52		
35	A_{440}	0.52227	rawdata!O58	
36	A_{620}	0.16819	rawdata!P58	
37	A_{440}	0.52227	IF(OR(D35<lowA,D35>HighA)," ",D35)	A440_
38	A_{620}	0.16819	IF(OR(D36<lowA,D36>HighA)," ",D36)	A620_

192

39			IF(OR(A440_=" ",A620_=" "),"	
40			",((A620_ - A440_ * E2i_/E4i_)	
41	[I] mol kg^{-1}	0.000005	/ (E1i_- E3i_ * E2i_ / E4i_))	I_
42			IF(OR(A440_=" ",A620_=" "),"	
43			",((A440_ - A620_* E3i_/ E1i_)	
44	[HI] mol kg^{-1}	0.000032	/ (E4i_ - E3i_* E2i_ / E1i_))	HI_
45	[BCG]$_T$ mol kg^{-1}	0.000036	IF(HI_=" "," ",I_+HI_)	Itot_
46	[H$^+$] mol kg^{-1}	0.000232	IF(Itot_=" "," ",Ki_*HI_/I_)	H_
47	[OH$^-$] mol kg^{-1}	0.000000	IF(H_=" "," ",Kw_/H_)	OH_
48	I/Io (D)	0.558	IF(Itot_=" "," ",Itot_/Io_)	D
49			IF(Itot_=" "," ",Ct_*(1-D)*I14^2	
50	[CO$_2$] mol kg^{-1}	0.000525	/(H_^2+K1_*H_+K1_*K2_))	
51			IF(Itot_=" "," ",Ct_*(1-D)*K1_*	
52	[HCO$_3^-$] mol kg^{-1}	0.000002	H_/(H_^2+K1_*H_+K1_*K2_))	HCO3_
53	[CO$_3^{2-}$] mol kg^{-1}	0.000000	IF(Itot_=" "," ",Ct_*(1-D)*K1_* K2_/(H_^2+K1_*H_+K1_*K2_))	CO3_
56	R	0.32203	IF(OR(A440_=" ",A620_=" ")," ",A620_/A440_)	R
57	e2-Re3	2.23396	IF(R=" "," ",e2e_-R*e3e_)	denom
58	spec pH	3.634124	IF(OR(denom<0.1,R=" ")," ", -LOG(H_))	pH_
59			IF(OR(pH_=" ",pH_>highpH	
60			,pH_<lowpH)," ",(Acy*D-TA*	
61			(1-D)-H_-HI_+OH_+HCO3_	
62	residual mol kg^{-1}	0.000002	+2*CO3_))	r_
63	residual^2	2.46E-12	IF(r_=" "," ",r_^2)	r2_
64	C$_T$	0.001193	SOLVER PARAMETER	Ct_
65	TA	0.002385	SOLVER PARAMETER	TA
66	Σ(residual)^2	0.0E+00	NA to this ex. spreadsheet	NA

B.3   Excel macros

B.3.1   Routine for automatic solver (SOLVETA)

The following Visual Basic program performs calculations on data in the

worksheet B.2.5. As explained earlier (see introduction to B.2.5), cell references listed at

the beginning of the program do not match Section B.2.5 because the worksheet was

rearranged and shortened to fit a printable page. For example, TA in the spreadsheet

shown in Section B.2.5 is cell C65, but the macro refers to cell F6. It would be

impractical to present the program here to match Section B.2.5 because the spreadsheet

193

shown there is an example of a calculation for only one titration point. The correct cell

references are therefore required before running this program.

```
'SOLVETA
'Visual Basic TA calculation program for Excel
'written by T. Martz
'
'This program (1) Solves for TA and Ct by using SOLVER to minimize
'the sum of the squared residuals for a user defined range of titration
'points. (2) Filters the resulting set of squared residuals, throwing out
'values that exceed the limit 2.5e-11. (3) Recalculates the TA and TCO2
'using the filtered set.
'
'NOTE: for SOLVER to function from this module, the VB SOLVER reference
'must be added to the 'references' folder of the VBAProject
'for this spreadsheet
'
'NOTE: this macro is linked to a spreadsheet control button.
'after the button is clicked, the user must click OK twice to accept
'the results each time SOLVER is run
'
'Cell References:
'E6 - TCO2
'F6 - TA
'G6 - unfiltered sum of residuals
'H6 - filtered sum of residuals
'column AA - squared residuals
'column AB - filtered squared residuals


Sub solveTA()
'TCO2 = 0 command commented out; TCO2 = 0.5*TA
    'Range("E6").Select ' set TCO2 = 0
    'ActiveCell.FormulaR1C1 = "=0"

'set TA = 0
    Range("F6").Select
    ActiveCell.FormulaR1C1 = "=0"
'set cell G6 equal to the sum of all squared residuals
    Range("G6").Select
    ActiveCell.FormulaR1C1 = "=SUM(R[2]C[20]:R[300]C[20])"
'run SOLVER
    'SolverOk SetCell:="$G$6", MaxMinVal:=2, ValueOf:="0", ByChange:="$F$6,$E$6"
        'commented out TCO2 as an adjustable parameter
    SolverOk SetCell:="$G$6", MaxMinVal:=2, ValueOf:="0", ByChange:="$F$6"
    SolverSolve
'clear the column right adjacent to the column of squared residuals
    Columns("AB:AB").Select
    Selection.ClearContents
'set the column right adjacent to the column of squared residuals
'equal to the column of squared residuals
    Range("AB8").Select
    ActiveCell.FormulaR1C1 = "=RC[-1]"
```

194

```
Range("AB8").Select
Selection.AutoFill Destination:=Range("AB8:AB300")
'filter the new column of squared residuals
Columns("AB:AB").Select
Selection.AutoFilter
Selection.AutoFilter Field:=1, Criteria1:=">2.5e-11", Operator:=xlAnd
Selection.ClearContents
'set cell H6 equal to the sum of the filtered squared residuals
Range("H6").Select
ActiveCell.FormulaR1C1 = "=SUM(R[2]C[20]:R[300]C[20])"
'run SOLVER
'SolverOk SetCell:="$H$6", MaxMinVal:=2, ValueOf:="0", ByChange:="$F$6,$E$6"
    'commented out TCO2 as an adjustable parameter
SolverOk SetCell:="$H$6", MaxMinVal:=2, ValueOf:="0", ByChange:="$F$6"
SolverSolve
End Sub
```

B.4 Kloehn programs

As mentioned in Section 4.4.1, Kloehn Syringe pumps (Versa 6; 6-way

distribution valve) were used in the early instrument design. These programs were

written in Kloehn Control 1.03, Kloehn Ltd.'s script language.

B.4.1 Program for single absorbance measurements (KLPABSORB)

This program is intended to run in constant optical monitoring mode, without

communication between Kloehn pump and TFX11. For example, KLPABSORB would

be triggered on the Kloehn pump and when prompted (see below), the user would start

STABAVE (Section B.1.1) on the TFX11, and then trigger the Kloehn pump, bringing it

out of halt mode. This particular version of KLPABSORB is intended for use with a ~6

mL stirred flow cell and a 10 mL syringe barrel.

```
//KLPABSORB
//Kloehn Control script program for user-assisted absorbance measurements
//on a stirred flow cell, with a single Kloehn syringe pump
//Written by T.Martz

//****************CONSTANTS*******************
CONSTANT <varName> = <float>        flocel, 1 // line to flowcell located at valve port 1 (A)
CONSTANT <varName> = <float>        sample, 2 // sample located at port 2
CONSTANT <varName> = <float>        blank, 6 // blank at port 6
CONSTANT <varName> = <float>        Flushspeed, 500 // high speed for flushing
CONSTANT <varName> = <float>        Fillspeed, 1500 // speed for drawing sample
CONSTANT <varName> = <float>        Tfillspeed, 500 // speed for drawing A/I
```

195

```
CONSTANT <varName> = <float>        Titrspeed, 500 // speed for titration points

//******************VARIABLES******************
VARIABLE <varName> = <int>   sampleloop, 0
VARIABLE <varName> = <int>   pumploop, 0

DO
      l        VALVE_PORT = <int> [CCW]      blank, CCW
      l        SET speed = <float>       1500
      l        ASPIRATE <float> [IMM or SYNC]       45000, IMM // draw 9.5 mL blank
      l        VALVE_PORT = <int> [CCW]      flocel
      l        SET speed = <float>       500
      l        DISPENSE <float> [IMM or SYNC]       45000, IMM // flush 9.5 ml sample
               ASSIGN <varName> = <int or float>       pumploop, pumploop + 1
               PRINTF <text>   "pump # = %d", pumploop
LOOP <int>     8

PRINTF <text>   "Trigger TT blank and hit Run"
      l        HALT    // wait for user reply to resume program

DO
      l        VALVE_PORT = <int> [CCW]      sample
      l        SET speed = <float>       700
      l        ASPIRATE <float> [IMM or SYNC]       45000, IMM // draw sample
      l        VALVE_PORT = <int> [CCW]      flocel
      l        SET speed = <float>       500
      l        DISPENSE <float> [IMM or SYNC]       45000
               ASSIGN <varName> = <int or float>       sampleloop, sampleloop + 1
               PRINTF <text>   "pump # = %d", sampleloop
LOOP <int>     8
```

B.4.2   Program for alkalinity titrations (KLPTITR)

The version of KLPTITR given below is written for two Kloehn pumps connected

by RS485, and interfaced to a TFX11. This program is written to titrate TA in the usual

range ~ 2000-2500, on a ~ 6 mL stirred flow cell, with a titrant syringe volume of 5 mL

and a sample syringe volume of 10 mL. As described in the Kloehn Users Manual, this

configuration requires that the pump receiving serial communication from the PC is on

channel 1 (on the pump's rear PCIB), and the second 'slave' pump is set to channel 2.

TFX11 communication is established through single input and output logic channels for

both processors. Interfacing instruments running on different programs in different

languages is typically undesirable, but in certain situations it is the fastest approach. In

this case a great deal of time was saved because no common language existed for both

196

processors (i.e. no LabView™ VIs were available for the TFX11, and our experience with Kloehn VIs was still very rudimentary) and nearly complete programs had already been developed in both processors' respective languages. The TFX11 program that runs simultaneously with KLPTITR is TTKLOEHN (Section B.1.4).

Some of the basic principles that I used when establishing communication between the TFX11 and Kloehn pumps are given here to facilitate any future projects that require this (rather awkward) arrangement. Kloehn pumps were powered by their own DC adapters and the TFX11 was powered by a separate DC supply. A logic ground was established between both processors. It is crucial that the logic ground is separate from the power ground. The Kloehn's output logic operates at $1 = 0.5$ V, $0 = 0.0$ V and the TFX11 output logic is $1=5.0$V, $0=0.0$V. The TFX11 input voltage recognition logic is: >2.0 V $= 1$; <0.7 V $= 0$; 0.7-2.0 V $=$ indeterminate. Consequently, logic changes in the Kloehn output voltage (0-0.5 V) do not register on the TFX11. The Kloehn OUT1 channel was therefore connected in parallel to the TFX11's constant $+5$V pin, through a 4.7 kΩ 'pull-up' resistor. The other end of the Kloehn OUT1 channel then operated on the same 5/0 logic as the TFX11. Communicating with a Kloehn digital input requires an external switch that connects to the digital ground. Because this is an added complexity and only one input channel is required, the Kloehn 8-bit digital voltmeter was used as a logical input by choosing a threshold voltage (1V) to represent the 1-0 crossover.

```
//KLPTITR
//pump and valve control for stirred flowcell titration
//Tattletale - Kloehn communication program
//Written by T.Martz

//*****************CONSTANTS*******************
CONSTANT <varName> = <float>        flocel, 1 // line to flowcell located at valve port 1 (A)
CONSTANT <varName> = <float>        titrant, 6 // A/I located at valve port 6 on pump 2
CONSTANT <varName> = <float>        sample, 6 // sample located at valve port 6 on pump 1
CONSTANT <varName> = <float>        pretitrVol1, 37000 // initial addition of A/I
```

197

```
CONSTANT <varName> = <float>          pretitrVol2, 2000  //pretitration
CONSTANT <varName> = <float>          titrfillVol1, 37000
CONSTANT <varName> = <float>          titrfillVol2, 35000
CONSTANT <varName> = <float>          pretitrAdj, 200 // incremental titration step volume
CONSTANT <varName> = <float>          titrVol, 200 // titration volume increment
CONSTANT <varName> = <float>          Flushspeed, 500 // high speed for flushing
CONSTANT <varName> = <float>          Fillspeed, 1500 // speed for drawing sample
CONSTANT <varName> = <float>          Tfillspeed, 1500 // speed for drawing A/I
CONSTANT <varName> = <float>          Titrspeed, 500 // speed for titration points


        //*****************VARIABLES*******************
VARIABLE <varName> = <int>    pumploop, 0
VARIABLE <varName> = <int>    titrloop, 0
VARIABLE <varName> = <int>    adjloop, 0


Start            ASSIGN <varName> = <int or float>        pumploop, 0
ASSIGN <varName> = <int or float>        adjloop, 0
ASSIGN <varName> = <int or float>        titrloop, 0
SET out1 = <bit> 0



//**********WAIT FOR PUMP #2 PURGE SIGNAL FROM TT**********
PRINTF <text>     "WAITING FOR A/I PURGE COMMAND FROM TATTLETALE"
PurgeWait     1        JUMP_IF (analog > <int>) to <label>        100, purgeAI
              1        DELAY <float>  1
              1        JUMP to <label> PurgeWait


        //*********PURGE REMAINDER OF A/I FROM SYRINGE # 2**********
purgeAI          PRINTF <text>   "!!!!!!!!!!!!!!!    PURGING A/I   !!!!!!!!!!!!!!!"
              2        VALVE_PORT = <int> [CCW]     flocel // send valve to flowcell for flush
              2        SET speed = <float>       Flushspeed
              2        INIT    //initialize pump to zero position    W4


draw             //*************DRAW A/I MIXTURE (PUMP 2)**************
              2        VALVE_PORT = <int> [CCW]     titrant, CCW // open valve ccw to titrant
              2        SET speed = <float>       Tfillspeed
              2        ASPIRATE <float> [IMM or SYNC]        titrfillVol1 // draw A/I mixture
              2        VALVE_PORT = <int> [CCW]     flocel, CCW // open valve ccw to flowcell


//*****NOTIFY TT PURGE IS FINISHED*********
              1        SET out1 = <bit> 1 // bring SAMI out of 'FLUSHWAIT'
              1        DELAY <float>  5
              1        SET out1 = <bit> 0 //


//**********WAIT FOR PUMP #1 FLUSH SIGNAL FROM TT**********
PRINTF <text>     "WAITING FOR A/I PURGE COMMAND FROM TATTLETALE"
FlushWait     1        JUMP_IF (analog > <int>) to <label>        100, sampleflush
              1        DELAY <float>  1
              1        JUMP to <label> FlushWait


sampleflush                    // FULL SYRINGE FLUSH
              1        VALVE_PORT = <int> [CCW]     flocel // send valve to flowcell for flush
              1        SET speed = <float>       Flushspeed
              1        INIT    //initialize pump to zero position    W4
```

198

```
DO
        1       VALVE_PORT = <int> [CCW]      sample, CCW
        1       SET speed = <float>      Fillspeed
        1       ASPIRATE <float> [IMM or SYNC]        41000, IMM // draw 9.5 mL sample
        1       VALVE_PORT = <int> [CCW]      flocel
        1       SET speed = <float>      Flushspeed
        1       INIT [IMM or SYNC]
                ASSIGN <varName> = <int or float>        pumploop, pumploop + 1
                PRINTF <text>    "pump # = %d", pumploop
LOOP <int>      10



//********TELL TATTLETALE BLANK IS READY************
        1       SET out1 = <bit> 1 // bring SAMI out of 'FLUSHWAIT'
        1       DELAY <float>  5
        1       SET out1 = <bit> 0 //



//***********WAIT FOR TT END OF BLANK SIGNAL**********
PRINTF <text>   "WAITING FOR BLANK"
TitrWait 1      JUMP_IF (analog < <int>) to <label>       100, Pretitration
        1       DELAY <float>  1
        1       JUMP to <label> TitrWait


Pretitration    //*********LARGE PRETITRATION A/I ADDITION*************
        2       SET speed = <float>      Flushspeed
        2       DISPENSE <float> [IMM or SYNC]        pretitrVol1

        2       VALVE_PORT = <int> [CCW]      titrant, CCW // open valve ccw to titrant
        2       SET speed = <float>      Tfillspeed
        2       ASPIRATE <float> [IMM or SYNC]        titrfillVol2 // draw A/I mixture
        2       VALVE_PORT = <int> [CCW]      flocel, CCW // open valve ccw to flowcell

        2       SET speed = <float>      Flushspeed
        2       DISPENSE <float> [IMM or SYNC]        pretitrVol2


//*****NOTIFY TT PRETITR. IS FINISHED*********
        1       SET out1 = <bit> 1 // bring SAMI out of 'PULSEREPLY'
        1       DELAY <float>  5
        1       SET out1 = <bit> 0 //


//*********MEDIUM PRETITRATION ADJUSTMENTS*********
Adjust          PRINTF <text>    "ADJUSTING PRETITRATION"
        2       SET speed = <float>      Titrspeed
adjloop 1       JUMP_IF (analog > <int>) to <label>       100, AdjDispense
        1       JUMP to <label> adjloop

AdjDispense     2       DISPENSE <float> [IMM or SYNC]        pretitrAdj
                ASSIGN <varName> = <int or float>        adjloop, adjloop + 1
                PRINTF <text>    "pretitration adjustment # = %d", adjloop
        1       DELAY <float>  2
        1       JUMP_IF (analog > <int>) to <label>       100, Titration
        1       JUMP to <label> Adjust


//**********SMALL TITRATION STEPS FOR DATA ACQUISITION******
```

199

```
Titration          PRINTF <text>   "!!!!!!!!!!!!!!!TITRATION & DATA
                   ACQUISITION!!!!!!!!!!!"
          2        SET speed = <float>       Titrspeed
titrloop  1        JUMP_IF (analog < <int>) to <label>       100, AcqDispense
          1        JUMP to <label> titrloop
AcqDispense  2          DISPENSE <float> [IMM or SYNC]        titrVol
                   ASSIGN <varName> = <int or float>      titrloop, titrloop + 1
                   PRINTF <text>   "pump # = %d", titrloop
          1        DELAY <float> 2
          1        JUMP_IF (analog < <int>) to <label>       100, Return
          1        JUMP to <label> Titration


Return  1          DELAY <float> 5
        1          JUMP to <label> Start

        1          DELAY <float> 1
```

200

Appendix C   Purity of the Acid-Base Indicator

Accurate indicator molar absorptivities are crucial parameters for accurate and precise performance of TMT (as described in Section 3.4, values of εb were measured for the stirred flowcell). Many subtle problems arise in measuring molar absorptivity, however. The protocols followed for indicator solution preparation and absorbance measurement (e.g. choice of buffer system, ionic strength, temperature, brand of spectrophotometer, optical bandpass) contribute to enormous differences between the values of εb calculated. Another very significant factor that introduces almost certain inter-laboratory confusion (but seems to receive less attention than warranted) is the purity of the indicator salt used to prepare the stock solution. Actually, one must consider both *dye content* and *dye purity*. Dye content refers to the percentage of total dyes (species that absorb light in the visible spectrum) in the bottle of indicator salt. This is usually the number printed on the side of the bottle and it can be taken to mean that, for example, if dye content is 95% w/w, then a bottle with 25g of indicator salt will have ~ 1.25 g of optically inactive materials such as inorganic salts, solvents of crystallization, antidusting agents or dispersants (Sigma-Aldrich, personal communication, Section C.2). Dye purity refers to the percentage of the synthesis target contained in the optically active fraction of the material in the bottle. Dye purities are located on the certificate of analysis at the Sigma-Aldrich website. These percentages are determined by chromatography and silver nitrate titration. Different dye lots will then only have the same molar absorptivities if their dye purities are equal, impurities are composed of the same compounds, and differences in dye content are accounted for. Indicator dye lots of differing dye purity have differently shaped absorbance spectra and do not map onto one

201

another by a scalar quantity. Depending on the particular indicator and its synthesis route, purity issues may or may not present a serious problem. For example, Yamazaki et al. (1992a) report that, after recrystallization, impurities in bromocresol green are 'nearly colorless'. In contrast, Mosley et al. (2004) suggest dye impurities led to disagreement between the pK_a of m-cresol purple determined in their lab and that determined by Clayton and Byrne (1993). Our laboratory noticed significant, measurable differences in molar absorptivity ratios between two dye lots of bromocresol green. These differences may point toward impurities including under-brominated sulfonephthalein precursors of BCG, such as m-cresol purple (Kolthoff, 1937). Presumably due to such difficulties, few researchers choose to publish molar absorptivity values. Indeed, very little published data exists whereby molar absorptivity ratios (i.e. dye purity) may be compared between different laboratories or different dye lots. In light of the various issues described above, I believe that molar absorptivities can in fact be determined with high accuracy for a single indicator dye lot, but must always be redetermined for each bottle of dye on the specific instrument that is to be used for subsequent absorbance measurements, while accounting for ionic strength and temperature dependencies.

Sulfonephthalein indicators are usually purchased as their singly protonated, monosodium salt. As a general reference for this appendix, all of the molecular and ionic forms of BCG are shown in Figure C.1.
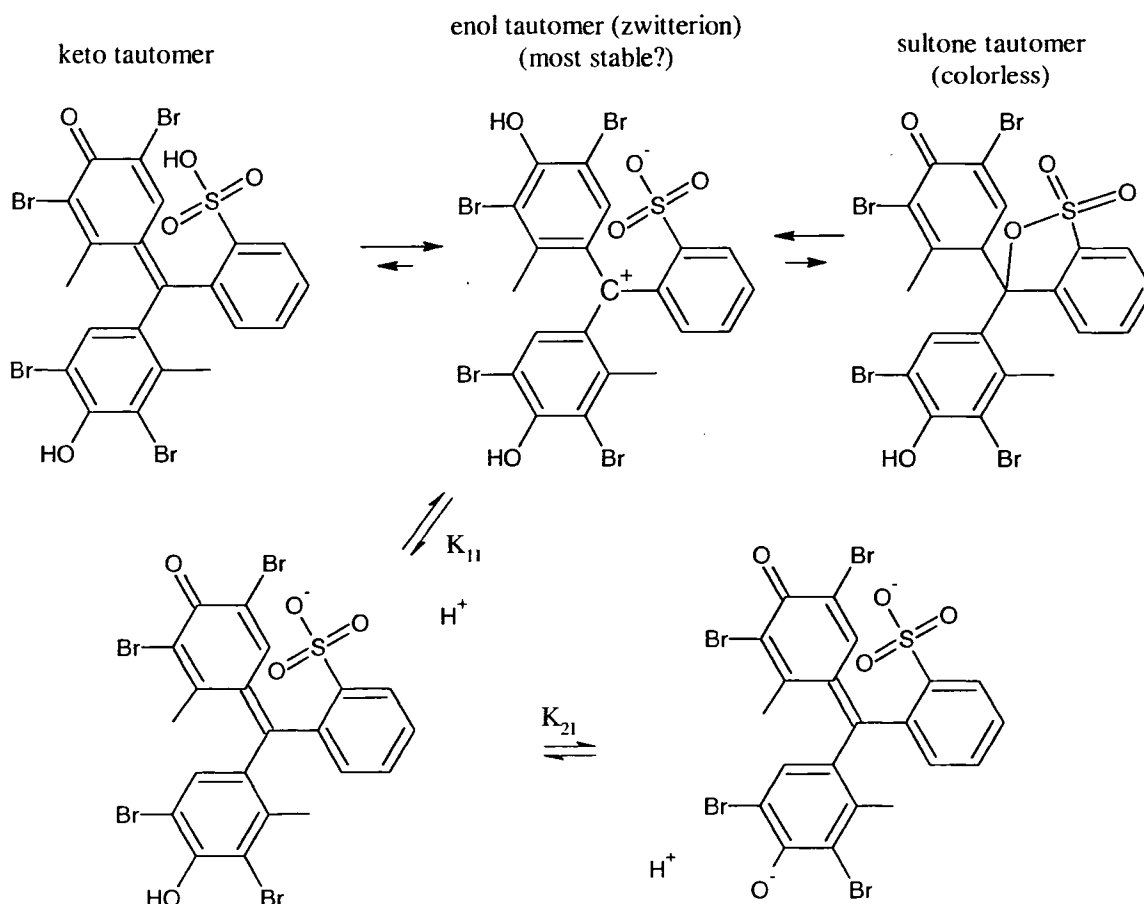
202

keto tautomer   enol tautomer (zwitterion) (most stable?)   sultone tautomer (colorless)

Figure C.1 Bromocresol green's $(3',3'',5',5''$-Tetrabromo-m-cresolsulfonephthalein) three fully protonated constitutional isomers and their two dissociations. The sultone tautomer is probably not present in solution (Kolthoff, 1937). Keto tautomers are typically the most stable form of the first two structures shown (favoring the first structure) but the sulfonic acid group is probably a stronger acid than the hydroquinone group (favoring the second structure). For all sulfonephthaleins, the H_2I and I^{2-} forms have a similar absorbance spectrum which parallels the symmetry between the enol tautomer and the I^{2-} structures shown here (Aragoni et al., 1995).

C.1 UV-VIS (dis)agreement between dye lots of BCG

Direct comparison of molar absorptivities provides the most compelling evidence of a colored impurity in the monoprotic sodium salt of BCG. As described above, for two dye lots with different dye content, the molar absorptivity spectrum of one lot is a scalar multiplication of the other. This statement also holds for changes in dye purity, given that the impurity does not absorb light. Differences in dye content and purity are therefore detected by UV-VIS spectrophotometry by inspecting the superimposed molar absorptivity spectra of different dye lots. This approach is relatively straightforward, but

203

demands very accurate and reproducible experimental methods of both solution preparation and absorbance measurement.

Indicator solutions were prepared at high and low pH to maximize one form of the indicator. The general procedures followed for solution preparation are found in Section 3.1. Absorbance measurements were made on the Cary 300 at 1cm pathlength and 25°C. As shown in Figure C.2, molar absorptivity is reproducible to ~ 0.1% where absorbance is greater than ~0.3 (absorbance maximum ~0.9). The % relative standard deviation
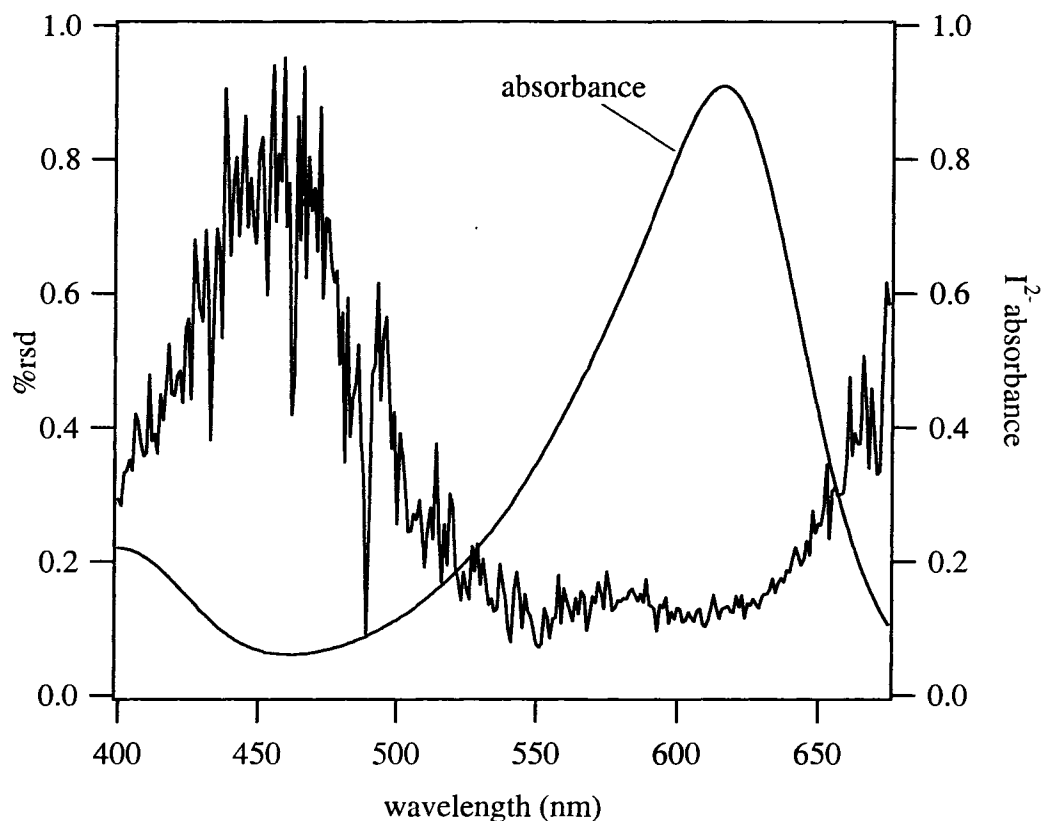

Figure C.2 Molar absorptivity % relative standard deviation of four separately prepared solutions of I^{2-} (left axis) and the nominal absorbance of the solutions (right axis).

shown in Figure C.2 is from four solutions prepared from the same indicator stock. The reproducibility at 616 nm corresponds to a molar absorptivity value of ~48000 ± 50 m^- $^1cm^{-1}$. This level of precision is sufficient to resolve the differences between different dye

lots. As shown in Figure C.3, at 616 nm the difference in ε_I between the two dye lots is

~2100 $m^{-1}cm^{-1}$. From 400-491 nm, the HB dye lot has a higher ε_I. At 492 nm, the spectra

cross and the DI lot has a greater ε_I until after the absorbance maximum where they cross
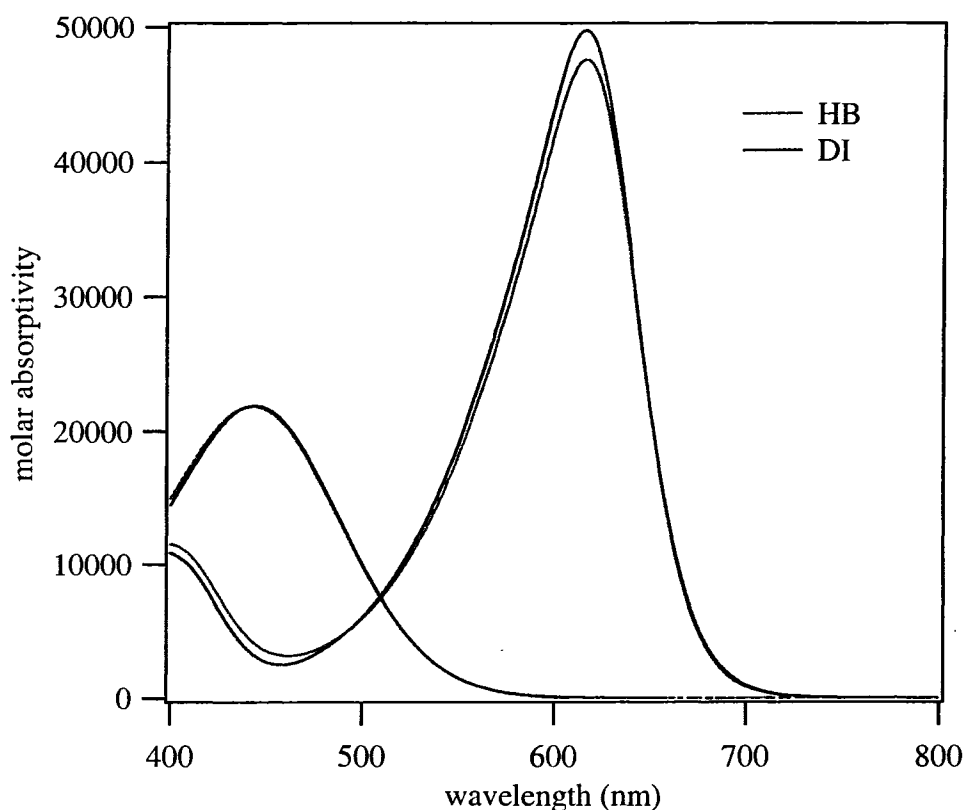

Figure C.3 Molar absorptivity (in $m^{-1}cm^{-1}$) spectra of two dye lots of BCG.

again at 651 nm. Above 652 nm, the HB ε_I is slightly more prominent. The HI⁻ spectra

are also in disagreement (Figure C.4). The HI⁻ absorbance maxima differ by 1 nm with

the HB λ_{max} = 443 nm and the DI λ_{max} = 444 nm. Although less drastic in magnitude than

the I^{2-} spectra, the HI⁻ molar absorptivities lend an important clue in terms of dye purity.

The HI⁻ λ_{max} of BCG has been reported as 444 nm in several previous studies. This

suggests that the dye lot 02830HB is contaminated with a colored impurity. Given the

reported percentages of dye content and purity, however, both lots may simply contain
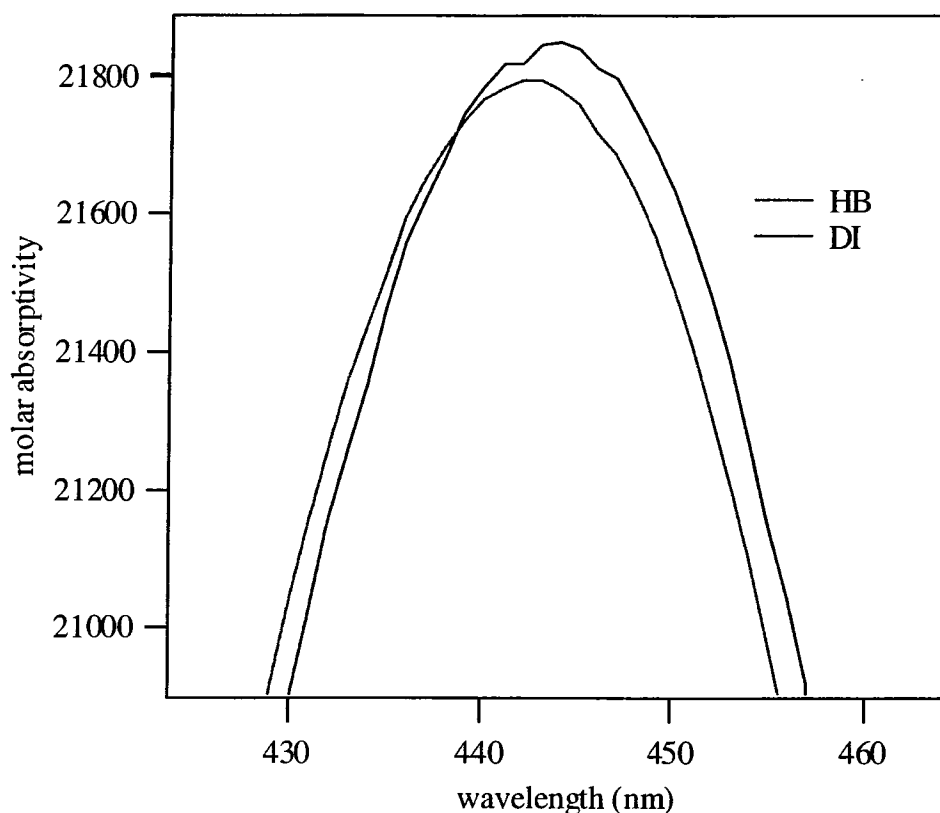
205

Figure C.4 Expanded view of the HI⁻ molar absorptivity spectra shown in Figure C.3.

different amounts of the same colored impurity. The isosbestic wavelength, λ_{iso}, of BCG was found at 509.5 nm for the DI lot and 509.8 for HB lot. King and Kester (1990) report λ_{iso} = 509.5 nm for BCG in NaCl. The difference in λ_{iso} between the lots therefore also points toward an impurity in the HB. It is more difficult to draw conclusions from the singly protonated spectra because HI⁻ is never fully isolated. For example, lowering the pH of an HI⁻ solution from 1.9 to 0.15 (BCG in ~0.7 m HCl) decreases the molar absorptivity measured (after correcting for I^{2-}), probably due to the appearance of the H_2I form. It is not possible to correct BCG spectra for the presence of H_2I because pK_{II} is theorized to be -4.4, preventing observation of the H_2I absorbance spectrum at ionic strengths anywhere near I = 0.7 m (at $[H^+]$ ~ 0.7, pH ~0.15).

The next step in a UV-VIS investigation of dye impurity is a full spectral analysis of the pH dependence of the spectra. If a BCG precursor is present, it is likely to have a pH dependence. The procedure would follow three steps: (1) Solutions are prepared analytically at small pH steps over the entire pH transition of BCG and absorbance is measured on each solution. (2) Using molar absorptivity spectra of HI^- and I^{2-}, absorbance is modeled for the pH and concentration values from the analytical preparations. (3) The observed and generated spectra are analyzed graphically and numerically for disagreement. Subtracting modeled from observed absorbance reveals the spectrum of the colored impurity.

C.2 Sigma-Aldrich internal document & email correspondence

In the Fall of 2003, I contacted Sigma-Aldrich in hopes of shedding light on the observations I had recently made on BCG (C.1). After several unsuccessful attempts to speak with one of their chemists, I was finally given contact number and e-mail address (after they realized that I was not going to quit calling until they gave it to me). Below I have transcribed an internal document that I received via fax from Aldrich Technical Services and the contents of an e-mail from one of the chief synthesis chemists in the stains and dyes department (Richard Bruesewitz)

Original Document: Aldrich Technical Services, Received by fax September 2003.

Dye Content

The concept of "Dye Content" is not rigorously defined. The term was originally defined as the percent by weight of dyes in commercial dyes which were frequently contaminated or purposely diluted with noncolored materials such as inorganic salts, solvents of crystallization, and other additives such as antidusting agents, dispersants, etc. Hence, the term refers to the percent by weight of total dyes in the mixture and should not be confused with dye purity.

Determination

207

There are several methods of determining the dye content of a dye, and the method to be used is somewhat dependent on the characteristics of the dye.

1. Elemental Analysis
This is a general method useful for most dyes, and involves comparison of the percent carbon and nitrogen found with that calculated for the assumed structure. The values obtained for carbon and nitrogen should agree; lack of agreement indicates possible contamination by carbon or nitrogen containing impurities.

2. UV-Visible Spectrometry
This is a general method that requires comparison of extinction coefficients or E(1%) values for a dye sample versus those for a reference standard whose dye content has been independently determined by some other method. This is a general method applicable to most dyes, and is reliable to the extent that the reference standard is well characterized. The conditions under which the spectra are obtained (solvent, concentration) should be as close as possible, since some dyes are notorious for the deviation from Beer's law.

3. Gravimetric Determination
This method is limited to those dyes which can be quantitatively precipitated from aqueous solution as the free acid, which is recovered by filtration, dried, and weighed. This method is specified by the Biological Stain Commission for the determination of the dye content of Eosin Y, and by the FDA for Erythrosin (FD&C Red No. 3).

4. Titanium Trichloride Titration
Most dyes are relatively easily reduced to colorless "leuco" compounds. This procedure involves titration of the dye sample with a standard solution nof TiCl$_3$ to some color change. Most heterocyclid dyes (thiazine, oxazine, diazine) as well as triaryl methane dyes are reduced to colorless diaryl hydrazines. It is essential that the stoichiometry of the reduction to the end point be known, i.e., the number of equivalents required to reach the endpoint. There are also a number of operational difficulties involved. Oxygen must be rigorously excluded from the system and the titrant has a poor shelf life, requiring frequent restandardization. The quality of the results obtained with TiCl$_3$ titrations is highly dependent upon the analyst's skill and experience.

Obviously, all of these methods have their strengths and weaknesses.

It is extremely important to not confuse the concept of dye content with that of dye purity. The former refers to the total percentage of dye(s) in

208

the sample, while the latter refers to the purity of the dye as determined [by] chromatographic methods such as HPLC or quantitative TLC or NMR. Thus, it is possible to have a dye sample with a dye content of 100% and a dye purity of 50%, or a dye content of 50% and a dye purity of ·100%.

Original email:
> **Subject:** Re: dye imputities?
> **From:** Rick Bruesewitz
> **Date:** Thu, 30 Oct 2003 14:23:46
> **To:** Todd Martz

> *Todd,*
> *Bromocresol green is 3',3'',5',5''-tetrabromo-m-cresolsulfonephthalein and it is made by brominating m-Cresol Purple (Aldrich p/ 85789-0) and then converting to the sodium salt. Most likely impurities are under brominated species. Bromocresol Green is typically used as a pH indicator and ACS tests require a specific pH range for the visual transition interval. Small amounts of lower brominated material do not change the transition interval enough to lessen its use as a pH indicator; however it could change the spectrum slightly which is more sensitive than the human eye.*

C.3 Electrophoresis

Dr. Chris Palmer and Erika Rauk ran capillary electrophoresis (Agilent CE)

separations on BCG. The unit is equipped with an optical flow cell connected to a diode

array (200-600 nm range) capable of absorbance measurements on the capillary eluent.

The BCG peak was detected at high pH where I^{2-} dominated the speciation. The

parameters that produced the best results were: BCG $\sim 1 \times 10^{-5}$ M, 70 mM borate buffer

(pH $\sim$ 9.2), capillary length = 48 cm, capillary potential = 20 kV, at 25°C. Under these

conditions, BCG retention time was ~10.6 min. The absorbance spectrum of the BCG

peak is shown in Figure C.5. The chromatograms of one separation are shown in Figures

C.6 and C.7. As seen in Figures C.6 and C.7, there is only one detectable eluent peak.

Although no colored impurities were detected, the instrumental noise is close to the

magnitude of the expected impurity. If impurities are present as underbrominated

209

precursors of BCG, they would be expected to elute at a significantly faster time. It is therefore unlikely that multiple sulfonephthalein molecules are buried in the analyte peak at 10.6 minutes. Future studies of BCG by capillary electrophoresis would be more sensitive to the small impurities if the detection system was configured for measurements shifted more toward the visible end of the spectrum where sulfonephthaleins absorb light more strongly.
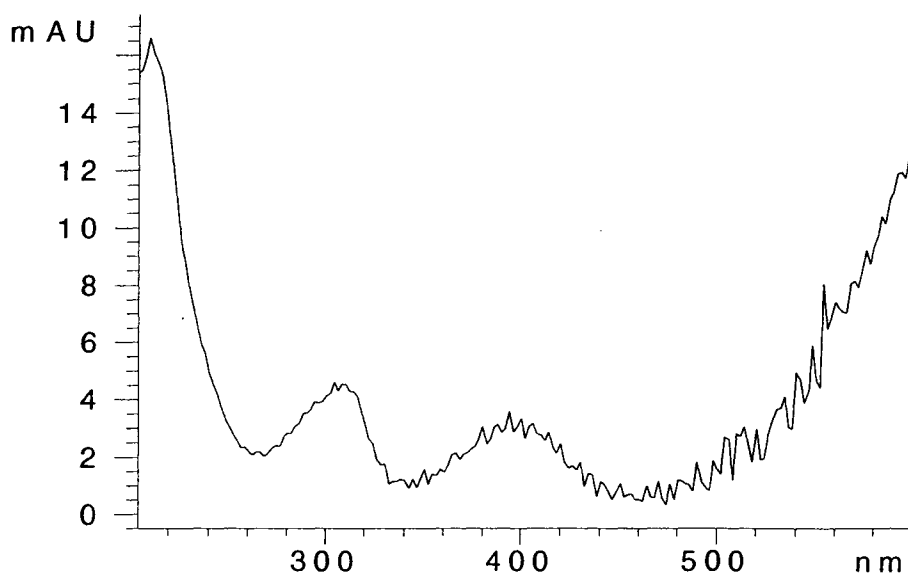

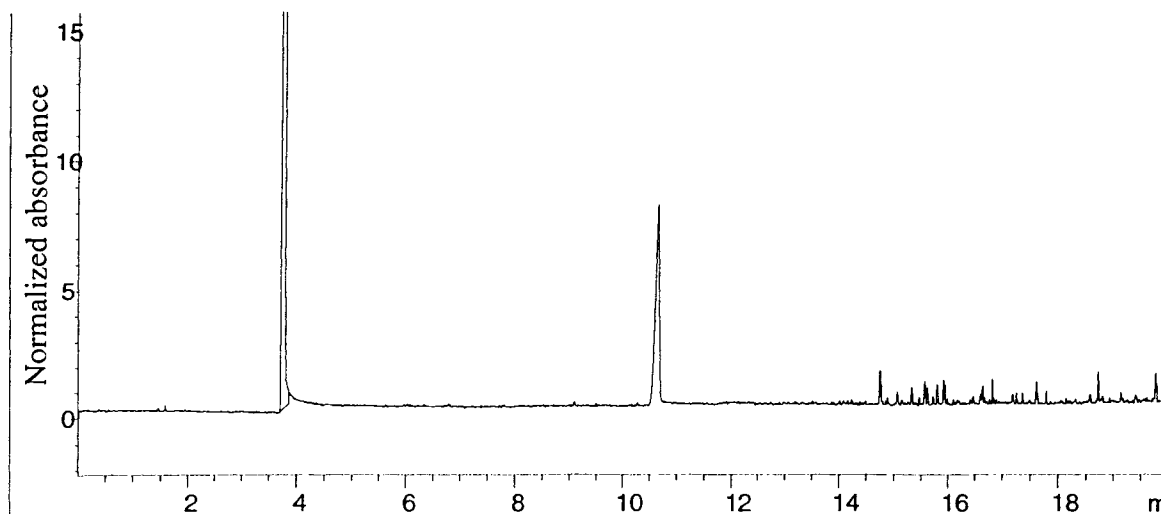**Figure C.5** Absorbance spectrum of the BCG peak eluted by capillary electrophoresis.

Figure C.6 Capillary electrophoresis chromatograph of BCG monitored at 244 nm. The peak at 3.8 min is acetone. The peak at 10.6 minutes is BCG.
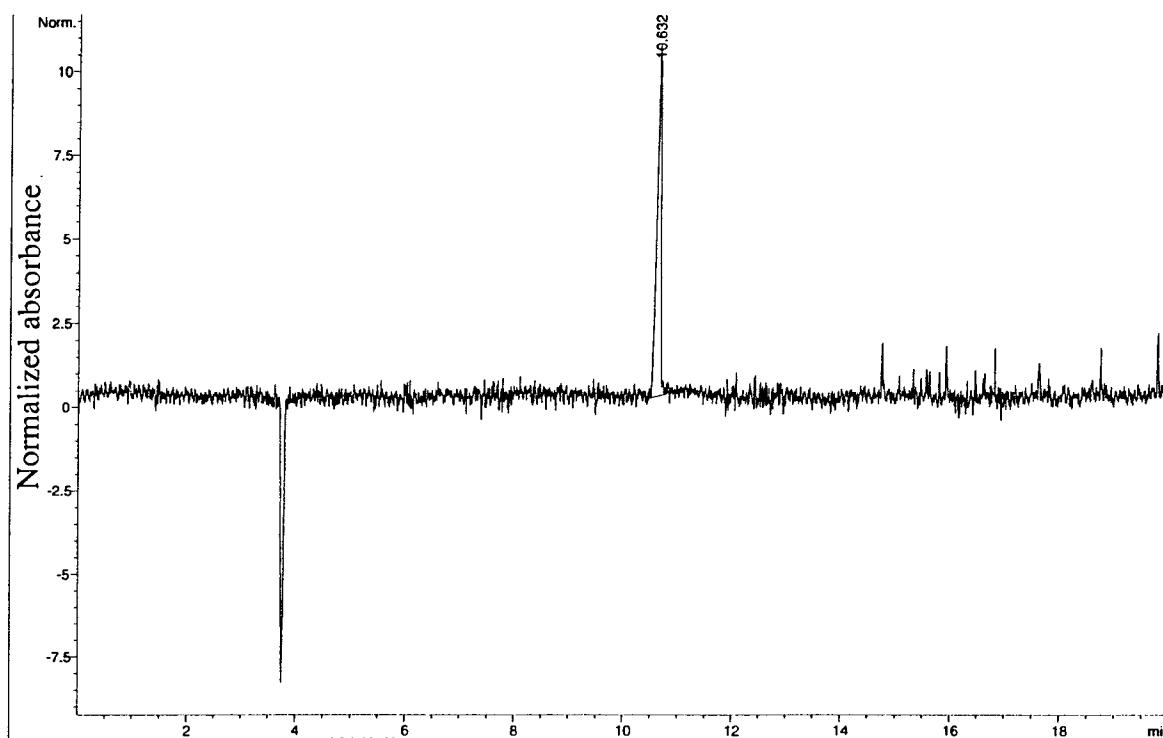
210

Figure C.7 Capillary electrophoresis chromatograph of BCG monitored at 550 nm. The peak at 3.8 min is acetone. The peak at 10.6 min is BCG.

C.4 TOF Mass Spectrometry

Dr. Reggie Spaulding carried out time-of-flight mass spectrometry on BCG using a Micromass LCT with electrospray ionization. It was hoped that this soft ionization technique would result in little or no molecular fragmentation. Mass spectra of the molecular ions originally present in the sodium salt of BCG would then reveal the under-brominated precursors theorized to contaminate the salt.

Samples (9:1 solution of 1×10^{-4} M BCG:MeOH) were introduced through an LC unit by simple loop injection (i.e. no column). A sample cone voltage of 30 V gave the least fragmentation. Adjusting pH of the sample had little or no effect on the spectra. As shown in Figures C.8 and C.9, positive ion mode was rich in peaks, while negative ion mode was relatively poor. Masses corresponding to BCG and its underbrominated forms are given in Table C.1.
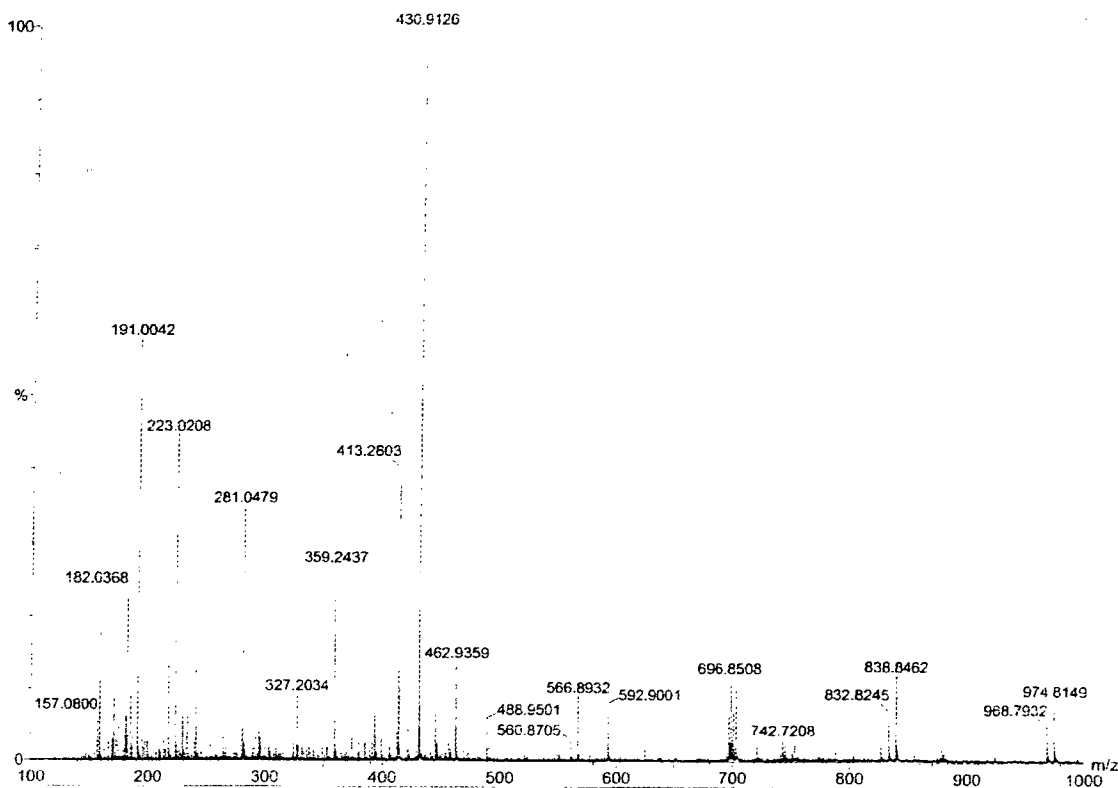
211

Figure C.8 Positive ion mass spectrum of BCG. Obtained by TOF-MS with electrospary ionization, sample cone voltage = 30 V.

Mass spectra of halogenated sulfonephthaleins will exhibit isotopic clusters due to the stable isotopes of Br and S (McLafferty, 1973)[65]. Bromine has two natural isotopes, ^{79}Br and ^{81}Br, occurring in nearly equal relative proportions. ^{32}S and ^{34}S, with relative proportions of about 22 to 1, respectively, account for most of the natural isotopic abundance of Sulfur. It is straightforward to show that an ion with four Br atoms will exhibit five peaks of varying intensity, each separated by two mass units[66]. Similarly, an ion with one S atom will have two peaks of relative proportion 22:1, also separated by two mass units. The combination of these effects is calculated using a binomial

---

[65] Stable isotopes of O and C contribute very little to the isotopic cluster pattern, because they occur in relatively trace amounts.

[66] In a molecule with one Br atom, the two isotopes of Br result in two molecular ion peaks of roughly equal relative proportion, separated by two mass units. Likewise, two Br atoms give three peaks, each separated by two mass units, with a relative abundance of 1:2:1; three Br atoms give four peaks in relative abundance of 1:3.3:3.3:1; and four Br atoms give five peaks in relative abundance of 1:1.5:6:1.5:1.

212

expansion which gives the relative abundance of the spectra at each mass unit possible by the different combinations of isotopes. A simplistic description of the isotopic signature of BCG is as follows: An ion with four Br atoms and one S atom exhibits five Br peaks corresponding to each S isotope, resulting in two overlaid five-peak clusters. The peaks in each cluster will be separated by two mass units due to the Br isotope. The cluster of peaks corresponding to ^{34}S should be much less abundant than the peaks corresponding to ^{32}S. The combination of average elemental masses for Br and S results in a shift of about 1 mass unit between the two clusters, giving peaks on 1 unit intervals, instead of 2 unit intervals. As shown in Figure C.10, the cluster of peaks from 694.77 to 703.97 (positive ion, Figure C.8) closely matches this description.
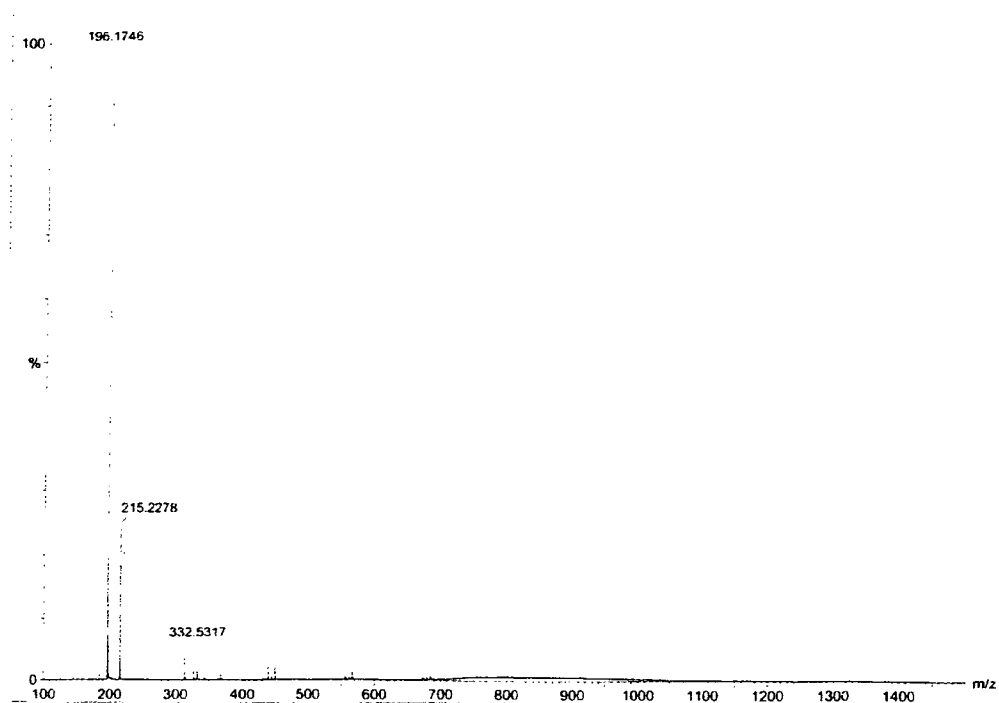

Figure C.9 Negative ion mass spectrum of BCG. Obtained by TOF-MS with electrospary ionization, sample cone voltage = 30 V.

Table C.1 Sulfonephthalein ions, their formulas and masses. MCP is m-cresol purple, the precursor of BCG.

ion	chemical formula	mass
H_2BCGH^+	$C_{21}H_{15}Br_4O_5S$	699
Na_2HBCG^+	$C_{21}H_{13}Br_4O_5SNa_2$	743
$NaH_2BCG^+ - 2Br + 2H$	$C_{21}H_{16}Br_2O_5SNa$	563
$NaH_2MCP^+ -2H + 2Br$	$C_{21}H_{16}Br_2O_5SNa$	563
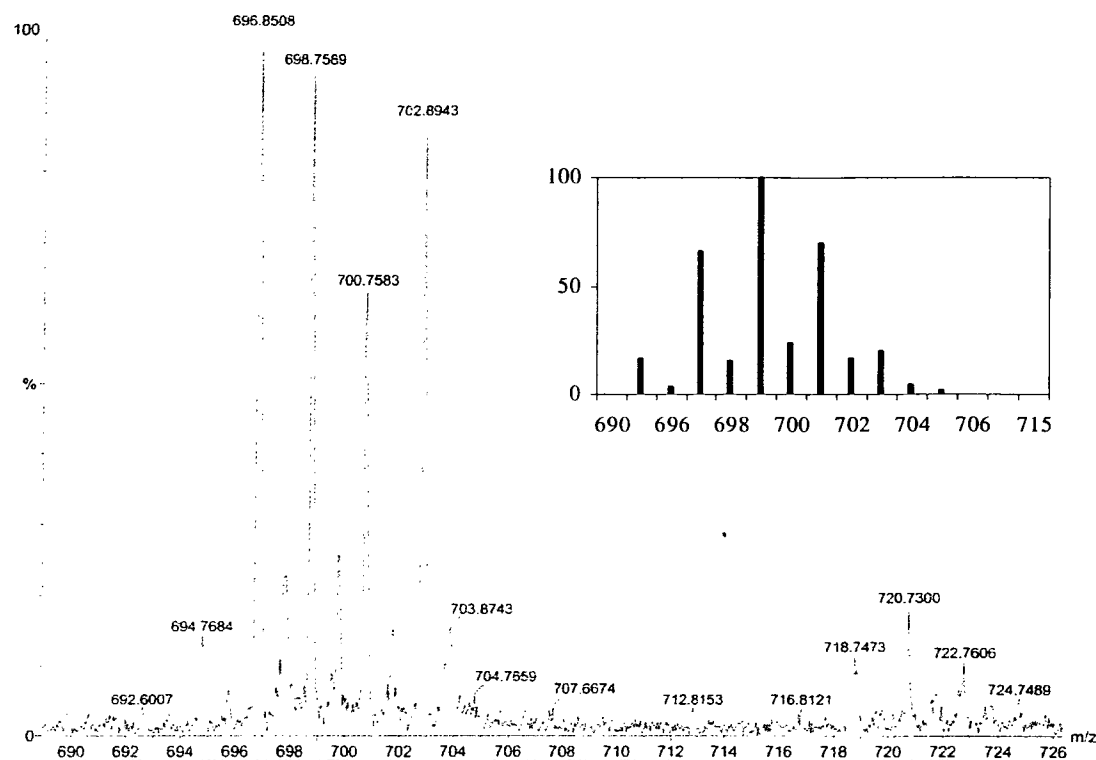
Figure C.10 Expanded view of Figure C.8 over the region of Bromocresol green and the theoretical appearance of the isotopic cluster (inset).

Because the electrospray process was destructive, degradation products dominated the spectrum, with very little of the original ion present (Figure C.8). The partially brominated ion $C_{21}H_{16}Br_2O_5SNa^+$ (Table C.1) may be responsible for the peak around 561 (Figure C.8) but, because fragmentation occurred, it is impossible to tell if this is the underbrominated BCG (partially brominated MCP) present in the indicator salt or degraded BCG, formed during electrospray. Impurities were therefore not directly observable, because they cannot be separated from degradation products. Two different

214

dye lots of BCG were analyzed, but differences were not discernable due to the high fragmentation.

C.5 Conclusions

Over the last three years I carried out or initiated various experiments designed to elucidate the purity of NaHBCG. As a whole, the experiments were inconclusive. They are presented here mainly as a guide for those wishing to pursue studies of indicator purity. Although I was unable to demonstrate, by independent methods, that the sodium salt of BCG contained a colored impurity, the method most sensitive to colored impurities (UV-VIS, Section C.1) strongly suggests that at least one dye lot does indeed contain a colored impurity. If this is the case, the results underscore the importance of dye lot in studies involving highly accurate pH measurement. As such, researchers conducting these types of studies should beware using literature values of molar absorptivities or ratios thereof, when using a dye lot different than that used to determine the literature value. It seems most likely that the impurity would be underbrominated forms of BCG, such as meta cresol purple. Regrettably, the electrospray process destructively ionized BCG, making it difficult to identify underbrominated precursors by TOF-MS. Electrophoresis was not sensitive enough to resolve peaks in the 1% dye impurity range. A more robust technique for a thorough study of sulfonephthalein dye purity would probably consist of a combination of the methods described in Sections C.3 (i.e. a separation) and C.4 (mass spectrometric detection). There is little reported in the literature regarding the application of these methods to sulphonephthalein molecules. A good starting point might be an HPLC-based version of the MALDI-MS technique reported by Kruger et al. (2001) for several sulfonephthaleins.

215

I chose to focus on measuring the impurity rather than eliminating it. As mentioned in the introduction to this appendix, some researchers have attempted to purify sulfonephthaleins by recrystallization. Our laboratory attempted this with Cresol red but found no increase in molar absorptivities (J. Carr, pers. comm.). This finding is similar to that of Yamazaki et al. (1992a). This result can be misinterpreted as the indicator salt having no colored impurities, if those impurities simply recrystallized along with the indicator. HPLC is potentially the best approach but, until the different impurities in the eluent can be measured, the separation cannot be optimized by selecting the appropriate column. Following this logic, it seems critical that optimization of the detection of impurities must precede the separation and purification of the indicator.

216

Appendix D   Uncertainty Calculations

Uncertainty analysis is a helpful technique in determining which parameters will dictate both precision and accuracy. The EURACHEM/CITAC working group provides an excellent reference for the general theory of uncertainty calculations (Ellison et al., 2000). For simple problems involving only a few arithmetic operations, the combined standard uncertainty, U_c is directly calculated from the original equation of the value of interest (for simple chemical examples see Kocherlakota et al., 2002). This approach involves evaluating uncertainties for operations of multiplication and division separately from operations of addition and subtraction. In effect, the equation's uncertainty is calculated from the inside-out, alternating between the multiplication/division model and the addition/subtraction model.

Rigorous calculation of the U_c by the propagation of error method described above quickly becomes a burdensome process as the number of variables increases. For complex functions of mixed operations, the U_c is therefore estimated using the numerical approximation to the partial derivative of each parameter with respect to the function. As described by Kragten (1994), spreadsheets are ideal for such calculations. The inputs required are (1) the original equation of the value for which U_c is to be calculated, (2) approximate values of each variable in the equation, and (3) estimates of the individual uncertainties for each variable.

D.1   Quantifying uncertainty with a spreadsheet

This appendix details the methods followed in creating Figure 2.8. As described in the EURACHEM/CITAC Guide *Quantifying Uncertainty in analytical measurement* (Ellison et al, 2000), a spreadsheet can be used to approximate the standard uncertainty of

217

a measurement by numerical differentiation. This approach involves assigning each variable to a cell and calculating the value of interest from these cells. Then, one at a time, each variable's uncertainty is added and the analytical value is recalculated separately for every variable. As an example, consider the preparation of a solution of Na_2CO_3 in deionized water. The four variables needed to calculate the TA are the mass of Na_2CO_3, formula weight of Na_2CO_3, purity of the salt and the mass of H_2O. Figure D.1 shows the spreadsheet used to calculate the combined standard uncertainty, U(TA), and Figure D.2 gives the formulas and names assigned to each cell in the calculation. The four variables without error are entered in column C, rows 5-8, and TA is calculated in cell C11. Cells C5-C8 and C11 are given descriptive names (using the Excel name box), which carry the value of the cell as an absolute reference. The individual uncertainties are entered in row 3 columns D-G and also given descriptive names.

A1	B	C	D	E	F	G
2			U(g Na_2CO_3)	U(FW)	U(%purity)	U(g H_2O)
3			0.0002	0.001	0.001%	0.10
4	variable	value		value + uncertainty		
5	grams Na_2CO_3	0.2500	0.2502	0.2500	0.2500	0.2500
6	FW Na_2CO_3	105.99	105.99	105.991	105.99	105.99
7	% purity	99.997%	99.997%	99.997%	99.998%	99.997%
8	g H_2O	1000.00	1000.00	1000.00	1000.00	1000.10
9						
10			TA	TA(gsalt'...)	TA(...FW'...)	TA(...%purity'...)	TA(...gH₂O'...)
11			0.002359	0.002361	0.002359	0.002359	0.002358
12				U(TA(gsalt'))	U(TA(FW'))	U(TA(%purity'))	U(TA(gH₂O'))
13				1.89E-06	-2.23E-08	2.36E-08	-2.36E-07
14			U(TA)	U(TA(gsalt'))²	U(TA(FW'))²	U(TA(%purity'))²	U(TA(gH₂O'))²
15			0.000002	3.56E-12	4.95E-16	5.56E-16	5.56E-14

Figure D.1 Snapshot of an example spreadsheet for calculating the combined standard uncertainty of a carbonate standard for freshwater TA.

218

A1	B	C	D	E	F	G
2			U(g Na$_2$CO$_3$)	U(FW)	U(%purity)	U(g H$_2$O)
3			0.0002 (Ugsalt)	0.001 (UFW)	0.001% (Upurity)	0.1 (UgH2O)
4	variable	value	value + uncertainty			
5	grams Na$_2$CO$_3$	0.25 (gsalt)	gsalt+Ugsalt	gsalt	gsalt	gsalt
6	FW Na$_2$CO$_3$	105.99 (FW)	FW	FW+UFW	FW	FW
7	% purity	99.997% (purity)	purity	purity	purity+Upurity	purity
8	g H$_2$O	1000 (gH2O)	gH2O	gH2O	gH2O	gH2O+UgH2O
9						
10		TA	TA(gsalt'...)	TA(...FW'...)	TA(...%purity'...)	TA(...gH$_2$O'...)
11		(gsalt*purity/FW)/(gH2O/1000)	(D5*D7/D6)/(D8/1000)	(E5*E7/E6)/(E8/1000)	(F5*F7/F6)/(F8/1000)	(G5*G7/G6)/(G8/1000)
12			U(TA(gsalt'))	U(TA(FW'))	U(TA(%purity'))	U(TA(gH$_2$O'))
13			D11-TA	E11-TA	F11-TA	G11-TA
14		U(TA)	U(TA(gsalt'))^2	U(TA(FW'))^2	U(TA(%purity'))^2	U(TA(gH$_2$O'))^2
15		SQRT(SUM(D15:G15))	D13^2	E13^2	F13^2	G13^2

Figure D.2 Calculations from Figure D.1. For named cells (C5-C8 and D3-G3), the name carries the numerical value of a cell as an absolute reference and the name assigned to a cell is shown in parenthesis following the value entered into the cell.

In columns D-G, rows 5-8 reference the four variables in column B, adding in the uncertainty component (row 3) and row 11 calculates TA using the set of variables for each respective column. In each column, an uncertainty value is added to only one variable (highlighted cells). Row 11 thus contains one TA value without error (C11) and four values with varying amounts of error (D11-G11). Each TA uncertainty element is calculated from the difference between the correct value and the value with error (row 13). The differences are squared to eliminate negative values (D15-G15). The square root of the sum of the squared differences is the combined standard uncertainty, U(TA), cell C15.

The spreadsheets used to create Figure 2.8 are too big to show on a single page. Because a titration was the focus and [H$^+$] weighs heavily on which variables dominate the uncertainty, this 16-variable spreadsheet was repeated 18 times for different acid increments, corresponding to different [H$^+$] values.

D.2 Uncertainty of ε, [I]$_{stock}$, and Acy

In Section 2.4, U$_c$ is calculated for a seawater alkalinity titration. Kragten's method was quite useful in generating Figure 2.8 because there are several variables to

219

consider and the importance of each component that contributes to U_c varies with pH, requiring a separate analysis of U_c for each titrant addition. This calculation would prove very tedious by simple propagation of error calculations. As a simplification step, the U_C was first calculated individually for εb, I_{stock} and Acy, and these numbers were then used to calculate U_c for TA. Moreover, estimating the probable errors associated with each of these solutions is an important step that warrants a separate calculation.

Due to the importance of molar absorptivity, ε, throughout this study, examination of ε measurement uncertainty was critical in minimizing errors. The uncertainty of ε was calculated by propagation of error for several different scenarios using the equation

$$\frac{{}^{\lambda}A\left(g\,stock + g\,H_2O(dilut.) + g\,X\right)}{\left(b \times g\,stock\,\dfrac{\dfrac{g\,salt + \%\,dc + \%\,dp}{FW_{NaHBCG}}}{g\,H_2O(stock)\Big/1000}\right)} \cdot \qquad \textbf{D.1}$$

Table D.1 gives a brief description of the variables used in Equation D.1, their values and their estimated uncertainties. Equation D.1 describes a measurement of ε at one wavelength (channel) for an indicator solution prepared from a stock solution of the indicator salt. As shown in Figure D.3, the uncertainty in ${}_{620}\varepsilon_l$ for a solution prepared according to the values given in Table D.1 is mostly due to absorbance errors, followed by pathlength errors and grams of the indicator salt; when it is assumed that errors in % dye purity and % dye content do not contribute. In Table D.1 and Figure D.3, grams of NaCl (added to set ionic strength) are not shown, but the uncertainty in this value adds less than 0.1 $m^{-1}cm^{-1}$ to U_C. Assuming that the same sample chamber (pathlength) and

220

indicator stock solution are used throughout a series of experiments, absorbance accuracy and precision are the dominating components of a molar absorptivity measurement.

Table D.1 Parameters, their values and estimated errors for the accurate preparation of solutions to be used for ε measurements (see Figure D.3).

parameter	description	value	estimated error
g salt	grams of indicator salt added to stock	2.0000	0.0001
% dc	percent dye content %w/w	90%	0%
% dp	percent dye purity %w/w	97%	0%
FW	formula weight of the indicator salt	720.02	0.0001
g stock H_2O	grams of H_2O used to dissolve indicator salt (stock solution)	2400.00	0.01
g stock	grams stock solution added to buffered indicator solution	19.0000(I^{2-}) 28.0000(HI^-)	0.0001
g dilut. H_2O	grams H_2O in buffered indicator solution	600.00	0.01
g X	grams 0.1 M NaOH or HCl added to indicator solution to buffer pH	5.0000(NaOH) 40.0000(HCl)	0.01
λA	approximate absorbance at peak wavelength	~ 0.9	0.0005
b	optical pathlength	1.0000	0.0001

This (desirable) situation is only achieved with good analytical solution preparation. For example, preparing several 1000 mL I^{2-} solutions of indicator directly from the salt (~0.01g salt) for a concentration similar to that of Table D.1 results in $U_{c(620\varepsilon_I)} \sim 450\ m^{-1}cm^{-1}$. Similarly, using stock solution prepared from a different dye lot with a ~1% difference in dye content results in $U_{c(620\varepsilon_I)} \sim 500\ m^{-1}cm^{-1}$.
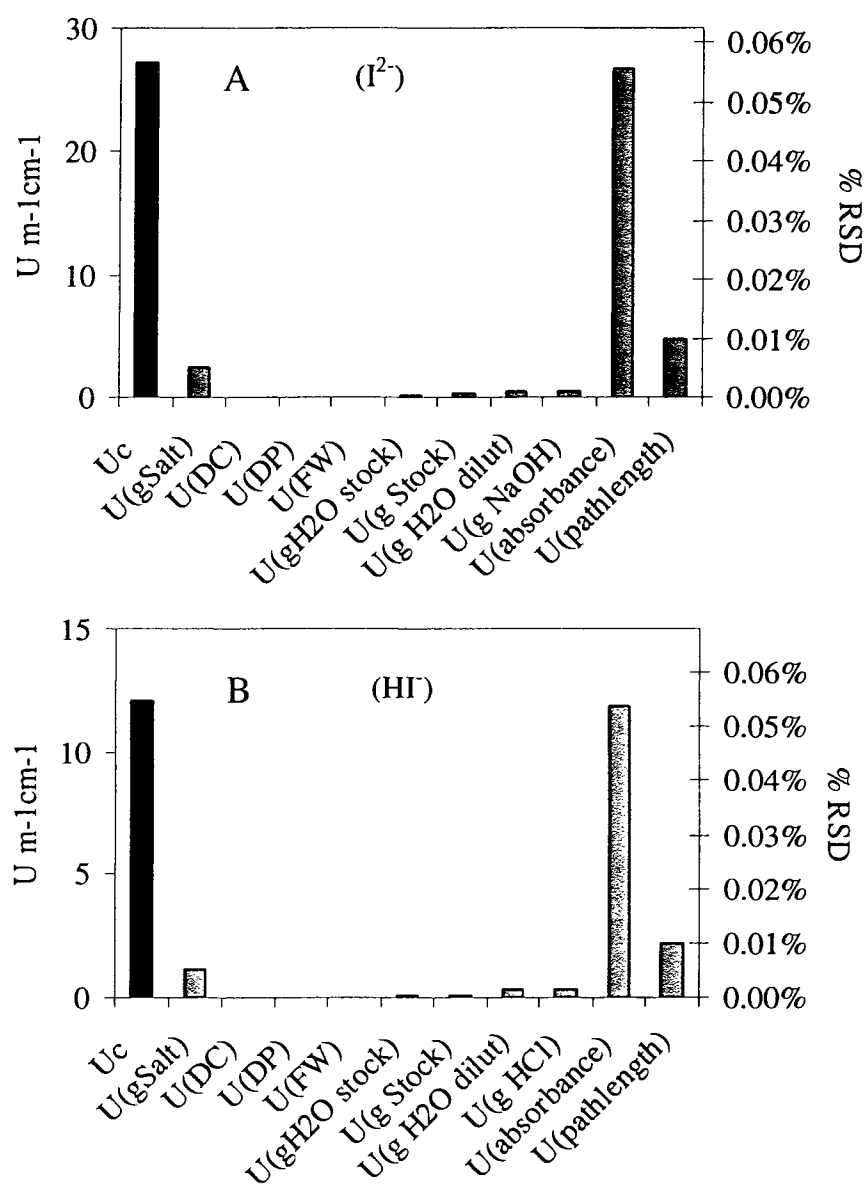
221

Figure D.3 Uncertainty analysis for measuring the molar absorptivity of (A) unprotonated and (B) singly protonated BCG at their respective peak wavelengths. See Table D.1 for corresponding values and estimated errors.

One aspect of the measurement not considered in Equation D.1 is the error resulting from slight pH changes due to the error in grams of NaOH or HCl. While insignificant for a solution of I^{2-}, errors related to small differences in pH (from weighing errors in grams HCl) should be considered when measuring $_\lambda\varepsilon_{HI}$ because the small absorbance due to I^{2-}

must first be subtracted from the measured absorbance before calculating $_\lambda\varepsilon_{HI}$. The

model, however, predicts that the concentration (and hence absorbance) changes in HI^-

and I^{2-} from weighing out the 0.1 M HCl are due mostly to dilution by HCl, rather than

shifts in speciation caused by the small differences in pH associated with the different

masses of HCl.

Beginning with the indicator stock solution, it is seen that the probable errors

(~1%) in both dye purity (dp) and dye content (dc) are the most important terms for the

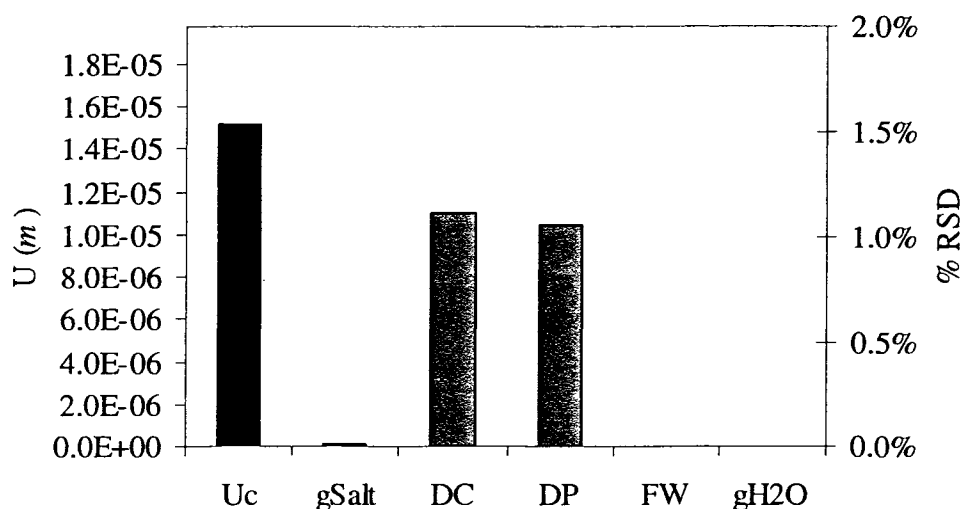'true' accuracy of the value I_{stock} (Figure 2.9, Table 2.2).

Figure D.4 Uncertainty of I_{stock} based on the expected errors in the solution preparation.

Table D.2 Values used to calculate Figure D.4.

parameter	value	estimated error	uncertainty in [I]stock
g NaHBCG	2.0000	0.0001	4.948E-08
% dye content	90%	1.00%	1.100E-05
% dye purity	95%	1.00%	1.042E-05
FW	720.02	0.00	6.872E-10
g H2O	2400.00	0.01	4.123E-09
[I]stock	9.8956E-04		1.515E-05

Because we were primarily interested in obtaining internally consistent measurements, a

single large batch (i.e. 2.4 L, Table 2.2) of indicator stock was used to prepare a set of

223

solutions for molar absorptivity studies and titrant. As shown in Figure 2.10, eliminating the effect of DC and DP errors, I_{stock} accuracy is mostly due to error associated with weighing out the indicator salt, with a small contribution from the mass of water in which the salt is dissolved. Next, the two components of the titrant, I_0 and Acy, are each considered separately for the same preparation of the titrant mixture. Acy is very sensitive to small protic impurities, so these are considered for both NaCl and NaHBCG salts. From the Fisher certificate of analysis for biological grade NaCl, values for protic impurities typically range between 0.001-0.002% HCl w/w.
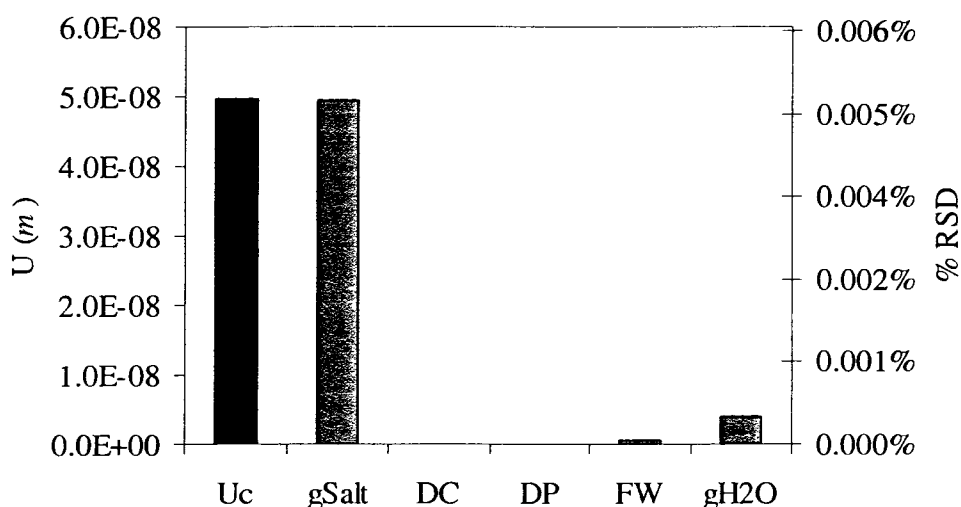

Figure D.5 Uncertainty of I_{stock} without errors from dye purity and dye content.

This translates into 16-32 μmol H per mol NaCl. It is difficult to estimate the protic impurity of the indicator salt. It is unlikely that NaHBCG contains an appreciable amount of a basic impurity, as the potentiometric pH of a stock solution is ~3.9-4.0; exactly that calculated using an equilibrium model. It seems more likely that a sulfonephthalein impurity would be acidic[67], because both acid forms are less soluble and precipitate from solution easier than the dibasic form. It would be helpful to have more

---

[67] This is not the case for Cresol Red, which seems to contain a basic impurity, based on electrode measurements of the stock solution.

224

information from the dye manufacturer regarding the exact condition under which the salt

of a particular indicator is recrystallized after synthesis. The dye content (~90%) leaves

much room for error in the estimation of impurities. Because the stock solution's

potentiometric pH agrees closely with its predicted pH, there is probably not more than

1% HCl w/w contained in the 10% impurity fraction. Using this number as a worst case

scenario, and assuming that the impurity is in fact HCl, a 1% impurity translates into

about 0.2 mol HCl per mol BCG. As shown in Figure 2.11 and Table 2.3, protic

impurities in the salts dominate the combined uncertainty of the titrant Acy.
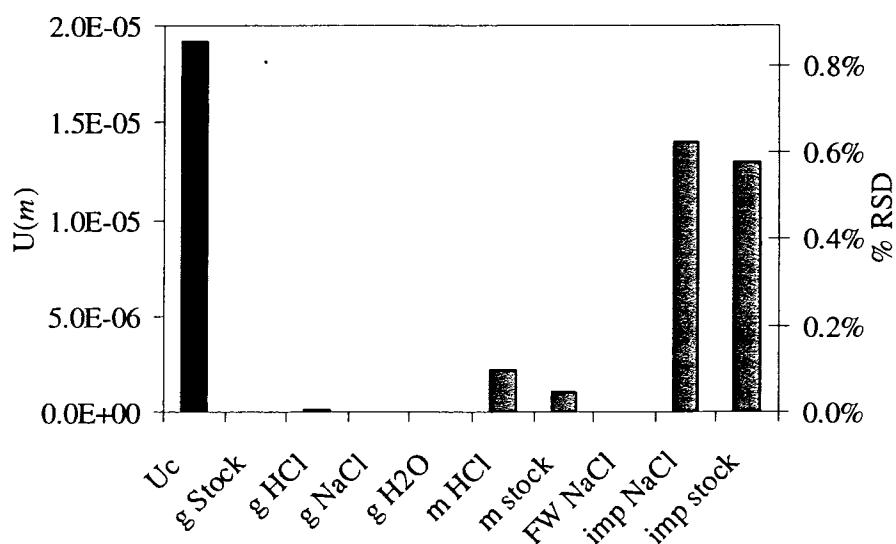

Figure D.6 Uncertainty in titrant Acy based on the estimated errors of each contributing parameter.

Although the contribution from the stock impurity is questionable, the error due to NaCl

impurity is comparatively certain. Unlike the indicator stock issues (see above), Acy

errors cannot be circumvented as easily. Acy inaccuracies will appear when a standard

solution of known TA is titrated. This problem is discussed in detail in Section 4.4.2.

225

Table D.3 Values used to calculate Figure D.6.

parameter	value	estimated error	uncertainty in Acy
g stock	450.00	0.01	1.82E-09
g HCl	150.00	0.01	1.42E-07
g NaCl	281.00	0.01	3.26E-09
g H2O	6000.00	0.01	3.26E-09
m HCl	0.1000	0.00010	2.18E-06
m stock	9.90E-04	1.51E-05	9.90E-07
FW NaCl	58.443	0.00	0.00E+00
imp NaCl	0.00E+00	2.00E-05	1.40E-05
imp Stock	0.00E+00	2.00E-01	1.29E-05
Acy	0.002245		1.920E-05

226

Appendix E Procedures for volumetric/gravimetric calibration

E.1 Calibration of a Kloehn pump

The procedures followed for the calibration of a syringe pump are described in

(Dickson, 2002)[68]. The general approach involves relating the volume dispensed (by a

specific glass barrel) to the exact step number of the pump's motor (read out by a

computer) using a function (typically linear or polynomial). Because each glass barrel

and plunger are different, the function derived by this calibration procedure is valid only
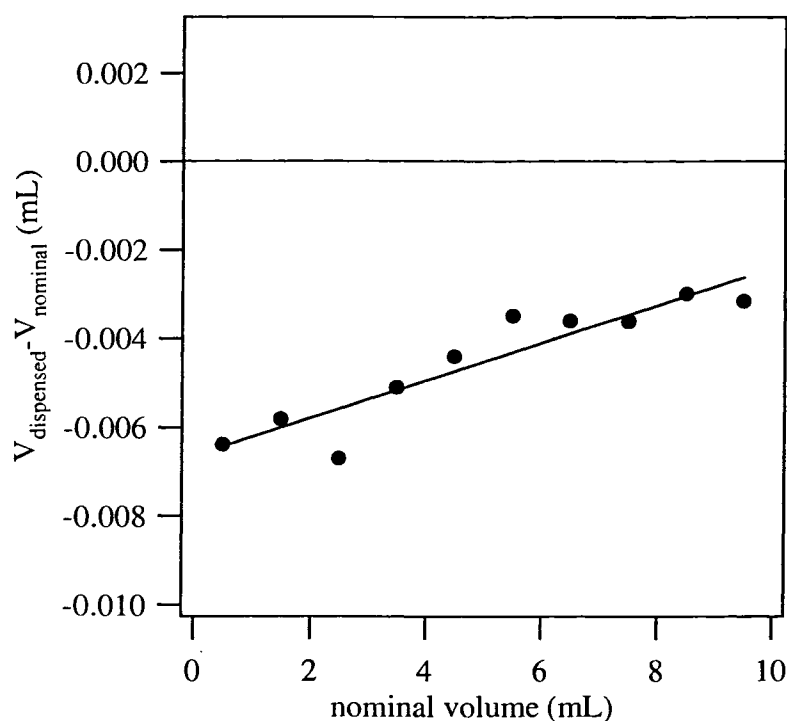
for a specific syringe.

Figure E.1 Kloehn pump volumetric calibration. Nominal volume is calculated from the step number of the pump motor and the rated volume of the syringe barrel. The function used to calculated volume dispensed for this particular pump was taken as a linear function: $V_{dispensed} = V_{nominal}(1+4.21\times10^{-4})-6.64\times10^{-4}$.

---

[68] This is an in-house procedure used in Andrew Dickson's laboratory. The document (and personal directions) was given to me by G. Anderson at SIO.

227

The volume change due to thermal expansion of the glass over the temperature change encountered in our laboratory is negligible[69]. The volumetric errors shown in Figure E.1 are small, but significant. For example, the correction results in a 3-4 μm difference in the titrant Acy (Section 3.6). The reproducibility of each point in Figure E.1 is $1\sigma \sim \pm 0.001$ mL, but this number should be regularly verified for at least one increment near the expected operation region of the syringe.

E.2 Density measurements

The density of solutions was measured using a 100 mL volumetric flask and open-face balance readable to 0.01 g. Flasks were first washed and dried in the oven[70]. Next, the dry weight of the flask was recorded, the flask was filled to the mark[71] with deionized water, and the weight and temperature of the water in the flask were recorded. The flask was then emptied and air dried. The procedure was then repeated for a solution of unknown density.

All weights are corrected for air-buoyancy. Using the well-established temperature-density relationship for pure H_2O, the volume of the flask is calculated. Thermal expansion of the glass was insignificant, and thus not accounted for (see footnote 69). The density of the second solution is calculated from the volume of the flask and the mass of the solution. Using different flasks, this procedure was reproducible to $\sim 0.04\%$.

---

[69] Volume changes associated with thermal expansion for the syringe barrel (section E.1) and the volumetric flask (Section E.2) are smaller than the resolution of the pump and scale, respectively.
[70] Drying volumetric glassware may change the volume contained.
[71] If the mark was passed the excess water was removed with a transfer pipet.

228

References

1) Almeida, C.M.N.V.; Lapa, R.A.S.; Lima, J.L.F.C.; Zagatto, E.A.G.; Araujo, M.C.U. 2000. An automatic titrator based on a multicommutated unsegmented flow system. Its application to acid-base titrations. *Anal. Chim. Acta* 407, 213-223.

2) Anderson, D.H.; Robinson, R.J. 1946. Rapid electrometric determination of the alkalinity of seawater. *Ind. Eng. Chem.*, 18, 767-769.

3) Anderson, L.A.; Sarmiento, J.L. 1994. Redfield ratios of remineralization determined by nutrient data analysis. *Global. Biogeochem. Cycles* 8, 65-80.

4) Anfalt, T.; Graneli, A.; Strandberg, M. 1976. Probe photometer based on optoelectronic components for the determination of total alkalinity in seawater. *Anal. Chem.* 48, 357-360.

5) Aragoni, M.C.; Arca, M.; Crisponi, G.; Nurchi, V.M.; Silvagni, R. 1995. Characterization of the ionization and spectral properties of sulfonephthalein indicators. Correlation with substituent effects and structural features. Part II. *Talanta.*, 42, 1157-1163.

6) Aronson, R.B.; Bruno, J.F.; Precht, W.F.; Glynn, P.W.; Harvell, C.D.; Kaufman, L.; Rogers, C.S.; Shinn, E.A.; Valentine, J.F. 2003. Causes of coral reef degradation. *Science.* 302, 1502-1503.

7) Arrhenius, S. 1912. *Theories of Solutions.* Yale University Press, New Haven, 247 pp.

8) Avakian, P.; Hsu, W.Y.; Meakin, P.; Snyder, H.L. 1984. Optical absorption of perdeuterated PMMA and influence of water. *J. Polymer Sci.* 22, 1607-1613.

9) Baker, B.C. 1997. Keeping the signal clean in photosensing instrumentation. *Sensors Magazine*, online, June edition.

10) Balch, W.M.; Holligan, P.M.; Ackleson, S.G.; Voss, K.J. 1991. Biological and optical properties of mesoscale coccolithophore blooms in the Gulf of Maine. *Limnol. Oceanogr.* 36, 629-643.

11) Bates, N.R. 2002. Seasonal variability of the effect of coral reefs on seawater CO_2 and air-sea CO_2 exchange. *Limnol. Oceanogr.* 47, 43-52.

12) Bates, N.R.; Michaels, A.F.; Knap, A.H. 1996. Alkalinity changes in the Sargasso Sea: geochemical evidence of calcification? *Mar. Chem.* 51, 347-358.

13) Bates, N.R.; Samuels, L.; Merlivat, L. 2001. Biogeochemical and physical factors influencing seawater fCO_2 and air-sea CO_2 exchange on the Bermuda coral reef. *Limnol. Oceanogr.* 46, 833-846.

14) Bates, R.G. **1964**. Determination of pH: theory and practice. Wiley & Sons, New York, 435 pp.

15) Bradshaw, A.L.; Brewer, P.G.; Shafer, D.K.; Williams, R.T. **1981**. Measurements of total carbon dioxide and alkalinity by potentiometric titration in the GEOSECS program. *Earth and Planetary Sci. Lett.*, 55, 99-115.

16) Bradshaw, A.L.; Brewer, P.G. **1988**. High precision measurements of alkalinity and total carbon dioxide in seawater by potentiometric titration – 1. Presence of unknown protolyte(s). *Mar. Chem.* 23, 69-86.

17) Breland, J.A.; Byrne, R.H. **1992**. Determination of seawater alkalinity by direct equilibration with carbon dioxide. *Anal. Chem.* 64, 2306-2309.

18) Breland, J.A.; Byrne, R.H. **1993**. Spectrophotometric procedures for determination of seawater alkalinity using bromocresol green. *Deep-Sea Res. I.*, 40, 629-641.

19) Brewer, P.G. **1978**. Direct observation of the oceanic CO_2 increase. *Geophys. Res. Lett.* 5, 997-1000.

20) Brewer, P.G.; Wong, G.T.F.; Bacon,, M.P.; Spencer, D.W. **1975**. An oceanic calcium problem? *Earth Planet. Sci. Lett.* 26, 81-87.

21) Broecker, W.S.; Peng, T.-H. **1982**. *Tracers in the sea.* Lamont-Doherty Geological Observatory, Columbia University, Palisades, N.Y.

22) Butler, J.N. **1998**. *Ionic Equilibrium.* Wiley-Interscience, New York, 559 pp.

23) Byrne, R.H.; Robert-Baldo, G.; Thompson, S.W.; Chen, C.T.A. **1988**. Seawater pH measurements: an at-sea comparison of spectrophotometric and potentiometric methods. *Deep Sea Res.* 35, 1405-1410.

24) Carbon Dioxide Information Analysis Center (CDIAC), Global Ocean Data Analysis Project (GLODAP), http://cdiac.esd.ornl.gov/oceans/glodap/Glodap_home.htm.

25) Chen, C.-T.A. **1978**. Decomposition of calcium carbonate and organic carbon in the deep oceans. *Science* 201, 735-736.

26) Chen, C.-T.A. **2002**. Shelf-vs. dissolution-generated alkalinity above the chemical lysocline. *Deep-Sea Res. II* 49, 5365-5375.

27) Chen, C.-T.; Millero, F.J. **1979**. Gradual increase of oceanic CO_2. *Nature* 227, 205-206.

28) Chen, C.-T.A.; Pytkowicz, R.M.; Olson, E.J. **1982**. Evaluation of the calcium problem in the South Pacific. *Geochemical J.* 16, 1-10.

29) Chung, S.-N.; Lee, K.; Feely, R.A.; Sabine, C.L.; Millero, F.J.; Wanninkhof, R.; Bullister, J.L.; Key, R.M.; Peng, T.-H. **2003**. Calcium carbonate budget in the Atlantic Ocean based on water column inorganic carbon chemistry. *Global Biogeochem. Cycles* 17, 4-1 – 4-16.

30) Chung, S.-N.; Park, G.-H.; Lee, K.; Key, R.M.; Millero, F.J.; Feely, R.A.; Sabine, C.L.; Falkowski, P.G. **2004**. Postindustrial enhancement of aragonite undersaturation in the upper tropical and subtropical Atlantic Ocean: The role of fossil fuel CO_2. *Limnol. Oceanogr.* 49, 315-321.

31) Clayton, T.D.; Byrne, R.H. **1993**. Spectrophotometric seawater pH measurements: total hydrogen ion concentration scale calibration of m-cresol purple and at-sea results. *Deep-Sea Res. I* 40, 2115-2129.

32) Corliss, J.B.; Dymond, J.; Gordon, L.I.; Edmond, J.M.; von Herzen, R.P.; Ballard, R.D.; Green, K.; Williams, D.; Bainbridge, A.; Crane, K.; van Andel, T.H. **1979**. Submarine thermal springs on the Galapagos Rift. *Science* 203, 1073-1083.

33) Culberson, C.; Pytkowicz, R.M.; Hawley, J.E. **1970**. Seawater alkalinity determination by the pH method. *J. Mar. Res.*, 28, 15-21.

34) Deffeyes, K.S. **1965**. Carbonate equilibria: a graphic and algebraic approach. *Limnol. Oceanogr.* 10, 412-426.

35) DeGrandpre, M.D.; Hammar, T.R.; Smith, S.P.; Sayles, F.L. **1995**. In situ measurements of seawater pCO_2. *Limnol. Oceanogr.* 40, 969-975.

36) de Villiers, S. **1998**. Excess dissolved Ca in the deep ocean: a hydrothermal hypothesis. *Earth Planet. Sci. Lett.* 164, 627-641.

37) de Villiers, S.; Nelson, B.K. **1999**. Detection of low-temperature hydrothermal fluxes by seawater Mg and Ca anomalies. *Science* 285, 721-723.

38) Dickson, A.G.; Riley, J.P. **1978**. The effect of analytical error on the evaluation of the components of the aquatic carbon dioxide system. *Mar. Chem.* 6, 77-85.

39) Dickson, A.G. **1981**. An exact definition of total alkalinity and a procedure for the estimation of alkalinity and total inorganic carbon from titration data. *Deep Sea Res.*, 28A, 609-623.

40) Dickson, A.G. **1984**. pH scales and proton-transfer reactions in saline media such as seawater. *Geochim. et Cosmochim. Acta* 48, 2299-2308.

41) Dickson, A.G., **1992**. The development of the alkalinity concept in marine chemistry. *Mar. Chem.*, 40, 49-63.

42) DOE **1994**. *Handbook of methods for the analysis of the various parameters of the carbon dioxide system in sea water.* Version 2, Dickson, A.G. and Goyet, C. eds. ORNL/CDIAC-74.

43) Dickson, A.G. **2001**. Reference materials for oceanic CO_2 measurements. *Oceanog.* 14, 21-22.

44) Dickson, A.G. **2002**. Dosimat® burette calibration procedure. In-house document, Andrew Dickson Laboratory, Scripps Institution of Oceanography.

45) Dickson, A.G.; Afghan, J.D.; Anderson, G.C. **2003**. Reference materials for oceanic CO_2 analysis: a method for the certification of total alkalinity. *Mar. Chem.*, 80, 185-197.

46) Dyrssen, D.; Hansson, I. **1972-1973**. Ionic medium effects in seawater – A comparison of acidity constants of carbonic acid and boric acid in sodium chloride and synthetic seawater. *Mar. Chem.*, 1, 137-149.

47) Dyrssen, D.; Sillén, L.G. **1967**. Alkalinity and total carbonate in seawater. A plea for p-T-independent data. *Tellus*, 19, 113-120.

48) Edmond, J.M. **1970**. High precision determination of titration alkalinity and total carbon dioxide content of seawater by potentiometric titration. *Deep Sea Res.*, 17, 737-750.

49) EURACHEM/CITAC **2000**. *Quantifying uncertainty in analytical measurement.* 2nd edition, Ellision, S.L.R.; Rosslein, M.; Williams, A. eds.

50) Feely, R.A.; Sabine, C.L.; Lee, K.; Millero, F.J.; Lamb, M.F.; Greely, D.; Bullister, J.L.; Key, R.M.; Peng, T.-H.; Kozyr, A.; Ono, T.; Wong, C.S. **2002**. In situ calcium carbonate dissolution in the Pacific Ocean. *Global Biogeochem. Cycles* 16, 1144, doi:10.1029/2002GB001866.

51) Feely, R.A.; Sabine, C.L.; Lee, K.; Berelson, W.; Kleypas, J.; Fabry, V.J.; Millero, F.J. **2004**. Impact of anthropogenic CO_2 on the $CaCO_3$ system in the oceans. *Science* 305, 362-366.

52) Fletcher, P.J.; van Staden, J.F. **2003**. Determination of carbonate and hydrogencarbonate by titration using sequential injection analysis. *Anal. Chim. Acta* 485, 187-194.

53) Forsythe, G.E.; Malcolm, M.A.; Moler, C.B. **1977**. Computer methods for mathematical computations. Prentice Hall, NJ.

54) Frankignoulle, M.; Canon, C.; Gattuso, J.-P. **1994**. Marine calcification as a source of carbon dioxide: positive feedback of increasing atmospheric CO_2. *Limnol. Oceanogr.* 39, 458-462.

55) Gloor, M.; Gruber, N.; Sarmiento, J.; Sabine, C.L.; Feely, R.A.; Rodenbeck, C. **2003**. A first estimate of present and preindustrial air-sea CO_2 flux patterns based on ocean interior carbon measurements and models. *Geophys. Res. Lett.* 30, 10-1 – 10-4.

56) Gran, G. **1952**. Determination of the equivalence point in potentiometric titrations, part II. *Analyst* 77, 661-671.

57) Graneli, A.; Anfalt, T. **1977**. A simple automatic phototitrator for the determination of total carbonate and total alkalinity of seawater. *Anal. Chim. Acta* 91, 175-180.

58) Gruber, N.; Sarmiento, J.L.; Stocker, T.F. **1996**. An improved method for detecting anthropogenic CO_2 in the oceans. *Global Biogeochem. Cycles* 10, 809-837.

59) Hallock, P. **2005**. Global change and modern coral reefs: New opportunities to understand shallow-water carbonate depositional processes. *Sedimentary Geol.* 175, 19-33.

60) Hansson, I.; Jagner, D. **1973**. Evaluation of the accuracy of Gran plots by means of computer calculations: Application to the potentiometric titration of the total alkalinity and carbonate content in seawater. *Anal. Chim. Acta.* 65, 363-373.

61) Harned, H.S.; Owen, B.B. **1958**. *The physical chemistry of electrolyte solutions.* Reinhold, New York, 803 pp.

62) Herdman, W.A. **1923**. *Founders of Oceanography.* Edward Arnold, London, 340 pp.

63) Hey, M.J.; Hilton, A.M.; Bee, R.D. **1994**. The formation and growth of carbon dioxide gas bubbles from supersaturated aqueous solutions. *Food Chem.* 51, 349-357.

64) Hikita, H.; Konishi, Y. **1984**. Desorption of carbon dioxide from supersaturated water in an agitated vessel. *AlChE J.* 30, 945-951.

65) Holligan, P.M.; Viollier, M.; Harbour, D.S.; Camus, P.; Champagne-Philippe, M. **1983**. Satellite and ship studies of coccolithophore production along a continental shelf edge. *Nature* 304, 339-342.

66) Holligan, P.M.; Fernandez, E.; Aiken, J.; Balch, W.M.; Boyd, P.; Burkill, P.H.; Finch, M.; Groom, S.B.; Malin, G.; Muller, K.; Purdie, D.A.; Robinson, C.; Trees, C.C.; Turner, S.M.; van der Wal, P. **1993**. A biogeochemical study of the coccolithophore, *Emiliania huxleyi*, in the North Atlantic. *Global Biogeochem. Cycles* 7, 879-900.

67) Hood, R.R. **2001**. Modeling biogeochemical cycles in the post-JGOFS era. *Oceanog.* 14, 75.

68) Horowitz, P.; Hill, W. **1989**. *The Art of Electronics*. Cambridge, UK, 1125 pp.

69) Hu, W.; Haddad, P.R.; Hasebe, K.; Tanaka, K. **2001**. A novel ion chromatographic method based on cation-exchange and acid-base interactions for the simultaneous determination of total alkalinity and monovalent cations in samples of μL volume. *Analyst* 126, 555-558.

70) Husheer, S. **2001**. PhD. Thesis, University of Otago, New Zeland.

71) Ingle, J.D.; Crouch, S.R. **1988**. *Spectrochemical Analysis*. Prentice Hall, New Jersey, 590 pp.

72) IUPAC **1997**. Inezedy, J.; Lengyel, T.; Ure, A.M. eds. Compendium of Analytical Nomenclature.

73) Karl, D.M.; Dore, J.E.; Lukas, R.; Michaels, A.F.; Bates, N.R.; Knap, A. **2001**. Building the long-term picture: the U.S. JGOFS time-series programs. *Oceanog.* 14, 6-17.

74) Keir, R.S.; Kounaves, S.P.; Zirino, A. **1977**. Rapid determination of the "titration alkalinity" of seawater by equilibration with CO_2. *Anal. Chim. Acta* 91, 181-187.

75) Kilpatrick, M.; Eanes, R.D. **1953**. The dissociation constants of acids in salt solutions. II. Acetic acid. *J. Am. Chem. Soc.* 75, 586-587.

76) King, D.W.; Kester, D.R. **1989**. Determination of seawater pH from 1.5 to 8.5 using colorimetric indicators. *Mar. Chem.* 26, 5-20.

77) King, D.W.; Kester, D.R. **1990**. Spectral modeling of sulfonephthalein indicators: Application to pH measurements using multiple indicators. *App. Spectrosc.* 44, 722-727.

78) Kleypas, J.A.; Buddemeier, R.W.; Archer, D.; Gattuso, J.-P.; Langdon, C.; Opdyke, B.N. **1999**. Geochemical consequences of increased atmospheric carbon dioxide on coral reefs. *Science* 284, 118-120.

79) Kocherlakota, N.; Obenauf, R.; Thomas, R. **2002**. A statistical approach to reporting uncertainty on certified values of chemical reference materials for trace metal analysis. *Spectroscopy* 17, 20-32.

80) Kolthoff, I.M. **1937**. *Acid-base indicators*. Macmillan, New York, 414 pp.

81)   Korn, M.; Gouveria, L.F.B.P.; de Oliveria, E.; Reis, B.F. **1995**. Binary search in flow titration employing photometric end-point detection. *Anal. Chim. Acta*, 313, 177-184.

82)   Kragten, J. **1994**. Calculating standard deviations and confidence intervals with a universally applicable spreadsheet technique. *Analyst* 119, 2161-2165.

83)   Kruger, R.; Pfenninger, A.; Fournier, I.; Gluckmann, M.; Karas, M. **2001**. Analyte incorporation and ionization in matrix-assisted laser desorption/ionization visualized by pH indicator molecular probes. *Anal. Chem.* 73, 5812-5821.

84)   Langdon, C.; Takahashi, T.; Sweeney, C.; Chipman, D.; Goddard, J.; Marubini, F.; Aceves, H.; Barnett, H.; Atkinson, M.J. **2000**. Effect of calcium carbonate saturation state on the calcification rate of an experimental coral reef. *Global Biogeochem. Cycles* 14, 639-654.

85)   Lee, K.; Choi, S.-D.; Park, G.-H.; Wanninkhof, R.; Peng, T.-H.; Key, R.M.; Sabine, C.L.; Feely, R.A.; Bullister, J.L.; Millero, F.J.; Kozyr, A. **2003**. An updated anthropogenic CO_2 inventory in the Atlantic Ocean. *Global Biogeochem. Cycles* 17, 1116, doi:10.1029/2003GB002067.

86)   Levenspiel, O. **1972**. *Chemical reaction engineering*. John Wiley & Sons, New York, 578 pp.

87)   Liang, Y.Y. **1990**. Automation of Karl Fisher water titration by flow injection sampling. *Anal. Chem.* 62, 2504-2506.

88)   Martz, T.R.; Carr, J.J.; French, C.R.; DeGrandpre, M.D. **2003**. A submersible autonomous sensor for spectrophotometric pH measurements of natural waters. *Anal. Chem.* 75, 1844-1850.

89)   McLafferty, F.W. **1973**. *Interpretation of mass spectra*. W.A. Benjamin, Inc., Reading, MA, 278 pp.

90)   Mehrbach, C.; Culberson, C.H.; Hawley, J.E.; Pytkowicz, R.M. **1973**. Measurement of the apparent dissociation constants of carbonic acid in seawater at atmospheric pressure. *Limnol. Oceanogr.* 18, 897-907.

91)   Mesquita, R.B.R.; Rangel, A.O.S.S. **2004**. A sequential injection system for the spectrophotometric determination of calcium, magnesium and alkalinity in water samples. *Analytical Sciences* 20, 1205-1210.

92)   Metrohm Automated Titration Systems (MATi): www.metrohm.com.

93)   Michaels, A.F.; Karl, D.M.; Capone, D.G. **2001**. Element stoichiometry, new production and nitrogen fixation. *Oceanog.* 14, 68-74,76-77.

235

94) Millero, F.J.; Lee, K.; Roche, M. **1998**. Distribution of alkalinity in the surface waters of the major oceans. *Mar. Chem.*, 60, 111-130.

95) Millero, F.J.; Zhang, J.Z.; Lee, K.; Campbell, D.M. **1993**. Titration alkalinity of seawater. *Mar. Chem.*, 44, 153-165.

96) Milliman, J.D. **1993**. Production and accumulation of calcium carbonate in the ocean: budget of a nonsteady state. *Global Biogeochem. Cycles* 7, 927-957.

97) Milliman, J.D.; Troy, P.J.; Balch, W.M.; Adams, A.K.; Li, Y.-H.; Mackenzie, F.T. **1999**. Biologically mediated dissolution of calcium carbonate above the chemical lysocline? *Deep-Sea Res. I* 46, 1653-1669.

98) Mosley, L.M.; Husheer, S.L.G.; Hunter, K.A. **2004**. Spectrophotometric pH measurement in estuaries using thymol blue and m-cresol purple. *Mar. Chem.* 91, 175-186.

99) Murata, A.; Takizawa, T. **2002**. Impact of a coccolithophorid bloom on the CO_2 system in surface waters of the eastern Bering Sea shelf. *Geophys. Res. Lett.* 29, 1547, doi:10.1029/2001GLO13906.

100) Pankow, J.F. *Aquatic Chemistry Concepts,* Ch. 10; Lewis, Chelsea, **1991**.

101) Park, K.P. **1969**. Oceanic CO_2 system: an evaluation of ten methods of investigation. *Limnol. Oceanogr.* 14, 179-186.

102) Ramette, R.W.; Culberson, C.H.; Bates, R.G. **1977**. Acid-base properties of tris(hydroxymethyl)aminomethane (Tris) buffers in seawater from 5 to 40 °C. *Anal. Chem.* 49, 867-870.

103) Redfield, A.C.; Ketchum, B.H.; Richards, F.A. **1963**. The influence of organisms on the composition of seawater, in *The Sea*, vol. 2, 26-77, Hill, M.N. ed. Interscience, New York.

104) Riley, J.P.; Skirrow, G., **1965**. *Chemical Oceanography*. Academic Press, London, 712 pp.

105) Robertson, J.E.; Robinson, C.; Turner, D.R.; Holligan, P.; Watson, A.J.; Boyd, P.; Fernandez, E.; Finch, M. **1994**. The impact of a coccolithophore bloom on oceanic carbon uptake in the northeast Atlantic during summer 1991. *Deep-Sea Res. I* 41, 297-314.

106) Roche, M.P.; Millero, F.J. **1998**. Measurement of total alkalinity of surface waters using a continuous flowing spectrophotometric technique. *Mar. Chem.* 60, 85-94.

107) Ruzicka, J. **1988**. *Flow Injection Analysis,* 2nd ed. J. Wiley: New York,.

236

108) Ramsing, A.U.; Ruzicka, J.; Hanson, E.H. *Anal. Chim. Acta.* **1981**, 129, 1-17.

109) Sabine, C.L.; Key, R.M.; Johnson, K.M.; Millero, F.J.; Poisson, A.; Sarmiento, J.L.; Wallace, D.W.R.; Winn, C.D. **1999**. Anthropogenic CO_2 inventory of the Indian Ocean. *Global Biogeochem. Cycles* 13, 179-198.

110) Sabine, C.L.; Key, R.M.; Feely, R.A.; Greeley, D. **2002a**. Inorganic carbon in the Indian Ocean: distribution and dissolution processes. *Global Biogeochem. Cycles* 16, 15-1 – 15-18.

111) Sabine, C.L.; Feely, R.A.; Key, R.M.; Bullister, J.L.; Millero, F.J.; Lee, K.; Peng, T.-H.; Tilbrook, B.; Ono, T.; Wong, C.S. **2002b**. Distribution of anthropogenic CO_2 in the Pacific Ocean. *Global Biogeochem. Cycles* 16, 1083, doi:10.1029/2001GB001639.

112) Sarma, V.V.S.S.; Ono, T.; Saino, T. **2002**. Increase of total alkalinity due to shoaling of aragonite saturation horizon in the Pacific and Indian Oceans: Influence of anthropogenic carbon inputs. *Geophys. Res. Lett.* 29, 32-1 – 32-4.

113) Shiller, A.M.; Gieskes, J.M. **1980**. Processes affecting the oceanic distributions of dissolved calcium and alkalinity. *J. Geophys. Res.* 85, 2719-2727.

114) Skoog, D.A.; Holler, F.J.; Nieman, T.A. *Principles of Instrumental Analysis.*, 5th ed.; Harcourt & Brace, Chicago, **1998**.

115) Soli, A.L., Byrne, R.H. **2002**. CO_2 system hydration and dehydration kinetics and the equilibrium CO_2/H_2CO_3 ratio in aqueous NaCl solution. *Mar. Chem.*, 78, 65-73.

116) Stumm, W.; Morgan, J.J. **1996**. *Aquatic Chemistry, 3rd ed.*, Wiley-Interscience, New York, 1022 pp.

117) Suzuki, A. **1998**. Combined effects of photosynthesis and calcification on the partial pressure of carbon dioxide in seawater. *J. Oceanogr.* 54, 1-7.

118) Suzuki, A.; Kawahata, H. **2003**. Carbon budget of coral reef systems: an overview of observations in fringing reefs, barrier reefs and atolls in the Indo-Pacific regions. *Tellus* 55B, 428-444.

119) Suzuki, A.; Nakamori, T.; Kayanne, H. **1995**. The mechanism of production enhancement in coral reef carbonate systems: model and empirical results. *Sedimentary Geol.* 99, 259-280.

120) Sverdrup, H.U.; Johnson, M.W.; Fleming, R.H. **1942**. *The Oceans.* Prentice Hall, Englewood Cliffs, 1087 pp.

121) Takahashi, T.; Sutherland, S.C.; Sweeney, C.; Poisson, A.; Metzel, N.; Tilbrook, B.; Bates, N.; Wanninkhof, R.; Feely, R.A.; Sabine, C.S.; Olafsson, J.; Nojiri, Y. **2002**. Global sea-air CO_2 flux based on climatological surface ocean pCO_2, and seasonal biological and temperature effects. *Deep-Sea Res. II* 49, 1601-1622.

122) Tanaka, H.; Dasgupta, P.K.; Huang, J. **2000**. Continuous on-line true titrations by feedback-based flow ratiometry. The principle of compensating errors. *Anal. Chem.* 72, 4713-4720.

123) Thompson, T.G.; Bonnar, R.U. **1931**. The buffer capacity of seawater. *Ind. Eng. Chem.*, 3, 393-395.

124) Turner, D.R.; Knox, S.; Whitfield, M; dos Santos, M.C. **1987**. Flow injection titration of alkalinity in natural waters. *Anal. Proc.* 24, 360-362.

125) Wanninkhof, R.; Doney, S.C.; Peng, T.-H.; Bullister, J.L.; Lee, K.; Feely, R.A. **1999**. Comparison of methods to determine the anthropogenic CO_2 invasion into the Atlantic Ocean. *Tellus* 51B, 511-530.

126) Watanabe, A.; Kayanne, H.; Nozaki, K.; Kato, K.; Negishi, A.; Kudo, S.; Kimoto, H.; Tsuda, M.; Dickson, A.G. **2004**. A rapid, precise potentiometric determination of total alkalinity in seawater by a newly developed flow-through analyzer designed for coastal regions. *Mar. Chem.* 85, 75-87.

127) Wolery, T.J.; Sleep, N.H. **1976**. Hydrothermal circulation and geochemical flux at mid-ocean ridges. *J. Geology* 84, 249-275.

128) Yamazaki, H.; Gohda, S.; Sperline, R.P.; Freiser, H. **1992a**. Spectrophotometric determination of acid dissociation constant of bromocresol green. *J. Fac. Sci. Technol. Kinki Univ.* 28, 181-188.

129) Yamazaki, H.; Sperline, R.P.; Freiser, H. **1992b**. Spectrophotometric determination of pH and its application to determination of thermodynamic equilibrium constants. *Anal. Chem.* 64, 2720-2725.

130) Yao, W.; Byrne, R.H. **1998**. Simplified seawater alkalinity analysis: use of linear array spectrophotometers. *Deep-Sea Res. I.* 45, 1383-1392.